Condition Assessment of In-Service Timber Utility Poles Utilizing Advanced Digital Signal Processing and Multi-Sensors Array

By

Bahram Jozi

A thesis submitted in fulfilment

of the requirements for the degree of

Doctor of Philosophy

Faculty of Engineering and Information Technology

University of Technology Sydney

February 2015

CERTIFICATE OF AUTHORSHIP/ORIGINALITY

I certify that the work in this thesis has not previously been submitted for a degree nor has it been submitted as part of requirements for a degree except as fully acknowledged within the text.

I also certify that the thesis has been written by me. Any help that I have received in my research work and the preparation of the thesis itself has been acknowledged. In addition, I certify that all information sources and literature used are indicated in the thesis.

Signature of candidate

Bahram Jozi

February 2015

Acknowledgements

This PhD project could not have been possible without the support provided by numerous people. In particular, I would like to express my special appreciation and thanks to my supervisor, Professor Robin Braun for his outstanding guidance, encouragement, wisdom and caring support provided throughout this project. Superior appreciations for my supervisor, Associate Professor Jianchun Li for his encouragement, help and support during my PhD. Utmost gratitude is also forwarded to Prof. Bijan Samali who had given the author invaluable advice, outstanding encouragement and assistance through the course of his study. Special thanks for supervisor, Dr. Ulrike Dackermann for her supports, guidance, and help through my studies.

The author also gratefully acknowledges the financial assistance provided by the University of Technology Sydney, Centre for Built Infrastructure Research (CBIR), and Centre for Real-time information Networks (CRIN) of the Faculty of Engineering, UTS, and Energy Australia an industrial partner.

Moreover, the author would like to acknowledge the Structures Laboratory staff for their help in the experimental and field work. Special thanks must also go to Peter Brown, Rami Haddad, David Hooper, David Dicker, and Richard Turnell. I would also like to thank the members of timber pole project; Amir, Saad, Roman and Ning. To friends and/or colleagues at UTS, the author wishes to express his gratitude. A special appreciation and thanks to my family. Words cannot express how grateful I am to my mother, father, my lovely sisters, and my beloved fiancée for all of the sacrifices that you have made on my behalf. Your prayer for me was what sustained me thus far.

The administrative and the support staff at UTS Faculty of Engineering and IT, Phyllis Agius, Craig Shuard, Van Lee and the IT support team for performing an excellent job in keeping the show running.

To My lovely **Mum**, **Dad, Sisters,**

and **beloved wife**

List of Publications Based on This Research

Journal Articles

1. Jozi, B., Braun, R, and Li, J., (2014), 'A novel, fast, and accurate ultrasonic Non-Destructive Testing method for condition assessment of timber structures utilizing narrow-band chirp excitation', *Journal of Ultrasonics,* (submitted and under Review).

Conference Papers

1. Bahram Jozi, Ulrike Dackermann, Robin Braun, Jianchun Li and Bijan Samali, (2013), 'SEPARATION OF BI-DIRECTIONAL STRESS WAVES FOR THE NON-DESTRUCTIVE CONDITION ASSESSMENT OF IN-SERVICE TIMBER UTILITY POLES', *The 6th International Conference on Structural Health Monitoring of Intelligent Infrastructure*, 9-11 December 2013, Hong Kong.

2. Bahram Jozi, Ulrike Dackermann, Robin Braun, Jiaunchun Li, and Bijan Samali, 'APPLICATION AND IMPROVEMENT OF CONVENTIONAL STRESS-WAVE-BASED NON-DESTRUCTIVE TESTING METHODS FOR THE CONDITION ASSESSMENT OF IN-SERVICE TIMBER UTILITY POLES', *23rd Australasian Conference on the Mechanics of Structures and Materials (ACMSM23)*, 9-12 December 2014, Byron Bay, Australia. (Accepted for presentation)

3. B. Jozi, R. Braun. (2012), 'Design and Develop a sensor and network of sensors in order to investigate the integrity of utility timber poles', *1st Australian Conference on the Applications of systems Engineering ACASE'12,* 6-8 February 2012, Sydney, Australia.

Table of Contents

List of Figures

List of Acronyms

1D	One Dimensional
2D	Two Dimensional
BW	Bending Wave
CW	Compression Wave
DFT	Discrete Fourier Transform
FEM	Finite Element Model
FFT	Fast Fourier Transform
FIR	Finite Impulse Response
F-K	Frequency Wavenumber
FT	Fourier Transform
FW	Flexural waves
GW	Guided Wave
IFFT	Inverse Fast Fourier Transform
IIR	Infinite Impulse Response
IR	Impulse Response
LW	Longitudinal Wave
NDE	Non Destructive Evaluation
NDT	Non Destructive Testing
PCA	Principal Component Analysis
QNDE	Quantitative Non-Destructive Evaluation
SE	Sonic Echo
SKM	Short Kernel Method
SVD	Singular Value Decomposition

Abstract

Timber utility poles play a significant role in the infrastructure of Australia as well as many other countries. There are over 5 million timber utility poles currently used in Australian energy networks, which are more than 80% of total utility poles in the network. Due to the advanced age of Australia's timber pole infrastructure, significant efforts are undertaken by state authorities on maintenance and asset management to prevent utility lines from failure. However, the lack of reliable information regarding their in-service condition, including the embedment length or the degree of deterioration or damage below ground level makes it extremely difficult for the asset managers to make decisions on the replacement/maintenance process with due consideration to economy, operational efficiency, risk/liability and public safety. For example, in order to avoid any failure and considering the public safety, each year approximately 300,000 poles are replaced in the Eastern States of Australia with up to 80% of them still being in a very good serviceable condition, resulting in significant waste of natural resources and money.

In order to address this problem, an R&D program commenced in 2011 at the University of Technology Sydney in collaboration with the Electricity Network Association of Australia. The aim of this study is to design and develop a Non-Destructive Testing (NDT) method with acceptable accuracy, whilst being cost efficient for the condition assessment of the in-service timber utility poles. This research project contains three phases, which will be explained briefly in the following paragraphs.

Several stress wave based NDT methods are currently available and have been used in field applications over the past decades as simple and cost-effective tools for identifying the condition and underground depth of embedded structures, such as poles or piles in service. In this regard, in the first phase of this research, the applicability and efficiency of the currently available NDT methods on the condition assessment of the timber utility poles is investigated through simulation and laboratory tests. Results of the first phase reveal that these surface NDT methods face significant challenges in the condition assessment of the timber utility poles. These challenges are due to presence of uncertainties such as complicated material properties and imperfect body (i.e. timber

pole natural cracks), environmental conditions, interaction of soil and structure, defects and deteriorations as well as an impact excitation type. It is necessary to mention that access to the top of the in-service timber utility poles is prohibitive due to the presence of the electrical or communication wires. In this regard, the hammer impact is applied to the timber pole on its side.

In order to address these complicating factors, in the second phase of this research some advanced digital signal processing methodologies are selected, modified, and employed from different groups of methodologies that can most probably provide solutions. The efficiency of these methodologies is investigated through simulation, laboratory, and field tests. Results of the second phase of this research illustrate that the behaviour of the timber pole under the lateral hammer impact excitation is very complicated. In fact, if dealing with this high level of complexities is not impossible, it is a very difficult task.

In this regard, in the third phase of this research a novel, fast, and accurate ultrasonic narrowband NDT method is proposed as an alternative proposition for the condition assessment of the timber structures. The efficacy of the proposed methodology is verified through the laboratory experiments.

1 Chapter 1: Introduction

1.1 Background

Circular timber poles are used widely for utility poles by electrical distribution and telecommunications industries in Australia as well as in many other countries. There are more than 5 million utility timber poles used in the Australia's energy network for distribution of power and communications. Anecdotal evidences suggest that more than 70% of timber poles were installed after the end of World War II and these poles are likely to require replacement or remedial maintenance in the future. While other countries are facing the same challenges to ensure the optimum management of extensive pole replacement, Australian asset managers are also facing critical timber pole supply shortages.

When life cycle cost is considered, timber poles are significantly cheaper than other alternative materials such as steel, concrete or fibreglass-reinforced plastic composite materials. Furthermore, non-timber poles have different conductive and strength properties and often require different fittings. While alternative materials may be practical to be used for manufactured poles, the cost to completely replace the timber poles is most likely to be prohibitive. In addition, timber poles have considerable environmental advantages compared to the other materials. Less energy is required to produce timber poles and significantly less greenhouse gases are produced.

Lack of reliable information regarding their in-service condition, including the embedment length or the degree of deterioration or damage below ground level makes it extremely difficult for the asset managers to make decisions on the replacement/maintenance process with due consideration to economy, operational efficiency, risk/liability and public safety. While there are a number of techniques used to prevent deterioration and decay (from a combination of insects and fungi) of timber piles/poles, a widespread practice is to simply replace all the piles at regular time intervals. This practice for replacement is currently based on traditional methods of determining a timber pole condition by visual inspection and sounding. Unfortunately,

these methods are not accurate and do not give an adequate indication of pole condition. In fact, these methods in many cases rely on interpretation of information and measurable parameters, which leads to unnecessary replacement of the piles/poles. For example, each year around 30,000 electricity poles are replaced in the eastern states of Australia, despite the fact that up to 80% of these poles are still in a very good serviceable condition. In this regard, a need for a non-destructive testing procedure that produces more quantitative results about the timber pole condition has been developed and meeting that need has become necessary.

Different types of Non Destructive Testing (NDT) methods were developed in the past and used to evaluate the embedment depth and the quality of materials of embedded structures such as concrete piles. Some of these tests have also been utilised on timber piles or poles. Although various types of NDT methods have been developed for evaluating the embedment depth and below ground quality of piles, they are not economical, nor are they environmental friendly or the analysis of their results is not straightforward. Thus, there is a serious need to develop reliable methods, which are economical, environmental friendly and adequately consider the inherent variability of the materials, [1]. Stress wave based NDT methods can potentially offer simple and cost-effective tools for identifying the in-service condition of timber poles. However, when it comes to field applications, these developed/to be developed surface NDTs face a significant challenge due to the presence of uncertainties such as complicated material properties and imperfect body (i.e. timber pole), environmental conditions, interaction of soil and structure, defects and deteriorations as well as coupled nature of unknown length and condition.

NDTs utilising stress wave for determination of the unknown depth of foundations and defects of piles/poles can be divided into two groups: Surface NDT, if access is required only at the surface of the testing structures, or Borehole NDT, if a borehole is drilled close to the foundation structure and extends along its length. Considering the cost/benefit, complexity and applicability in the field, the NDT to be considered as a start point in this research will be limited to the surface stress wave based methods. Therefore, the current available NDTs relevant to the condition assessment of the timber pole are Sonic-Echo (SE) method (based on longitudinal waves) [2], Bending Wave

(BW) method (based on flexural waves) and [3], Ultraseismic (US) method (based on longitudinal and flexural waves) [3].

This industrial supported research project started in 2011 in the University of Technology Sydney (UTS), and aims at developing accurate and reliable non-destructive assessment tools for the timber poles based on the stress wave techniques. It is necessary to mention that the project has started from the outset with minimum information available about the timber pole including the effects of its orthotropic material properties, and wave propagation in the timber pole.

This research project can be explained briefly in three phases as follows:

1. Given that several surface stress wave based NDT methods are currently available for the condition assessment of the timber utility poles, the first phase of this research involves full-scale investigations for use of selected aforementioned NDT methods for identification of in-ground length of embedded timber poles through finite element (FE) modelling data analysis, laboratory experiments and field testing. This phase of the project provides comprehensive evaluation of the selected NDT methods in terms of reliability, accuracy, and quantifying limitations for the timber poles. Furthermore, the research in this phase will provide guidelines for implementation of these NDT methods including any necessary improvements of the methods and their analysis and application on timber materials. It is worth mentioning that all of these tests are performed with the hammer impact, which excites the timber pole in a broadband low frequencies range of 0 to 5 kHz. It should also be remembered that in the low frequency range, 0-5 kHz is considered as a broadband impact excitation.

2. Results of the first phase reveal that currently available surface stress wave based NDT methods are not mature enough for condition assessment of the in-service timber poles due to complicating factors such as orthotropic material properties, soil embedment, and complex wave behaviour under broadband low frequency range excitation. Given that the currently available surface stress wave based methods are not suitable for the condition assessment of the in-service timber pole, in the second phase of this research some advanced digital

signal processing methodologies are selected, modified, and employed (from different groups of methodologies that can most probably provide solutions) to address these complicated factors. All of the methods are investigated through FE data analysis, laboratory experiments and field testing. A hammer impact is applied on the side of the pole due to practical constraints (i.e. in field testing, access to the top section of timber utility poles is prohibitive because of the presence of the electrical wires). It is also applied at a 45º angle in order to maximize the chance of producing longitudinal wave in the lateral impact.

3. Based on the results of the second phase of this research, the behaviour of the timber pole under the lateral and angled broadband low frequency impact excitation (i.e. hammer impact on the side of the timber pole at a 45° angle) is very complicated. Given the fact that if dealing with this high level of complexities is not impossible, it is very difficult, in the third phase of this research a novel, fast, and accurate ultrasonic narrowband NDT method is proposed as an alternative proposition for condition assessment of the timber structures. The efficacy of the proposed methodology is verified through the laboratory experiments.

Figure 1.1 demonstrates the procedure diagram of this research project.

1.2 Research Scope

This research is concerned with the development and use of robust and cost effective surface stress wave based NDTs for length determination in timber pole/pile structures. The scope of this study is limited to the following areas:

1. The investigation, application, and improvement (if applicable) of currently available surface stress wave based non-destructive methods for the timber pole condition assessment through numerical (simulation), and experimental tests.

2. The investigation of the surrounding environment, including soil embedment that influences the performance of current and proposed methods, especially those associated with field applications.

INTRODUCTION

Timber utility poles represent a significant part of Australia's infrastructure and their condition assessment is crucial in order avoid any failure, which can cause fatal and not amendable consequences. In this regard, an industrial funded research project has started and aimed to provide an accurate and reliable Non-Destructive methodology for the condition assessment of the timber utility poles. More details can be found in chapter 2.

PROBLEM DEFINITION

Several NDT methods have been developed during the past decades to evaluate the condition of the concrete piles and occasionally timber piles. amongst all, surface stress wave based methods are the most fast, economic and environmental friendly ones. However, these methodologies are not mature enough for the condition assessment of the timber utility poles due to complicating factors such as orthotropic material properties, soil embedment, and complex wave behaviour in the timber pole under lateral and angled broadband low frequency impact excitation (i.e. hammer impact on side of the timber pole at a 45° angle). More details can be found in chapters 2 and 5.

PROPOSITIONS

1. Given that the currently available surface stress wave based NDTs are not mature enough for the condition assessment of the timber utility poles, specific advanced digital signal processing methodologies are selected, modified and employed to address the existing complexities.
2. Given that the behaviour of the timber pole under the broadband low frequency impact excitation is very complicated and dealing with this high level of complexities is very difficult, a novel, fast and accurate ultrasonic narrowband NDT method is proposed as an alternative proposition for condition assessment of the timber structures.

1. Broadband low frequency impact excitation

METHODOLOGY

Timber pole is defined as a Linear Time-Invariant (LTI) system from signal processing point of view.

Most common and effective advanced digital signal processing methodologies are selected from two groups of methodologies that are most probable to provide solution.

All selected methodologies are modified and employed on the data obtained from numerical (simulation), experimental, and field testings.

RESULTS

Selected methodologies are very effective on the simulated isotropic timber poles, and the embedment length can be estimated with very high accuracy. While they do not provide satisfactory results in simulated orthotropic timber poles as well as experimental and field testings. This happens due to the highly complex behaviour of the timber pole under the lateral and 45° broadband low frequency hammer excitation.

2. Narrowband high frequency excitation

METHODOLOGY

A novel, fast and accurate ultrasonic NDT is proposed as an alternative proposition for condition assessment of imber structures.

An ultrasonic NDT system is designed and implemented.

Two types of tests are performed which are related to the currently available ultrasonic single frequency time-of-flight test (in order to create a benchmark for further comparisons), and proposed ultrasonic NDT in this research

RESULTS

Effectiveness and accuracy of the proposed methodology is verified through the experimental testings on the timber structure.

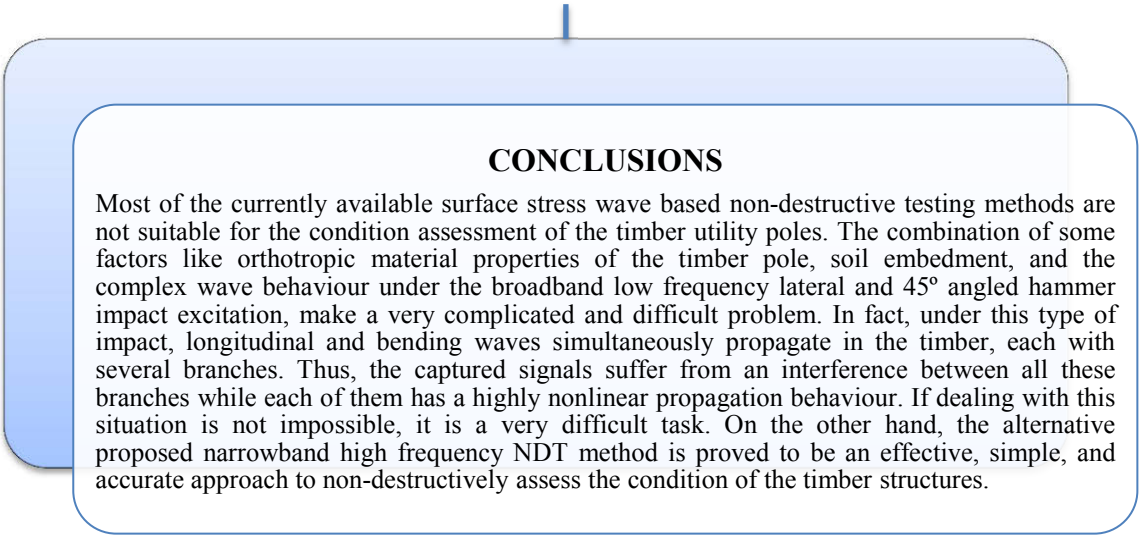

Figure 1.1: Procedure diagram of this research project

3. The investigation of various advanced digital signal processing techniques in order to estimate the wave velocity and determine the embedment length of the utility timber poles. Aforementioned digital signal processing methods are:

    a. Short Kernel Method [4]

    b. Deterministic signal separation methods such as deconvolution, and digital filters [5] [6] [7]

    c. Blind signal separation methods such as Principal Component Analysis (PCA), Singular Value Decomposition (SVD), and *K*-mean clustering algorithm [8] [9] [10]

    d. Frequency-Wavenumber (F-K) velocity filtering [11]

    It is also necessary to consider that deterministic signal separation, blind signal separation, and frequency-wavenumber velocity filtering are the three groups of advanced digital signal processing methodologies that are the most probable to provide solutions.

4. The numerical verification of selected aforementioned advanced digital signal processing methods with the following aims and details:

a. Verification with isotropic material properties to gain understanding of stress wave propagation in timber poles without any uncertainties related to the experimental testing.

b. Verification with orthotropic material properties to not only gain more understandings of stress wave propagation in timber poles more related to the real in-field ones, but also to make comparisons with the isotropic case.

5. Investigations of applicability and effectiveness of the mentioned advanced digital signal processing methodologies on the condition assessment of the timber poles through experimental and in-field testings.

6. Providing an alternative proposition for condition assessment of the timber structures, and validating the proposition through the experimental investigations.

1.3 Research Objectives

The literature review suggests that there is very limited research conducted in surface wave based NDTs on the pole applications, while applications on piles are rather field practice- driven from practicing engineers and consultants, which are based on the methods developed a few decades ago.

The aim of this research is to evaluate the condition of the piles/poles considering the interaction between poles and their surrounding soil. In this regard, firstly currently available surface stress wave based NDT methods are investigated, then based on the obtained results and given that currently available NDT methods are not suitable and accurate enough for this research aim, several advanced digital signal processing techniques are nominated, modified, and employed to deal with the intrinsic complexities of the project. The capabilities and limitations of the employed advanced digital signal processing methods are investigated using numerical, experimental, and field studies. Finally, given that the behaviour of the timber pole under the lateral and angled broadband low frequency impact excitation is very complicated and dealing with this high level of complexities is very difficult, a novel, fast and accurate ultrasonic

narrowband NDT method is proposed as an alternative proposition for the condition assessment of timber structures.

The specific objectives of this research work are:

1. To conduct numerical investigations to evaluate and assess the current NDT techniques in terms of reliability, accuracy and limitations, with the following objectives:

    a. To investigate the applicability and effectiveness of the currently available surface stress wave based NDTs on the condition assessment of the timber poles.

    b. To develop an understanding of the stress wave propagation of the longitudinal and bending waves utilizing multi-sensors array.

    c. To improve the currently available surface NDT methods in terms of the stress wave velocity estimation and determining the embedded length of the timber poles.

    d. To investigate the impact of the environment including soil embedment on the wave propagation from the signal processing point of view.

    e. To investigate the applicability of the lateral and 45º angled impact at a reachable height above the ground level (i.e. 1.5 m) on the condition assessment of the timber pole.

    f. To study selected and modified advanced digital signal processing methods from a different group of possible solutions (i.e. deterministic signal separation and blind signal separation methods) for the timber pole condition assessment under the broadband low frequency hammer impact excitation.

2. To conduct laboratory, and in-field investigations to validate the modified methods with the following details:

a. To investigate the applicability and effectiveness of the currently available surface stress wave based NDTs on the condition assessment of the timber poles

b. To experimentally investigate the applicability of the lateral and 45º angled impact at a reachable height above ground level (i.e. 1.5 m) on the condition assessment of the timber pole

c. To study selected and modified advanced digital signal processing methods for the timber pole condition assessment under the broadband low frequency hammer impact excitation

d. To experimentally investigate the impact of environmental conditions such as soil embedment on the wave propagation from the signal processing point of view

3. To propose, and experimentally validate a novel, fast and accurate narrowband high frequency (ultrasonic range) NDT technique as an alternative solution for the condition assessment of the timber structures. Experimental investigations include design and implement an ultrasonic NDT system in order to experimentally investigate and compare the efficiency and accuracy of the proposed narrowband high frequency NDT methodology with the conventional ultrasonic NDT method.

1.4 Summary of Contributions

The principal contribution of this study is to comprehensively investigate the applicability and effectiveness of not only currently available surface stress wave base NDT methods, but also several advanced digital signal processing methodologies on the condition assessment of the timber utility poles under broadband low frequency impact excitation, and to identify their limitations and in some cases make improvements to increase the reliability of outcomes. More details of the original contributions of this research follow:

From a literature review, it is realized that there are only the few works reported on using surface stress wave based NDTs to determine the embedded length in timber structures. Thus, in the first phase of this study, existing surface stress wave based non-

destructive methods are examined for length determination of the timber pole. The timber pole has also been impacted on its side at a reachable height above the ground level by a hammer (lateral and 45º angled broadband low frequency excitation). This is not only due to practical constraints (i.e. in-field testing, access to the top section of timber utility poles is prohibitive) but also to gain an understanding of the generated waves/wave branches. Furthermore, changes in geotechnical and boundary conditions and interference of other media on determination of length of the timber poles are considered. Based on the results obtained from the first phase, in the second phase of this research several advanced digital signal processing methodologies have been chosen and modified to deal with the existing complexities in this project. These complexities are due to the complicated timber pole behaviour and response under the lateral and 45° angled broadband low frequency hammer impact excitation. Considering the results from the first phase and the second phase of this research, in the third phase a novel, fast, and accurate ultrasonic NDT methodology has been proposed and validated in order to overcome the intrinsic complexities that exist in the timber structures condition assessment utilizing surface stress wave based NDTs. The contributions of this study in point form are as follows:

1. Selecting currently available surface stress wave based NDTs numerically and experimentally investigated in terms of reliability, accuracy and limitations, for determination of embedded length of poles below the ground level. It is worth mentioning that the first criterion of the condition assessment of the timber poles is embedment length estimation (more explanations can be found in section 2.2).

2. Providing the limitations of the currently available surface stress wave based NDT methods through numerical, experimental, and field tests investigations.

3. Providing recommendations for improvements of selected currently available surface stress wave based NDT methods for the utility timber poles.

4. Nominating, and investigating the applicability and effectiveness of some advanced digital signal processing methodologies to overcome the intrinsic complexities, which exist in the project. In order to cover the most possible types of solutions, the advanced digital signal processing methodologies have been selected from the three groups of digital signal processing techniques that

are most probable to provide solutions (i.e. deterministic signal separation, blind signal separation, and frequency-wavenumber velocity filter methodologies).

5. Providing the limitations of selected advanced digital signal processing methodologies through the numerical, experimental and field tests investigations.

6. Providing the limitations of the lateral and 45° angled broadband low frequency hammer impact excitation on the condition assessment of the timber utility poles.

7. Proposing and verifying a novel ultrasonic NDT as an alternative solution to the complexities that intrinsically exist in the Non-Destructive condition assessment of the timber structures.

1.5 Outline of the Thesis

This thesis consists of eight main chapters, organised as follows:

Chapter 1 presents an introduction to the work, the objectives of the study, the scope of the work and the contribution to knowledge.

Chapter 2 outlines a literature review and a brief history of timber pile/poles in Australia and a review of different non-destructive test techniques that can be used or already employed for determining length and condition of timber/concrete piles/poles. This chapter also covers classification of different wave types including relevant characteristics of those wave types. This chapter then provides details of the signal processing methodologies that have been used in the currently available surface stress wave based NDTs, which are then explained and studied. In the final section of this chapter, the limitations of the currently available NDTs and the necessity of utilizing advanced digital signal processing have been briefly explained.

Chapter 3 provides the mathematical explanations of the selected advanced digital signal processing methodologies which have been modified and employed in this project to deal with the existing complexities. In this chapter, firstly the timber pole is defined as a Linear Time-Invariant (LTI) system from a signal processing point of view. In this definition, captured signals from sensors that are attached to the timber pole are

mathematically expressed as the convolution of the input signal to the pole (i.e. hammer impact) with the impulse response of the timber pole. In this regard, all useful and vital information for the condition assessment of the timber pole exists in its impulse response, which is firstly needed to be extracted from the captured signals and then analysed separately for different criteria of the condition assessment. In this project the first criterion of the condition assessment (i.e. determination of the embedment length of the timber pole under the ground) is being considered.

In order to extract the useful information from the captured signals, the probable groups of methodologies that can provide solutions to this problem are nominated. These methods are categorized into the three main groups of; deterministic signal separation, blind signal separation, and frequency-wavenumber velocity filter. Then the most common and effective signal processing methodologies are selected, modified and employed from each group. Wiener and predictive deconvolution, and digital filters are selected from the deterministic signal separation methods. Principal Component Analysis (PCA), Singular Value Decomposition (SVD), and *K*-mean clustering are chosen amongst the blind signal separation methods.

Chapter 4 describes the test procedures and test equipment used in the experimental and field testings. The overview of the test specimens, and experimental set-ups for different types of tests are presented in this chapter. In the longitudinal and flexural impact method, a stress wave is generated with an impact from a modal hammer. In the both cases, the responses are measured with accelerometers, and the input and response are recorded with a program coded in the LabVIEW programming language.

Chapter 5 presents the results of the longitudinal and lateral impact tests performed on the experimental testings under a standing-on-soil or an embedded condition to verify the applicability of currently available surface stress wave based NDTs presented in Chapter 2. A longitudinal wave has been induced by a hammer impact to the top of the pole and a flexural wave is induced by a hammer impact to the side of the pole, and the response is measured by means of the accelerometers. The accelerometers were mounted to the side of the pole. The results are analysed to determine the stress wave velocity and embedded length of a timber pole. Limitations of currently available surface stress wave based NDTs that were briefly addressed in the last section of chapter 2 are discussed comprehensively in this chapter.

In Chapter 6, results of employing selected and modified advanced digital signal processing methodologies (which are provided in Chapter 3) on the data obtained from the numerical, experimental and field testings with lateral and 45° angle hammer impact are provided. Limitations of the aforementioned impact type on the non-destructive condition assessment of the timber pole are discussed and studied systematically in this chapter.

In Chapter 7, a novel, fast and accurate ultrasonic NDT methodology is proposed as an alternative solution for the condition assessment of the timber structures. This methodology is proposed based on the results and understandings obtained from previous chapters (which are related to the complexities, which exist due to the broadband low frequency excitation especially when it is applied on the side of the specimen with a 45° angle). In this chapter, firstly the proposed methodology is fully explained. Then the experimental test procedures, different types of performed tests and equipment that was utilized are described. In this phase of the research, firstly, an ultrasonic NDT system is designed and implemented, and then two types of tests are performed. The first set is related to the ultrasonic single frequency time-of-flight testing which is currently available and extensively utilized in industry and research all around the world. The first set is performed with the intention of achieving the required accuracy of the implemented ultrasonic NDT system and have a benchmark to compare the results of the proposed methodology with. The second sets of tests are related to the proposed methodology. In the last section of this chapter, effectiveness and accuracy of the proposed methodology is verified through provided results of the experimental testings. The proposed methodology in this chapter shows a significant potential to be used in industrial applications.

Chapter 8 summarises the work presented in this thesis and presents conclusions regarding:

- The applicability and limitations of the currently available surface stress wave based non-destructive testing methods on timber utility poles condition assessment

- The effectiveness and limitations of selected and modified advanced digital signal processing methodologies on the timber utility poles condition assessment under broadband low frequency lateral and 45° angled excitation.
- The limitations of the broadband low frequency (i.e. hammer) lateral and 45° angled excitation on the Non-Destructive condition assessment of the timber pole
- The effectiveness and accuracy of the proposed alternative proposition on condition assessment of the timber structures

This chapter also draws conclusions and gives recommendations for future work.

2 Chapter 2: Literature review

2.1 Timber poles as a critical infrastructure

Timber utility poles play a significant role in the infrastructure all around the world especially in Australia, which have been taken for granted [12]. They have been widely used as utility poles for power and telecommunications networks. As reported by [13], there are more than 5 million utility timber poles currently in-service throughout Australia's energy networks (Table 2.1).

Table 2.1: Estimated quantities of poles in-service throughout Australia in 2004 [13]

State / Territory	Timber	Concrete	Metal	Other	State Total
New South Wales (NSW)	2,055,651	93,398	40,229	400	2,189,678
Queensland (Qld.)	1,260,042	35,951	27,764	0	1,323,757
Victoria (Vic.)	823,934	265,282	21,949	5,370	1,116,535
South Australia (SA)	0	78	211	655,763	656,052
Tasmania (Tas.)	194,451	46	7,108	6,868	208,473
Western Australia (WA)	681,536	12,334	20,808	0	714,678
Northern Territory (NT)	0	95	38,125	0	38,220
Australian Capital Territory (ACT)	50,098	7,031	2,758	375	60,262
Total	5,065,712	414,215	158,952	668,776	6,307,655

According to the review of Australian Timber Pole Resources for energy networks conducted by [14], many of the currently installed timber poles are required to be replaced or receive remedial maintenance over the next decade. Based on the cost assumption of $500 for a new timber pole, 1.75 billion dollars would need to be invested to achieve 3.5 million replacement timber poles that may soon be required. Furthermore, poles are required for new lines, costing 13.5 million dollars per annum with the assumption of constant demand at half of the total demand by utilities in 2005

in the future years. Besides, Australian timber pole stakeholders are facing a critical pole supply shortage.

Although using alternative materials may be practical in some locations, the cost to completely replace timber poles is likely to be too expensive. Considering the whole life cycle costs, timber poles are significantly cheaper than most manufactured alternative poles made of steel, concrete or fibreglass-reinforced composite materials. Besides, non-timber poles have different conductive and dynamic strength properties and require different fittings.

Timber poles produced from sustainably-managed forests are a renewable resource, and in addition to economic benefits, life cycle analysis show that timber poles have considerable environmental advantages compared with poles constructed from more energy intensive manufactured materials. Considering raw material production, treatment, installation, inspection, maintenance and disposal, it has been emphasized that considerably less energy is required to produce timber poles and significantly less greenhouse gases are therefore, produced [15].

The major disadvantages of using timber poles are the current supply shortage, their shorter service-life, the requirement of more maintenance and the need for recycling industries to continue to be established and preservative recovery technologies to be fully optimised.

Timber is a natural material and its properties could not be controlled by manufacturing and these properties show intrinsic variability. The presence of natural defects such as knots, splits, and checks, and the wide diversity of species available for various end uses, add to this variability.

Wood may be described as an orthotropic material. It has unique and independent mechanical properties in the directions of three mutually perpendicular axes: longitudinal, radial, and tangential. The longitudinal axis is parallel to the fibre; the radial axis is normal to the growth rings (perpendicular to the grain in the radial direction); and the tangential axis is perpendicular to the grain but tangent to the growth rings. These axes in wood are shown in Figure 2.1. The speed of sound varies with grain direction because the transverse modulus of elasticity is much less than the longitudinal

value. The speed of sound across the grain is about one-fifth to one-third of the longitudinal value [16].

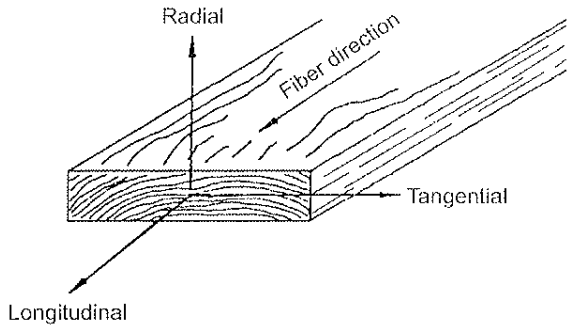

Figure 2.1: Three principal axes of wood with respect to grain direction and growth rings [16]

The speed of sound decreases with increasing temperature or moisture content in proportion to the influence of these variables on the modulus of elasticity. The environmental conditions in which wood is used are very important because moisture content of the wood dramatically affects its mechanical properties and its vulnerability to degradation by decay [17].

2.2 Timber piles/poles condition assessment criteria

Timber poles are used as simple cantilever beams and/or slender columns. As reported by Rural Utilities Service construction standards, these poles may have a maximum line angle of 5 degrees [18]. Because tangent poles are not supposed to be located at a sharp angle turn in the line, they typically resist only the forces due to wind, ice, gravity, and the forces from unbalanced tension in the conductors or other utility wires. For some poles, in addition to horizontal forces and their resulting moments caused by the wind and vertical forces from permanent actions, poles must resist loads in both horizontal and vertical directions due to guywires. Consequently, they should have adequate embedded length to resist those forces. For some of the utility poles that were installed in the past, no information is available regarding the depth of the utility poles. In this regard, a first step in the in-service timber utility poles condition assessment is embedment length estimation [15].

Furthermore, environmental factors such as weather, age, or even moisture can damage the timber poles. However, the main damage occurring around the ground line is

associated with fungi. [19] suggested four typical decay patterns of a timber pole's cross section below the ground line as illustrated in Figure 2.2.

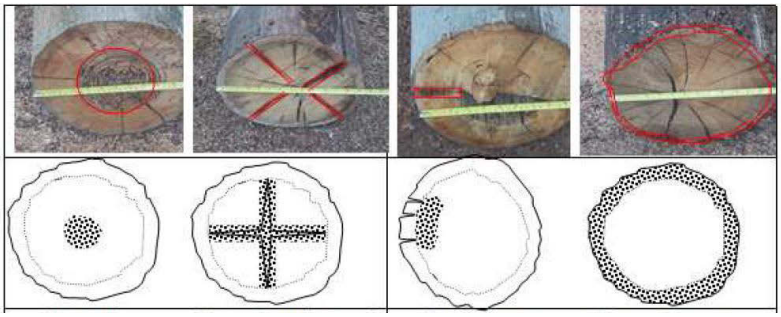

Decay from center zone	Decay from internal cracks	Decay due to external cracks	Decay from outer surface
Type 1	Type 2	Type 3	Type 4

Figure 2.2: Possible decay patterns in underground sections of utility poles [19]

It is also worth mentioning that since timber pole is an orthotropic by nature even single wave propagation is complicated (see section 2.6) and processing of the signals captured by sensors attached to the pole is a difficult task. This situation is worse when there are at least two types of waves propagating through the timber pole simultaneously. Considering this situation, only first step of the condition assessment of the timber poles (i.e. embedment length estimation) is considered and investigated in this research.

2.3 Conventional methods for assessment of timber structures

Currently used inspection methods for timber poles involve visual inspection, probing, sounding, drilling and coring.

2.3.1 Visual inspection method [20]

"Visual inspection is the simplest method that has been used in locating deterioration in the timber structures. An inspector observes the structure for signs of actual or potential deterioration, noting areas for further investigation. Visual inspection requires strong

light and strongly depends on the experience of the inspector. This method is useful for detecting intermediate or advanced surface decay. Visual inspection cannot detect decay in the early stages, when remedial treatment is most effective. Furthermore, it cannot accurately determine the extent of deterioration in timber structures. This method should never be considered as the sole method for condition assessment of the timber structures [20]."

2.3.2 Probing [20]

"Probing with a moderately pointed tool, such as an awl or knife is another primitive method that has been used to locate decay near the wood surface as indicated by excessive softness or a lack of resistance to the probe penetration and the breakage pattern of the splinters. A brash break indicates decayed wood, whereas a splintered break reveals sound wood. Although probing is a simple inspection method, experience is required to interpret the results. Care must be taken to differentiate between decayed and water-softened wood that may be sound but somewhat softer than dry wood. It is also sometimes difficult to assess damage in soft-textured woods such as western red cedar [20]."

2.3.3 Sounding [20]

"In this method, the wood surface is struck with a hammer or other objects, and then based on the tonal quality of the ensuing sounds, a trained and experienced inspector can interpret dull or hollow sounds that may indicate the presence of large interior voids or decay. Even though sounding is widely used, it is often difficult to interpret the results because conditions other than decay can also contribute to variations in sound quality. Moreover, sounding provides only a partial picture of the extent of decay present and will not detect wood in the early or intermediate stages of decay. Nevertheless, sounding has still been used in the inspection process and can quickly identify seriously decayed structures. When suspected decay is encountered, it must be verified by other methods such as boring or coring. Practical experience has shown that sounding only works with members less than 89 mm (3.5 inches) thickness [20]."

2.3.4 Drilling and coring [15]

"Drilling and coring are the most common methods used to detect internal deterioration in the wood members. Both techniques are used to detect the presence of cavities and determine the thickness of the residual shell when voids are present. Drilling and coring are similar in many aspects and are discussed together. Drilling is usually done with an electrical power or hand-crank drill equipped with a 9.5- to 19-mm- (3/8- to 3/4-inches) diameter bit. Power drilling is faster, but hand drilling allows the inspector to monitor drilling resistance and may be more beneficial in detecting pockets of deterioration. In general, the inspector drills into the member in question, noting zones where the drilling becomes easier, and observes the drill shavings for evidence of decay. The presence of common wood defects, such as knots, resin pockets, and abnormal grain, should be anticipated while drilling and should not be confused with decay [15]."

2.4 Non-Destructive Evaluation (NDE)

The field of Non-destructive Testing (NDT) is a wide, multi-disciplinary field that plays a critical role in assuring about the functionality of structural components and systems in a reliable and cost-effective approach. In NDT, engineers design and implement tests that locate and characterize material conditions and defects that might otherwise cause disasters such as planes to crash, reactors to fail, trains to derail, etc.. These tests are performed in a manner that does not affect the future usefulness of the object or material. In other words, NDT allows parts and material to be inspected and measured without causing any damage to them. Because it allows inspection without interfering with a product's final use, NDT provides an excellent balance between quality control and cost-effectiveness. It has wide applications in a variety of engineering fields such as mechanical, electrical, and civil engineering [21]. There have been major developments in NDTs in the past 30 years. It was firstly acknowledged in the mid-1970s that for NDTs to meet the needs of high-technology industries, such as aerospace, oil, and gas, it needed to become a more quantitative science-based technology. Research was initiated in several countries, and as a result new capabilities were developed that are part of what is now called "quantitative non-destructive evaluation," (QNDE) and is commonly referred to as non-destructive evaluation (NDE) and quantitative non-destructive evaluation (QNDE) [22] [23].

2.5 Non-destructive evaluation methods for assessment of timber structures

NDT has been applied massively in the field of the Civil engineering especially in the condition assessment of structures and materials. As mentioned earlier, timbers are one of the main and important materials that have been used as an infrastructure in civil engineering. In this regard, a large number of non-destructive tests have been proposed and effectively applied on timber structures' condition assessment. In the case of piles/poles, most effective NDT methods are visual inspection, sounding and stress wave. As previously explained, the reliability of the visual inspection and sounding methods depend heavily on the experience of the technician or test performer [24]. On the other hand, stress wave methods are much simpler and economical. Stress waves can be made in the structure because of deformation caused by an impact excitation. These waves propagate through the structure like a propagation of sound waves through the air. Due to the dependency of these waves' velocity to the modulus of elasticity, Poisson's ratio, density, and geometry of the structure [1], studying these waves can give the structure's condition.

Stress wave methods can be categorized into two main groups, surface wave based methods and borehole methods. In surface wave based method, there is only need to have access to the structure surface in order to apply excitation impact, and attach transducers to detect wave reflections. In the borehole methods, a borehole is needed to be drilled near the structure in order to send the transducer along the hole and monitor the wave reflections. Although borehole methods are so accurate in finding the embedded length of the shallow structures under the ground, they are not only so expensive but also not able to provide embedded length of such foundations with underlying pile caps [25].

In surface stress-wave-based method, a disturbance caused by the excitation impact propagates through a medium in terms of three different waves: longitudinal waves (also known as dilatational, P-wave, or compressional wave), bending waves (also known as flexural waves), and Rayleigh waves (also known as R-wave, surface wave). In the longitudinal waves, the direction of vibration is the same as the direction of propagation, which means particles of the medium move in the same or the opposite

direction to the motion of the wave. In contrast, in the bending waves, medium particles movement is perpendicular to the direction of the wave travel. Rayleigh wave travels across surfaces and moves in ellipses in planes normal to the surface and similar to the direction of wave propagation (see Figure 2.3) [1].

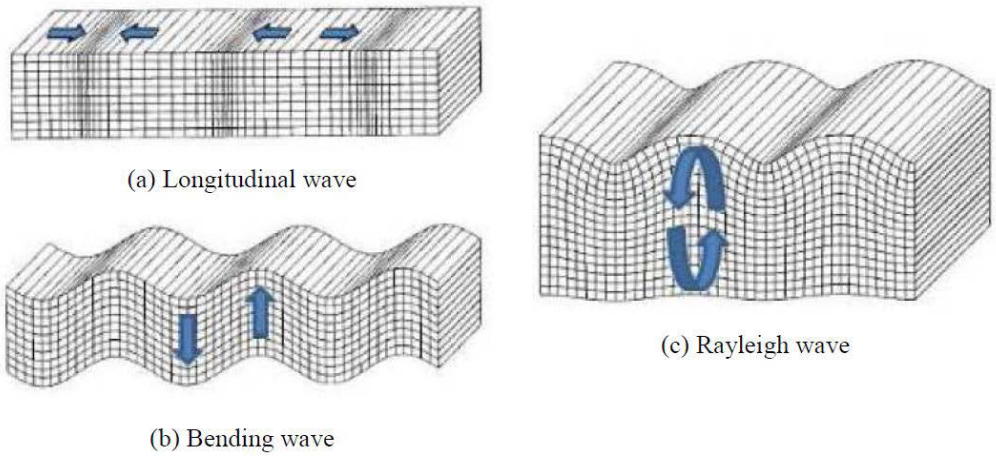

Figure 2.3: Three different kinds of stress waves [26]

Through the past decades, several surface stress-wave-based NDT methods have been proposed based on the different types of wave processing. For instance, based on the longitudinal wave Sonic-Echo, and based on the bending wave Short Kernel method, have been introduced. Some methods use both of the longitudinal and flexural waves such as Ultraseismic. In the following, each of the surface stress-wave-based methods and two of the most common and effective borehole methods are explained. It is essential to consider that since the borehole methods are very costly and not environmentally friendly, they have not been used in this research.

2.5.1 Sonic-Echo method (SE)

Sonic-Echo method (also known as Seismic Echo, Impulse Echo, Pulse Echo method and Pile Integrity Test), is the first surface stress wave based NDT method to become commercially available [27] [28] [29]. In this test, the excitation impact is applied on top of the pile/pole structure which causes the longitudinal wave. The next step is to identify the signal associated with the stress wave travelling from the impacted point, reflecting at the bottom surface of the pile and travelling back to the transducer. The reflected wave (echo) can be measured in terms of a displacement, velocity, or

acceleration as a function of time by one sensor located near the impact location. Figure 2.4 shows the Sonic-Echo test setup.

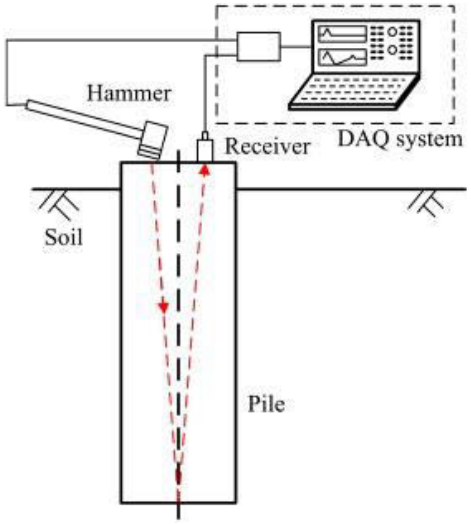

Figure 2.4: Sonic-Echo method [2]

Once the travelling time Δt of the echo is determined, the length L of the pile can be estimated through the equation (2.1) [2], (see Figure 2.5).

$$L = \frac{V_c \Delta t}{2} \tag{2.1}$$

Where V_c is the longitudinal wave velocity in the pile.

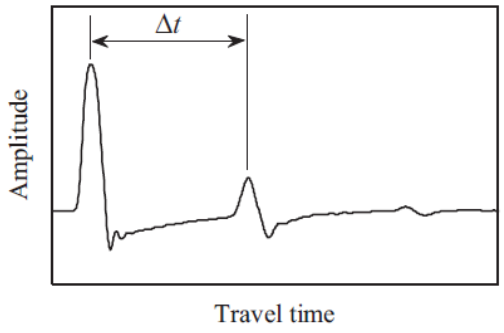

Figure 2.5: Captured signal in the Sonic-Echo method test (ibid)

Huang et al investigated the effect of defect depth and size on a captured reflection by numerical data without noise. They introduced a defect depth to pile diameter ratio L_D, and defect size ratio as the size of defect to diameter of the pile R_D. Their results (Figure 2.6) illustrated that if the defect depth ratio surpasses 20%, or the defect size ratio fall

behind 15%, reflection detection (showed by an arrow in Figure 2.6) would be almost impossible. The situation is worse in the presence of noise [30].

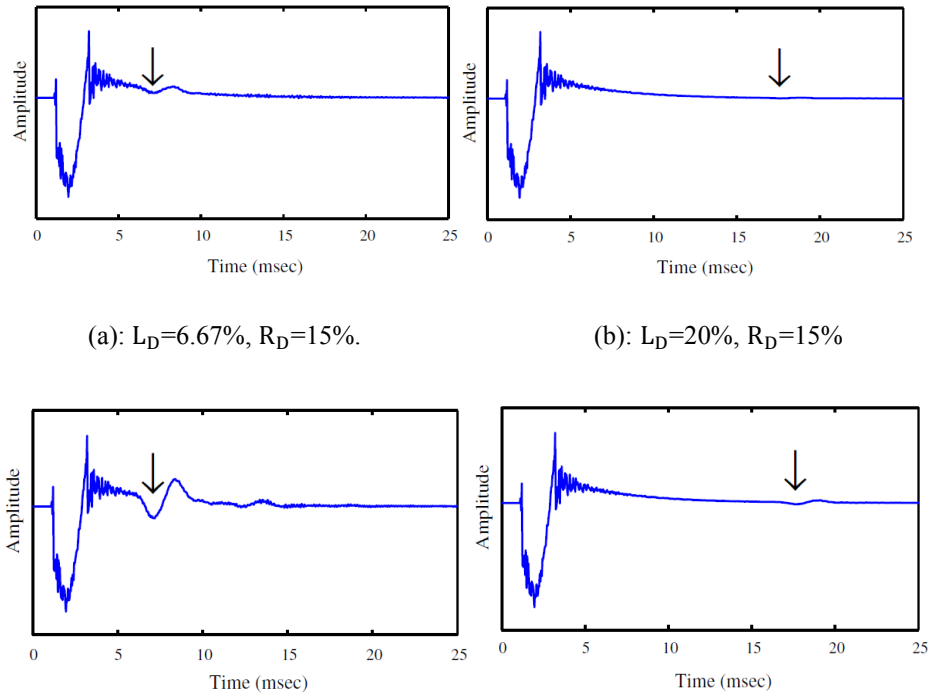

(a): L_D=6.67%, R_D=15%. (b): L_D=20%, R_D=15%

(a): L_D=6.67%, R_D=59%. (b): L_D=20%, R_D=59%

Figure 2.6: Huang et al investigation on damage depth L_D and size R_D. (ibid)

The Federal Lands Highway Administration [25] tested several foundation piles of bridges. After collecting the data and analysis, researchers found that the SE method works best for piles or drilled shafts without any structure on top. Typically, this method is performed on piles for ratios of length-to-diameter (L/D) up to 20:1. When these methods are applied to piles with length-to-diameter ratios higher or equal than 30:1, they are only reliable for softer soils due to the effects of the soil on the results. This method also can only detect large damage with cross-sectional area greater than 5% of the pile diameter. A study conducted by the University of Houston at the National Geotechnical Experimentation Site also revealed that for a pile with L/D ratio of less than 20:1, the pile length can be predicted more accurately and the success rate can reach at least 80%. If the L/D rate increases to 30, the success rate will decrease rapidly.

Another limitation of these methods can be addressed as they work best for columnar type foundations such as piles and drilled shafts. There is also need to have an access to the top of the structure. In cases where the superstructure is in place, the SE data becomes more difficult to interpret because of many reflections.

Another shortcoming of this method is being highly dependent to the experience of the test performer (as the reflection peak will be chosen in the plot by the examiner). Texas A&M University [31] carried out a series of comparative NDTs on nine bored piles using the SE method. The piles were tested at the National Geotechnical Experimental Sites at Texas A&M University with five piles being embedded in sand and four piles in clay. Five companies were invited to conduct the SE testing, and piles embedded length and condition was not exposed to them; results were obtained directly after the site testing. The comparison between length predictions and actual feature led to the following findings. Firstly, the length prediction will not be accurate when two damages are presented in a pile. Secondly, the accuracy of the result heavily depends on the operators' experience. For defects detection, the comparison of the results also revealed some significant issues. Firstly, the experience of the engineer plays an important role in the testing and the interpretation of the measurement results. Secondly, the size and location of the defect will affect the accuracy of the testing. Thirdly, the stiffness of the surrounding soil of the pile will influence the results.

2.5.2 Bending wave method

As the top of the deep foundation or pole is not always accessible, the Bending Wave (BW) method is introduced to evaluate the foundation non-destructively if the side of the structure/foundation could be accessed [32]. The Bending Wave (BW) method, which uses flexural (bending) waves rather than the longitudinal waves that used in the Sonic-Echo method, can be used to investigate the unknown depth and integrity of deep foundations. The method is typically used on a slim or rod-like medium. In the bending wave, velocity is inversely proportional to the wavelength; as a result, maximum velocity decreasing occurs at wavelengths that are longer than the pole diameter. In the case of length estimation, dispersive analysis in which wave data is extracted from a selected group of frequencies is required. These frequencies are analysed for the individual time required to travel to the bottom of the structure and back. Bending

waves can be produced by applying a horizontal impact on a pile, and it is necessary to utilize at least two sensors. Figure 2.7 shows the test setup for the bending wave method. In this method, there is no need to have an access to the top of the structure which is great advantage.

The problem of the bending wave propagation in cylindrical structures was first investigated in terms of elastic equations by [32]. More information of the derivation can be found in [33], [34] and [35]. The solution describes the motion of a wave of infinite duration travelling along a homogeneous, isotropic, linearly elastic cylinder of a constant diameter. The solution obtains expressions for both phase and group velocities of flexural waves. [34], and [36] produced graphs showing the relationship between the ratio of the cylinder's radius to the wave length of the wave for a given value of Poisson's ratio for the material. Since the frequency equation consists of Bessel functions, there are an infinite number of solutions to the problem as discussed by [37]. The general elastic equations have not been solved for transient bending wave motion in a tapered cylinder of finite length. Neither have they been solved for a tapered cylinder composed of an orthotropic material [38].

To calculate the length of a structure, the BW method requires special signal processing techniques, such as Short-Kernel Method (SKM) analysis [39] [38] [40] or flexural wave identification (FWI) method [41]. In Short kernel method, as proposed by [39], the so-called phase velocity (which is the velocity associated with a particular frequency) of the travelling wave is determined. From SKM plots, one can identify the initial wave arrivals and the reflections (echoes), and calculate the depths and locations of the reflection events. In the SKM analysis, one or more cycles can be used as a "Kernel Seed".

The SKM procedure is as follows: the Frequency Response Function (FRF) of each sensor is calculated. This can be done by firstly transferring the time domain signals of the impact hammer and the sensors into the frequency domain by Fast Fourier Transform (FFT), and then dividing them together.

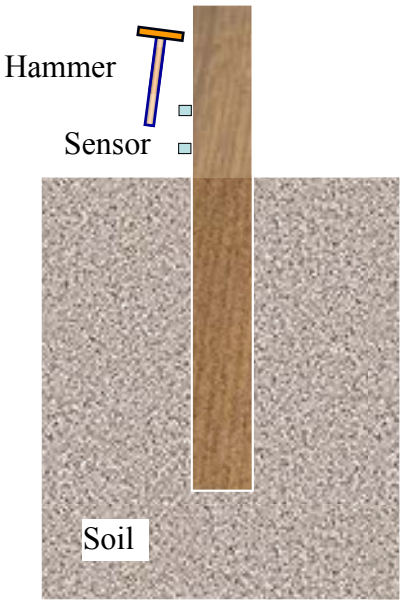

Figure 2.7: Bending wave method test setup [15]

From FRF analysis, the central frequency that shows the most consistency in all sensors is chosen for the SKM kernel seed, a kernel seed signal is formed and then cross correlated to the corresponding captured signals in all sensors. There will be several positive peaks in the plot of the output of cross-correlation (SKM plot); the global maximum of the output represents the location where the kernel fits best with its frequency counterpart. Repeating the process for all sensors and comparing the results in terms of their global maximum, one can obtain the frequency velocity using equation (2.2) [42].

$$V_{BW} = \frac{\Delta L_{BW}}{N_{pts} * \Delta t_{Sampling}} \tag{2.2}$$

In equation (2.2), V_{BW} is the phase velocity of the kernel, ΔL_{BW} is the distance between two sensors, N_{pts} is the number of data points by which the feature (peak) has shifted between the two sensors, and $\Delta t_{Sampling}$ is the sampling time interval. As mentioned earlier, there are a series of peaks in the SKM plot, the length is determined by identifying significant peaks (features) of the first arrival and the returning signals (reflections/echoes from an end of the specimen) in the SKM plot of a single sensor signal by equation (2.3):

$$L_{BW} = V_{BW} * \frac{N_{pts} * \Delta t_{echo}}{2} \quad (2.3)$$

Shortcomings of the BW method are as follows; due to the high attenuation associated with flexural waves travelling down a pole/pile, results of this method for the assessment of poles with embedment length greater than 5 m are not as reliable as the longitudinal wave methods. Further, the signal processing is very complicated, and relies on the experience of the operator. The complication of signal processing can become particularly problematic when the impact is applied in the middle of the pole/pile; in this case, reflections from top and tip of the pole interfere with each other, and cause distortion in measured signals. In 1998, the Federal Lands Highway Administration tested forty timber piles with lengths varying from around 2 m to 18 m using the BW method with SKM analysis. After data collection and analysis, a comparison between the computed length and the actual length was undertaken on 26 out of the 40 piles. The researchers found that the length difference ranged widely from -11.8% to 8.7% for 16 piles out of the 26 piles they compared [25]. In general, limitations of the BW methods combined with environmental effects and complexity of data processing lead to less accuracy than the SE method.

2.5.3 Ultraseismic method

Ultraseismic (US) is the most recent and advanced surface NDT industrial method developed by Olson Engineering [43]. This technique investigates the length and integrity of shallow and deep foundations. Its principle is similar to the Sonic-Echo method but more effective in the presence of many reflection boundaries. To start the test, top or near top (if top surface is not accessible) is struck by hammer and the signal will be captured by one inertial sensor, then the sensor will be moved along the structure in increments of 15 – 30cm and the test will be repeated again, with this procedure repeated several times. If the sensor is moving in the longitudinal direction, the method is called vertical profiling, and if it moves toward horizontal axes, it is called horizontal profiling. Figure 2.8 shows the Ultraseismic vertical profiling (which is utilized in this project) test procedure.

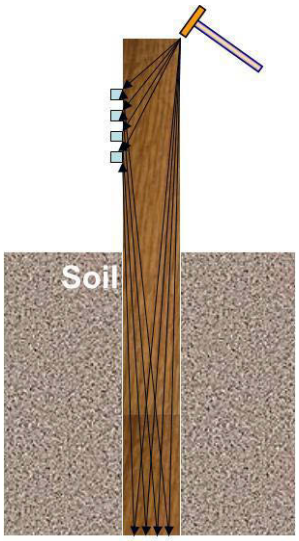

Figure 2.8: The Ultraseismic vertical profiling test setup [15]

One of the major advantages of this method is to be less affected by the presence of superstructure on top of pile [43]. Signal processing in this method has three main steps, stacking, gain, and digital filtering [44]. Stacking is used to increase the signal to noise ratio, and also to highlight the dominant wave type caused by the impact. For instance, vertical impacts are comparatively rich in compressional wave energy, although more flexural/Rayleigh (surface) wave energy is generated. In this case stacking can decrease the effect of the Rayleigh wave [43]. Gain is used when the amplitude of the captured signal in not sufficient. Finally, a digital filter (which will be explained in section 2.7) is applied to remove noise and undesirable high frequency components. Figure 2.9 shows the embedded length estimation results of the Ultraseismic vertical profiling (first reflection refers to the pile cap and the second one refers to the bottom of the pile). According to the Federal Lands Highway Administration report in 1998, under complex substructure condition, the US method is able to provide much more accurate depth prediction than the SE method [1]. Huang et al. at the ChaoYang University of Technology found that the error of the embedded length estimation of intact piles using the US method is within a range of 5% [45]. Some limitations of this method can be addressed as being sensitive to the type of the soil that pole or pile is embedded in, since little energy will be reflected in the case of stiff soils. It also requires more time to perform the test and process the data in comparison with the SE or bending wave method. There is also need for an accessible surface of at least 1.53 meters or more to perform the test [43].

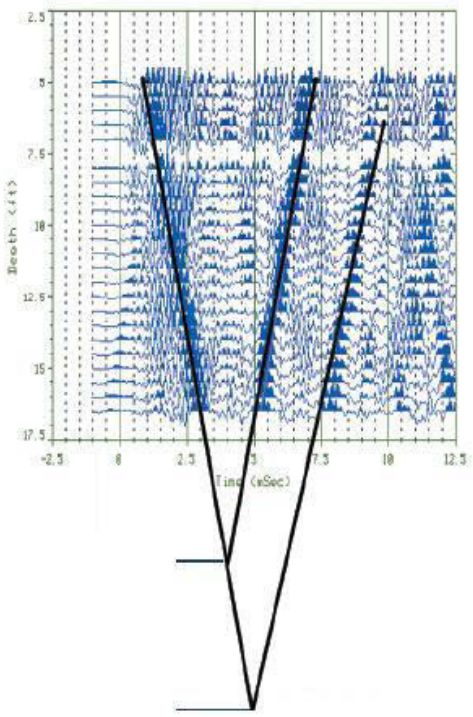

Figure 2.9: Stacked, gained and filtered record of US testing [46]

2.6 Waveguide propagation in the cylindrical timber pole

Many conventional stress-wave-based NDT methods (e.g. Sonic-Echo method) are based on a one-dimensional wave propagation theory [34]. This theory is based on the kinematics of deformation. It assumes that the wave is travelling like planes in one direction while it has the same amplitudes in the other directions [34].

Figure 2.10 illustrates the plane waves' propagation in one-dimensional wave theory.

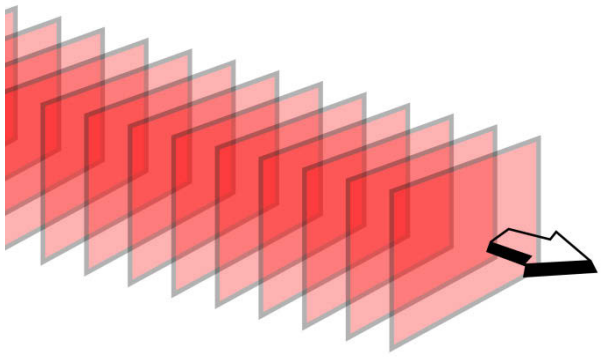

Figure 2.10: plane waves' propagation in one-dimensional theory

In this condition, the effect of lateral deformation (Poisson's effect) has not been considered in the derivation of the wave equation. Consequently, the initial condition dominates the wave behaviour. Even though the one-dimensional wave theory considers an infinite media, reflection and transmission can occur if a material interface exists. Such a boundary condition, which can only be present in the direction of propagation can only change the wave amplitude but not its velocity. As a result, the wave velocity, for instance in the Sonic-Echo method, is assumed to be constant in the medium [47].

On the other hand, when the wave is propagating through the medium, which is not infinite such as a plate-like or a cylindrical structure, the boundary imposes mechanical variables such as stress and/or strain constraints, which cause the wave to be reflected at the boundary, often yielding a change of the waves' type and their directions. In this situation, the oriented waves are called guided waves [48] [49]. Figure 2.11 is the simple illustration of the different characteristics of the one-dimensional wave and the guided wave in the plate-like structure.

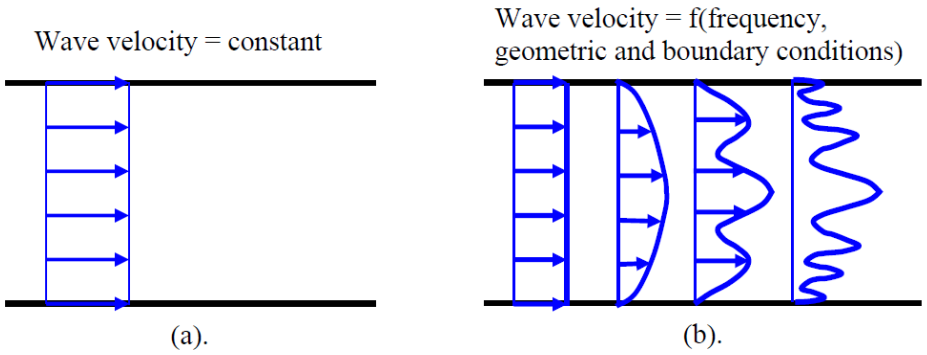

Figure 2.11: The illustration of (a) one-dimensional wave, and (b) guided wave in the plate-like structure [48]

Guided Waves (GW) exist in any finite media including elastic or inelastic materials [48]. The difference of the GWs in elastic or inelastic materials is that the waves in an elastic medium follow the theory of elasticity [50] and those in an inelastic media follow the elastic-viscous constitutive law. Lynch in his PhD thesis [51] presented the governing equations and their solutions of the wave guide propagation based on the theory of elasticity in an elastic isotropic cylindrical structure embedded in soil. He demonstrated the dependency of the wave guide propagation on variables such as the geometry and material properties of the structure, soil properties, frequency, and boundary conditions. Lynch works are briefly provided in Appendix-A. The wave guide

equations are solved for the angular frequencies (ω), and the roots are the wavenumbers (ξ) (which can be complex numbers). The relation between the real part of the wavenumber and the frequency is called the dispersion relation.

Phase velocity V_{ph} and group velocity V_{gr} can be derived from the dispersion relation by:

$$V_{ph} = \frac{\omega}{\mathrm{Re}(\xi)'} \tag{2.4}$$

$$V_{gr} = \frac{\omega}{\mathrm{Re}(d\xi)'}$$

The relation between the wave velocity and the frequency is called the spectrum relation.

As mentioned earlier, timber pole is an orthotropic material, which is vital to be considered in the solution of the dispersion relation. Saad. M. investigated the effects of the different material properties on the dispersion relation in the timber poles. He studied the wave propagation in the timber pole for both isotropic and orthotropic material properties. Details of his works can be found in [47] and [52]. In this study, material properties for the isotropic timber pole are as follows: the density (ρ) was set to 950 kg/m^3, the elastic modulus (E) to 23,000 MPa, and the Poisson's ratio (ν) to 0.3. For the orthotropic modelling material properties in Table 2.2 and Table 2.3 were used. The material properties of the soil are $\rho = 1{,}520 \mathrm{kg/m^3}$, $E = 100\mathrm{MPa}$, and $\nu = 0.3$.

Table 2.2: Elastic modulus values of simulated orthotropic timber pole

	Radial Direction	Transversal Direction	Longitudinal Direction
Elastic modulus (MPa)	1,955	850	23,000

Table 2.3: Shear modulus and Poisson's ratio values of simulated orthotropic timber pole

	Radial Transversal	Transversal Longitudinal	Radial Longitudinal
Shear Modulus (MPa)	357	1,037	1,513
Poisson's ratio	0.682	0.023	0.044

The phase velocity vs. frequency plots (spectrum relation) for the timber pole with isotropic and orthotropic material properties are demonstrated in Figure 2.12.

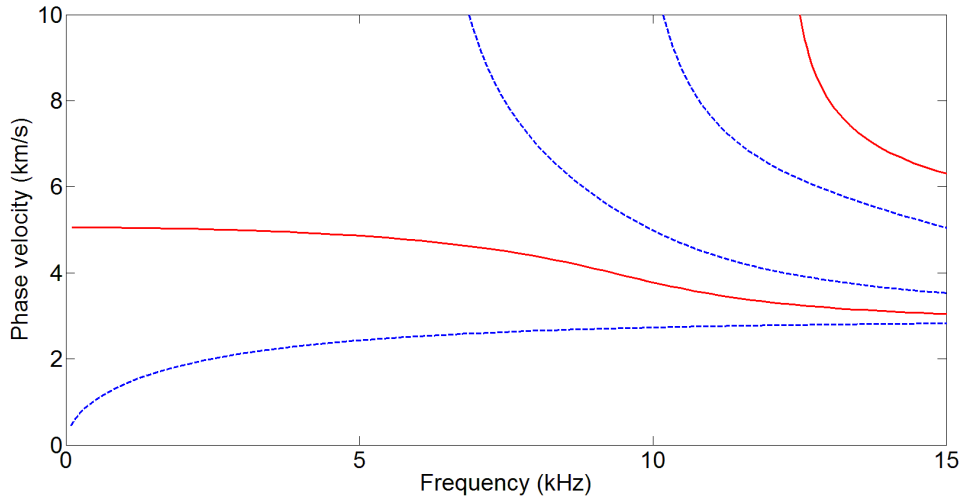

(a)

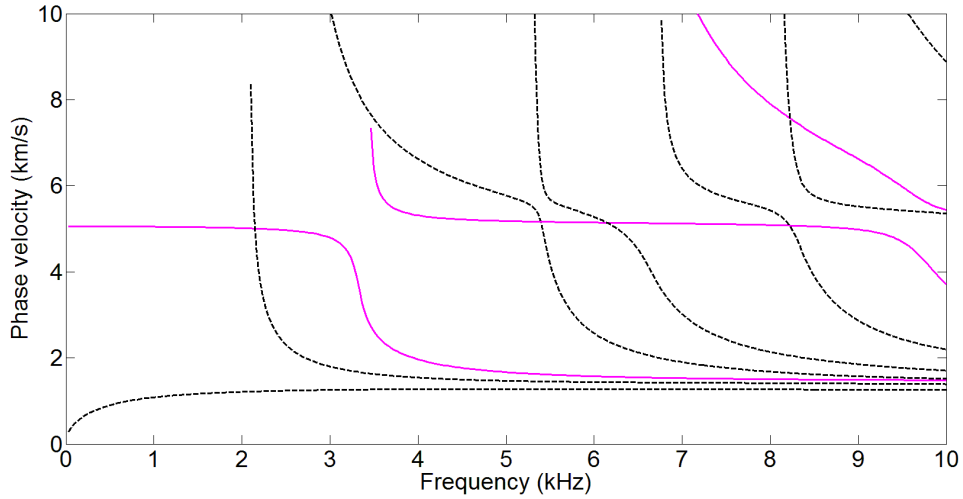

(b)

Figure 2.12: The spectrum curves of the cylindrical timber poles in (a) the isotropic; and (b) the orthotropic cases. Dashed lines represent the flexural wave branches and hard lines represent the longitudinal branches [52]

As can be seen in Figure 2.12 (a), only one branch exists for each type of the waves in the frequency range of 0 to 5KHz. Moreover, all of the frequency components in this range have approximately same velocity. It can also be seen that the velocity of the longitudinal wave is much higher than the flexural one. On the other hand as can be seen in Figure 2.12 (b), there two branches of the longitudinal and three branches of the flexural waves exist in the same frequency range for the simulated timber pole with the orthotropic material properties. Moreover, the longitudinal wave is no longer the dominant wave. These facts (differences between isotropic and orthotropic material properties) make a very complicated situation even in the perfect timber pole (i.e.

without any cracks and voids). More information and details about different types of waves and their propagation in the timber poles with and without cracks and voids can be found in [47].

2.7 Digital Filters

Digital filters are broadly used in the processing of the digital signals [53]. These signals can be from several applications such as speech, image, and video processing, data communications, radar, and seismic and oil exploration. The most common digital filters are Linear Time-Invariant (LTI) filters, because they are simple to analyse, design, and apply. Other filter types such as adaptive filters, which are the combination of the LTI filters and optimization algorithms, have different design procedures in which filter coefficients are optimized by specific optimization algorithms. An LTI digital filter can be individually recognized in the time-space domain by its impulse response, and alternatively in the frequency domain by its transfer function, which can be calculated by the discrete-time Fourier transform (DTFT) of the impulse response in the time domain. Digital filter design has been studied extensively by researchers through the past decades. Realization and design of the digital filters is highly dependent on the theory, applications, and technologies. For most applications, it is ideal to be able to design frequency-selective filters which can pass the specific frequency components of the signal without causing any change or distortion to the signal and remove the rest of the frequency components. In this case, the desired design specifications are given in the frequency domain by specifying a desired frequency response, which in general, includes complex numbers, the real part is related to the magnitude response, and the imaginary one is related to the phase response.

The most important features in the filter design are in terms of having specific frequency response, amplitude and phase response and being casual and stable. Four main common filters based on their frequency response are (as shown in Figure 2.13):

- Low-pass, which are used to remove unwanted high frequency spectrum.
- Band-pass, which are used to maintain a specific range of frequency in the spectrum.

- High-pass which works like the low-pass and just removes the low frequency components.
- Band-stop that can remove a specific range of frequencies in the spectrum.

Causality of the system besides being linear and time invariant means that the output of this system at any time depends only on the past and present values of its input. Stability in linear systems or Bounded-Input Bounded-Output stability means that for any bounded input, the response of the system would never be infinity or unlimited, or in other words, there is no value that can make the denominator of the system's transfer function (z-transform of the system impulse response) zero.

Digital filters can be categorized into two main types: Finite Impulse Response (FIR) filters in which the impulse response is nonzero for only a limited number of samples, and Infinite Impulse Response (IIR) filters that have an infinite number of non-zero samples [54].

In the following, these two types will be briefly studied.

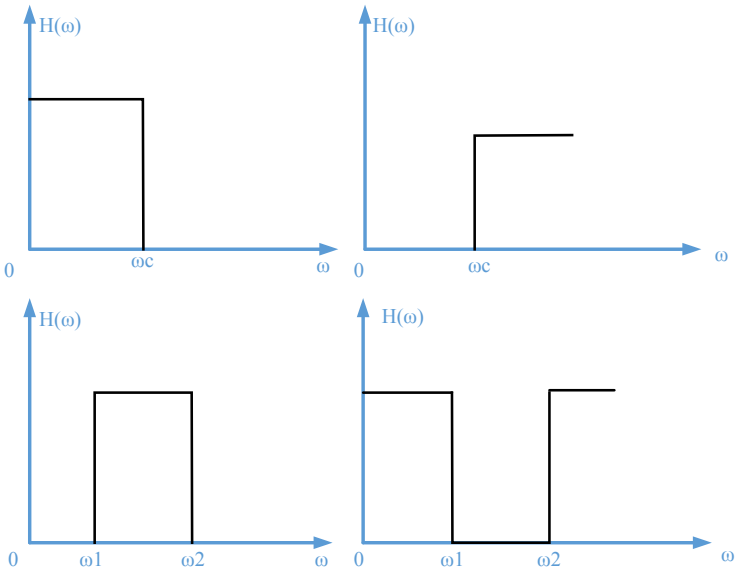

Figure 2.13: (a): Low-pass, (b): High-pass, (c): band-pass, and (d): Stop-band digital filters

2.7.1 Finite Impulse Response filters

FIR filters are feed forward filters in which the output sequence is a linear combination of the current and past input samples [53]. Figure 2.14 shows a block diagram of these filters. The input data will be shifted constantly, weighted with the filter coefficients, which determine the filter characteristics and then summed up (equation (2.5)) [53].

$$y(n) = \sum_{i=0}^{M} x(n-i)h(i) \tag{2.5}$$

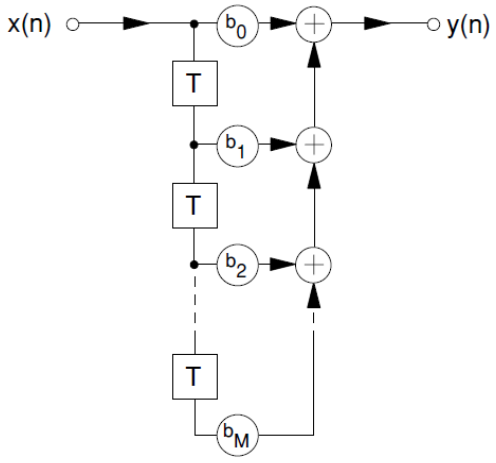

Figure 2.14: Block Diagram of the FIR filters [53].

From equation (2.5), the filter transfer function can be derived as:

$$H(z) = \sum_{i=0}^{M} h(i)z^{-i} \tag{2.6}$$

Equation (2.6) shows that the FIR filters' impulse response has a finite length, so they can be realized using the convolution operation [55] and it can be applied directly in the time-space domain, or in terms of the FFT in the frequency domain. Designing an FIR filter is usually done by calculating the optimal impulse response samples (filter's coefficients) that best approximate the design specifications. The impulse response length M (filter order) can be fixed; it could also be considered as an optimization parameter. FIR filters are always stable as their transfer function has no poles except

maybe at zero. The most important feature of the FIR filters is in having a linear phase change, which is very important in many signal processing applications; it is desirable to pass some frequency components of the signal with minimal distortion especially in the phase components. In this regard, linear-phase systems are mainly desirable as their effect is a pure time delay [55]. Another major advantage of the FIR filters is in being insensitive to round-off noise which happens in coefficient quantization as they have no feedback loops. Finally, specific design procedures (e.g. Parks-McClellen) can make optimum trade-off between the filter design factors (filter order, transition bandwidth, and ripples in stop and pass band (Figure 2.15)) [54].

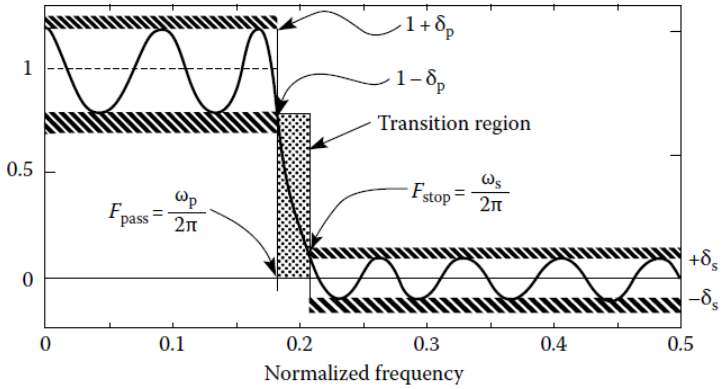

Figure 2.15: Filter design specifications for low pass FIR filter [54]

In Figure 2.15, δ_p and δ_s are the ripples in the passband and stopband. FIR filters have been widely used in the field of non-destructive testing where echo or reflection detection is vital. Fasel used FIR filters for structural damage classifications procedure in [56]. Ohta et al. also used FIR filters for flaw detection procedure in [57].

2.7.2 Infinite Impulse Response

IIR filters are feedback filter types in which the output sequence is a combination of the current input and previous outputs (equation (2.7)). [54]

$$y(n) = \sum_{i=0}^{M} b_i x(n-i) - \sum_{j=0}^{N} a_j y(n-j) \tag{2.7}$$

Figure 2.16 shows a block diagram of these filters. In contrast to the FIR filter, the right side of this figure with coefficients (a) is a feedback part. The left side of the block

diagram with (b) coefficients is similar to the FIR filter structure, which is the non-recursive part. From equation (2.7), IIR filter transfer function can be derived as:

$$H(z)=\frac{Y(z)}{X(z)}=\frac{\sum_{i=0}^{M} b_i z^{-i}}{\sum_{j=0}^{N} a_j z^{-j}} \tag{2.8}$$

Equation (2.8) of the IIR filters can be realized using the convolution operation [55]. In this equation, since a degree of the numerator usually is no greater than the denominator, filter order (N) is a degree of the denominator.

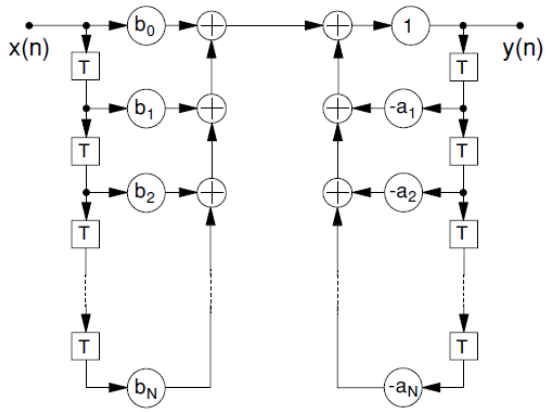

Figure 2.16: Block diagram of the IIR filters [53]

Considering the filter, the number of previous output samples that are needed to be stored for the purpose of calculating current output is also determined. Similar to the FIR filter design, designing an IIR filter is usually done by calculating the optimal impulse response samples (filter's coefficients b and a) that best approximates the design specifications. Filter order can be fixed, but it could also be considered as an optimization parameter. The IIR filters can be unstable as their transfer function has poles that can lie on or out of unit circle in the z-plane (because of the feedback loop). They are also sensitive to round-off noise which can be amplified in the feedback loop and can destructively affect the response of the filter and its stability by disturbing the poles locations and pushing some of them to more unstable portions on the unit circle. Design of a casual and realizable linear phase IIR filter is impossible [55]. The major advantage of the IIR filter is having lower order in comparison to FIRs, and as a result,

its design is much less complicated as fewer parameters are needed to be calculated or stored (for previous outputs).

The IIR filters have been applied in NDTs where the amplitude of the signal is much more significant than its phase [58] [59].

2.7.3 Digital filter designs

The general filter design problem can be briefly explained as follows. First determine the ideal frequency response (filter specifications such as: ripples in the band-pass, stop-band attenuation, and the transition bandwidth), then find a realizable IIR or FIR filter type whose frequency response approximates the ideal one. Then the realizable filter will be created by optimizing some measure of the filter's performance, for example, minimizing the filter order, transition bandwidth, or the pass band attenuation. For this purpose, an appropriate design procedure needs to be selected. For the FIR filters two main methods are the windowing method [55], and the Parks–McClellan (or Remez) algorithm [60]. The windowing method consists of many different types such as Kaiser, Hamming, Hanning, etc. by which edge overshoots, the transition bandwidth, and the ripples can be controlled. The Remez algorithm, on the other hand, minimizes the Chebyshev error norm which leads to equiripple designs (Equiripple filter). It is also possible to design the FIR filter with arbitrary magnitude which is introduced in [61] [62]; there are also other FIR design methods like constrained least-squares proposed by Selesnick et al in [63], and linear programming based introduced in [64] and [65].

2.8 Signal Processing of the conventional surface stress-wave-based methods

2.8.1 The discrete and fast Fourier transform

The Fourier series was firstly introduced by Jean Baptiste Joseph Fourier in 1807 [66]. It was the first algorithm that applied trigonometric series systematically to problem solving. Fourier series and the Fourier integral allow transformation of physically realizable time-domain waveforms to the frequency domain and vice versa [66].

A typical signal captured in the NDT methods is non-periodic by nature. To transform these signals, which are obtained as a function of time, to a function of frequency, the Fourier transform can be utilized. The continuous Fourier transform of x(t) is defined as;

$$X(f) = \int_{-\infty}^{\infty} x(t) e^{-j2\pi(f)(t)dt} \tag{2.9}$$

Equation (2.9) is used to define a signal in the frequency domain for a continuous time interval. As a matter of fact, all of the signals that are captured in practice are in discrete form; a variation of the Fourier transform was developed for use in digital signal processing [66]. The discrete Fourier transform (DFT) of $x(n\Delta t)$ is defined as:

$$X(k\Delta f) = \Delta t \sum_{n=0}^{N-1} x(n\Delta t) e^{-j2\pi(k\Delta f)(n\Delta t)} \tag{2.10}$$

In which, $x(n\Delta t)$ is the discrete set of time samples that defines the signal to be transformed; $X(k\Delta f)$ is the setoff Fourier coefficients obtained by the DFT of $x(n\Delta t)$; Δt is the time increment between data points, sec; Δf is the frequency interval in the frequency domain $\left(\frac{1}{N\Delta t}\right)$, Hz; k is the index for the computed set of discrete frequency components, $k = 0,1,2, \ldots, N-1$; n is the time sample index, n=0,1,2,…,N-1; N is the total number of data points being considered from the discrete signal; X(f) is a complex number with a real component $X_{Re}(f)$ and an imaginary component $X_{Im}(f)$, and, therefore, can be represented as a vector in a complex coordinate system [67]. Using Euler's identity, $e^{\pm j\theta} = \cos\theta \pm j\sin\theta$, yields:

$$X(k\Delta f) = X_{\mathrm{Re}}(k\Delta f) - jX_{\mathrm{Im}}(k\Delta f) \tag{2.11}$$

while,

$$X_{\mathrm{Im}}(k\Delta f) = \Delta t \sum_{n=0}^{N-1} x(n\Delta t) \sin[2\pi(k\Delta f)(n\Delta t)] \tag{2.12}$$

and,

$$X_{\mathrm{Re}}(k\Delta f) = \Delta t \sum_{n=0}^{N-1} x(n\Delta t) \cos[2\pi(k\Delta f)(n\Delta t)] \tag{2.13}$$

where $X_{Re}(k\Delta f)$ is the real part of the frequency domain, and $X_{Im}(k\Delta f)$ is the imaginary part of the frequency domain.

By letting $f = k(\Delta f) = k/N\Delta t$, the magnitude of the discrete Fourier transform is defined as:

$$A(f) = |X(f)| = \sqrt{(X_{\mathrm{Re}}(f))^2 + (X_{\mathrm{Im}}(f))^2} \tag{2.14}$$

while the phase angle of the Discrete Fourier transform is defined as:

$$\phi(f) = \tan^{-1}\left(\frac{X_{\mathrm{Im}}(f)}{X_{\mathrm{Re}}(f)}\right) \tag{2.15}$$

Generally, the idea of the FFT is to transform a discrete signal in the time domain to the frequency domain by placing sine and cosine curves next to the discrete signal so the data points in the curves line up with the sample points in the signal. Points which are adjacent between the sine and cosine curves and the points representing the discrete signal are then multiplied (equation 2.12, 2.13). The resulting cross-products, one corresponding to the cosine curve and one corresponding to the sine curve are summed. This summation $X(k\Delta f)$, is in the form of the complex vector is the set of Fourier transform coefficients.

Using this set of frequencies obtained from the Fourier transform of the discrete waveform, a plot of amplitude versus frequency can be made, which will identify the most prominent frequency contained within the signal. Due to the lengthy calculations performed during discrete Fourier transform, a fast Fourier transform (FFT) algorithm is commonly used.

2.8.2 Short-Kernel Method (SKM)

SKM is a mathematical technique based on the cross-correlation procedure described by [68]. It was developed for digital signal processing and determines the location and the velocity of selected frequencies inside dispersive time records. In SKM, a single value of a specific frequency is indicated as follows:

$$SKM(j,k) = \sum_{i=1}^{N-1} g(\tau_i + j\Delta t) f[\tau_i, k]\Delta t \qquad with...j = 1toN2 - N1 \tag{2.16}$$

In equation (2.16), $SKM(j,k)$ is the j[th] term of the cross-correlation currently being performed at the k[th] frequency. g is the captured signal in one sensor; f is the kernel seed of the k[th] frequency used to perform the cross-correlation; N1 is the number of data points in the f; N2 is the number of data points in the g; and Δt is the time step at which the time record g is stored. Thus, equation (2.16) calculates each single SKM value as the cross-correlation of a given frequency with a discrete signal.

The SKM technique is better summarised in a more descriptive form through the following explanation. Firstly, the FRF is calculated in each sensor, and then the frequency component that has the most consistency in all of the sensors' FRF is chosen as the seed frequency. A kernel signal in then created by the seed frequency whose length is to be determined by the user. In the next step, the kernel signal is placed next to the captured signal in a way that its individual data points match with the data points in the captured signal. The process then begins by cross-multiplying the amplitude of the kernel at each time step by its corresponding signal amplitude. Products from all multiplications are then summed with all algebraic signs to obtain a single SKM value. This SKM value indicates how well the kernel fits with its frequency counterpart inside the data string. The value is graphed on an SKM plot at the point where the beginning of the kernel was placed. The kernel is then shifted along the data string by a predetermined number of points and the cross products are formed again (see Figure 2.17). Another SKM value result is to be plotted at the point where the kernel is now placed. This procedure is continued for some specified number of kernel shifts. The data points in the SKM plot corresponding to a significant maximum peak represents the location of good alignment between the kernel and its frequency counterpart in the signal. A positive global maximum represents the location where the kernel fits best and is in phase with its frequency counterpart, and a negative global maximum is a location where the kernel is also well-aligned, but out-of-phase by one hundred and eighty degrees with its frequency counterpart.

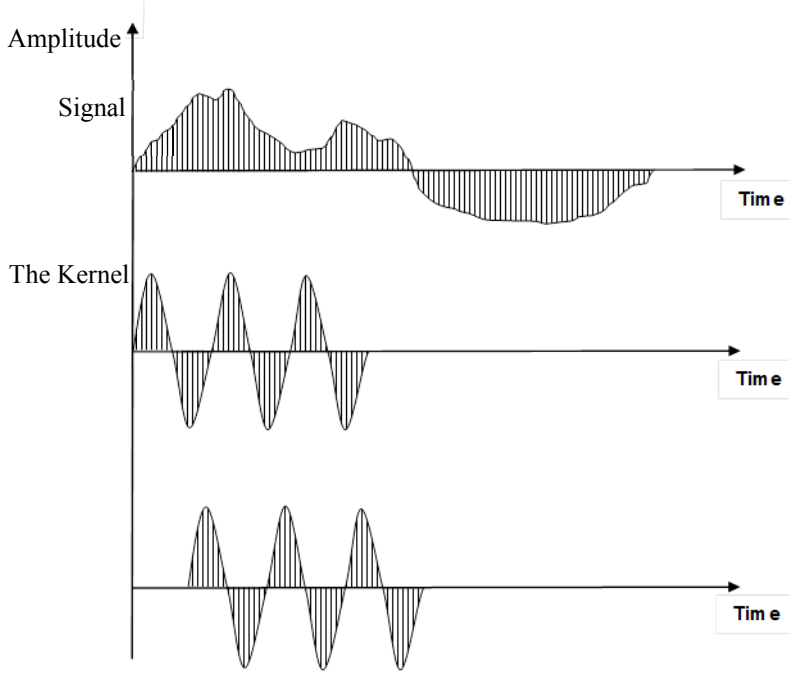

Figure 2.17: Kernel shifted along signal [15]

2.9 Limitations of conventional surface stress-wave-based NDT

The limitations of the current surface stress-wave-based NDT methods on the condition assessment of the piles are discussed earlier in their related sections. In this section the limitations of these methods in the condition assessment of the timber poles are briefly addressed, and then discussed and investigated completely in Chapter 5. Due to complicating factors such as orthotropic material properties, soil embedment, complex wave behaviour and other uncertainties, most of the currently available methods are not suitable for condition assessment of the timber poles in-service. In these methods, detecting the reflection peaks heavily relies on the experience of the test performer or the signal processor, and therefore is not an easy task especially in the embedded situations. Even if the reflection peaks are observable, the results contain relatively large errors. The situation is even worse in the Ultraseismic method in which both of the longitudinal and bending waves propagate simultaneously in the timber, and as a result, no clear pattern of reflections could be detected. This is due to the presence of the several branches related to both of these waves in the spectrum curves (see Figure 2.12(b)). In this regard, advanced digital signal processing is needed to separate these

waves and their related branches from each other prior to the condition assessment procedures.

2.10 Summary

This chapter firstly presented a review of the importance of the condition assessment of the in-service timber poles especially in Australia. It presented important literature published in the area of currently available Non-Destructive Testing methods over the past decades. Through the literature review, it was indicated that researchers have used broad types of NDTs to evaluate the quality of concrete materials. Although a large number of publications for other applications (e.g. condition assessment of the concrete piles) of these methods exist, the area of NDT methods for condition assessment of the timber materials is still an active field of research.

Amongst all of the NDTs, surface stress-wave-based methods can potentially offer simple, environmentally friendly and cost-effective tools for identifying the in-service condition of the timber poles. From the literature review, three methods were identified to be applicable in the field of non-destructive testing of the timber poles, which were explained in their related sections in this chapter.

In the next section of this chapter, the basics of the wave propagation in the cylindrical structures were briefly provided. Then different types of the digital filters that have been used in the NDT are explained, and finally the limitations of the currently available surface stress-wave-based NDT methods on the condition assessment of the timber poles, and the necessity of employing some digital signal processing methodologies were briefly addressed.

3 Chapter 3: Review of advanced digital signal processing techniques applicable on timber pole assessment

3.1 Introduction

As previously mentioned in Chapter 2, due to the complicating factors such as orthotropic material properties, soil embedment, complex wave behaviour and other uncertainties, most of the currently available methods are not suitable for condition assessment of the timber poles in-service. In fact, there is a need for some advanced digital signal processing techniques to separate the longitudinal and bending waves and their related branches from each other prior to the condition assessment procedures. In this chapter, firstly a signal processing model for the timber pole is presented. Next some modified advanced digital signal processing methodologies are proposed. These methods can be grouped into three categories as deterministic signal separation, blind signal separation, and frequency-wavenumber analysis (velocity filtering).

3.2 Timber pole as a Linear Time-Invariant System

Linear time-invariant (LTI) theory, which has originated from applied mathematics, studies the response of an LTI system to an arbitrary input signal. One of the direct applications of this theory is in reflection seismology, which is the reference science for the most of the advanced digital signal processing methodologies that are used in this research.

Reflection seismology is a branch of exploration geophysics that tries to estimate the properties of different layers of the Earth utilizing reflected seismic waves. Reflection seismology can be categorized into two main groups, vertical profiling which is used for instance on oil and petroleum exploration fields, and horizontal profiling which is used for example in marine seismology.

In general, seismic analysis typically involves: storage, signal processing and interpretation of data collected at each receiver [69] [70].The signal collected at each receiver is called a seismic trace and represents a superposition of reflections from the many sub-surface layers where the acoustic impedance changes [71]. The resultant seismic trace is often described as the convolution of a waveform (the source impulse) with a time series known as a reflectivity function [69] [71]. [72] [73], see Figure 3.1.

The earth's impulse response is of utmost importance in the signal processing of seismic signals. Here the earth is considered as a system in which the response is a reflection from each sub-surface layer. The reflection signals are impulses with amplitudes equal to the vertical reflection coefficients of the reflecting layers with time delays equal to their two-way reflection times [71].

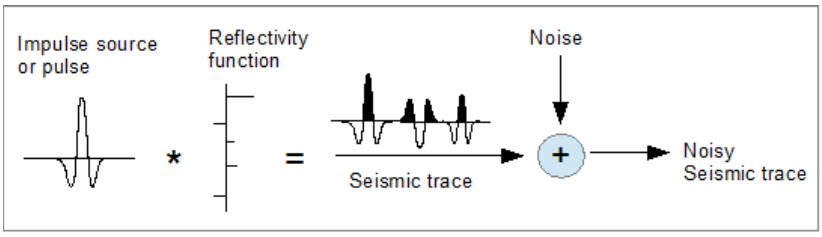

Figure 3.1: Depicts a seismic data model. Here we see that an impulse source is convolved (*) with a reflectivity function (that is related to the geological sub-surface) and with additive random noise, produces the noisy seismic trace [69].

The convolution theory models the input–output mapping of an LTI system. Deconvolution is the inverse mathematical operation that allows the recovery of the input signal from the output signal. An early application of the deconvolution has been in the reflection seismology signal processing. Robinson developed a pioneer work on the subject in his PhD thesis at MIT [74]. His research was followed by Wiener and Levinson. Actually, Robinson's work represented the first successful application of the recently developed Wiener theory on a prediction and filtering. His aim was to obtain information about the structure of the Earth by the estimation of the impulse response of a layered earth model, i.e., an FIR model [5].

In the deconvolution theory, availability of prior knowledge about the input signal or the LTI system's impulse response is necessary. In some field like telecommunications, since the transported signal (input signal) is of interest and importance, deconvolution is being used massively to recover the input signal from the received one, while is some

other applications like reflection seismology, since the behaviour of the wave is of the interest, deconvolution is used to remove or filter the input signal from the captured signal and preserve the impulse response of the earth. Similar to reflection seismology, in the condition assessment of the timber poles, an impulse response of the timber pole contains the useful information to be used in the condition assessment procedures. In this regard, the timber pole is considered as an LTI system in which the hammer impact excitation is the input and captured signals by the accelerometers are the outputs of the system. Figure 3.2 shows the aforementioned system.

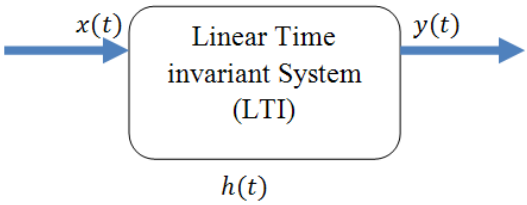

Figure 3.2: Timber pole as the LTI system

In this model the output of timber pole can mathematically be presented by the convolution theory, as shown in equation (3.1)

$$y(t) = x(t) * h(t) + n(t) \tag{3.1}$$

where *n (t)* denotes the noise.

In the rest of this chapter, three groups of the modified signal processing methodologies are presented. The first group is related to the convolution theory and is known as deterministic signal separation, the second group is related to the blind signal separation in which no prior information about the input signal or the impulse response of the system is available. The final group is related to the two dimensional filtering process, in which the captured signals are firstly transferred to the frequency-wavenumber domain. As previously mentioned in Chapter 2, the waveguide governing equations are solved for the frequencies and the roots are the wavenumbers, the relation between the wavenumber and the frequency is called the dispersion relation. In this regard, the last signal processing methodology is directly applied on the data that dispersion curves can be obtained from. This data was captured while the timber pole was excited by the hammer. It is also worth mentioning that the closest field to the timber pole embedment length estimation is reflection seismology. In reflection seismology, a signal that was

captured by sensor(s) includes not only noise, but also many unwanted and useless reflections from several layers of the earth. Signal processing techniques in this field are tried to minimize or remove noise or any unwanted reflections and patterns in the signal in order to obtain the most useful reflections (defined based on application and called primary reflections) for further processing or calculations. In this regard, in the second phase of this research, the most effective signal processing methodologies that are utilized in the field of reflection seismology are chosen from each groups (i.e. deterministic and blind signal separation) and implied on the problem of timber pole embedment length estimation. Results and discussions on applying the aforementioned modified advanced digital signal processing methodologies on the signals captured from the timber poles are provided in Chapter 6.

3.3 Deterministic Signal Separation

3.3.1 Deconvolution

As mentioned earlier, the captured signal can be modelled as a convolution of useful and unwanted information. One method to deal with this problem is the Deconvolution, which was proposed by Norbert Wiener of the Massachusetts Institute of Technology in 1949. His algorithm minimizes the mean square error of a desired signal and its estimation through the deconvolution process [6].

3.3.2 Wiener Deconvolution and filter

Wiener deconvolution is the first deconvolution method applied in seismology, and most of the other proposed deconvolution techniques can be assumed as direct developments of this method, or application of this method as a part of their suggested algorithm [75]. Based on the application and needs, this technique tries to minimize the effects of the unwanted parts in the captured signal. While standard filters are designed for a demanded frequency response, the design of the Wiener filter has a different approach. Based on having an approximate knowledge about the spectral properties of the desired signal and noise (such as autocorrelation and cross-correlation), the Wiener filter method tries to find the Linear Time-Invariant system (LTI) which can minimize the error of the output with desired output signal. In Wiener filters the basic

assumptions are that the desired signal and the convolved noise are stationary, and the filter is casual.

3.3.3 Wiener deconvolution and filter theory

As previously mentioned, the goal of the Wiener filter is to find an LTI system whose output approximates the desired signal based on the minimum mean square error method. Initial assumptions are: desired, and captured signal are zero mean signals, and the desired signal and the noise are independent (they are non-Gaussian signals). Equation (3.2) shows the output of the Wiener filter [76].

$$y(t) = h(t) * x(t) = \int_{\tau} h(\tau)x(\tau - t)d\tau \tag{3.2}$$

where * denotes the convolution, $s(t)$ is the desired signal, $x(t)$ is the captured signal by sensor, and $y(t)$ is the estimated signal should ideally be $s(t)$, and $h(t)$ is the system impulse response. Error can be specified as the difference between the estimated signal and the desired signal (equation 3.3)[76].

$$e(t) = s(t) - y(t) \tag{3.3}$$

the squared error is

$$e^2(t) = \big(s(t) - y(t)\big)^2 = s^2(t) - \big(2s(t) - y(t)\big)y(t) \tag{3.4}$$

and the expected value of the squared error is: (equation 3.5)

$$E\big(e^2(t)\big) = E\big(s^2(t) - \big(2s(t) - y(t)\big)y(t)\big) = R_S - E\big(2s(t) - y(t)\big)y(t) \tag{3.5}$$

where R_s is the autocorrelation function of $s(t)$. By substituting equation (3.2) in equation (3.5) we obtain:

$$E\big(e^2(t)\big) = R_S - 2E\left\{\left(s(t) - \int_{\tau} h(\tau)x(\tau - t)d\tau\right)\right\}\int_{\theta} h(\theta)x(\theta - t)d\theta \tag{3.6}$$

$$= R_S - 2\int_{\theta} h(\theta)\left\{E\big(s(t)x(\theta - t)\big) - \int_{\tau} h(\tau)E\big(x(\theta - t)x(\tau - t)d\tau\big)\right\}d\theta$$

R_s is constant, in this regard, this equation can be minimized by the minimizing the second part of the equation, which can be done if the expression inside the bracket equals zero. We have:

$$\int_{\tau} h(\tau)E\big(x(\theta-t)x(\tau-t)d\tau\big)=E\big(s(t)x(\theta-t)\big)$$
$$=\int_{\tau} h(\tau)R_x(\tau-\theta)d\tau=R_{xs}(\theta) \tag{3.7}$$

Equation (3.7) demonstrates the filtering procedure based on the input (i.e. the captured signal) and the output (i.e. the desired output). Equation (3.7) is called the Wiener-Hopf equation and is the fundamental equation of the Wiener theory. To solve this equation, the Wiener LTI system can be assumed as a causal finite impulse response filter. In this case, optimal filter coefficients (tabs) will be calculated by utilizing the autocorrelation of the desired and captured signals, and also the cross-correlation of these signals. Consider the block diagram of the FIR Wiener filter (Figure 3.3) with input signal $x[n]$, N and h, as the order and confidents of the filter. The output of the filter $y[n]$, can be obtained by equation (3.8) in the discrete form.

$$y[n]=\sum_{i=0}^{N} h_i x[n-i] \tag{3.8}$$

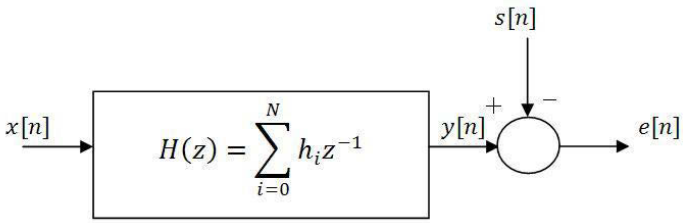

Figure 3.3: FIR Wiener filter block diagram

Error is indicated by $e[n]$ and is defined as $e[n]=s[n]-y[n]$. After some simplicity, the mean square error can be written as:

$$E\big(e^2(t)\big)=E\big(s^2[n]\big)+E\left\{\left(\sum_{i=0}^{N} h_i x[n-i]\right)^2\right\}-2E\left(\sum_{i=0}^{N} h_i x[n-i]s[n]\right) \tag{3.9}$$

In order to find the optimal coefficient vectors that can minimize the equation (3.9), its derivative with respect to h_i is needed to be equal to zero.

$$2\sum_{j=0}^{N} E(x[n-j]x[n-i])h_j - 2E(x[n-i]s[n]) = 0 \qquad i = 0, \dots, N. \tag{3.10}$$

and finally we have:

$$\sum_{j=0}^{N} R_x(j-i)\, h_j = R_{sx}[i] \qquad i = 0, \dots, N. \tag{3.11}$$

In matrix format, equation (3.11) can be written as:

$$\begin{bmatrix} R_x[0] & R_x[1] & \cdots & R_x[N] \\ R_x[1] & R_x[0] & \cdots & R_x[N-1] \\ \vdots & \vdots & \ddots & \vdots \\ R_x[N] & R_x[N-1] & \cdots & R_x[0] \end{bmatrix} \begin{bmatrix} h_0 \\ \vdots \\ h_N \end{bmatrix} = \begin{bmatrix} R_{sx}[0] \\ \vdots \\ R_{sx}[0] \end{bmatrix} \tag{3.12}$$

where the symmetry matrix R_x contains autocorrelation of $x[n]$. Filter coefficients can be calculated by solving equation (3.12).

It's also possible to define different types of error criteria; for instance Walden minimized the average mean-squared error and maximum mean-squared error as two different error criteria [77]. The Wiener filter has been widely used in the field of seismology; Hadziioanuo used this method to improve the signal to noise ratio of a captured noisy signal. [78]. Spiking deconvolution is another method which is based on the Wiener deconvolution. This method tries to compress the excitation impact (source wavelet in seismology) into a zero-phase spike (Dirac delta function); the aim is to remove the effect of the source wavelet and leave only the reflectivity function [69]. Some of the other deconvolution methods that are being used in seismology are: Homomorphic [79], dip dependant [80], and surface consistent deconvolutions [81, 82].

3.3.4 Predictive Deconvolution

As mentioned in the previous section, Wiener deconvolution as a supervised technique may only be applicable if the information of the excitation impact or the mixing system (the earth in seismology or the timber pole in this project) is available, or at least its estimation is acceptable [6]. In predictive deconvolution, which was firstly introduced in 1954 by Enders A. Robinson [7], the essential information is extracted from the captured signals themselves. In this method, it is vital for the captured signal to be wide-

sense stationary, and the different patterns, which exist in the impulse response of the LTI system be uncorrelated. In a wide-sense stationary signal, the energy of the original wavelet repeats in the specific periods. Multiples and unwanted reflections have similar energy to the original wavelet and are repeated between periods of time. In predictive deconvolution, the main goal is to remove multiples and unwanted reflections from the captured signals in order to obtain pure reflections (primary reflections), e.g. reflections from the earth or the bottom of a pole, and thereby to extract the desired output from the captured signal. The processing steps of the predictive deconvolution are as follows. First, the captured signal is divided into same size windows (same length time periods). Then, the energy in the beginning of the each window is assumed to be the main energy to be kept and every similar energy will be removed from the rest of the window. This is to say that the original wavelet energy, which is the reflection from the bottom of the pole and which comes back to the sensor is the desired output of each window and will be kept, while the other similar patterns will be removed. Mathematically, this can be modelled as follows:

$$\begin{bmatrix} R_x[0] & R_x[1] & \cdots & R_x[N] \\ R_x[1] & R_x[0] & \cdots & R_x[N-1] \\ \vdots & & \ddots & \vdots \\ R_x[N] & R_x[N-1] & \cdots & R_x[0] \end{bmatrix} \begin{bmatrix} h_0 \\ \vdots \\ h_N \end{bmatrix} = \begin{bmatrix} R_{sx}[\alpha] \\ \vdots \\ R_{sx}[N+\alpha] \end{bmatrix} \tag{3.13}$$

where α is the length of the desired output and N is the length of each window.

The predictive deconvolution method has been extensively applied in seismology all around the world; Hutchinson et al. applied this method for the noise attenuation in the Gulf of Maine [83], Bruno et al. used the predictive deconvolution in order to improve the resolution of volcano data (where usually high-resolution data is hard to obtain) in Italy [84]. Some other applications of the predictive deconvolution can be found in [85], [86].

3.4 Blind Signal Separation

Blind Signal or Source Separation refers to a group of unsupervised signal processing techniques in which the input signal or any information about it is not available [5]. In these methods, the system is assumed to be multi input multi output [87], which means that N signals are produced by different sources, these signals are then captured by M

sensors after travelling through the medium. Based on the statistical differences, the blind signal separation methods can separate the signals from all sources having only signals captured by the sensors. In this regard, firstly a data matrix of M*N is made with observations in the columns and different sensors in the rows, then the blind separation methods can be applied on this data matrix in order to separate the source signals. The main algorithms that are used in this research are Principal Component Analysis, Singular Value Decomposition, which do not involve any learning algorithm, and *k*-mean clustering algorithm, which contains a learning algorithm. It is worth considering that since this project was started from the outset, it was firstly assumed that all existing branches and waves in the timber pole have not only different statistical properties, but also are statistically independent (As it is a usual assumption in the most reflection seismology applications). In this regard, PCA, SVD, and *k*-mean clustering algorithm are implied to separate the several existing patterns in the captured signals before further processing such as up- and down-ward waves separation. More information on the effectiveness of aforesaid methods in the reflection seismology fields can be found in [69], [5], [88], [89], [90], [91].

3.4.1 Principal Component Analysis

Principal Component Analysis (PCA) or discrete Karhunen–Loève transform (KLT) is a mathematical process which transfers observations (data) that are possibly correlated, into a set of orthogonal values (features) which are linearly correlated and called principal components; this method is based on the second order statistics (covariance) [8]. Data has the most variance over the first principal component (which means that this component represents the most correlated and important feature of the data), while over the last component data has the smallest variance which means it is the most uncorrelated feature of the data (can be assumed as white noise) [8], [5]. See Figure 3.4.

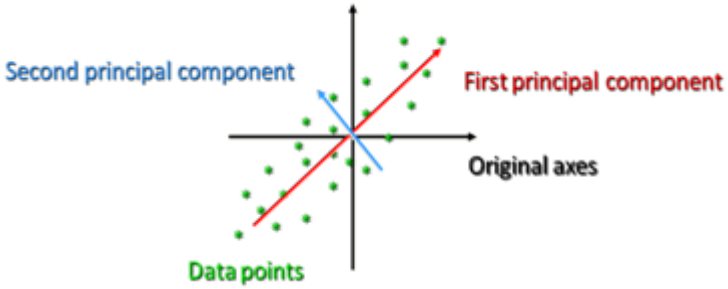

Figure 3.4: PCA data transformation, first and second principal components

The PCA mathematical procedure is as follows: firstly a data matrix (A) of M*N is made with observations in the columns and different sensors in the rows. Then the covariance matrix will be calculated using equation (3.14).

$$c_{ij} = \frac{1}{N}\sum_{i=1}^{N} a_{ij}a_{ji} \tag{3. 14}$$

where c and a denote each component of the covariance and dataset matrices. Writing the equation (3.14) in the matrix form gives:

$$C = \frac{1}{N}AA^T \tag{3. 15}$$

Often the scale factor $1/N$ is distributed throughout the matrix and the covariance matrix is written simply as AA^T. The eigenvalues of the covariance matrix represent the principal components, while the eigenvectors represent the orthogonal axes in the transferred domain. PCA has been utilized for the signal processing of seismology and petroleum exploration, some of the applications can be found in [92] and [93].

3.4.2 Singular Value Decomposition

Singular value decomposition (SVD) is a matrix factorization process in which M*N matrix X, will be decomposed into three matrices by equation (3.16) [10].

$$X = USV^T \tag{3.16}$$

where U and V are M*M and N*N unitary matrices, and S is M*N rectangular and diagonal matrix which holds the singular values (same as principal components in the PCA). Columns of U and V are called left and right singular vectors [94] [10] .

Equation (3.16) can be rewritten in terms of summation of the each singular value multiplied by its related left and right singular vectors. This is shown in equation (3.17).

$$X = \sum_{i=1}^{r} s_i u_i v_i^T \tag{3.17}$$

where the factor $u_i v_i^T$ is an M*N matrix and called the i^{th} eigen-image of the data matrix. SVD has been applied in many areas, in seismology; Freire et al. applied SVD to vertical seismic profiling in order to separate down-going waves (first arrivals to sensors) from up-going waves (reflections and multiples). They also used this method for the noise attenuation [89]. Bekara and Baan also applied SVD globally (applied on the complete signal) and locally (applied on the whole signal section by section separately) [88]. Vrabie et al. applied the combination of SVD and ICA in order to obtain better source (signal) separation in terms of better sensor to sensor correlation [90]. They also in [91] introduced three dimensional SVD; they assumed the data as dimensions of the time, sensor numbers, and the sensor directions.

3.4.3 *K*-mean clustering [9]

The term *K*-means clustering was first mentioned by James MacQueen in 1967 [95]. However, Stuart Lloyd was the first person who proposed the algorithm in 1957 as a method for pulse-code modulation. This method, rather than *K*-means clustering, is also referred to as the Lloyd-Forgy algorithm due to the fact that E.W.Forgy independently proposed the same methodology in 1965 [96]. About a decade later, Hartigan and Wong presented a more efficient version of this algorithm in [97] and [98].

K-means clustering aims to categorize N observations into K groups or clusters. It starts by choosing *K* points as the initial centroids for all clusters. Then each point in the dataset is assigned to the closest centroid based on a particular proximity measure chosen. Once the clusters are formed, the centroids for each cluster are updated. The algorithm then iteratively repeats these two steps until the centroids do not change or any other alternative relaxed convergence criterion is met. Figure 3.5 demonstrates the *K*-mean algorithm flowchart [9].

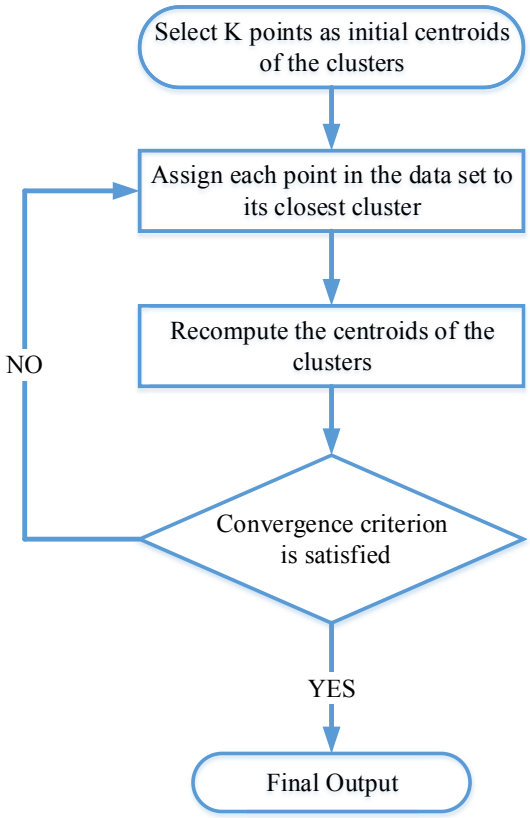

Figure 3.5: K-mean algorithm flowchart

Several proximity measures can be used within the *K*-means algorithm for splitting the data set into K groups such as Manhattan, and Euclidean distance, or Cosine similarity. In general as well as this work, the Euclidean distance metric is used for the *K*-means clustering. It is essential to consider that different values of *K* and proximity measures can significantly affect the final output. The objective function, which is employed by *K*-means as a convergence criterion, is called the Sum of Squared Errors (SSE) or Residual Sum of Squares (RSS). The mathematical formulation for SSE/RSS is as follows:

Given a dataset $A = \{x_1, x_2, ..., x_N\}$ consists of N points, the clusters obtained after applying *K*-means clustering can be denoted by $C = \{C_1, C_2, ..., C_k, ..., C_K\}$. The SSE for this clustering is defined in the Equation (3.18), where c_k is the centroid of the cluster C_K [9].

$$SSE(C) = \sum_{k=1}^{K} \sum_{x_i \in C_k} (c_k - x_i)^2 \tag{3.18}$$

The iterative assignment and update steps of the *K*-means algorithm aim to minimize the SSE function for all of the clusters. In the following, Mathematical procedure of minimization of the SSE and also a proof of the reason behind choosing the mean of the data points in a cluster as the prototype representative for a cluster in the *K*-means algorithm are provided. Here, C_k and c_k represent the k^{th} cluster and its mean, and x_i is a point in the k^{th} cluster. The SSE function can be minimized by its differentiating with respect to c_j and setting it equal to zero as shown in equation (3.19).

$$\frac{\partial}{\partial c_j} SSE = \frac{\partial}{\partial c_j} \sum_{k=1}^{K} \sum_{x_i \in C_k} \left(c_k - x_i\right)^2 = \sum_{k=1}^{K} \sum_{x_i \in C_j} \frac{\partial}{\partial c_j} \left(c_j - x_i\right)^2$$

$$= \sum_{x_i \in C_j} 2*(c_j - x_i) = 0 \Rightarrow \left|C_j\right|.c_j = \sum_{x_i \in C_j} x_i \Rightarrow c_j = \frac{\sum_{x_i \in C_j} x_i}{\left|C_j\right|} \qquad (3.19)$$

Based on the equation (3.19), the best descriptive for minimizing the SSE function of a cluster is the mean of the points in the cluster. In the *K*-means, the SSE value consistently decreases on each of the iterations. This monotonically decreasing behaviour will eventually converge to a local minimum [9].

K-mean clustering is one of the most frequently applied blind signal separation (or clustering) methods in a variety of fields especially in engineering and NDT. For instance, Yousefi et al have applied the K-mean clustering algorithm on the signals obtained from the acoustic emission to extract a general pattern of a specific damage on a glass/epoxy composite material. Their method consists of a discrete wavelet packet decomposition of AE signals accompanied with a clustering algorithm, which gives the distribution of the normalized AE signal energy on the frequency band [99]. Crivelli et al combined the K-mean algorithm with the Artificial Neural Network (ANN) for the damage detection and the real-time structural monitoring of a composite lightweight material [100]. Ihesiulor et al also utilized *K*-mean algorithm and ANN for a delamination prediction in laminated composite structures [101]. Some other applications of the *K*-mean clustering algorithm in engineering, image processing, and NDT can be found in [102], [103], [104], [105],[106].

3.5 Frequency-Wavenumber (F-K) Analysis

In Chapter 2, the one-dimensional Fourier transform has been explained. It is also shown that the waveguide governing equations can be solved for the frequencies and the roots are wavenumbers [47]. Since wavenumber refers to the spatial frequency in the space domain and the so-called frequency refers to the temporal frequency in the time domain, the waveguide propagation in the timber pole deals with two dimensional data [11]. In fact, capturing a signal at one sensor position is related to the sampling in time, while capturing signals in many sensor locations is related to the sampling in the space domain. Thus, the captured signals are in the two-dimensional domain of *(t, x)*. The two-dimensional Fourier transforms of these signals can obtain the relation between temporal frequencies and the spatial frequencies. For a sinusoidal signal, the frequency *f* is the number of cycles per unit of time; the same is valid for the spatial frequency *k*. Likewise, *k* is the number of wavelengths per space unit, so *k* is related to the wavelength by $k = \frac{1}{\lambda}$. The two-dimensional Fourier transform is provided in equation (3.20).

$$S(k,f) = \sum_{x=-\infty}^{\infty} \sum_{t=-\infty}^{\infty} s(x,t) e^{-2\pi i(kx-ft)} dtdx \tag{3.20}$$

As mentioned earlier in Chapter 2 and based on the theory of the waveguide propagation in the timber pole, a serious challenge in the stress-wave-based methods is the presence of the wave dispersion. In fact, the dispersion is formulated as a relation between wavenumbers and frequencies, which means that different types of waves travel in a structure with different frequencies/modes and different wave velocities. F-K analysis is one of the most extensively applied techniques used by researchers and in the industry for signal filtering based on the velocity [11]. The phase velocity v_p can be expressed in terms of the frequency and the wavelength as:

$$v_p = f.\lambda \tag{3.21}$$

This equation can also be written in the form of an angular frequency ω and the wavenumber *k*. Since $k = {}^{2\pi}/_{\lambda}$ and $\omega = 2\pi f$ it results in:

$$v_p = \omega / k \tag{3.22}$$

while digital filters are spatial domain filters and are based on the frequency components of the signal, F-K filters are the both spatial and temporal filters. As a result, F-K analysis enables filtering of the signal based on the different wave velocities that exist in the signal. Hence, it is ideal for the structures with dispersive materials. Hanna [107] applied this method to a seismic data to extract a desired signal based on its velocity. Michaels et al [11] separated different modes of the ultrasonic guided wave signals that were captured from a damaged composite plate by means of the F-K filtering; with this separation of modes, they could detect the crack in a plate.

Once the velocity filter has been designed and applied on the transformed data, two-dimensional inverse Fourier transform can be utilized to transfer the data back to the time-space domain. Equation (3.23) shows the two-dimensional inverse Fourier transform.

$$s(x,t) = \sum_{k=-\infty}^{\infty} \sum_{f=-\infty}^{\infty} S(k,f) e^{2pi(kx-ft)} dfdk \tag{3.23}$$

Since timber is an orthotropic material with natural finite boundaries, the wave dispersion and conversion is a serious challenge in this research. It is also worth considering that the challenge in this research is even more complex than the one in the reflection seismology. The reason is in reflection seismology semi-finite boundaries exist (i.e. one boundary, horizontal or vertical, is always infinite), while for the timber poles, the boundaries are not only finite in both directions, but the horizontal boundaries do also have a very close distance.

Details of the velocity filter design and implementation is provided in Chapter 6.

3.6 Summary

This chapter firstly presented a signal processing model for the in-service timber utility pole. Here the timber pole is considered as a Linear Time-Invariant (LTI) system, in which the output of the system (i.e. the captured signals by sensors) can be

mathematically expressed as the convolution of the input (i.e. the hammer excitation impact) with the impulse response of the LTI system (i.e. the timber pole).

Next, some modified advanced digital signal processing methodologies that were used in this research were explained. These methods can be grouped into three categories as deterministic signal separation, blind signal separation, and frequency-wavenumber analysis (velocity filtering).

Deterministic signal separation methodologies include the Wiener and the predictive deconvolution. In the Wiener deconvolution, the prior information about the input signal or the input signal itself is available, while in the predictive deconvolution the essential information is extracted from the captured signal itself.

Blind signal separation methods refer to the methods in which the input signal or any information about it is not available, and the signal separation is purely based on the differences between existing patterns in the captured signals. Separation in these methods can be done by finding the statistical differences between the existing patterns, or applying iterative and learning algorithms to cluster the dataset more efficiently. The blind signal separation methodologies that had been used in this research are Principal Component Analysis, Singular Value Decomposition, and *K*-mean clustering algorithm. The first two are non-learning blind signal separation algorithms, while *K*-mean clustering algorithm is the most popular and widely applied clustering algorithm that contains optimization and learning.

The Frequency-Wavenumber (F-K) analysis (velocity filtering) was also presented in this chapter. In this method, the data was considered having two dimensions of time and space. In this regard, two-dimensional Fourier transform was applied on the data, which resulted in presentation of the captured signals in the frequency-wavenumber domain.

It is also necessary to consider that the solution of the waveguide governing equations in the timber pole obtained the so-called dispersion relations, which refer to the relations between the frequencies and the wavenumbers. In other words, F-K domain analysis gives the opportunity of filtering the captured signals based on the dispersion relation curves.

4 Chapter 4: Experimental Test Setups for timber poles

4.1 Introduction

This chapter presents details of the surface stress-wave-based methods for non-destructive assessment of the timber poles being developed at the University of Technology Sydney as part of this research study. The equipment and testing procedures of the conventional and enhanced surface stress-wave-based techniques, i.e. Sonic-Echo (SE) method and Bending Wave (BW) method are described in this chapter. These methods are applied to the timber poles for the determination of the embedment length. For the presented methods, a step-by-step guide is provided on how to execute the tests, how to analyse the recorded data, and how to calculate the length of the test structures.

4.2 Test Equipment

The equipment necessary to perform surface stress-wave-based testing consists of: a modally tuned impact hammer, multiple sensors (piezoelectric accelerometers), a multi-channel signal conditioner, data acquisition cards and a personal computer equipped with signal acquisition software.

4.2.1 Hammer impact

For stress wave testing, the impact hammer used is a PCB model HP 086C05 of sensitivity 0.24 mV/N. The hammer is equipped with a load cell to measure the force of the impact. A metal hammer tip was used to investigate the impact force as shown in Figure 4.1. The metal tip is chosen due to its higher excitation frequency. It is worth considering that the higher the maximum excitation frequency is, the smaller the wavelengths that can be applied. Figure 4.2 show an example of the force spectrum from the hammer blow.

Figure 4.1: Impact hammer

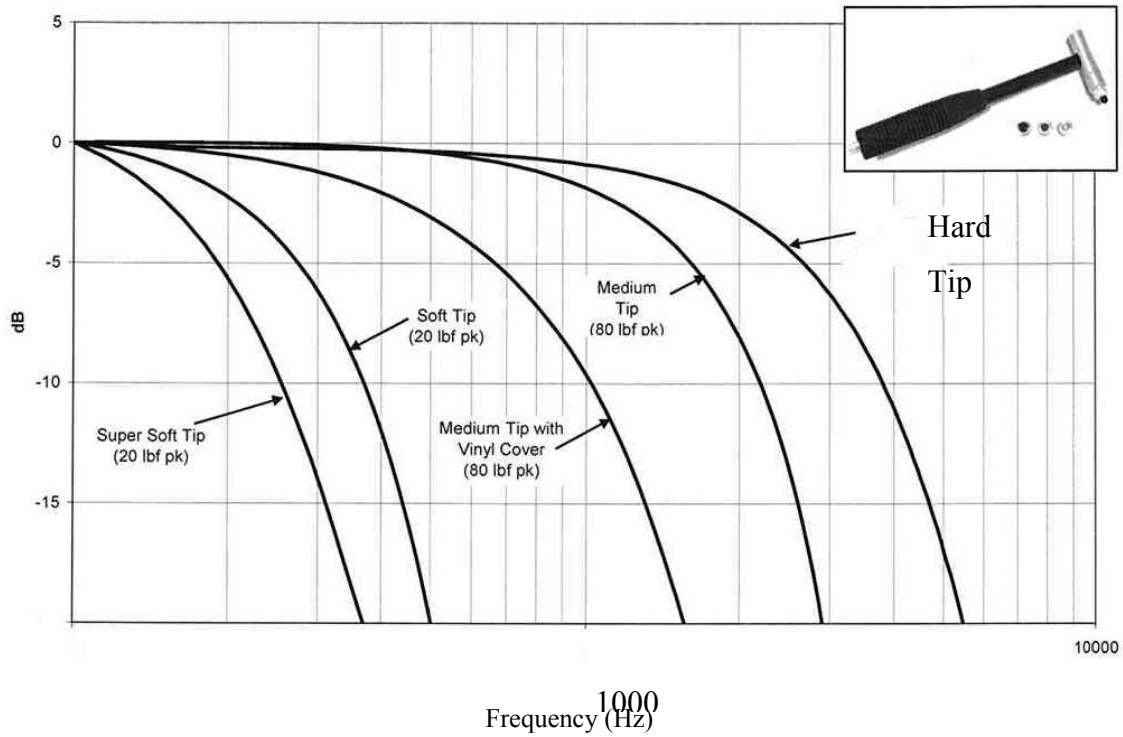

Figure 4.2: Typical response of hammer impact [108]

4.2.2 Accelerometers

To record the structural response, piezoelectric accelerometers were used. The employed accelerometers are PCB model 352C34 (see Figure 4.3), which are of low impedance, having a sensitivity range from 100 mV/g ±10%, and measurement frequency range is 0.5 to 10000 Hz with ±5% error, or 0.3 to 10000 Hz with ±10% error.

The accelerometers were mounted on the timber pole utilizing magnets and screws as illustrated in Figure 4.4.

Figure 4.3: Piezoelectric accelerometer model PCB 352C34

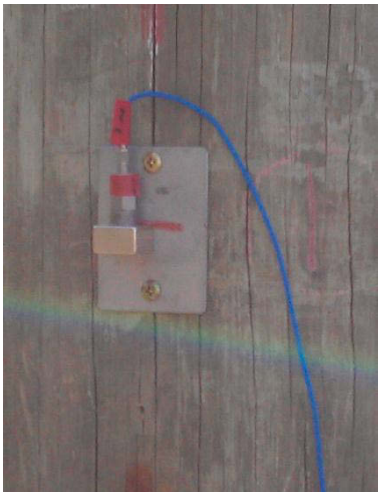

Figure 4.4: Accelerometers mounted to the timber pole utilizing magnets and screws

4.2.3 Signal Conditioning, data acquisition cards and computer

To amplify and condition the signals of the modal hammer and the piezoelectric accelerometers, a 12-channel signal conditioner (model PCB 483B03) is used (depicted in Figure 4.5). The data acquisition card employed for stress-wave-based testing at the University of Technology Sydney (UTS) is a middle range 8 channel system with 12-bit 4M samples/sec per channel model NI PCI-6133. Based on the requirements for this research, it is essential to utilise a data acquisition card that is able to record signals with a minimum sampling frequency of 1M samples/sec per channel. This high sampling frequency is set to avoid any round-up errors in detecting the peaks (first arrivals and reflections) time.

For data capturing, a personal computer (PC) equipped with the National Instrument software LabVIEW is used. As the size of the acquisition card did not fit the laptop, a PC was used for all laboratory and field testing as shown in Figure 4.6.

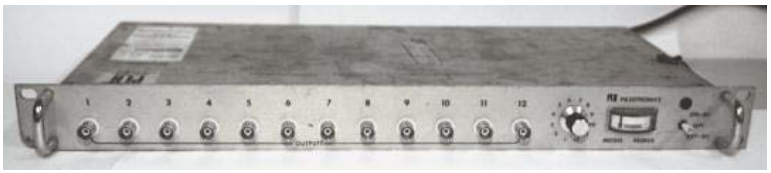

Figure 4.5: Multi-channel signal conditioner - model PCB 483B03

Figure 4.6: A personal computer for laboratory and field testing

4.2.4 Laboratory testing frame

A container, 1.2 m × 1.2 m in cross-section and 3 m in height which can contain sand/soil for embedding test specimens was used. A steel frame was assembled using equal angle steel for the columns and for support of the boundaries. Plywood was used for the boundaries. For three sides of the frame, fixed plywood was used and for the other side, the boundary was completed using a small frame of plywood as shown in Figure 4.7. Scissor lift and scaffold was used to assemble the frame and also for filling the soil and to impact the specimens as shown in Figure 4.8.

Figure 4.7: Steel frame used as a container

a) Scaffold to build the frame

b) Scissor lift to fill the soil into the frame

Figure 4.8: Using scaffold and scissor lift to build and access the top of the frame

4.3 Testing Scenarios

4.3.1 Testing Procedure

For various standing-on-soil and embedded tests, a step-by-step testing procedure, including the set-up of the equipment, the settings of the acquisition software and the execution of the tests, is described as follows.

1. Setting up of the personal computer, data acquisition system and signal conditioner (see Figure 4.10(a)).

Note: All electrical devices must be connected to the same power supply. If a generator is used, it must be earthed.

2. Attachment of the sensors and impact screw to the structure (Figure 4.10 (b) and (c)).

Note: The number and locations of the sensors depend on the type and requirements of the individual test. However in all tests, it must be assured that a firm connection between the structure and the sensors is established. Magnets were used to attach the accelerometers to steel plates (which are screwed to the structure) or directly to the screws that were drilled into the structure using a cordless drill (see Figure 4.10(b)). Figure 4.10(c) shows the final test setup.

3. Connections of the impact hammer and attached sensors to the signal conditioner, data acquisition system and personal computer.

To create a longitudinal or bending wave in the timber pole, the pole must be struck in a longitudinal or transverse axis direction, respectively. The impact must be controlled to reduce local crushing of the contact interface between the pole and the impact hammer. It is essential that the impact device itself is also able to withstand multiple impacts without crushing or damage.

4. Launching and setting up of data acquisition software (e.g. National Instrument LabView).

Note: In the data acquisition software, the sampling rate is set to at least 1 MHz for a frequency range of 100 Hz to 5 kHz and a minimum time duration of 0.5 s. To ensure

that the entire impact excitation signal is recorded, a pre-trigger delay of 0.01% of the test duration was set.

5. Execution of trial tests.

Note: To ensure that the testing equipment was set-up correctly and that all sensors were working properly, a number of trial tests were performed. The following features must be checked for the hammer and all sensor channels: noise-to-signal ratio of hammer and sensor signals (must be lower than 1%), amplitudes and shapes of the hammer and sensor signals, DC offsets of sensor signals and consistency of sensor signals between different tests.

6. Execution of actual tests (see Figure 4.10 (d)).

Note: For every test specimen, at least five tests were performed in order to check consistency and repeatability to provide averaged test results for increased robustness. The impact force was to be executed either at the head centre of the test specimen or at an impact screw firmly attached to the side of the structure. Figure 4.9 shows the captured signals in all eight sensors in one of the field tests which were repeated five times. The repeatability of the captured signals can be seen in this figure.

7. Saving of recorded data. Disconnecting, dismantling and packing of equipment.

Note: Any abnormalities, special occurrences or events were noted down for future reference.

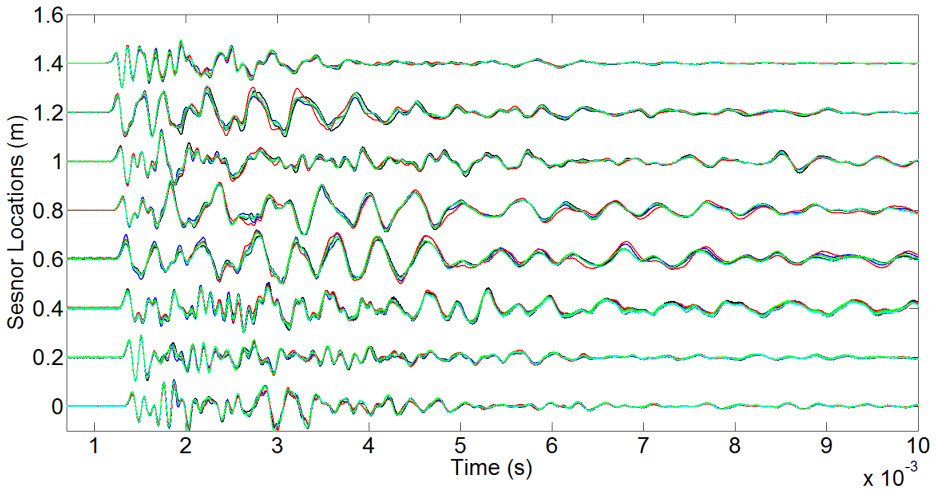

Figure 4.9: Captured raw signals in all eight sensors in one of the field tests which were repeated five times

Figure 4.10: Testing procedure: (a) setting up of equipment, (b) mounting of accelerometer, (c) attached impact screw and accelerometers and (d) execution of the test.

4.3.2 Test specimens

A timber pole representing an actual field specimen having imperfect geometry, complex material property and local defects was used as a test specimen in the structures laboratory of the University of Technology Sydney (UTS). All types of the tests have been executed on the timber poles in two conditions of standing-on-soil and embedded in soil. Figure 4.11 shows the standing-on-soil and embedded condition in

the Laboratory experiments. It is also essential to mention that sand is chosen as a soft soil in this research.

(a) (b)

Figure 4.11: Timber pole in (a): standing-on-soil, and (b): embedded in soil conditions

4.3.3 Test set-up for Sonic-Echo Method

In Sonic-Echo testing, the test structure is excited in the longitudinal direction with a modally tuned impact hammer. The impact location is at the top centre of the structure (only longitudinal waves are generated).

To record the time travel of the longitudinal stress waves, sensors are attached to the test structures to monitor the structural response. At least one sensor, measuring longitudinal vibration, is necessary to capture the reflection waves of the impact. However, in order to increase test reliability and accuracy, a number of sensors were mounted on the timber pole.

The test configuration for the laboratory testing conducted at UTS (with impact location on top of the specimen while it is embedded in soil) is shown in Figure 4.12. The sensors set-ups and impact location for standing-on-soil condition is the same as for the embedded one.

The number and positions of the sensors are determined based on the in-field test set-ups. For field testing of embedded timber poles, eight sensors were used and mounted in a line with spacing of 20 cm between the sensors as depicted in Figure 4.12 and Figure 4.10(c).

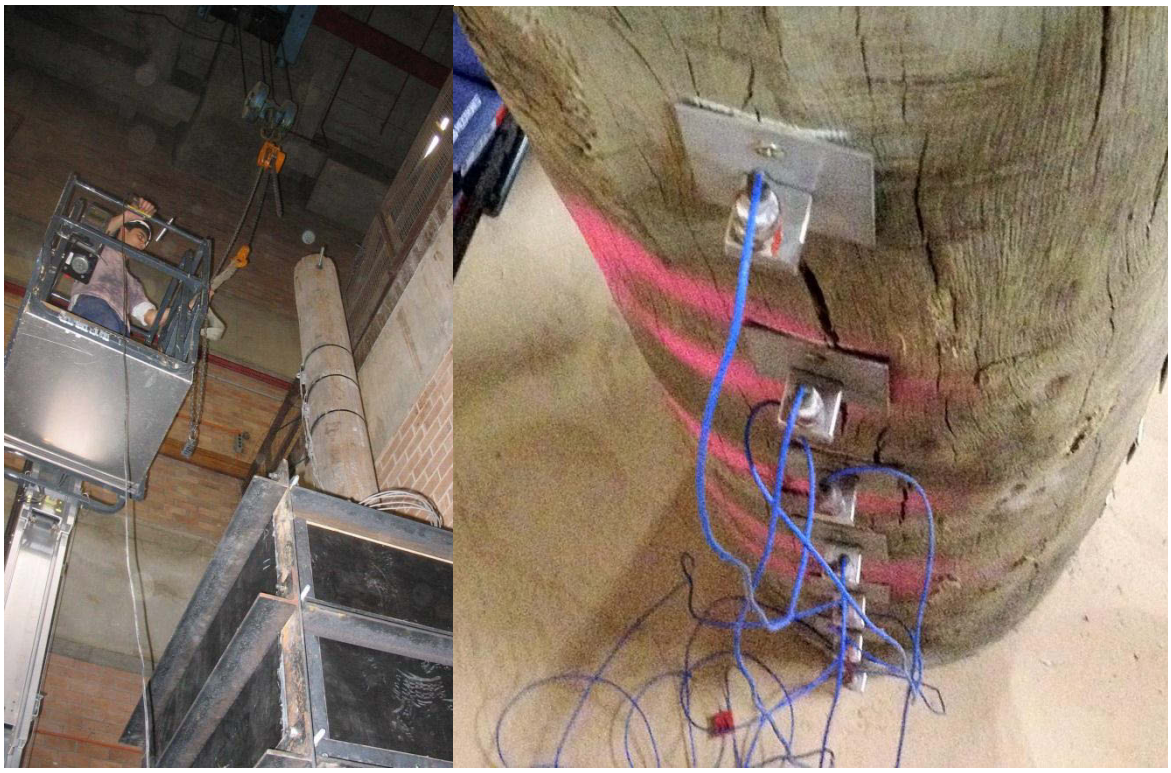

Figure 4.12:Test set-up of embedded testing in laboratory

4.3.4 Test Set-Up for Bending Wave Method

The test set-up, equipment and testing procedure of the BW method were similar to the SE testing described in the previous section. Whereas in SE testing, the impact was executed in the longitudinal direction (to generate longitudinal waves), in BW testing, the hammer strike was performed in the transverse direction (to generate flexural waves). To record the response of the structure, three sensors were used in the experimental tests to measure the initial arrival of the flexural waves and subsequent reflections (echoes). Since the BW method analyses reflective signals from flexural (bending) waves, the sensors were mounted in the transverse direction to monitor flexural wave vibration. To be able to calculate the FRFs of the sensor signals, the force signal of the impact hammer was recorded as well. The schematic of the test set-ups of the BW tests executed in the structures laboratories at UTS is illustrated in Figure 4.13.

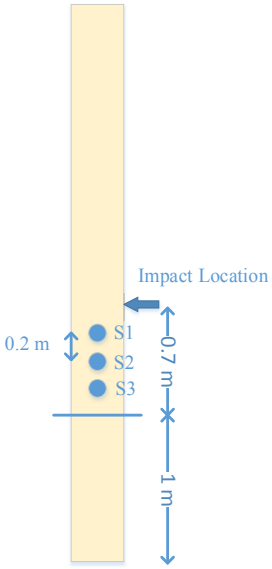

Figure 4.13: Schematic of the bending wave tests set-up

4.4 Field tests on Timber utility poles

4.4.1 Mason park not in-service timber poles embedded in soil

There are 15 intact timber poles installed at Mason Park, NSW, by Austgrid (the project's industry partner) with different embedment lengths to investigate the effects of the embedded length on different non-destructive tests. The location of the site, a plan view of the Mason Park and the site layout and embedded length for each timber pole are shown in Figure 4.14 and Figure 4.15 respectively. Figure 4.16 and Figure 4.17 display the timber poles before and after the installation on site.

Figure 4.14: Location of the Mason Park (courtesy of Google Maps)

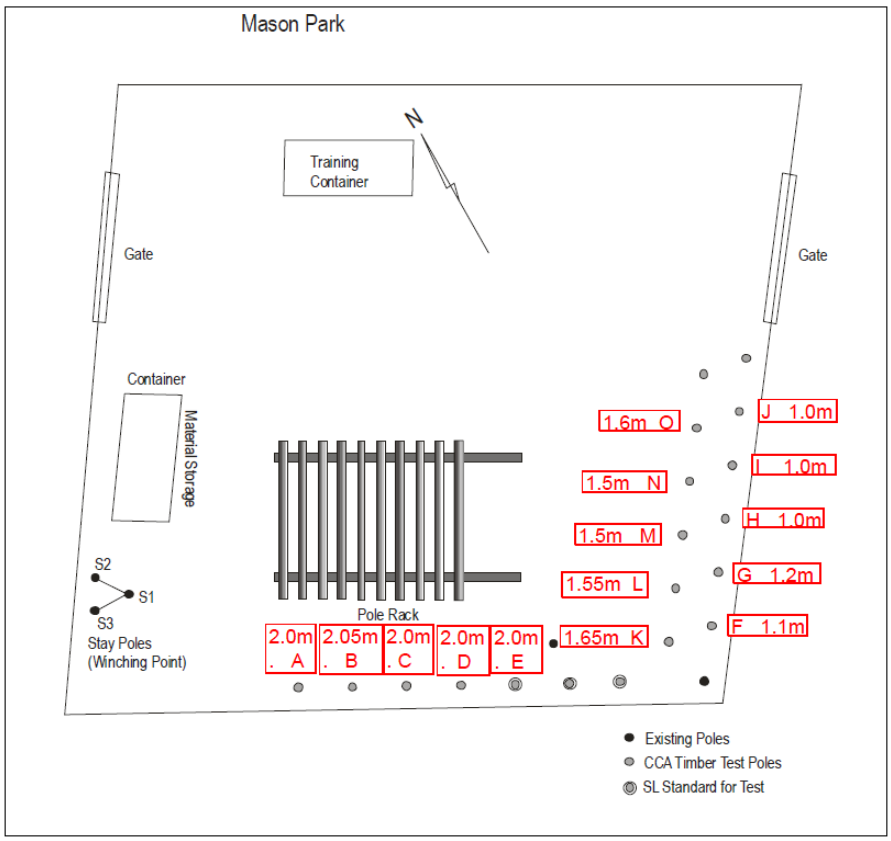

Figure 4.15: Location of timber poles at Mason Park

Figure 4.16:Timber poles before installation in Mason Park

Figure 4.17:Timber poles after installation in Mason Park

5 Chapter 5: Application of the conventional surface stress-wave-based tests on condition assessment of the timber pole

5.1 Introduction

This chapter presents firstly comprehensive investigations on the digital filters, their benefits, and limitations in order to choose the best type for the final equipment that is going to be delivered to the industry partner. It secondly presents numerical and experimental investigations of the conventional and currently available surface stress-wave-based methods for condition assessment of the timber poles (including Sonic-Echo method utilizing the longitudinal wave, Short Kernel Method utilizing the Bending wave, and Ultraseismic utilizing both of the longitudinal and the bending waves). A timber pole representing an actual field specimen having complex material property and local cracks is used for all lab tests. In the SE method, the acceleration-time history results are used to calculate the wave velocity followed by the evaluation of the embedded length of the specimen. For the Bending Wave, Short Kernel Method (SKM) was investigated to determine the phase velocity of the flexural wave and the embedded length. In the Ultraseismic method, the hammer impact excitation is applied on the side of the timber pole at a 45º angle, and multi-sensors array is used for capturing the signals. It is also worth considering that the hammer impact is applied on the side of the timber pole since access to the top of the pole is prohibited in real in-field application, and it is applied with a 45 degree of angle in order to maximize the probability of creating the longitudinal wave.

The structure of this chapter is as follows: firstly, results of the comprehensive digital filter investigation are presented, and then the results of analysis on the numerical data obtained from simulated timber poles with ANSYS software, followed by the laboratory tests results are presented.

The results of the Sonic-Echo method includes two sections, firstly a single sensor analysis (i.e. the conventional Sonic-Echo test procedure), secondly sensor array analysis, which is a suggestion of utilizing a multiple-sensors array in order to obtain the results that are more reliable. Results of the Bending Wave and the Ultraseismic methods are also presented. It should be mentioned that stress wave velocity calculation is a critical part of each method as this value will be used later for length determination of the specimen, and a slight errors in the velocity calculation can considerably increase the length estimation error. In addition, selection of the reflection peak is a major and most important part of each method as the length estimation procedure relies on the time difference between the arrival and reflection peaks and the estimated velocity. In this chapter, for each method velocity analysis followed by the length estimation procedure are provided.

5.2 Digital Filters Investigation

Digital filter is used to remove a range of unwanted frequencies in the signal. Because the timber pole itself acts as highly dispersive material, and embedment length estimation relies mainly on the reflection peaks detection, digital filter is needed to be designed and implemented in a way that causes minimum distortions especially in terms of the signal phase. It is essential to consider that slight changes in the position of the peak in time can considerably increase the length estimation error. Furthermore, a portable embedded system is required for the in-service timber utility pole condition assessment test; and in all portable embedded systems, power supply is a critical matter and choosing a digital filter, which uses power optimally, is crucial. In connection with these points, in the following a comprehensive research on the different types of the digital filters is presented. In all of the filters' designs, sampling frequency is 1MHz as were used in this project, and all of the filters are designed as a low-pass filter with cut off frequency at 3.6 kHz. All filters have been verified by both synthetic data which is a summation of three sinusoidal waves with frequencies of 3 kHz, 4 kHz, and 5 kHz, and a real test signal captured from the timber pole in service. Figure 5.1 and Figure 5.2 show the frequency and the time domains of both of the synthetic and field test signals.

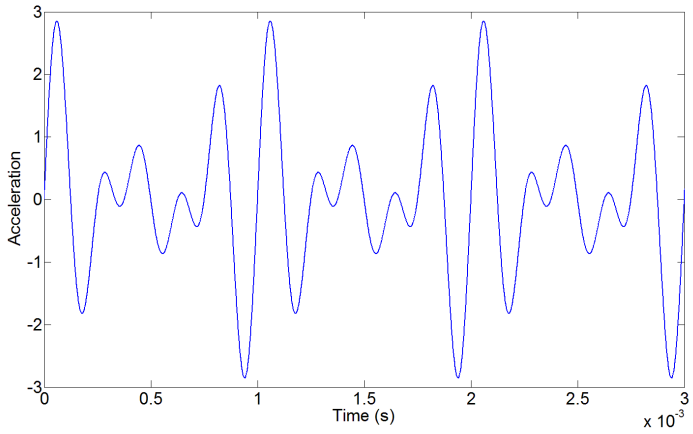

(a)

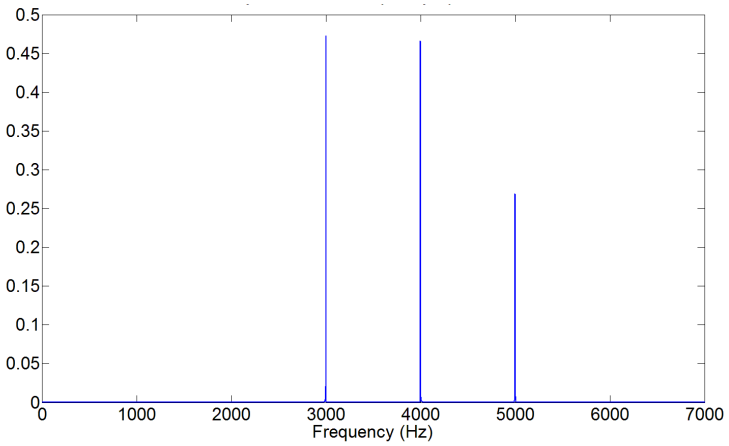

(b)

Figure 5.1: Frequency spectrum and the time domain representation of Synthetic data

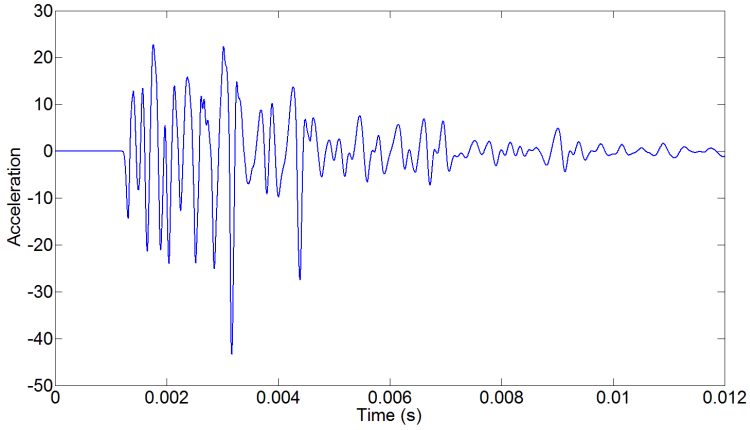

(a)

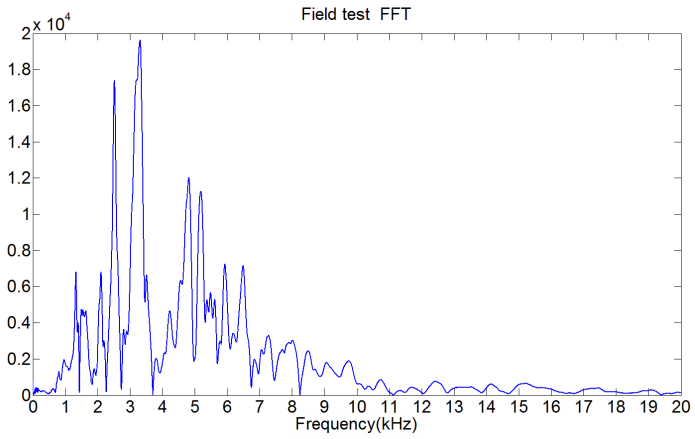

(b)

Figure 5.2: Frequency spectrum and the time domain representation of Field test data

5.2.1 FIR vs. IIR filters

As mentioned earlier in Chapter 3, IIR and FIR filters are two types of the digital filters that can be used in this project. Since it is necessary to preserve the signal phase and based on both filter types' characteristics, FIR filters are chosen to be used here. The main advantage of the FIR filters is to cause linear phase shift, which is amendable by applying zero-phase filtering process (explained in section 5.2.2), while IIR filters causes nonlinear phase shift, which is not amendable and can jeopardize the reliability of the results by repositioning the peaks in the time domain.

5.2.2 Different FIR filter design methods investigation

There are two main methods to design the FIR filters; windowing method, and Remez algorithm (which is based on the Chebyshev approximation). Each of the windowing

methods has its own characteristics that are summarized in Table 5.1. In this table, N is the filter order and T is the time interval between two samples in the time domain. The rectangular function has the narrowest transition bandwidth, as well as lower stop-band attenuation [53]. Considering the stop-band attenuation and the transition bandwidth, five different types of windows (Hamming, Hanning, triangular, Blackman and Kaiser) have been designed and compared to each other in this investigation. Equiripple filter based on a Parks–McClellan optimization algorithm has also been designed and results are compared to the best windowing method filter.

Table 5.1: Window functions characteristics for the FIR filters [53].

Window Type	Transmission width	Stop-band attenuation
Rectangular	2/NT	21 dB
Triangular	4/NT	25 dB
Hamming	4/NT	53 dB
Hanning	4/NT	44 dB
Blackman	6/NT	74 dB
Kaiser	variable	variable
Chebyshev	variable	variable

As four types of the window functions have fixed stop-band attenuation, for each of these window type filters, a Kaiser window with the same transition bandwidth has been designed and results are compared. Figure 5.3 shows the time and frequency spectrum results for the triangular, Hamming, Hanning, and Blackman windows with fixed transition bandwidth (300 Hz) applied to the synthetic data.

All of the filters are designed to be very sharp (bandwidth of the filter is 0.3 kHz while the signal bandwidth is 1000 kHz). It can be seen in Figure 5.2 that all windows are able to obtain the desired frequency range of the signal, which is a sinusoidal wave with 3 kHz frequency. However, in the triangular window, there will be a small attenuation in the pass-band (see the green oval in Figure 5.3 (a)).

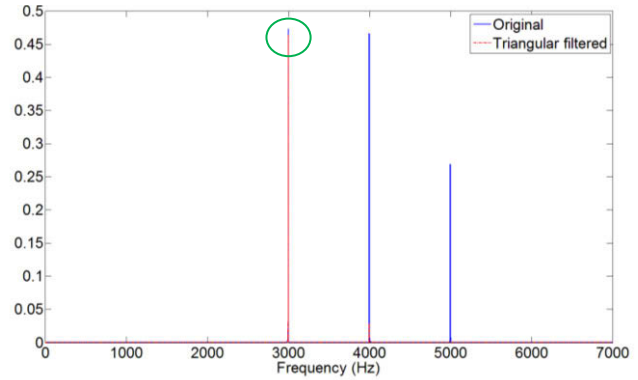

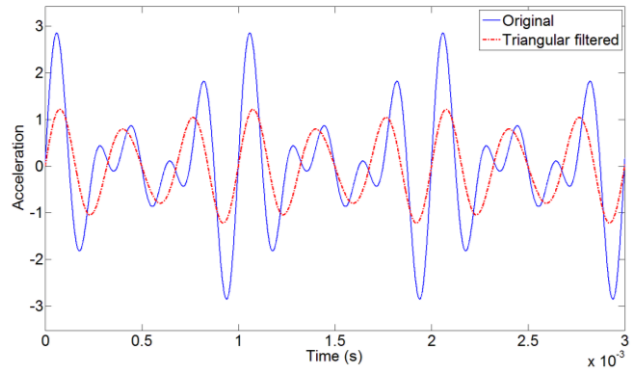

(a)

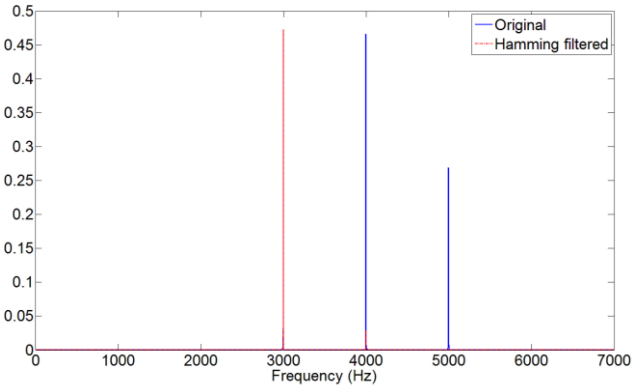

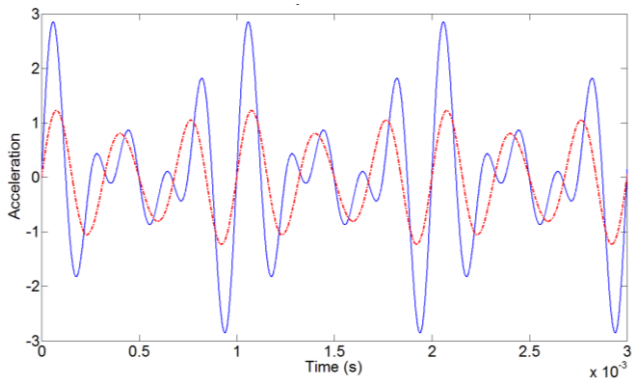

(b)

Figure 5.3: (a) Triangular, and (b) Hanning, Hamming, and Blackman windows time and frequency spectrum applied on the synthetic data. (Because of similarity of figures of these three filters, only the Hamming's output is provided).

The four window methods and the related Kaiser window are compared for their effectiveness based on their stop-band attenuation. Results demonstrated that the Kaiser window needs less numbers of tabs (lower filter order and consecutively lower power consumption and processing time) in comparison to the related constant stop-band attenuation window; see **Error! Not a valid bookmark self-reference.**.

Table 5.2: the comparison of four types of the window designs, and their related Kaiser Windows design applied on the synthetic data.

Window type	Stop-band attenuation	Filter order	Related designed Kaiser window order
Triangular	25dB	13300	3947
Hanning	44 dB	13300	8357
Hamming	53 dB	13300	10446
Blackman	74 dB	20000	15320

All above-mentioned designed filters have also been tested and validated by the captured signals from the in-service timber poles; results have shown in Figure 5.4.

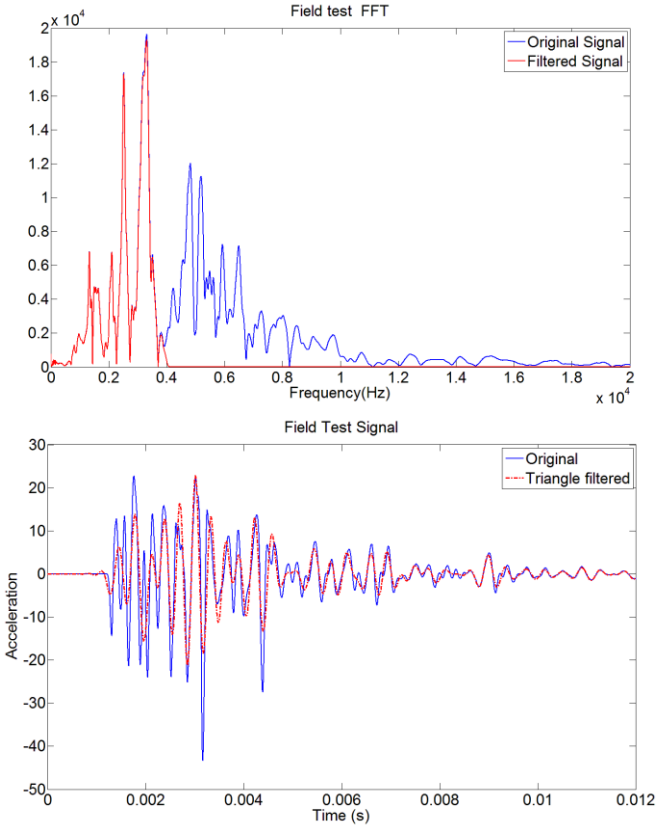

(a)

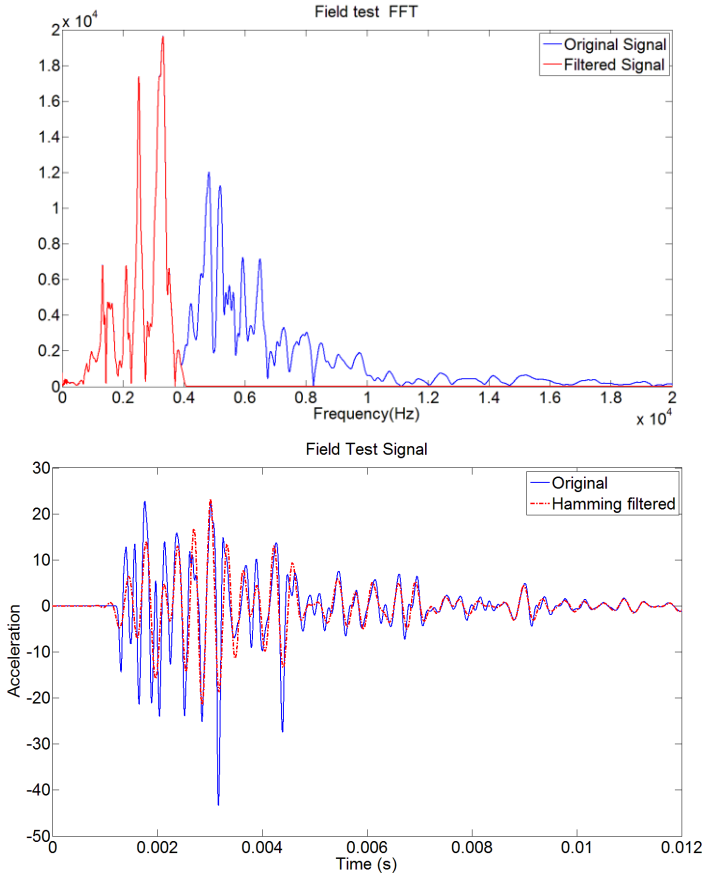

(b)

Figure 5.4: The frequency and time domain results of (a) the Triangular, (b) Hanning, Hamming, and Blackman windows applied on the captured signals from the in-service timber poles

As can be seen in Figure 5.6, all of the filters can obtain the desirable range of frequencies, although the triangular filter has a small attenuation in the pass-band. The filters are different from each other in terms of their orders (which determine the processing time and the power consumption). The linear phase distortion of all of the filters has been amended by a zero-phase filtering process. This filtering process is done by applying two FIR filters with the same design specifications but reverse tab sequences. The output of the first filter is phase shifted filtered of the input signal, and then this output is fed to the same FIR filter but with the reverse tab sequence. The overall output has twice the amplitude distortion (which is unavoidable), but zero phase change. Figure 5.5 shows the aforementioned filtering process.

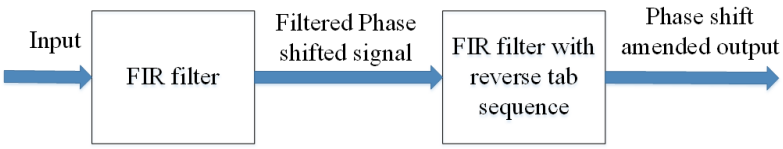

Figure 5.5: Zero-phase FIR filtering process.

Results of the non-zero and zero phase FIR filtering are presented and compared in Figure 5.6 and Figure 5.7.

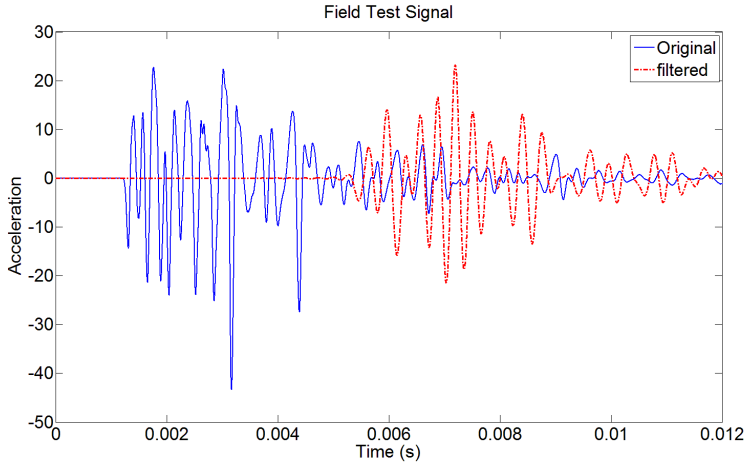

Figure 5.6: Non-Zero-Phase FIR filtering results

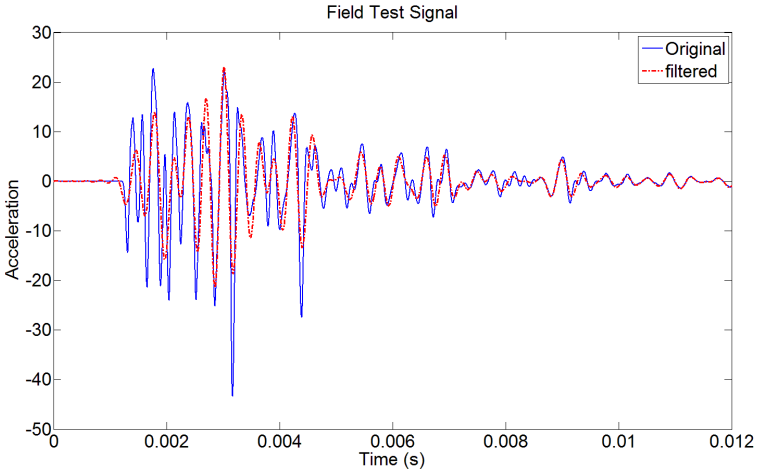

Figure 5.7: Zero phase FIR filtering results.

Considering

The four window methods and the related Kaiser window are compared for their effectiveness based on their stop-band attenuation. Results demonstrated that the Kaiser window needs less numbers of tabs (lower filter order and consecutively lower power

consumption and processing time) in comparison to the related constant stop-band attenuation window; see **Error! Not a valid bookmark self-reference.**.

Table 5.2, the best window method that can be used in this project is the Kaiser as it not only gives flexibility in choosing the stop-band attenuation, but also needs less tabs in comparison with the related fixed band-pass attenuation filters.

Finally, the Equiripple filter has been designed and compared to the Kaiser window. Both of the filters have the stop-band attenuation of 80dB. One important factor in the Equiripple filter design is a ripple in the band-pass, which determines the amplitude distortion. Here, two ripple values have been studied; 1dB, which obviously has noticeable effects on the amplitude of the desirable output signal, and 0.01dB, which leads to more tabs or higher order filter but the results are satisfactory. Figure 5.8 and Figure 5.9 show the results of the Equiripple filters with 1 and 0.01 dB ripples in the pass-band applied on the signal captured from the in-service timber pole.

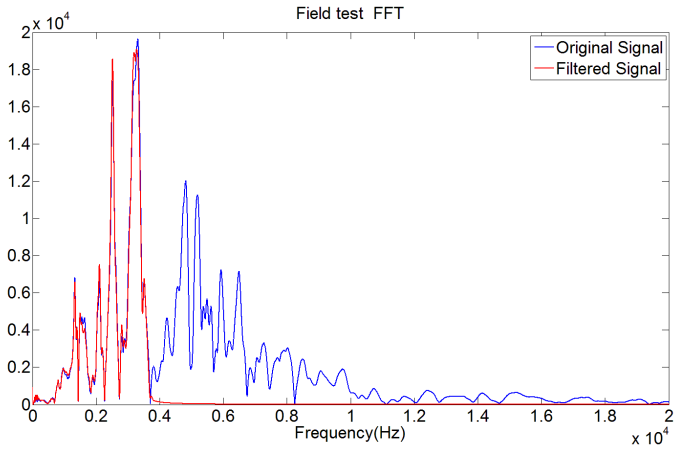

(a)

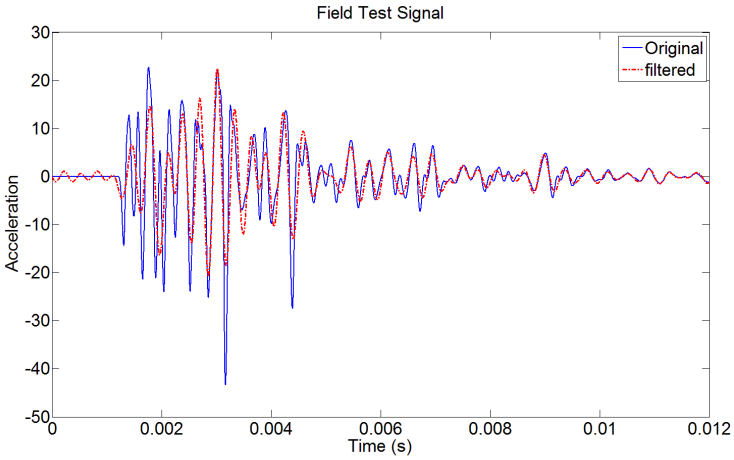

(b)

Figure 5.8: The frequency and time domain results of the Equiripple filter with 1 dB ripple in the pass-band applied on the field tests data

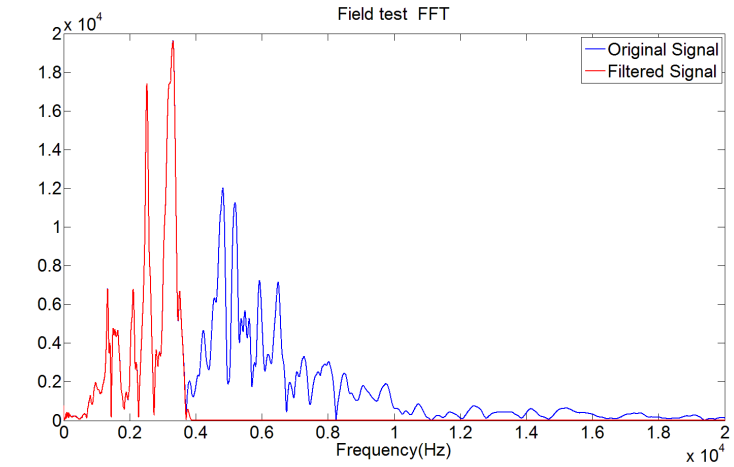

(a)

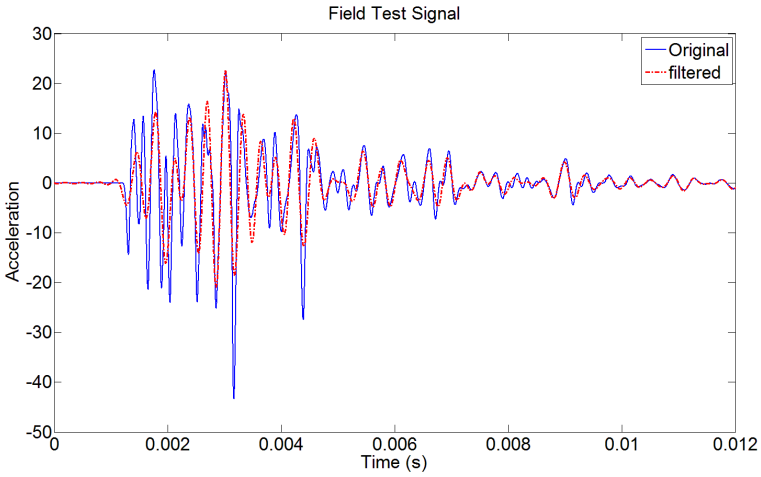

(b)

Figure 5.9: The frequency and time domain results of the Equiripple filter with 0.01 dB ripple in the pass-band applied on the field tests data

Figure 5.10 shows the Equiripple filter characteristics for the both 0.01 and 1 ripple in the band-pass. Intolerable amplitude distortion caused by 1 dB ripple in the pass-band can easily be seen in this figure. This amplitude distortion can also be seen in Figure 5.8 (a).

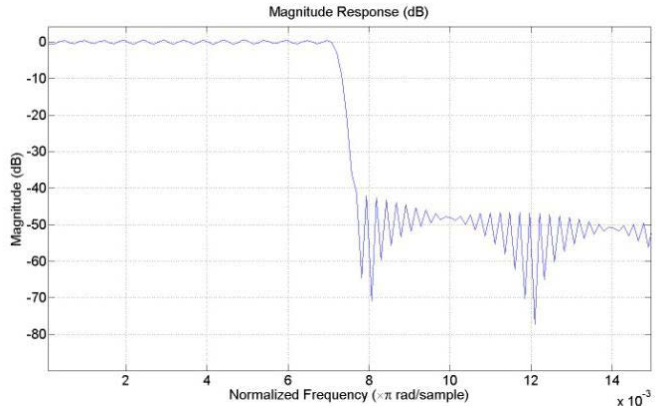

(a)

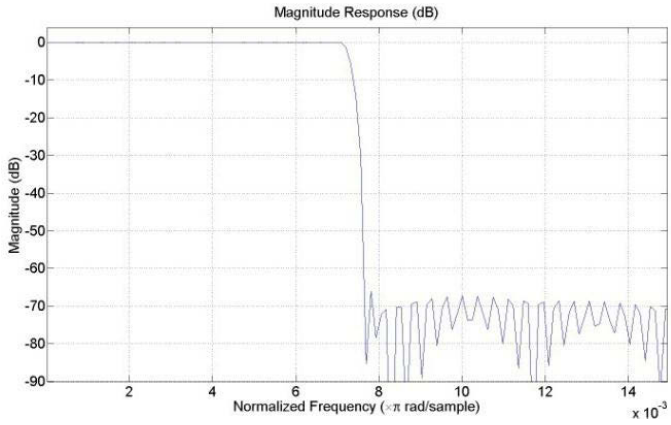

(b)

Figure 5.10 : The Equiripple filter with (a) 1 ripple, and (b) 0.01 ripple in the pass-band

A comparison between the Kaiser Window and the Equiripple has been shown in Table 5.3. As can be seen, although the Equiripple filter order with 1dB ripple in the pass-band is almost half of the Kaiser, its amplitude distortion is not tolerable. The Equiripple filter with 0.01dB not only has acceptable amplitude distortion but also has noticeably lower orders in comparison to the Kaiser window.

Table 5.3: The Equiripple and the Kaiser Filters comparison.

Filter type	Kaiser	Equiripple (1 dB ripple in band-pass)	Equiripple (0.01 dB ripple in band-pass)
Order	16744	8437	11083

The 0.01 dB Equiripple and the Kaiser filters' characteristics have also been shown in Figure 5.11. Although, the Kaiser window has 80 dB attenuation at the beginning of its stop-band, it is not an optimized filter as the stop-band attenuation goes as high as almost 130dB, which increases the power consumption and is not desirable. It is vital to

consider that the primary aim of this industrial supported research project is to design and implement a portable NDT system by which firstly the embedded length of the pole could be estimated. The sampling frequency of the system was set to 1MHz in order to avoid losing any information and designed digital filters were supposed to work not only on the narrow frequency range of 0 to up to 4 KHz (this is narrow band in comparison with 1MHz sampling frequency), but also the filters should be very sharp. In this regard, the filtering process could take at least couple of minutes. Considering that the laptop of the portable NDT system is running on the battery and supposed to work for at least couple of hours, minimizing the time process means minimizing power consumption.

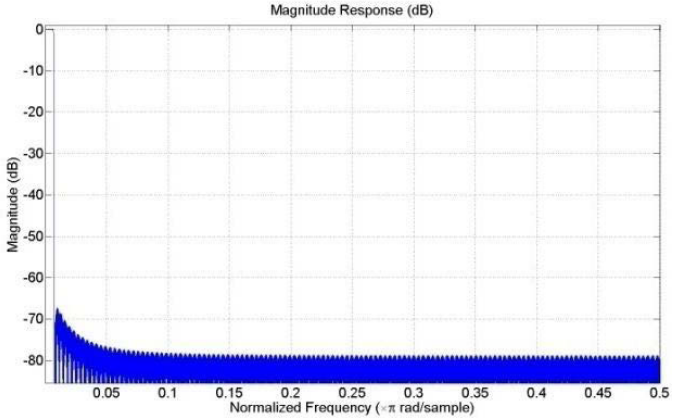

(a)

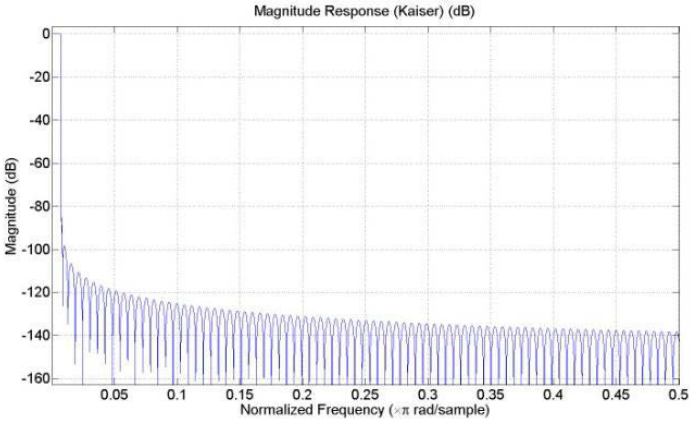

(b)

Figure 5.11: (a): Equiripple (0.01 dB ripple), and (b): Kaiser filter characteristics.

On the other hand, although the Equiripple filter's stop-band attenuation is not 80 dB from the beginning, it converges to the desirable attenuation value quickly. Based on all of the investigations in this work, the Equiripple FIR filter is chosen to be used in the

rest of the project for all of the data types (i.e. numerical data obtained from ANSYS, the signals captured from the laboratory and the field tests).

5.2.3 NDT digital filtering toolbox

A digital filtering toolbox has been designed and programed by GUI (Graphical User Interface) in MATLAB. This toolbox has been used not only in the timber pole project, but also by many other research students in the school of Civil and Environmental engineering in the University of Technology Sydney. Figure 5.12 illustrates a main page of the toolbox.

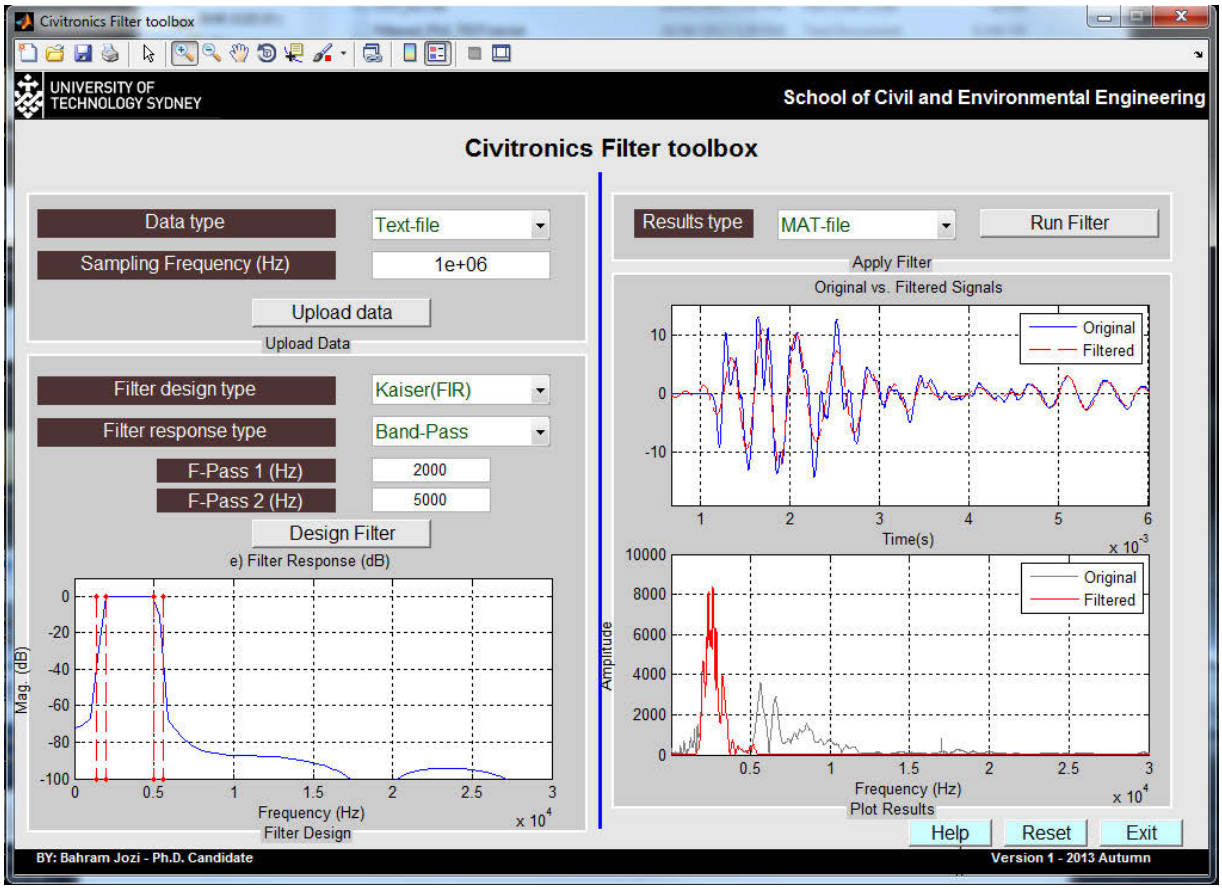

Figure 5.12: Main page of the designed digital filtering toolbox

The working procedure of this toolbox is as follows. Firstly, a data is needed to be uploaded; three types of data (Text-File, MATLAB type, and Microsoft Excel type) can be uploaded with any sampling frequencies (to be entered in a related window). Then the filter type should be chosen from the two best FIR filters (Kaiser and Equiripple), and the best IIR filter (Butterworth); they can also be applied as the low-pass, band-

pass, and high-pass filter with desired cut-off frequencies. Finally results can be saved as Microsoft Excel, MATLAB, or the Text-file format in the same directory as the program is running. Other features included in this toolbox are the filter amplitude response (lower figure on left side of Figure 5.12), and two plots containing a comparison of original signal vs. filtered signal in both of the time and frequency domains.

5.3 Finite Element modeled timber pole data analysis

5.3.1 Finite Element modelled timber pole specifications

Finite Element (FE) models of the timber pole with specific material and soil properties have been used. The numerical models were created and analysed with the software ANSYS using transient analysis. The modelled poles had 300 mm diameter and were 11 m or 12 m long, which are typical dimensions of the in-service utility timber poles. For the isotropic modelling of the timber, material properties are as follows: the density (ρ) was set to 950 kg/m^3, the elastic modulus (E) to 23,000 MPa, and the Poisson's ratio (ν) to 0.3.Typical hammer impact force (used in field tests) was applied to the surface of the pole. The location of the impact force varies based on the test type, e.g. on the top centre of the pole in the Sonic-Echo method, on the side of the pole almost 3 meters from the bottom with 90° in the bending wave method and 45° angle on the side for the Ultraseismic method. Impact duration also has been decided based on the real in-field test hammer duration. Four cases of the modelled timber pole that were analysed are as follows:

(a) Timber pole modelled with the isotropic material properties with a standing-on-soil condition.

(b) Timber pole modelled with the isotropic material properties with an embedded condition.

(c) Timber pole modelled with the orthotropic material properties with the standing-on-soil condition.

(d) Timber pole modelled with the orthotropic material properties with the embedded condition.

Standing-on-soil cases are used for length estimation without the effect of soil, and the embedded cases are used for the study of the soil effects on the reflection waves.

For the orthotropic modelling, material properties in Table 5.4 and Table 6.5 were used. The material properties of the soil are $\rho = 1{,}520\text{kg/m}^3$, $E = 100\text{MPa}$, and $\nu = 0.3$. The structural response was captured in the time domain with a time step of five microseconds (200 kHz sampling frequency). The response was recorded as displacement and by double differentiation; acceleration data was obtained and used for further signal analysis.

Table 5.4 : Elastic modulus values of simulated orthotropic timber pole

	Radial Direction	Transversal Direction	Longitudinal Direction
Elastic modulus (MPa)	1,955	850	23,000

Table 5.5: Shear modulus and Poisson's ratio values of simulated orthotropic timber pole

	Radial Transversal	Transversal Longitudinal	Radial Longitudinal
Shear Modulus (MPa)	357	1,037	1,513
Poisson's ratio	0.682	0.023	0.044

It is also worth mentioning that a colleague, who is working on the same industrial project but different research direction, provides the FEM simulations of the timber pole with different material properties. Nevertheless, a very narrow triangular impulse is applied to the timber pole to simulate the hammer impact in the FEM.

As mentioned earlier at the end of section 2.2. Orthotropic material properties of the timber pole make a complex problem. Since this research project has started from the outset, the scope of this research is to investigate the problem with minimum uncertainties. In this regard, only material properties of the timber pole along with the soil effects on the captured signals are investigated in this research, and the effects of voids, cracks, and knots are left for future PhD students.

5.4 Sonic-Echo method: Single Sensor Analysis

In this section, the applications of the Sonic-Echo method for the length estimation in all of the embedded cases of the simulated timber poles are investigated. The hammer

impact is applied on the top centre of the pole and eight sensors (S1-S8) are located along the pole with 0.2 m distance starting from 1.2 m and ends on 2.6 m from the bottom of the pole; one sensor (S0) is also located on the top of the pole near the impact location for the comparison. Figure 5.13 shows the impact and sensors locations for the Sonic-Echo test.

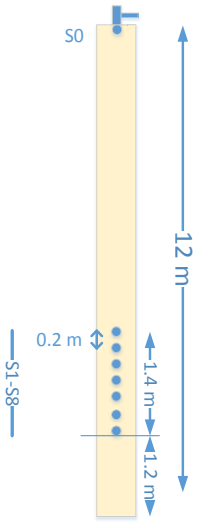

Figure 5.13: Sonic-Echo test set up

In the signal processing, firstly, a low-pass Equiripple FIR filter with cut-off frequency of 2 kHz filters the data, and the time difference between the first and second detected peaks is calculated for each of the sensors separately. This value then is multiplied to the pre assumed constant velocity related to the longitudinal wave in the timber (same as the conventional Sonic-Echo method), and finally the length of the pole is calculated and results are presented. It is also worth mentioning that the 2 KHz cut-off frequency for the low pass filter has been chosen based on spectrum curves. As it can be seen in Figure 2.12 (b), longitudinal waves (which are used in the sonic-echo method) have a single branch below 2 KHz. This makes it more feasible to detect the echo. Furthermore, the author has followed the Sonic-echo method instructions, which are explained in Chapter 2.

It is essential to consider that in the conventional Sonic-Echo method, a constant value is assumed as the wave velocity for both of the down-going and reflection waves. Here, the longitudinal wave velocity is assumed as 5000 m/s based on the dispersion curves provided in Chapter 2.

5.4.1 Isotropic Embedded in 1.2 m soil

Figure 5.14 shows the captured signals from S0 and S1. The first arrivals and the reflection peaks are highlighted with the red ovals.

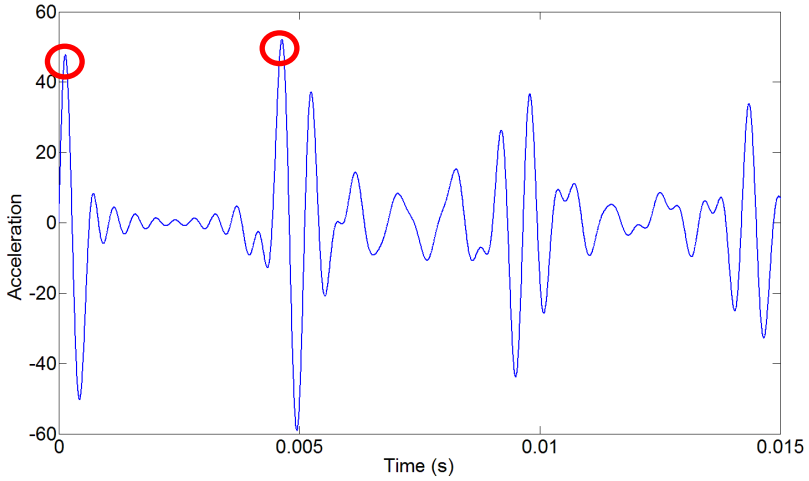

(a)

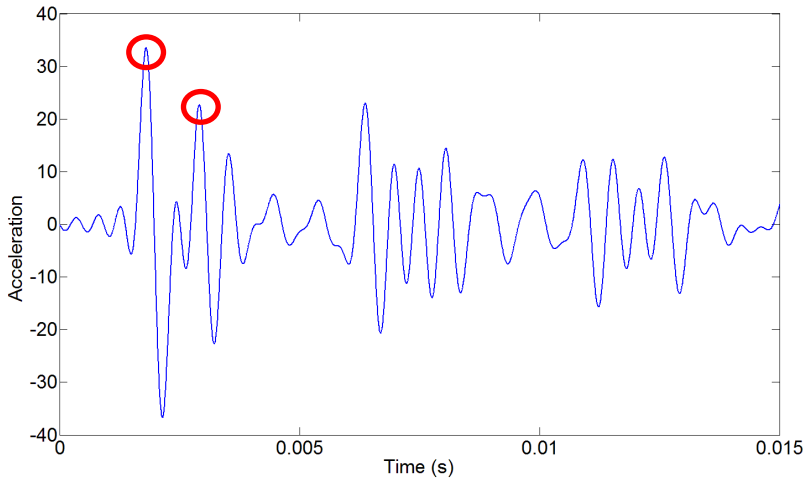

(b)

Figure 5.14: Acceleration signal captured from the simulated isotropic embedded in 1.2 m soil timber pole in (a) sensor S0 and (b) sensor S1.

The estimated length and estimation errors for all of the sensors are shown in Table 5.6. Figure 5.15 also shows the length estimation errors in the sensors S1 to S8 (S0 is not included since it is not in the sensors array).

Table 5.6: The length estimations and estimation errors for all attached sensors in the Sonic-Echo method for the simulated isotropic timber pole with embedded in 1.2 m soil condition

Sensor	Estimated Length (m)	Real Length (m)	Estimation Error %
S0	10.10	11	-8.15
S1	2.78	2.6	7.21
S2	2.6	2.4	8.33
S3	2.43	2.2	10.79
S4	2.21	2	10.62
S5	1.95	1.8	8.33
S6	1.73	1.6	8.59
S7	1.56	1.4	11.60
S8	1.47	1.2	22.91

The length estimation error in S0 is almost 8%. Two reasons can be addressed for this phenomenon; firstly, the assumption of the constant value for the wave velocity, secondly ignoring the soil effects as it absorbs the energy of the wave in the embedded section, and this leads to decrement in the wave velocity in the embedded section. As can be seen in Figure 5.15, the errors are different in different sensors. This phenomenon shows that the peaks related to the reflection wave are not perfectly aligned in one line as they are in the down-going wave (This is shown better in section 5.5 when multi-sensors array analysis has applied).

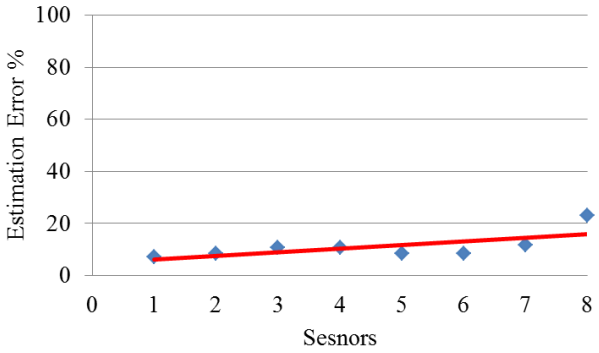

Figure 5.15: The length estimation errors for sensors S1-S8 in the Sonic-Echo method for the simulated isotropic timber pole with embedded in 1.2 m soil condition

5.4.2 Orthotropic Embedded in 1.2 m soil

Figure 5.16 illustrates the captured signals from S0 and S1. The first arrivals and the reflection peaks are also highlighted with the red ovals.

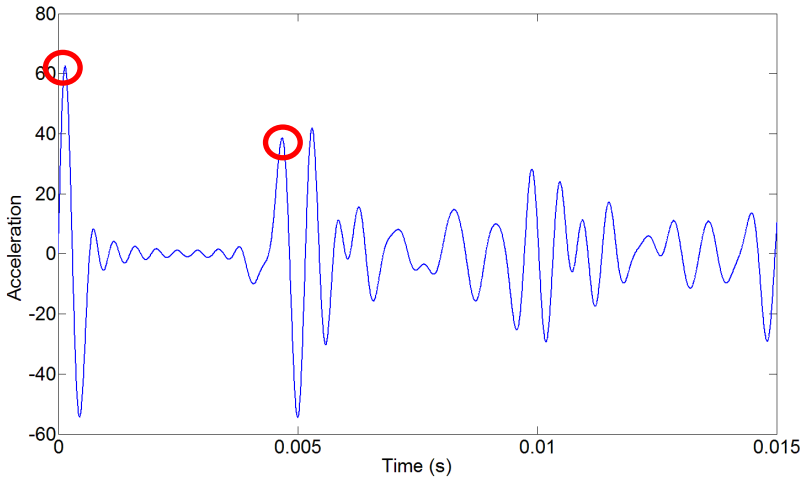

(a)

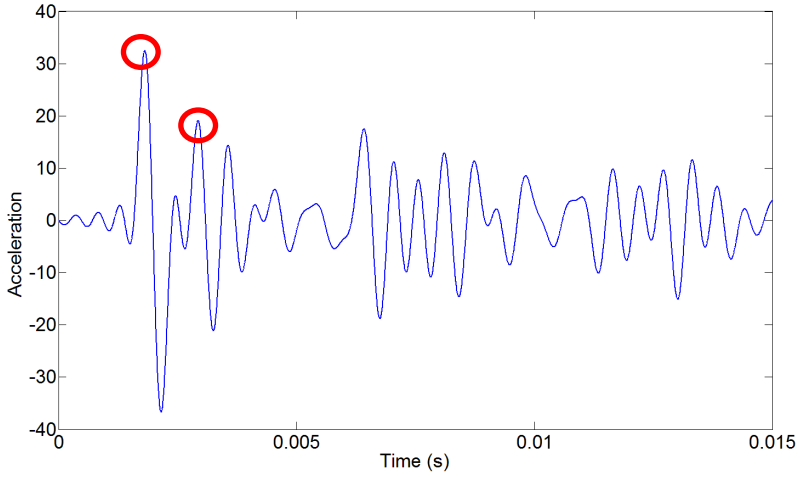

(b)

Figure 5.16: Acceleration signal captured from the simulated orthotropic embedded in 1.2 m soil timber pole in (a) sensor S0 and (b) sensor S1

Table 5.7 contains estimated lengths and estimation errors for all sensors. The length estimation errors in the sensors S1 to S8 are also provided in Figure 5.17.

Table 5.7 : The length estimations, and estimation errors for all of the sensors in the Sonic-Echo method for the orthotropic embedded in 1.2 m soil simulated timber pole

Sensor	Estimated Length (m)	Real Length (m)	Estimation Error %
S0	11.33	11	3.06
S1	2.78	2.6	7.21
S2	2.62	2.4	9.37
S3	2.45	2.2	11.36
S4	2.3	2	15
S5	1.56	1.8	13.19
S6	1.75	1.6	9.37
S7	1.61	1.4	15.17
S8	1.46	1.2	21.87

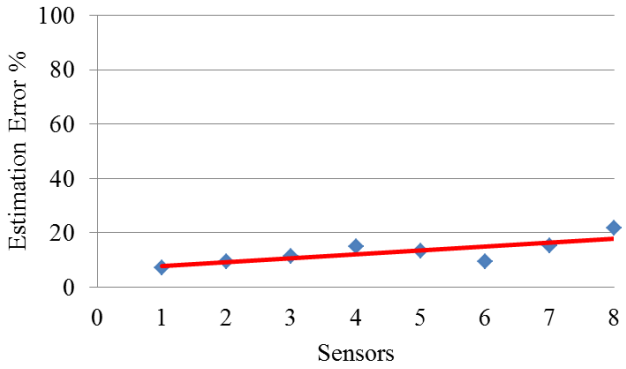

Figure 5.17: The length estimation errors in sensors S1-S8 in the Sonic-Echo method applied on the orthotropic embedded in 1.2 m soil simulated timber pole

5.5 Sonic-Echo: Multi-Sensors array analysis

As shown in the previous section, single sensor analysis suffers from some limitations such as a lack of velocity analysis, and the assumption of the same velocity for not only all poles (wave velocity varies from pole to pole), but also for both of the down-going and the reflection waves. The constant velocity assumption leads to the results and the length estimation error that depends on the sensor location. In this regard, in this section, a velocity analysis is performed utilizing a multi-sensors array, and then the obtained velocity value has been used to estimate the length of the pole. The length of the pole is estimated by two methods; firstly by crossing two lines obtained from the first arrivals and the reflection peaks in all of the sensors, and secondly a velocity decrement factor is considered for the embedded length estimation (will be explained shoertly). In the first method since the wave is travelling to the bottom of the pole and comes back to the sensors, crossing the two lines obtained from the peaks detected by sensors in a sensors array can actually obtain the crossing time (Δt), which itself is travelling time of the wave to the bottom of the pole. Substituting the obtained time in the simple travelling equation ($L_e = V * \Delta t$) can obtain the embedment length of the pole.

The velocity analysis procedure is as follows: after applying the low-pass filter on the signal, the first and the second peaks are detected in all of the sensors, and then a curve-fitting algorithm is being applied on both of the first and second sets of peaks to find the best fitting lines. Slopes of these two lines represent the down-going and the reflection

waves' velocities in the pole. It is worth considering that utilizing the curve-fitting algorithm decreases the sensitivity of the results to the time differences in all sensors.

5.5.1 Isotropic Embedded in 1.2 m soil

Figure 5.18 and Figure 5.19 show the velocity analysis and the embedded length estimation. It is essential to mention that the wave velocity under the soil decreases to 90% of its value above the soil due to the energy absorption by the soil [109]. In this regard, a decrement factor (λ) is considered in order to improve the accuracy of the embedment length estimation. Since not only the down going and echo wave velocities are different, but also both velocities decrease due to the soil energy absorption in the embedded section, simply crossing the two lines of the first and second peaks obtained from array of sensors can result in higher estimation error. In this regard, a single sensor is considered first (i.e. S8 on the soil level), then Equation (5.1) can be obtained by separately calculating the down-going wave and echo travelling distance (i.e. embedment length).

$$L_e = (t_8^2 - t_8^1) * \frac{V_u * V_d}{V_u + V_d} * Lambda \tag{5.1}$$

In Equation (5.1) t_8^2 and t_8^1 are the second and first detected peaks time, V_u and V_d are echo and down going wave

velocities, L_e is the embedment length, and λ is the decrement factor.

In Figure 5.19, the result of the embedment length estimation by considering the decrement factor is compared with the two line crossing method result.

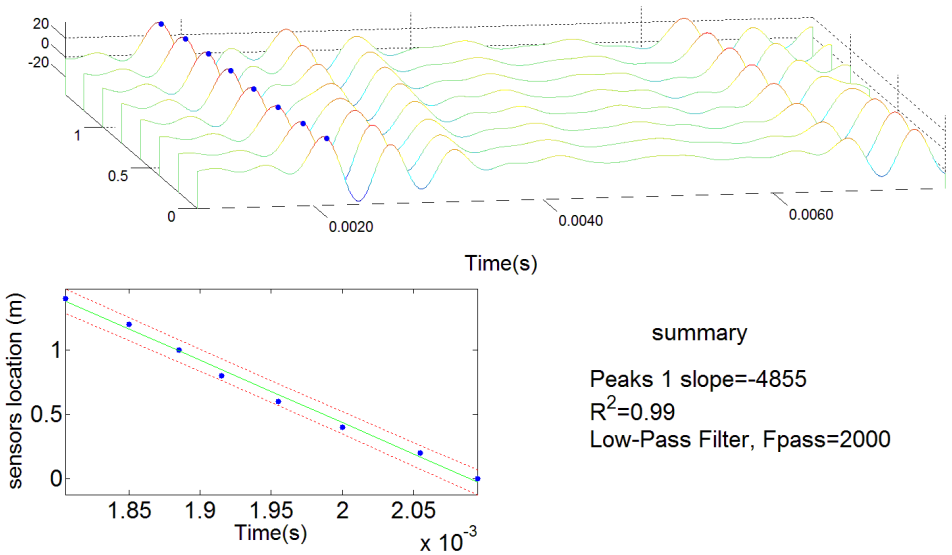

(a)

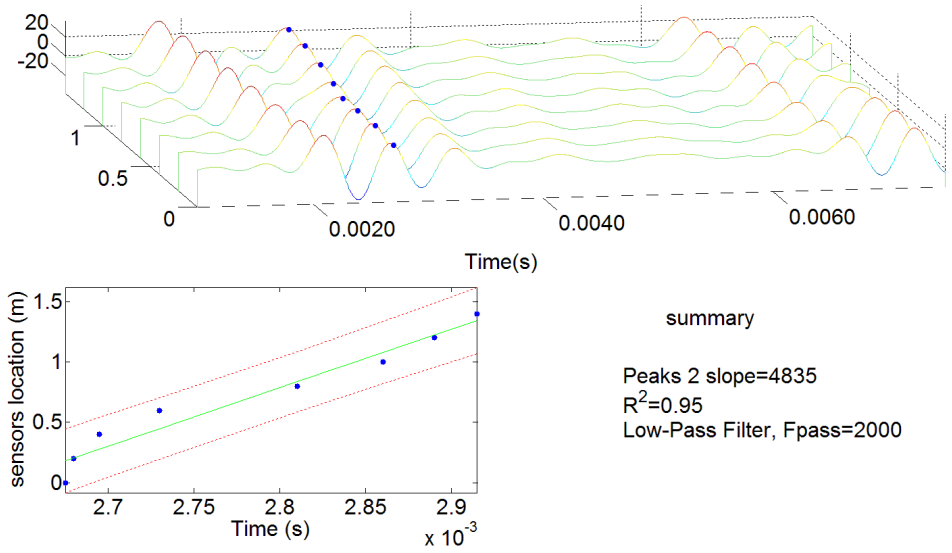

(b)

Figure 5.18: waterfall plot of the velocity analysis procedure and fitting accuracy utilizing S1 to S8 for (a) down-going wave, and (b) reflection wave

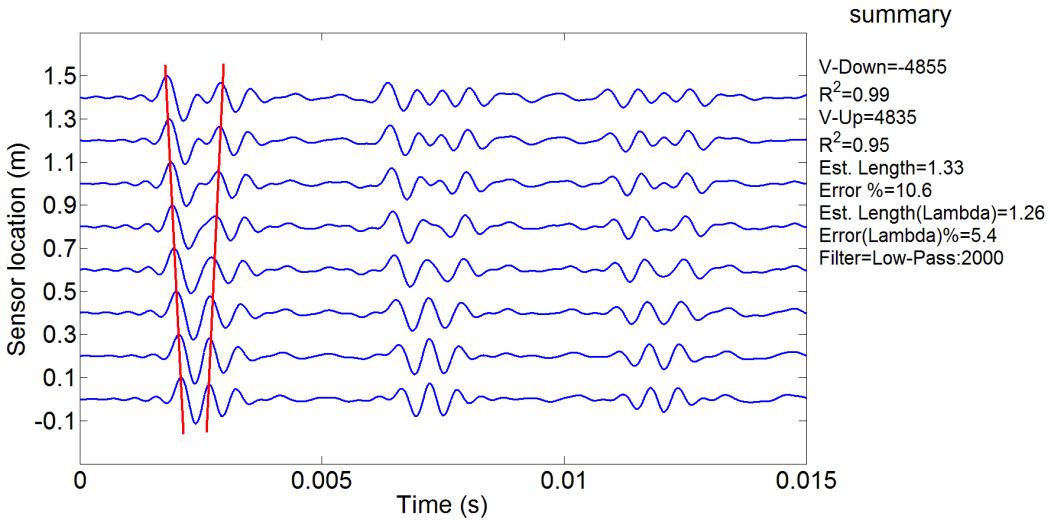

Figure 5.19: The embedment length estimation procedure, results and estimation error for isotropic embedded in 1.2 m soil simulated timber pole

Crossing the two lines related to the down-going and the reflection waves gives almost 10% of error in the length estimation. It can be seen that considering the decrement factor (Lambda) for the wave velocity in the embedded section can considerably improve the accuracy of the length estimation to almost 5.3%. It is worth considering that the fitting-accuracy demonstrates how well the peaks are aligned in one line. There is also a small overlap of the down going and echo wave packets (pulses) in sensors near the ground. This can be due to the small traveling distance and soil effect.

It is worth mentioning that since a hammer impact excites the timber pole in a broad range of frequencies (i.e. 0 to 4 KHz), a wave packet including all frequencies travels through the timber pole. It is also necessary to consider that the shape of the hammer impact is not directly applied and transferred to timber pole. The shape of the travelling wave packet depends on the wave-guide propagation theory, which is the research direction of a colleague and is out of scope of this research. More information can be found in [47].

5.5.2 Orthotropic Embedded in 1.2 m soil

The velocity analysis procedure and the length estimation are shown in Figure 5.20 and Figure 5.21.

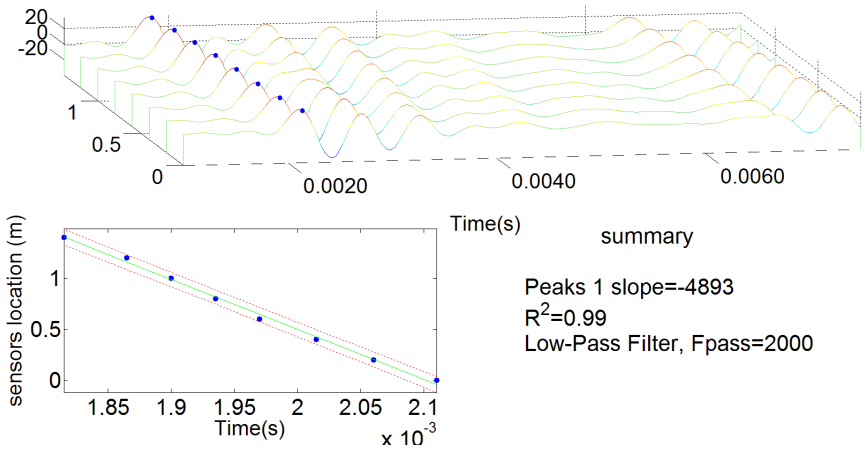

(a)

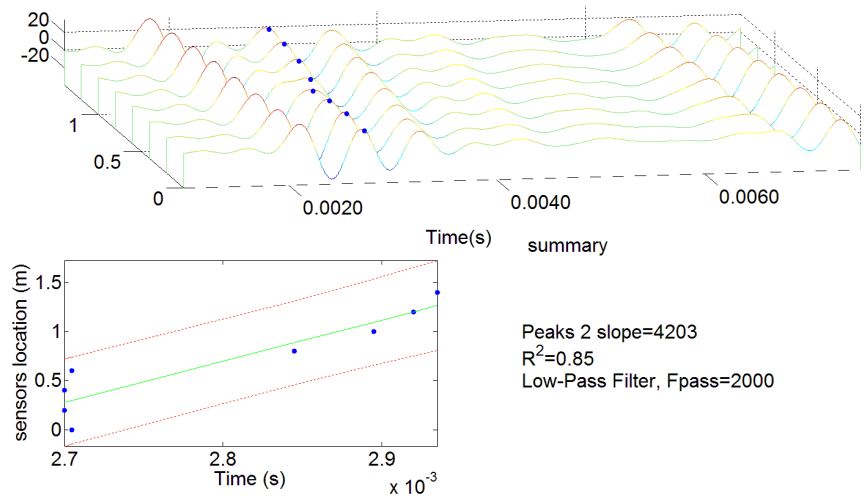

(b)

Figure 5.20: The waterfall plot of the velocity analysis procedure and the fitting accuracy utilizing S1 to S8 for (a) the down-going wave, and (b) the reflection wave

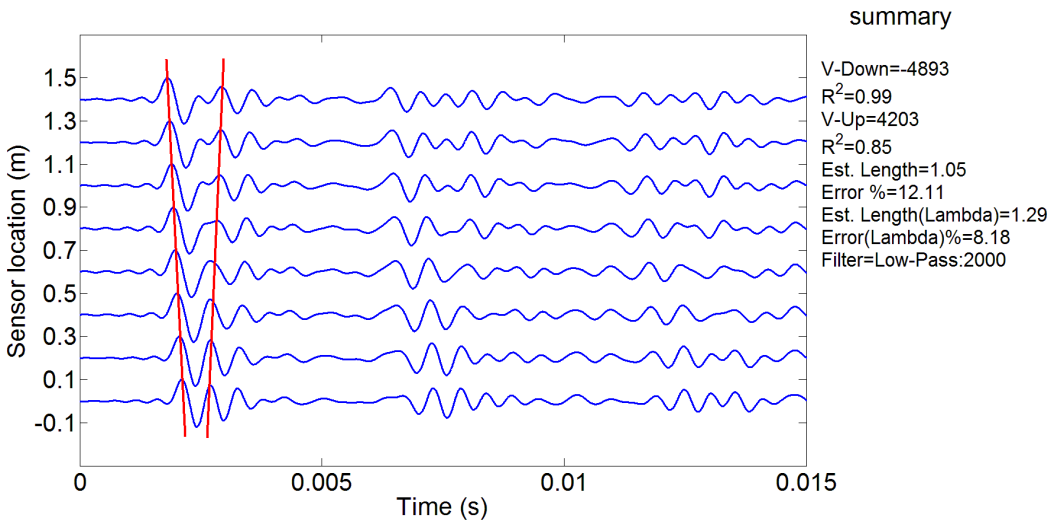

Figure 5.21: length estimation procedure, results and estimation error for orthotropic standing-on-soil simulated timber pole.

As can be seen, considering the velocity decrement factor in this case improves the accuracy of the embedment length estimation from 12% to 8%. It is worth mentioning that utilizing the multi-sensors array can improve the reliability of the Sonic-Echo method outputs in two aspects. Firstly in terms of making the velocity analysis feasible, secondly by decreasing the sensitivity of the results to the time differences in all sensors (i.e. crossing the two lines method do not use the time differences directly). It can be seen in Figure 5.19 and Figure 5.21 that the down-going wave's velocity can be estimated with 99% fitting accuracies, while the reflection wave fitting accuracies have decreased in comparison with the down-going wave ones. Higher fitting accuracy means that the peaks are aligned more perfectly in one line. Lower fitting accuracies in reflection waves demonstrate the level of distortion occurred to the reflection wave due to the soil effects and the material properties. It can also be seen in Figure 5.21 that the down going and the echo waves' velocities are significantly different. This can be due to the inaccuracy of the methodology and estimation errors.

5.6 Short Kernel Method (SKM) utilizing the Bending wave

As described earlier in Chapter 3, the Short Kernel Method (SKM) was the first proposed signal processing methodology to deal with the bending wave. Horizontal force is needed to be applied on the timber specimen to stimulate the bending wave.

Figure 5.22 shows the bending wave test setup. In the rest of this section, the applications of the SKM for a phase velocity and the length estimation of the timber pole will be investigated in all of the four cases including the isotropic standing-on-soil, the isotropic embedded in 1.5 m soil, the orthotropic standing-on-soil, and the orthotropic embedded in 1.5 m soil.

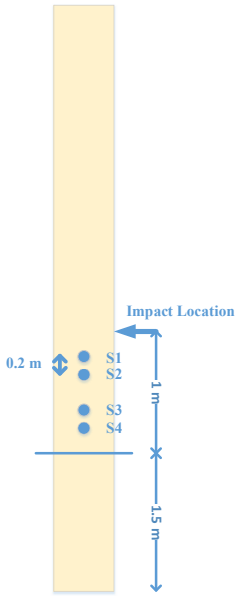

Figure 5.22: The bending wave test setup for the simulated timber pole for the both standing-on-soil and embedded conditions

5.6.1 Isotropic Standing-on-soil

The first step in the SKM is determining a seed frequency from the Frequency Response Functions (FRF) of the signals captured by the sensors. Figure 5.23 shows the FRFs of all four sensors.

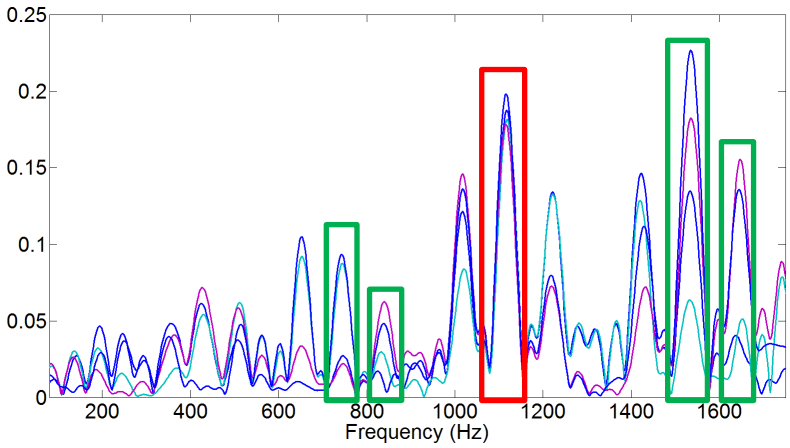

Figure 5.23: The Frequency response Functions of S1-S4 for the isotropic standing-on-soil simulated timber pole

As can be seen in Figure 5.23, many peaks can be detected from the FRF plot. In this research, five frequencies that show the most consistency in all sensors have been chosen amongst all for the phase velocity calculation (highlighted by the green and red ovals). The frequency 1120 Hz has been used for the length estimation (the red oval in Figure 5.23). This frequency has been chosen as it shows most consistency amongst all of the five chosen frequencies. Figure 5.24 shows the SKM outputs with the seed frequency of 1120 Hz in S1-S2, and S3-S4. The first arrivals and the reflection peaks are highlighted with the green ovals.

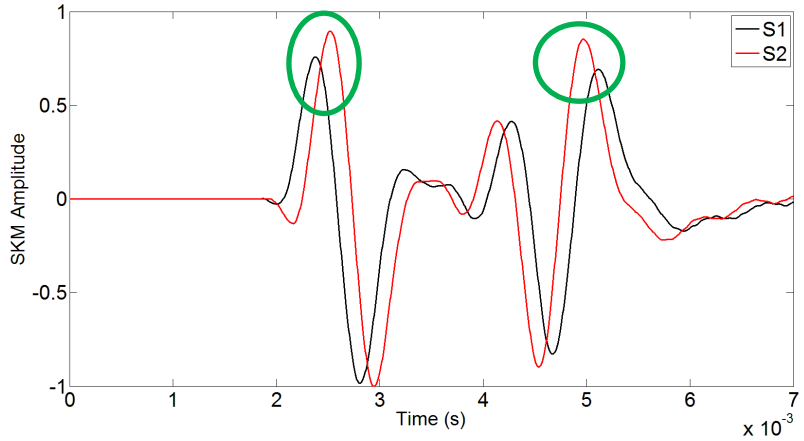

(a)

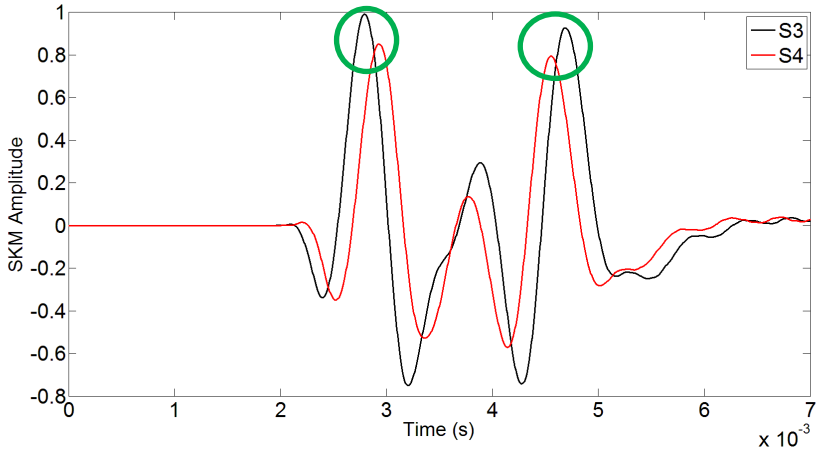

(b)

Figure 5.24: The SKM outputs with the seed frequency of 1120 Hz in (a):S1-S2, and (b): S3-S4.

Original Signals captured from S1 and S2 are provided in Figure 5.25 for comparison. It is worth mentioning that based on the SKM method the second largest peak (which shows the most correlation with the seed frequency) should be considered as the reflection peak. This is the reason of choosing the peaks that are highlighted with the green ovals.

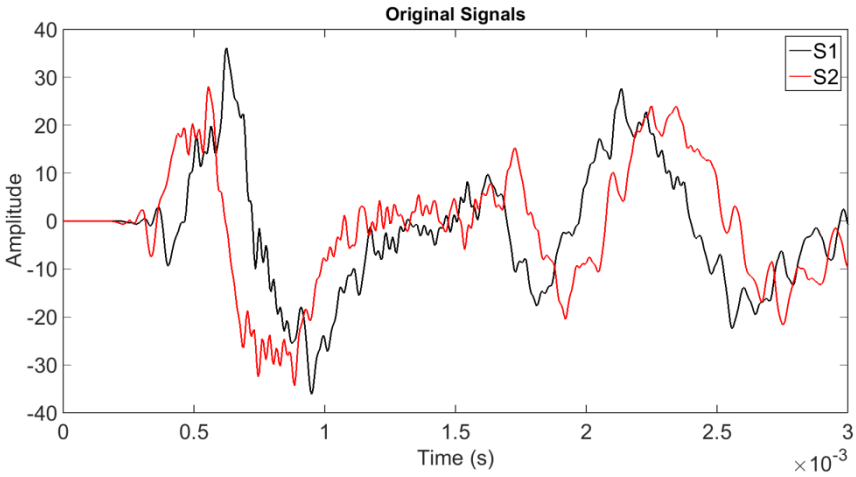

Figure 5.25: Original Signals captured by S1 and S2

As can be seen in Figure 5.24 (a) the down and up travelling waves look different. It is vital to consider that interpretation of SKM output is not as straightforward as raw waveforms. It can be seen in Figure 5.25, there is a clear time gap between down going and reflection waves. Nevertheless, this clear gap is not easily observable due to the side effects of the SKM application. It is also not unusual for the reflection wave to be

slightly different from the down going wave. This change in the shape can be due to the dispersion and boundary conditions of the timber pole.

Considering the time difference between the first peaks in S1-S2, or S3-S4, the phase velocity can be estimated utilizing Equations (5.3) and (5.4):

$$V_{P_{1120\,Hz}} = \frac{\Delta x_{S_1,S_2}}{S_2^{Peak1} - S_1^{Peak1}} * dt = \frac{0.2m}{5024 - 4994} * 5\text{e}{-6} = 1481(\text{m/s}) \quad (5.2)$$

$$V_{P_{1120\,Hz}} = \frac{\Delta x_{S_3,S_4}}{S_4^{Peak1} - S_3^{Peak1}} * dt = \frac{0.2m}{5095 - 5068} * 5\text{e}{-6} = 1481(\text{m/s}) \quad (5.3)$$

The estimated phase velocities for all of the aforementioned seed frequencies are provided in Figure 5.26. Related phase velocities obtained from the analytical solutions [47] are also provided for each of the seed frequencies for the comparison.

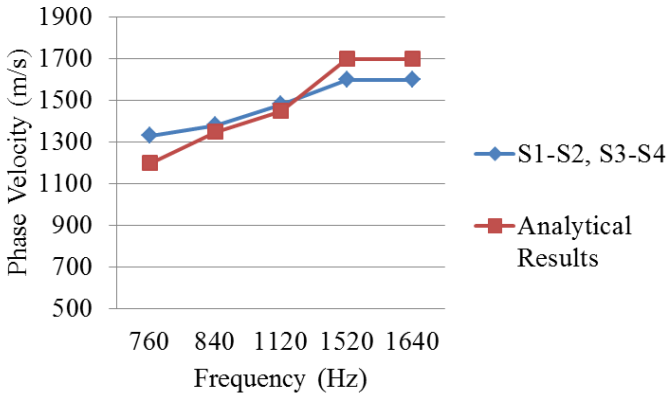

Figure 5.26: The estimated phase velocities for all of the seed frequencies utilizing S1-S2, and S3-S4 (the calculated phase velocities with S1-S2, and S3-S4 are same)

As can be seen, both of the sensor sets give the same results. Although the results are not exactly the same with analytical ones, both have the same trends, (velocity increases with the seed frequency increment).

The final step after the phase velocity calculation is the length estimation. Considering the first arrivals and the reflection peaks (see the green ovals in Figure 5.24), the length of the pole can be estimated using equations (5.5) (5.6) (5.7) (5.8).

$$L_{S1_{1120\,Hz}} = \frac{S_1^{Peak2} - S_1^{Peak1}}{2} * dt * V_{P_{1120\,Hz}} = \frac{5524 - 4994}{2} * 5\text{e}{-6} * 1481 = 1.97m \quad (5.4)$$

$$L_{S2_{1120\,Hz}} = \frac{S_2^{Peak2} - S_2^{Peak1}}{2} * dt * V_{P_{1120\,Hz}} = \frac{5498 - 5021}{2} * 5\text{e}{-6} * 1481 = 1.77m \quad (5.5)$$

$$L_{S3_{1120\,Hz}} = \frac{S_3^{Peak2} - S_3^{Peak1}}{2} * dt * V_{P_{1120\,Hz}} = \frac{5444 - 5068}{2} * 5\text{e}{-6} * 1481 = 1.4m \quad (5.6)$$

$$L_{S4_{1120\,Hz}} = \frac{S_4^{Peak2} - S_4^{Peak1}}{2} * dt * V_{P_{1120\,Hz}} = \frac{5417 - 5095}{2} * 5\text{e}{-6} * 1481 = 1.2m \quad (5.7)$$

Actual lengths and the estimation errors in all of the sensors are provided in Table 5.8.

Table 5.8: Actual lengths and the estimation errors for S1-S4

Sensor	Estimated Length (m)	Actual Length (m)	Error %
S1	1.97	2.4	-17.9
S2	1.77	2.2	-19.5
S3	1.4	1.8	-22.2
S4	1.2	1.6	-25

It can be seen in Table 5.8 that the average length estimation error is 20% for this case.

5.6.2 Isotropic Embedded in 1.5 m soil

Figure 5.27 illustrates the FRF in all of the sensors. The SKM procedures for this case are shown through Figure 5.28 to Figure 5.30.

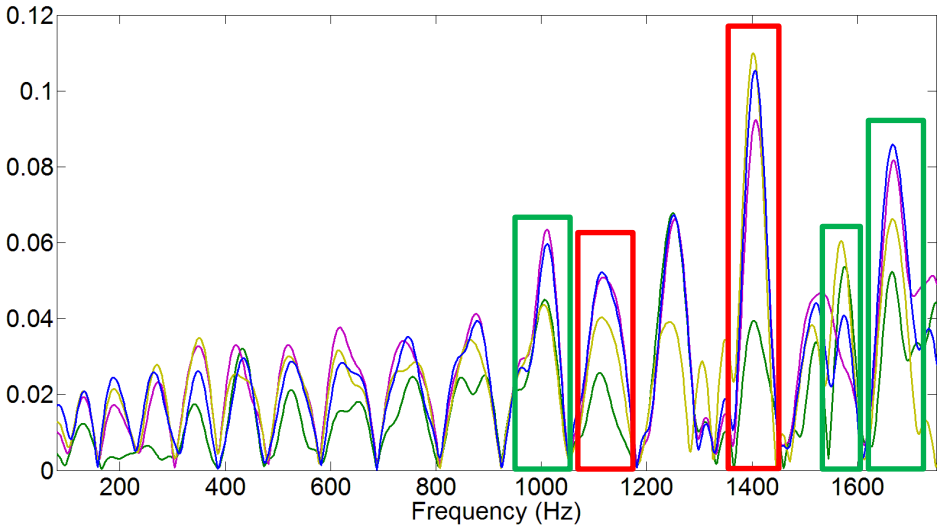

Figure 5.27: The FRF in all of the sensors in the bending wave test on the simulated isotropic embedded in 1.5m soil timber pole

As illustrated in Figure 5.27, the frequency component 1400 Hz shows the highest amplitude amongst all of the peaks in three out of the four sensors. There is also a peak in 1120 Hz, where all of the sensors have almost the same amplitude. In this regard, the SKM plots for both of the frequencies are provided in the following. Some of the other peaks also have been used for the velocity analysis. Figure 5.28 and Figure 5.29 show the SKM output plots in the frequency components 1120 and 1400 Hz. The first arrivals and the reflection peaks are also highlighted with the green ovals.

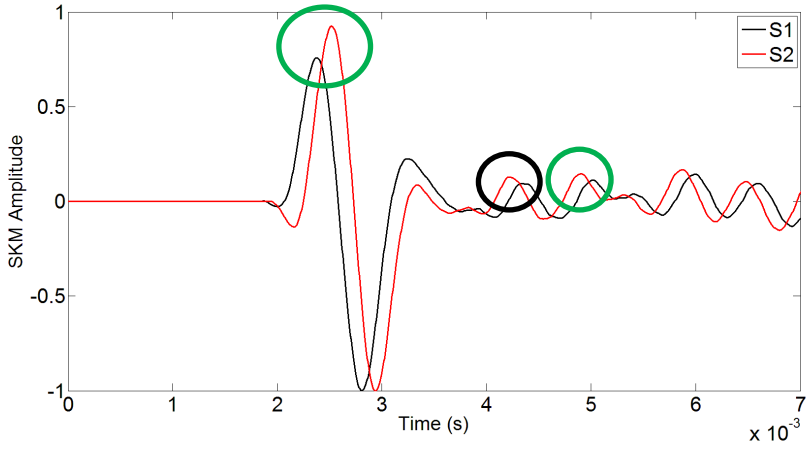

(a)

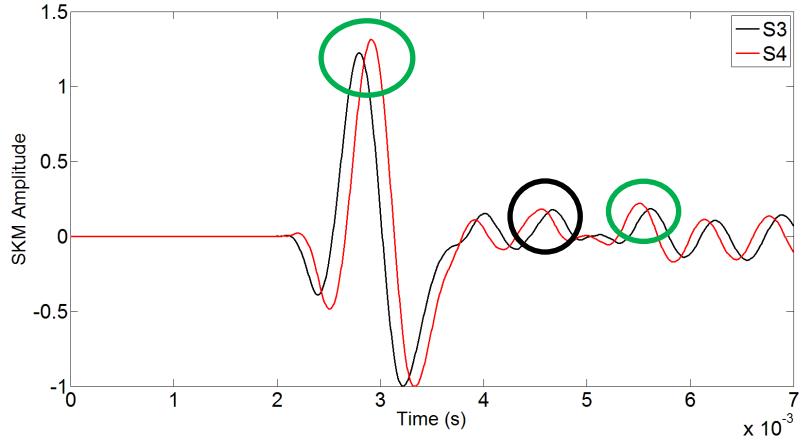

(b)

Figure 5.28: The SKM outputs with the seed frequency of 1120 Hz in (a):S1-S2, and (b): S3-S4

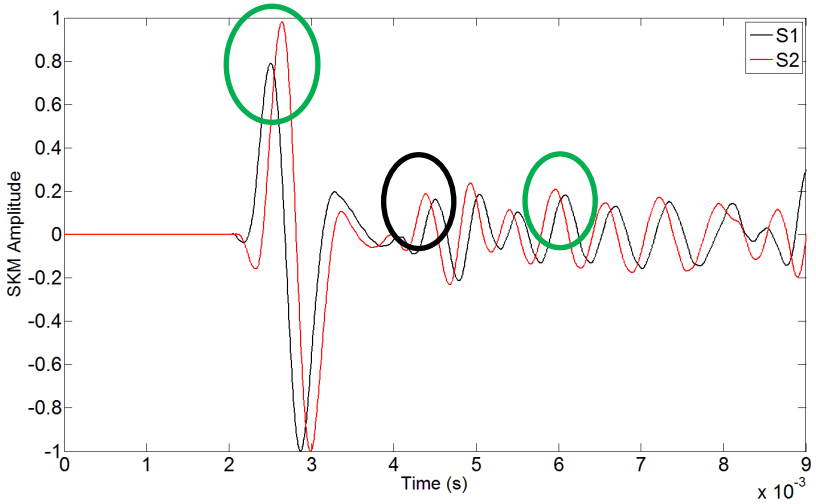

(a)

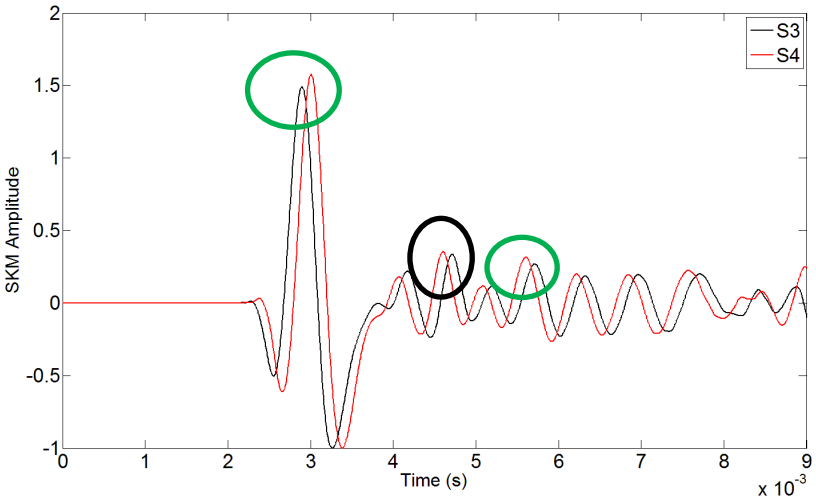

(b)

Figure 5.29: The SKM outputs with the seed frequency of 1400 Hz in (a):S1-S2, and (b): S3-S4

The effects of the soil can easily be seen by a simple comparison of Figure 5.28 and Figure 5.24. In fact, the presence of the soil makes reflection detection a very delicate procedure. The procedure depends on both of the experience of the test performer or the signal processor and the availability of prior information about the timber pole. By comparing Figure 5.28 and Figure 5.29, one can also realize the importance of the seed frequency determination. As can be seen, although in the 1120 Hz reflection peaks are much more clear and detectable because their amplitude is slightly higher than the previous peaks, they still can easily be mistaken for peaks in the black ovals. This situation is worse in the seed frequency 1400 Hz where reflection peaks amplitudes are the same or even less than their previous peaks (shown by the black ovals).

Figure 5.30 compares the estimated velocities in the different seed frequencies with their related analytical results. Although the estimation values are always lower than the analytical results, it more or less has the same increasing trend in the phase velocity as it is in the analytical results.

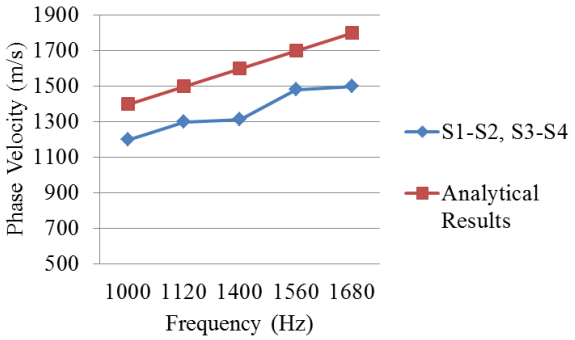

Figure 5.30: The estimated velocities in the different seed frequencies with their related analytical results

The embedment length estimation values and the error percentages in the 1120 Hz seed frequency are provided in Table 5.9.

Table 5.9: The embedment length estimation values and the error percentages in the 1120 Hz seed frequency

Sensor	Estimated Length (m) green ovals	Estimated Length (m) black ovals	Actual Length (m)	Error % green ovals	Error % black ovals
S1	2.3	1.7	2.4	-4.16	-29
S2	2.1	1.5	2.2	-4.54	-31
S3	1.9	1.23	1.8	5.55	-32
S4	1.7	1.07	1.6	6.25	-33

It should also be considered that although the estimation errors are considerably lower than in the standing-on-soil case (considering the green ovals), detection of the reflected peaks are not as straightforward and reliable as the standing-on-soil case. In the case of considering the peaks in the black ovals (which is more probable to happen), the average length estimation error is 30%.

5.6.3 Orthotropic Standing-on-soil

Figure 5.31 shows the FRF in all of the sensors. All of the highlighted ovals are used for the velocity estimation, and the frequency highlighted by the red oval has been used for the length estimation as it shows to be the most consistent set of the peaks amongst all.

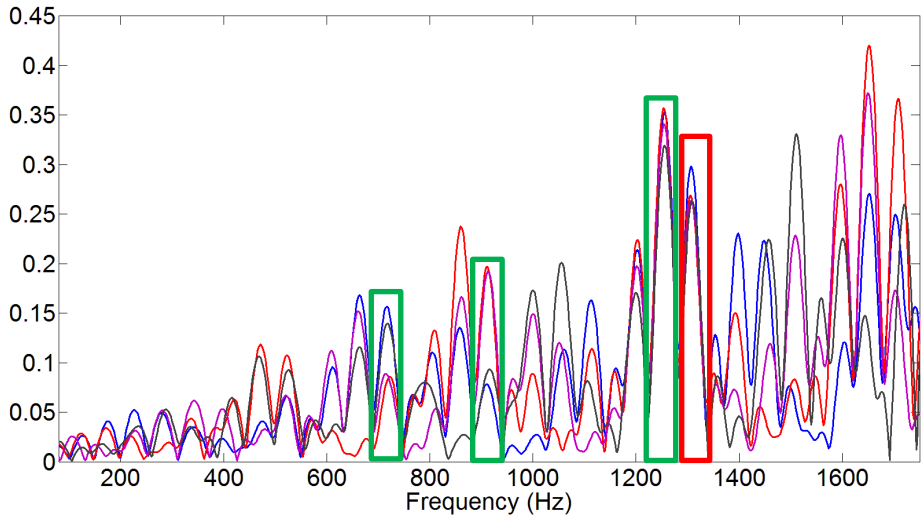

Figure 5.31: FRF in all of sensors in orthotropic standing-on-soil simulated timber pole

In Figure 5.32, the velocity calculations for the different seed frequencies are provided, where again although the velocities are not exactly the same as the analytical results, they have the same increasing trend.

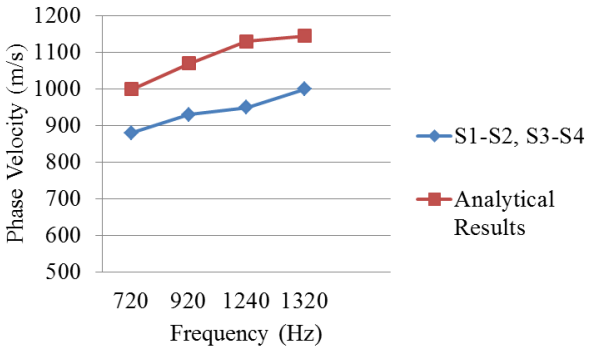

Figure 5.32: The velocity calculations for the different seed frequencies in the simulated orthotropic timber pole standing-on-soil

Figure 5.33 illustrates the SKM output plots in S1-S2 and S3-S4 for the seed frequency of 1320 Hz, which are the most consistent peaks in the FRF.

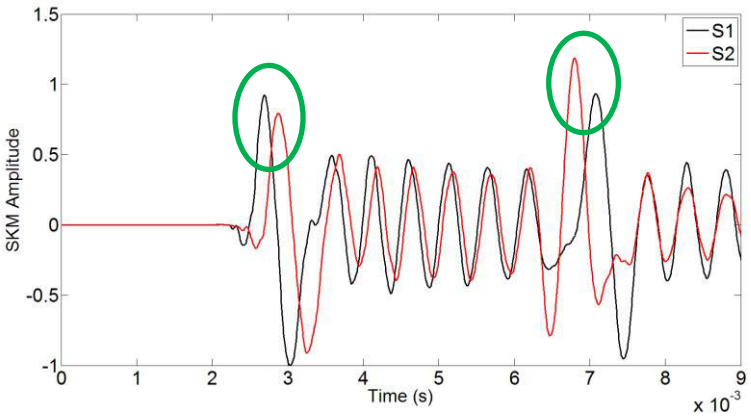

(a)

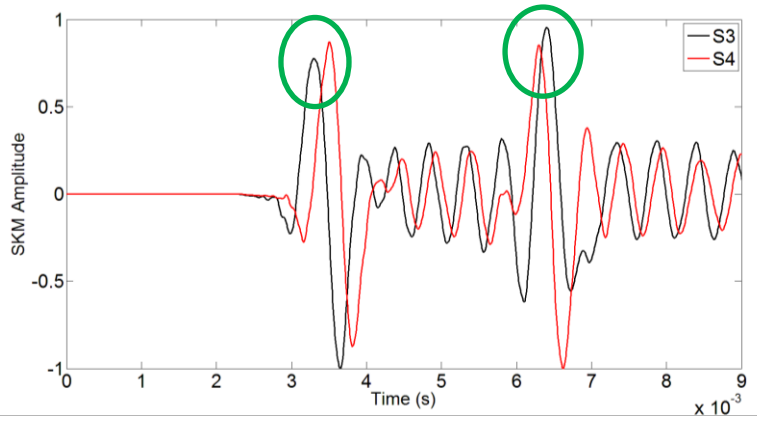

(b)

Figure 5.33: SKM output plots in S1-S2 and S3-S4 for the seed frequency of 1320 Hz

Table 5.10 also provides the length estimation values and errors.

Table 5.10: Length estimation values and errors for the simulated orthotropic timber pole standing-on-soil

Sensor	Estimated Length (m)	Actual Length (m)	Error %
S1	2.1	2.4	-12.5
S2	1.9	2.2	-14
S3	1.5	1.8	-17
S4	1.4	1.6	-12.5

5.6.4 Orthotropic Embedded in 1.5 m soil

The FRF plot of all the sensors, and SKM output plots with the seed frequency 1320 Hz are shown in Figure 5.34, and Figure 5.35. All of the highlighted ovals in Figure 5.34 are used for the velocity estimation, and the frequency that is highlighted by the red oval has been used for the length estimation.

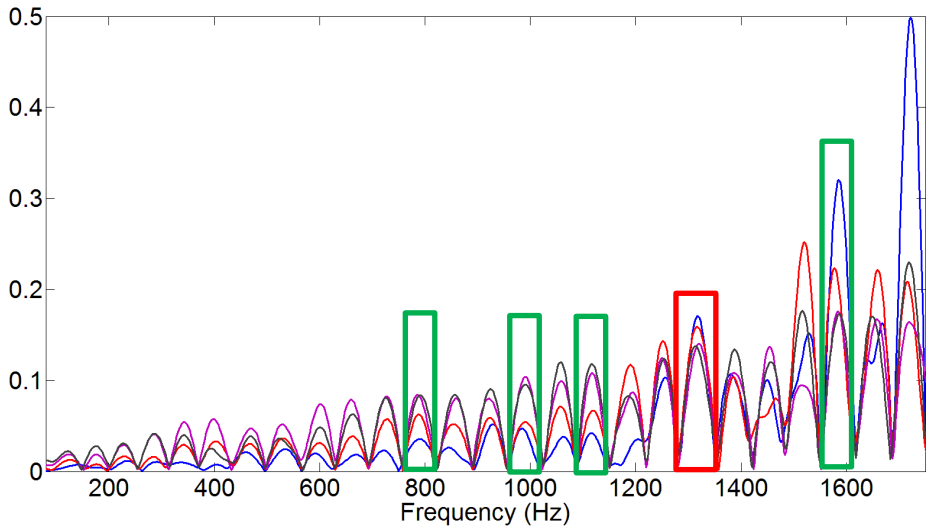

Figure 5.34: FRFs in all of the sensors in the orthotropic embedded in 1.5 m simulated timber pole

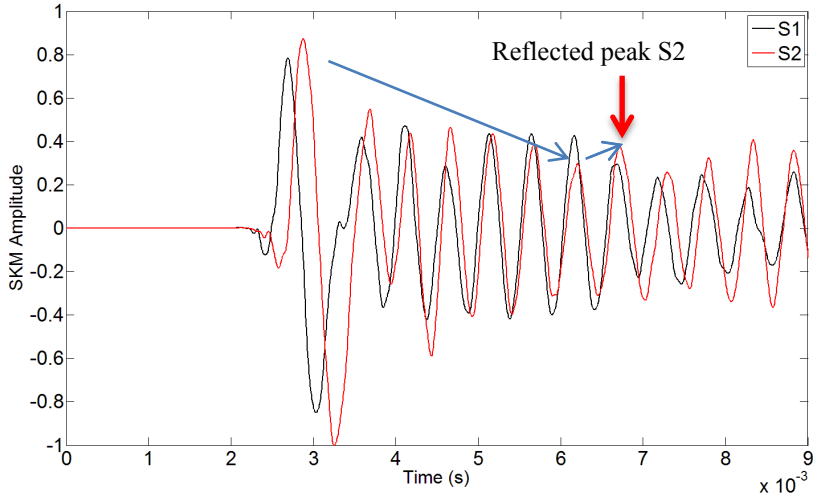

(a)

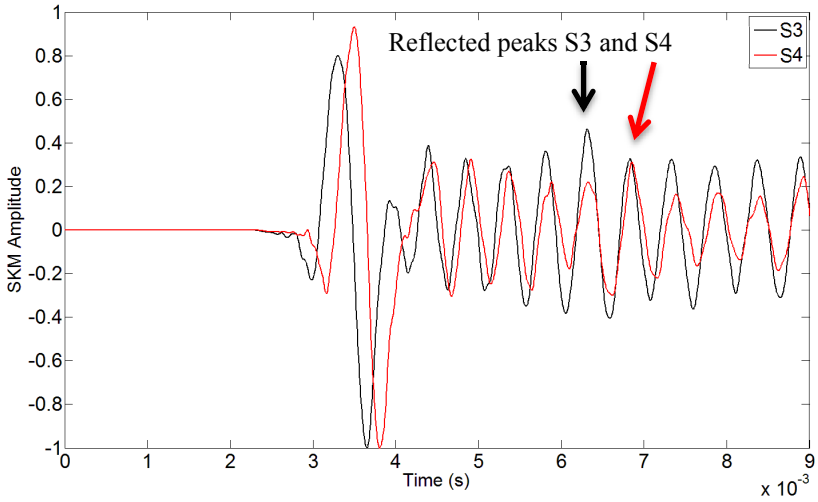

(b)

Figure 5.35: The SKM output plots with the seed frequency 1320 Hz for the orthotropic embedded in 1.5 m soil simulated timber pole

Arrows in Figure 5.35 have illustrated the procedure of the peak detection for each of the sensors. In (a), S1 does not show any specific pattern, and as can be seen the second largest peak is definitely a faulty one. However, in S2, the amplitudes of the peaks are decreasing until the reflected peak has arrived and creates an abrupt increase in the amplitude (as shown by the arrows). Following the same procedure in (b), the reflected peaks from both sensors could be detected. In Table 5.11, the estimated embedment lengths and related errors are provided.

Table 5.11: Estimated embedment lengths and related errors for the orthotropic embedded in 1.5 m soil simulated timber pole

Sensor	Estimated Length (m)	Actual Length (m)	Error %
S1	…	2.4	…
S2	1.9	2.2	-13.63
S3	1.64	1.8	-8.88
S4	1.7	1.6	6.25

Figure 5.36 also illustrates the velocity calculations for the different seed frequencies, and their related analytical values.

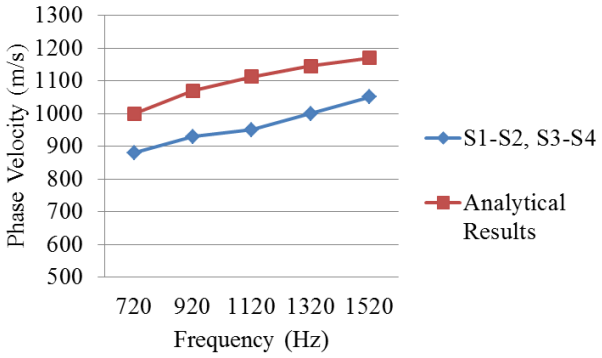

Figure 5.36: The velocity calculations for the different seed frequencies in the orthotropic embedded 1.5 m soil simulated timber pole

The reflection peak detection especially in the embedded cases is not an easy task. Even amongst the embedded cases, the reflection peak detection in the orthotropic case is more complicated than the isotropic one. It actually heavily depends on the seed frequency determination, and also the experience and judgement of the test performer.

5.7 Ultraseismic

The test set-up for the Ultraseismic testing is similar to the Sonic-Echo testing method, which was described earlier in this chapter. The only difference is that the impact location in the Ultraseismic test is on the side of the timber pole (3 m from the bottom of the pole) at a 45° angle.

It is also worth mentioning that the impact is applied to the centre of the cross section of the pole. In experimental tests, this is done by screwing the timber pole with 45° angle, and makes the impact on the screw. Since the Ultraseismic method utilizes both longitudinal and flexural waves simultaneously, the impact is made with 45° angle. It is worth considering that if the pole is excited with 0° angle, it makes pure longitudinal wave (Sonic-Echo method). If the pole is excited with 90° angle, it makes pure flexural waves (Short Kernel Method). It is also vital mentioning that the timber is not an ideal hard material and its surface dents perpendicularly to the hammer impact. In this regard, the 45° angle impact can excite the timber pole with both longitudinal and flexural waves. Explanations of this phenomena form the wave-guide propagation theory is out of scope of this research, but more details can be found in [47].

The impact location is determined based on the limitations in the real in-field tests where the top or near top surface of the pole is not accessible because of the presence of the electrical or the communications wires. In fact, maximum accessible surface of the pole is as high as a normal person feels comfortable to make the impact. In the following, the application of the Ultraseismic on different cases of the simulated timber pole will be investigated.

5.7.1 Isotropic Standing-on-soil

Firstly, signals captured from all of the sensors are low-pass filtered with the cut-off frequency of 3500 Hz. This cut-off frequency is determined based on firstly Ultraseismic method instructions [45], and secondly based on the spectrum curves (see Figure 2.12). Then utilizing multi-sensors array, the velocities of both the down-going and reflection waves are estimated, and finally the length of the pole is calculated. Figure 5.37 shows the velocity analysis procedures for the first arrivals (down-going wave), and the reflection waves.

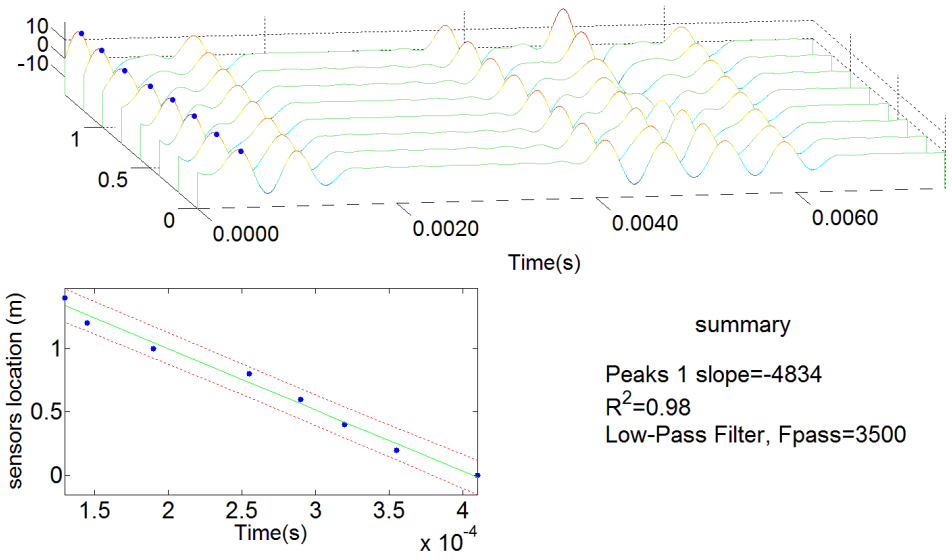

(a)

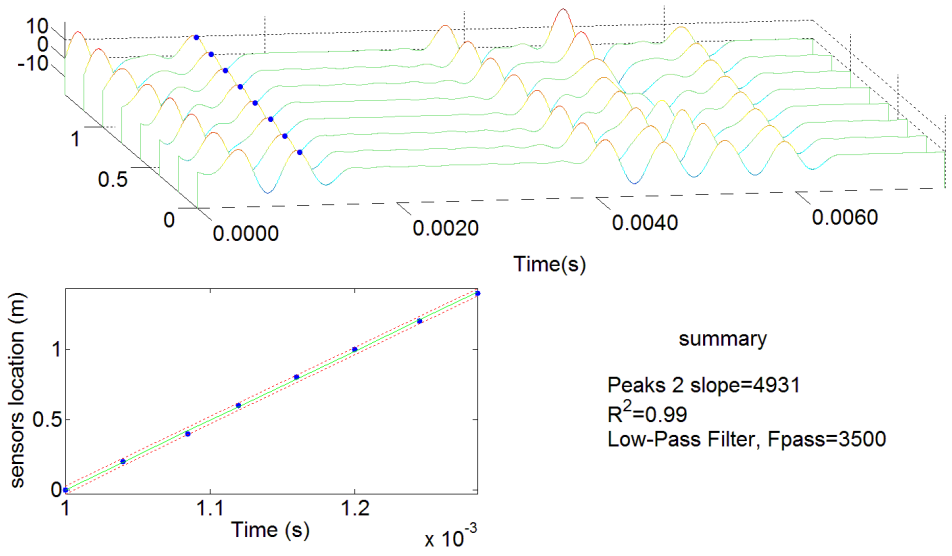

(b)

Figure 5.37: Ultraseismic velocity analysis procedures for (a) the down-going and (b) the reflection waves in the simulated isotropic timber pole with the standing-on-soil condition

Both of the down-going and reflection waves' velocities are estimated with high fitting accuracies. Similar to the Sonic-Echo sensor array analysis, the length can be estimated by crossing the two lines related to the down-going and the reflection waves. Figure 5.38 (a) illustrates the Ultraseismic plot of all of the sensors, the estimated length value, and the estimation error. The raw waveforms captured from the sensors are also provided in Figure 5.38 (b) for comparison.

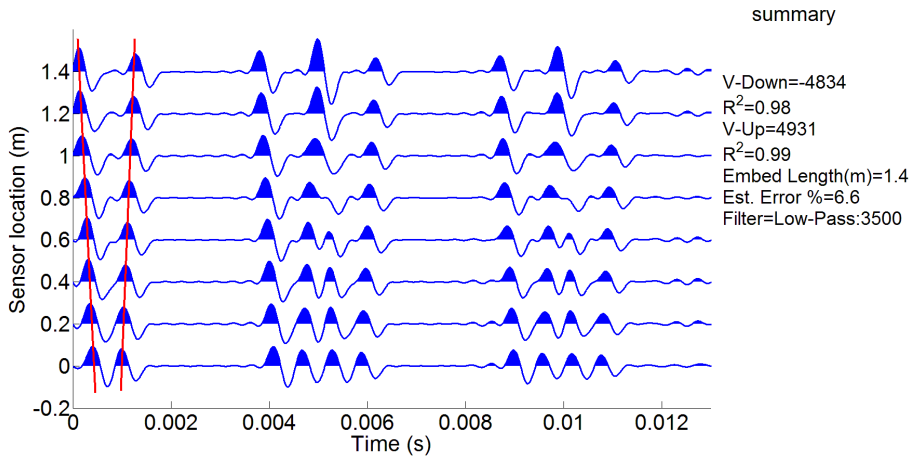

(a)

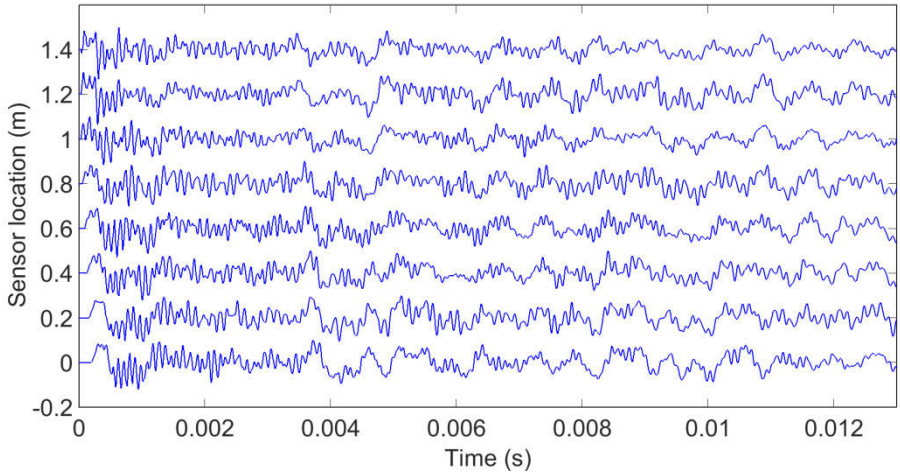

(b)

Figure 5.38: (a) Ultraseismic plot of all of the sensors, the estimated length value, and the estimation error, and (b) Raw signals captured from sensors in the simulated isotropic timber pole with the standing-on-soil condition

As can be seen, in the isotropic standing-on-soil, which is the simplest simulation case, the length can be estimated with a high accuracy with error less than 7%. It should also be mentioned that observable overlap of the down-going and reflection waves in the lower sensors is due to the relatively small travelling distance and large wavelength of these waves. However, this overlap has not occurred in the first and second peaks' time.

5.7.2 Isotropic Embedded in 1.5 m soil

Figure 5.39 and Figure 5.40 show the velocity analysis and the embedment length estimation procedure. It should also be considered that similar to the Sonic-Echo method due to the presence of the soil, the decrement factor (Lambda) is considered for

the embedment length calculation, and results are provided to compare with the line crossing method.

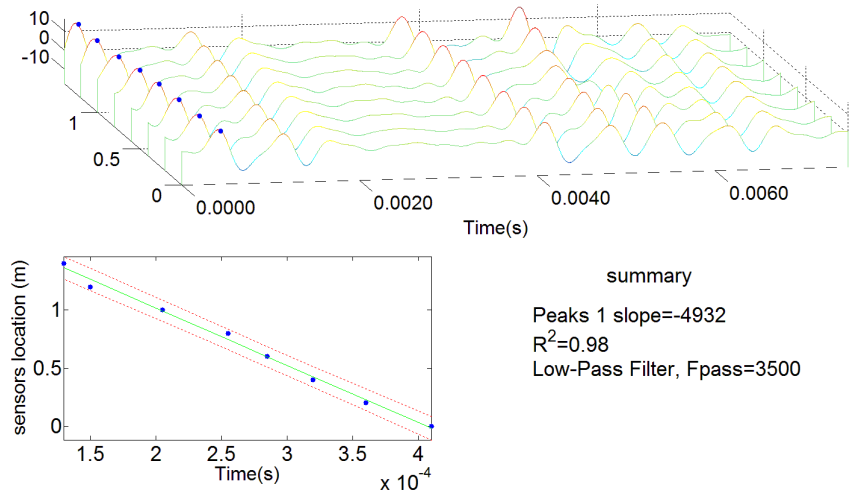

(a)

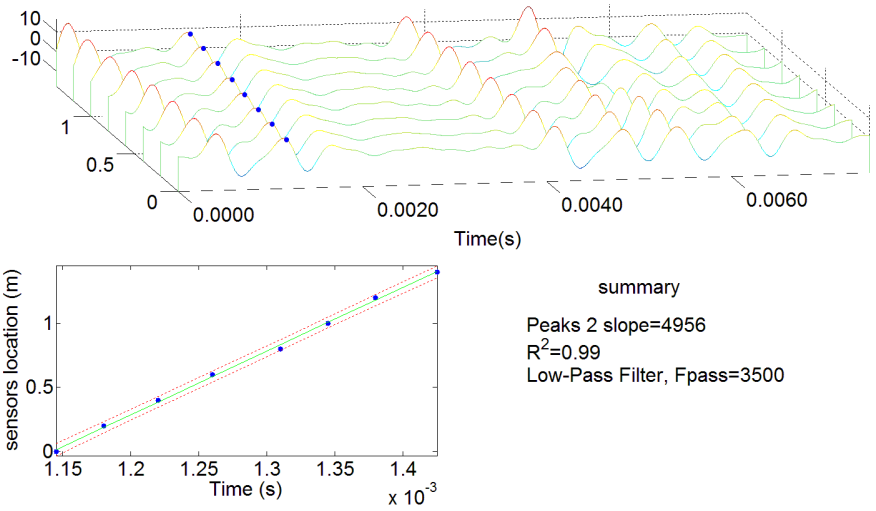

(b)

Figure 5.39: Velocity analysis procedures for (a) the down-going and (b) the reflection waves for the isotropic embedded in 1.5 m soil simulated timber pole

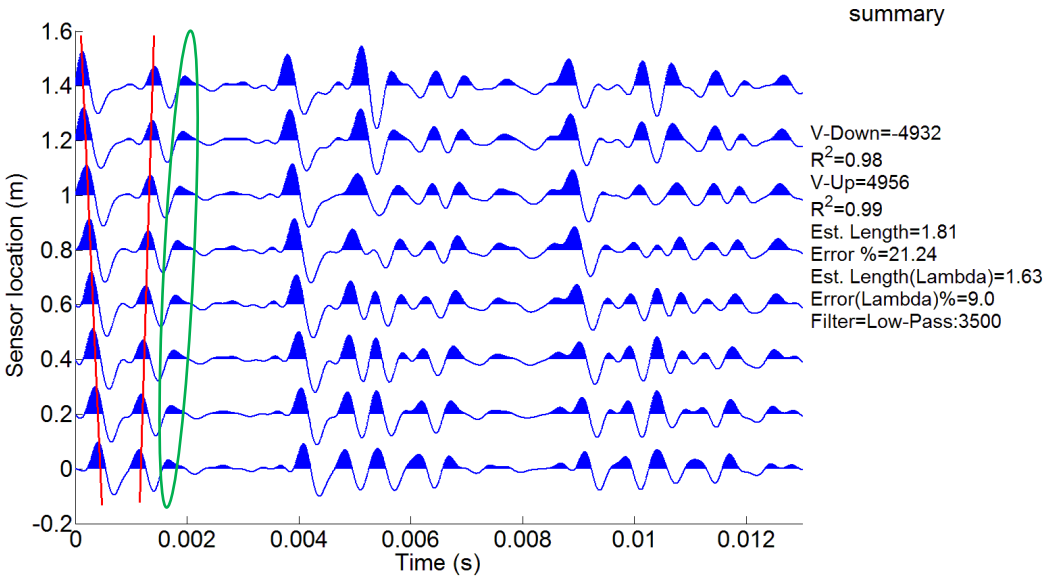

Figure 5.40: Ultraseismic plot of all of the sensors, the estimated length value, and the estimation error for the isotropic embedded in 1.5 m soil simulated timber pole

The embedment length estimation error in the line crossing method is almost 21%, while applying the decrement factor reduces the error to 9%, which is less than half of the line crossing method. As shown by the green oval, another set of peaks parallel to the reflection peaks appeared in the captured signal due to the presence of the soil.

5.7.3 Orthotropic Standing-on-soil

Figure 5.41 shows the Ultraseismic plot of the signals after the low-pass filtering.

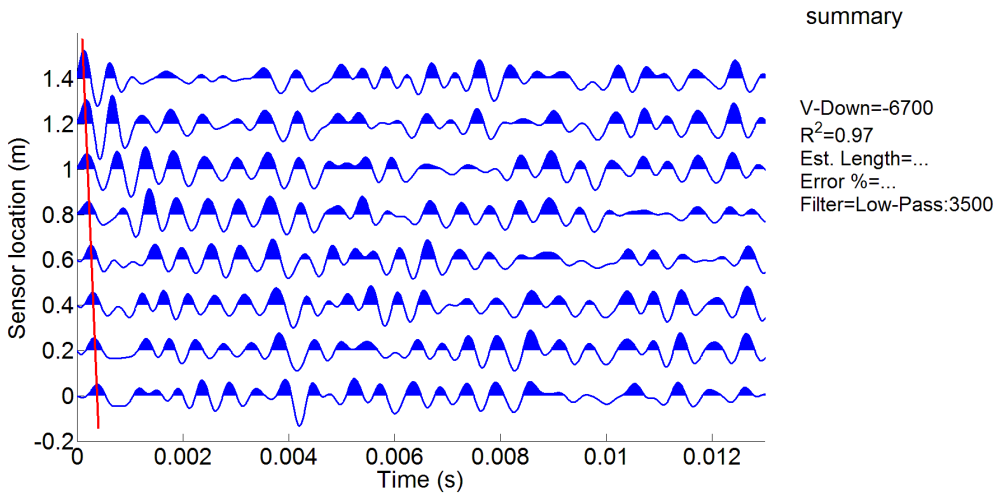

Figure 5.41: Ultraseismic plot of the signals after the low-pass filtering for the orthotropic standing-on-soil simulated timber pole

Figure 5.42 illustrates the peak detection and the velocity analysis procedures for the first arrivals peaks.

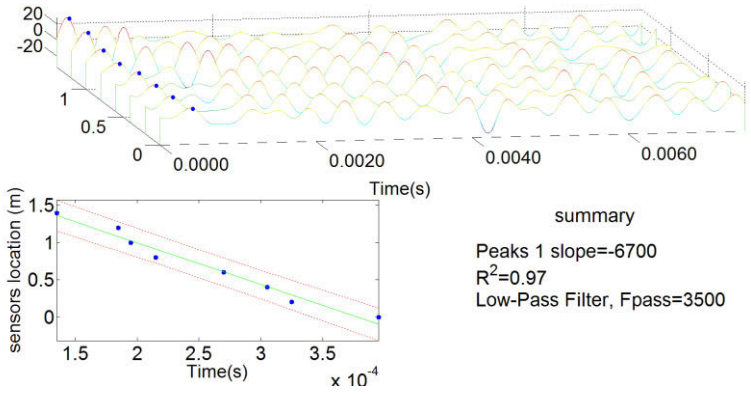

Figure 5.42: Velocity analysis procedure for (a) the down-going and (b) the reflection waves for the orthotropic standing-on-soil simulated timber pole

As can be seen in both of the Figure 5.41 and Figure 5.42, not only no clear pattern of the reflection waves can be detected in the orthotropic case, but also the down-going wave's velocity increased suddenly to 6700 m/s. This is due to the presence of the second and third branches of the bending wave in the frequency range of 0-3500 Hz. These branches have very high energy at the beginning, which increases the estimated velocity (see Figure 2.12).

5.7.4 Orthotropic Embedded in 1.5 m soil

Figure 5.43 shows the Ultraseismic plot of the signals after the low-pass filtering.

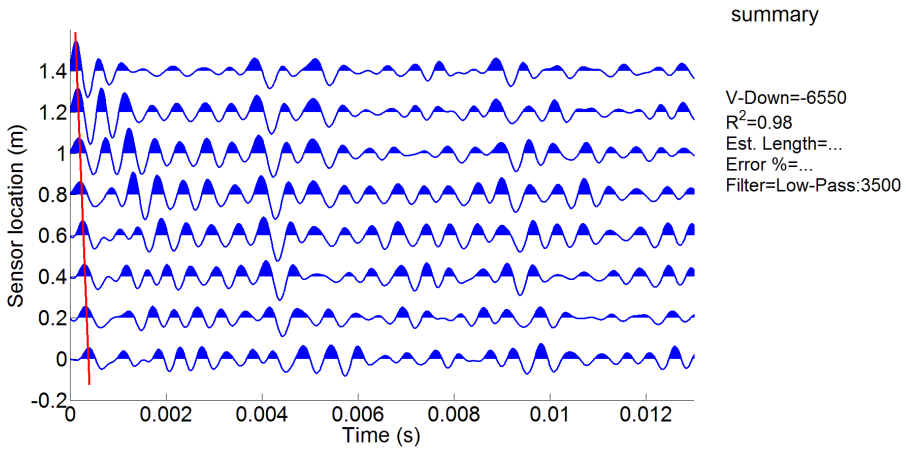

Figure 5.43: Ultraseismic plot of data after low-pass filtering in orthotropic embedded in 1.5 m soil simulated timber pole case.

Figure 5.44 also illustrates the peak detection and velocity analysis procedures for the first arrival peaks.

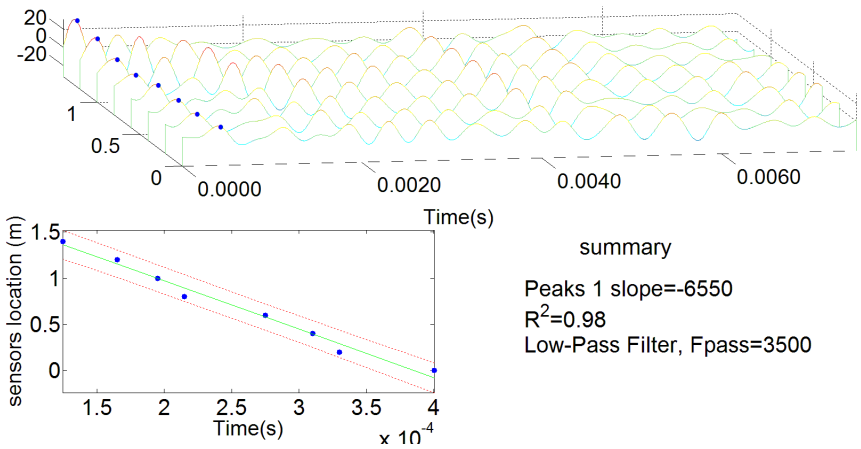

Figure 5.44: Velocity analysis procedures for (a) down-going and (b) reflection waves for orthotropic embedded in 1.5 m soil simulated timber pole case.

As can be seen in both of the orthotropic cases, the first arrival peaks are very clear, but the reflection peaks are not detectable. This is due to the impact excitation type and location, the timber pole material, and soil effects. All of these factors create a complicated dispersive behaviour. It should also be considered that the hammer impact is a broadband low frequency excitation type. In another words, the hammer impact can excite the timber pole in a very broad range of low frequencies from zero to almost 5 kHz. 45º impact creates both of the longitudinal and the bending waves that propagate simultaneously in the timber pole. In the range of 0-5 kHz not only both of the longitudinal and the bending waves exist, but also each has at least two branches. Furthermore, because of the aforesaid in-field test limitations, the impact is needed to be applied on the side of the pole, which itself increases the complications of the situation by creating simultaneous upward and downward travelling waves in the timber pole (while each of them includes both of the longitudinal and the bending waves with their branches). Interference between all of these patterns (up-travelling, down-travelling, longitudinal wave branches, and bending wave branches) creates a very complicated wave propagation pattern. In connection with these points, and in order to be able to detect the reflection peaks, pre-processing is needed to separate these pattern from each other.

5.8 Experimental Data Analysis

In this section, the applications of the conventional stress-wave-based methods on the condition assessment of the timber poles are investigated. Three methods that have been investigated are the Sonic-echo, bending wave utilizing Short Kernel Method, and Ultraseismic. All tests are performed on a 5m timber pole with a 30cm diameter in the cross-section. Two types of tests have been performed, one while the timber pole is standing on soil, and the other when it is embedded in the soil.

5.8.1 Sonic-Echo

Figure 5.45 shows the laboratory test setups for the Sonic-Echo method in the standing-on-soil and the embedded situations.

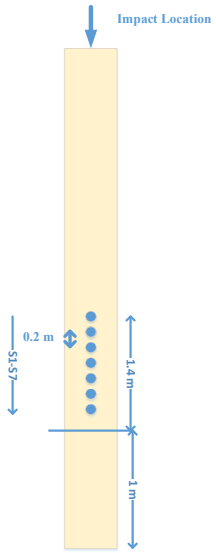

Figure 5.45: The test setups for the Sonic-Echo method in the standing-on-soil and the embedded conditions

The velocity analysis procedure is shown in Figure 5.46.

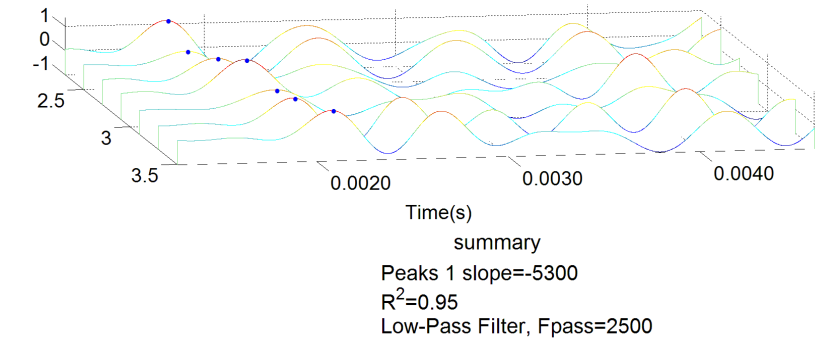

(a)

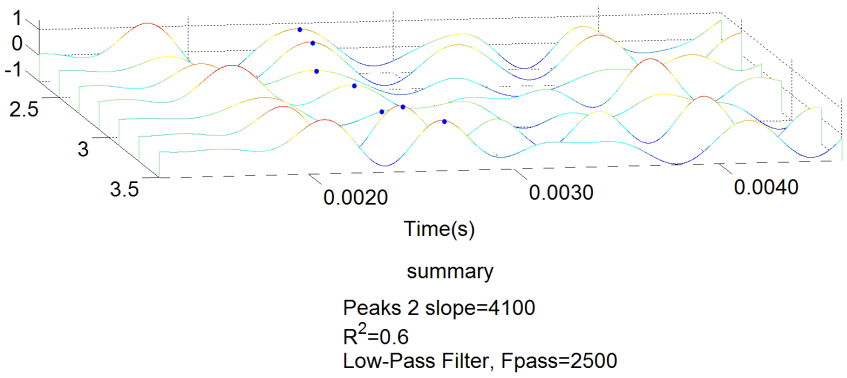

(b)

Figure 5.46: Velocity analysis procedure for (a) the down-going, and (b) the reflection wave in the experimental Sonic-Echo test

The down-going wave's velocity is estimated with 95% fitting accuracy. This means that the longitudinal wave has not been distorted very much, although in comparison with the simulated orthotropic standing-on-soil timber pole, this accuracy has dropped by almost 4%. In (b), it can also be seen that although the pattern of the reflection peaks can be seen, the fitting accuracy has dropped to 60%, which raises the question of the reliability of the results. Figure 5.48 shows the length estimation procedure for this case. Raw captured signals are also shown in Figure 5.47 for comparison.

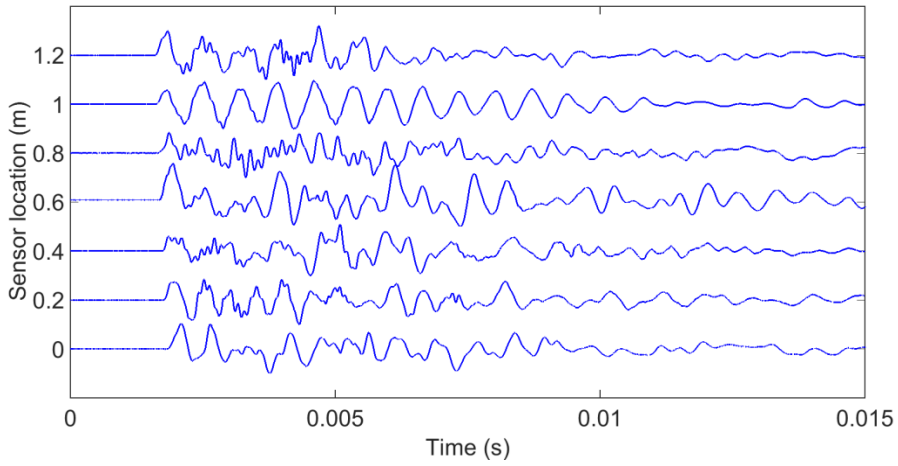

Figure 5.47:Raw captured signals of the Sonic-Echo method test in the timber pole with the standing-on-soil condition.

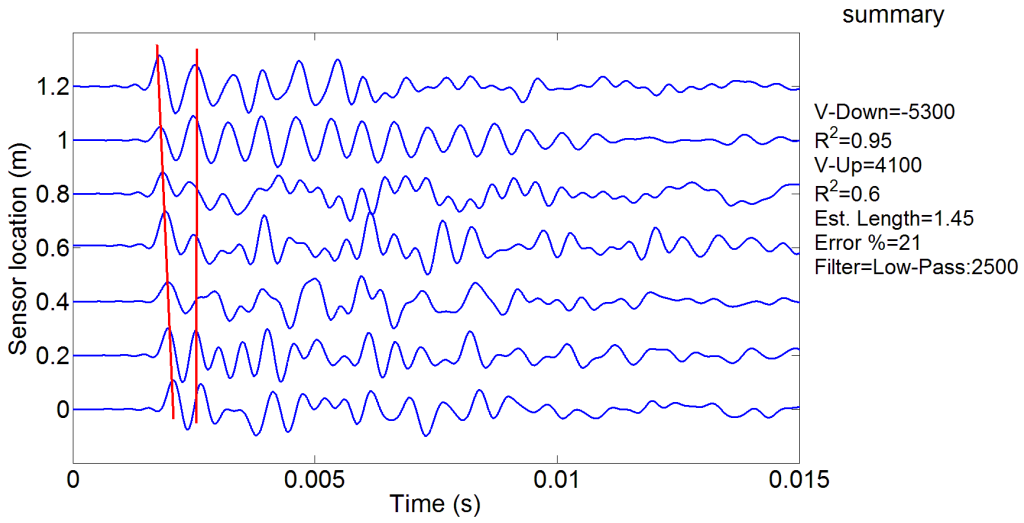

Figure 5.48: Length estimation procedure of the Sonic-Echo method test in the timber pole with the standing-on-soil condition

Velocity analysis procedure in the Sonic-Echo method for the timber pole embedded in 1 m soil is shown in Figure 5.49. It should be considered that S5 has not been considered in the analysis since the captured signal by this sensor is out of the range of the others.

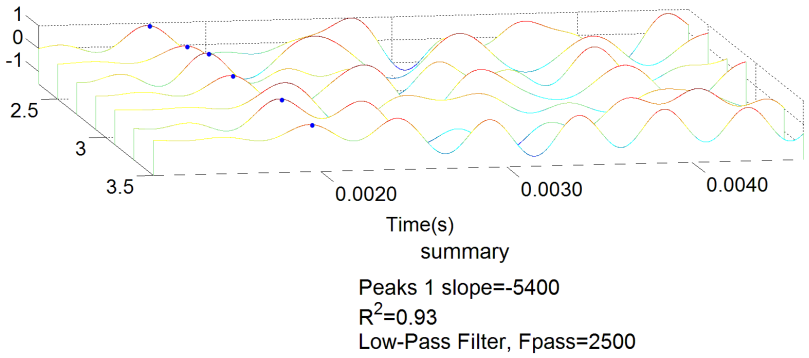

Figure 5.49: Velocity analysis procedure in the Sonic-Echo method for the timber pole embedded in 1 m soil

As can be seen in Figure 5.49, the velocity of the down-going wave is estimated as 5400 m/s with the fitting accuracy of 93%. By comparing the results of the embedded case with the standing-on-soil, the effects of soil can easily be seen, as sensors can detect no clear pattern of the reflections. Figure 5.50 illustrates the length estimation procedure.

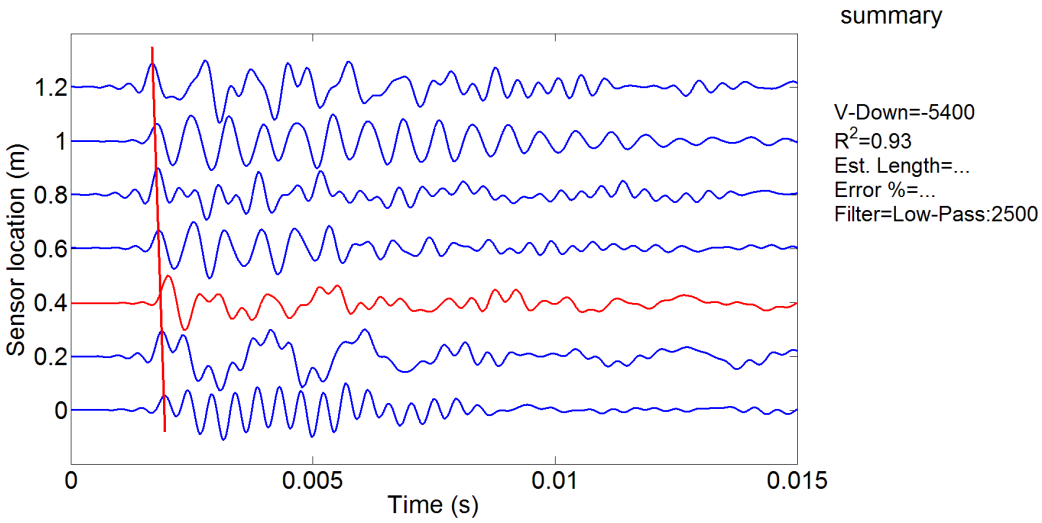

Figure 5.50: Length estimation procedure of the Sonic-Echo test in the timber pole embedded in 1 m soil. S5 in not considered in the analysis since its signal is out of the range of the others. (Red signal)

5.8.2 Short Kernel Method utilizing the bending wave

Figure 5.51 shows the bending wave test setup. In this test three sensors have been used and the impact has been applied 0.1 m above the S1 (top sensor).

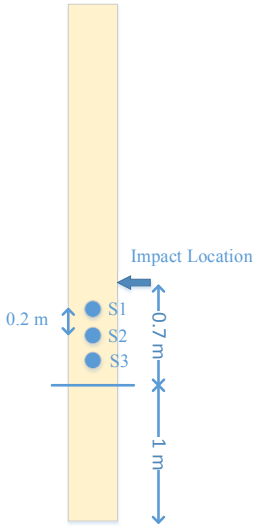

Figure 5.51: Bending wave laboratory test setup

The Frequency Response Functions of all of the three sensors are plotted on top of each other in Figure 5.52. Highlighted frequencies in the green ovals are used for the velocity calculations, and the red one is used for the length estimation.

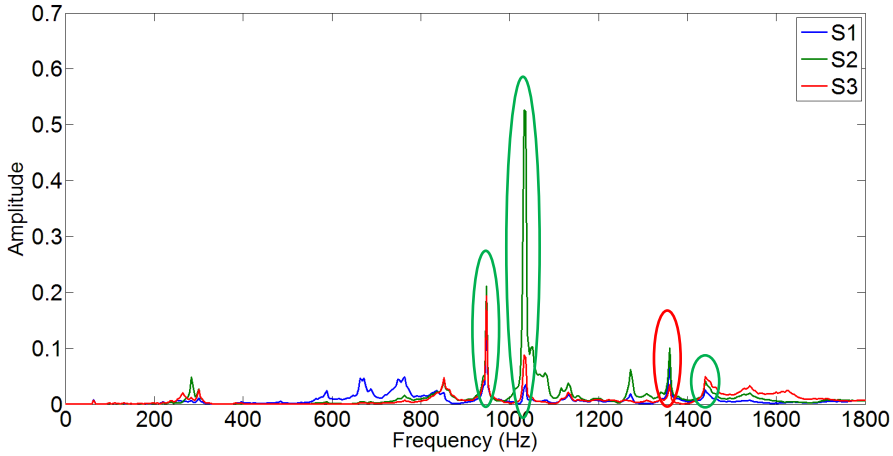

Figure 5.52: FRFs of S1, S2, S3.

The velocity calculation results are provided in Figure 5.53. As can be seen although the estimated velocities are not exactly the same as the analytical results, both have the same increasing trend as the seed frequency increases.

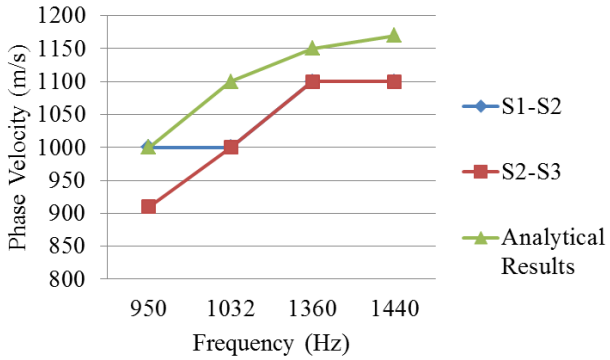

Figure 5.53: Velocity calculation results utilizing several seed frequencies

The length estimation results with the 1360 Hz seed frequency are provided in Table 5.12. As can be seen, the length can be estimated with the average of 19% error.

Table 5.12: Length estimation results utilizing 1360 Hz as a seed frequency

Sensor	Est. Length (m)	Real Length (m)	Error%
S1	1.364	1.6	-14.75
S2	1.1	1.4	-21.42
S3	1.056	1.2	-12

Figure 5.54 shows the results of the SKM with the 1360 Hz seed frequency in S1, S2, and S3.

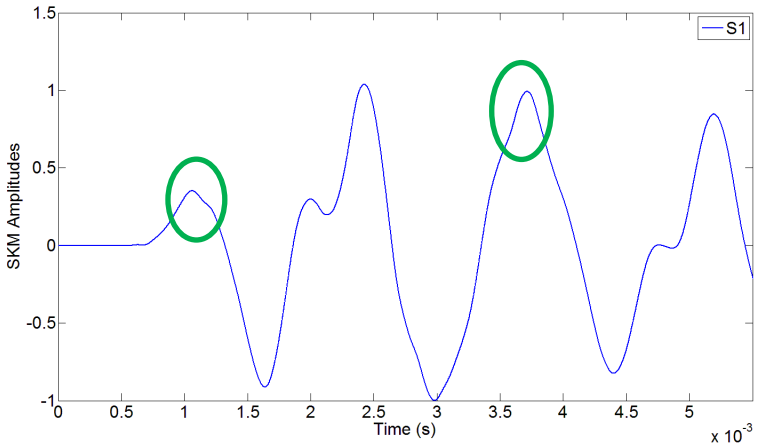

(a)

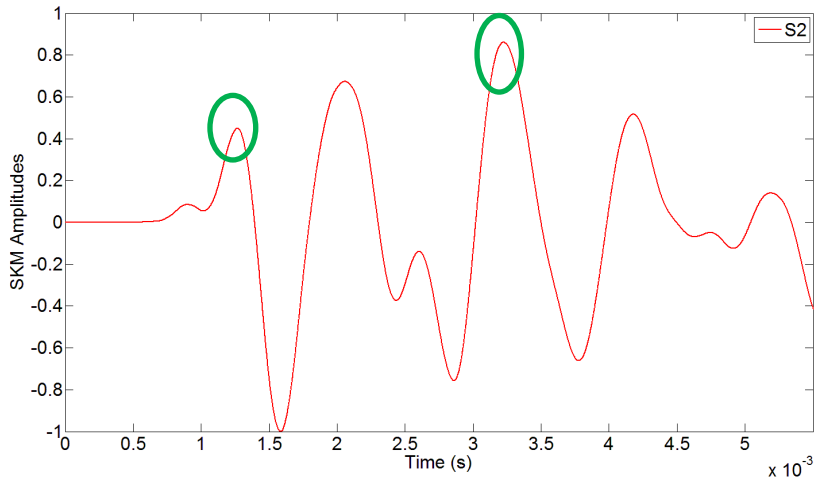

(b)

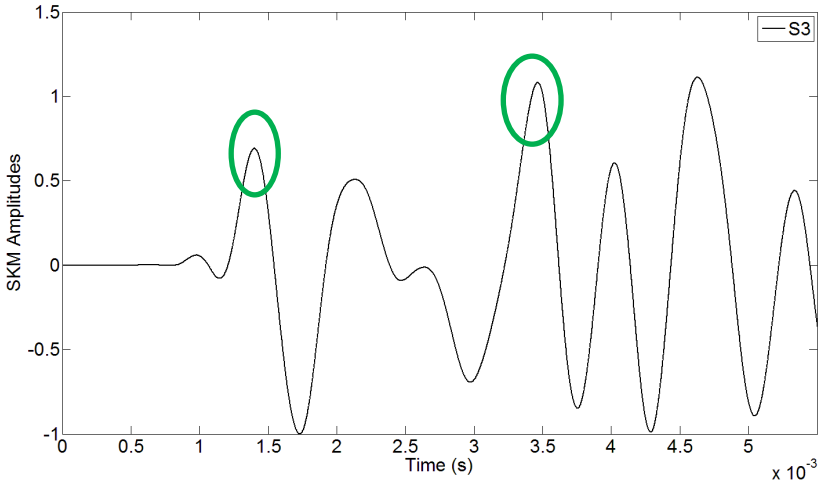

(c)

Figure 5.54: 1360 Hz seed frequency SKM results in (a) S1, (b) S2, and (c) S3

In Figure 5.55, the SKM plots of all of the sensors are plotted on top of each other for comparison and better understanding.

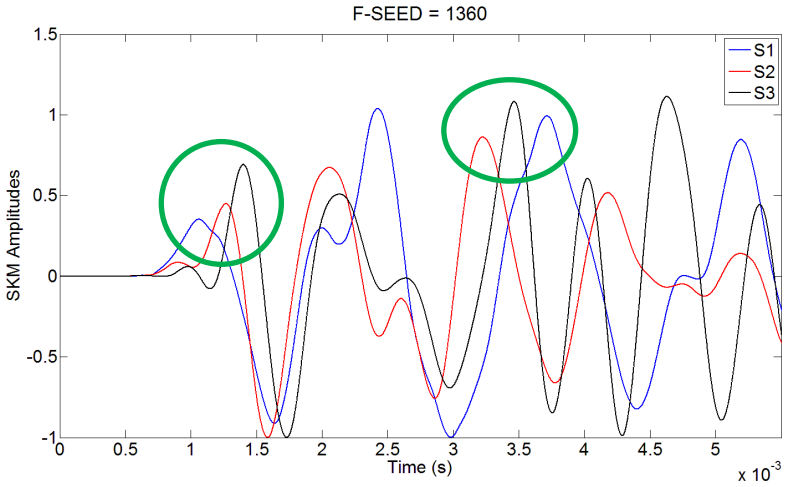

Figure 5.55: 1360 Hz seed frequency SKM results of S1, S2, and S3 comparison

In Figure 5.54, since the reflection peaks in S2 and S3 are the second largest peaks in the SKM plots, the reflection peaks detection is relatively easy. However, it is very tricky in S1 since the reflection peak is not the second largest peak. In fact, the second largest peak leads to unrealistic results. Furthermore, as shown in Figure 5.55, the reflection peak in S2 is not in the correct position as it should be between S1 and S3, which itself results in the higher length estimation error as shown in Table 5.12.

Figure 5.56 shows the FRFs in S1, S2, and S3 for embedded timber pole in 1 m soil.

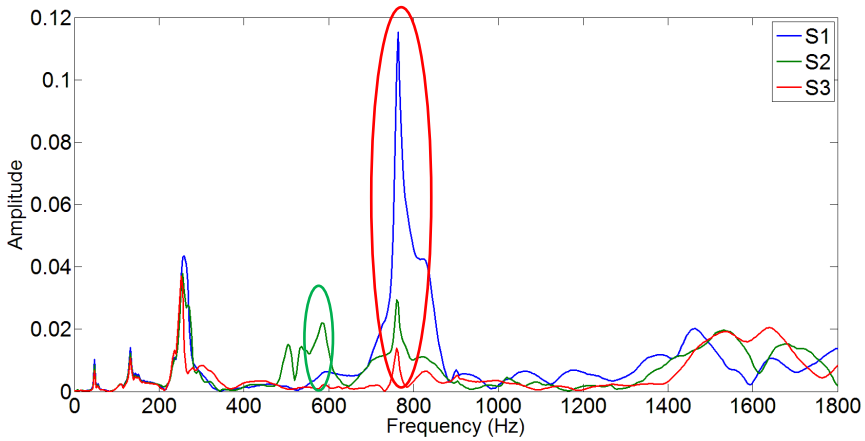

Figure 5.56: FRFs in S1, S2, and S3 for the embedded timber pole in 1 m soil

As can be seen, there are fewer numbers of peaks in the FRF of the embedded case in comparison to the standing-on-soil condition. It is also worth considering that although there are some peaks lower than 400 Hz, they have not been used since the wavelength of the related frequencies are very large and their results are not reliable.

Figure 5.57 illustrates the velocity estimation results. Again, although the estimated velocities are not the same as the analytical ones, both have the same trends of increasing.

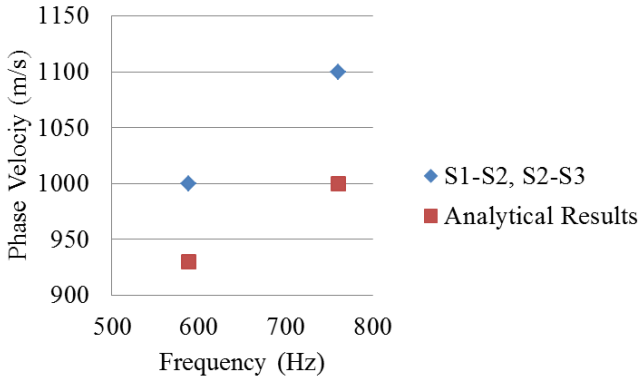

Figure 5.57: Velocity calculation results utilizing several seed frequencies

Table 5.13 also provided the estimated embedment lengths in all of the sensors using the frequency 760 Hz as the seed frequency.

Table 5.13: Estimated embedment lengths in S1, S2, and S3 using 760 Hz as the seed frequency

Sensor	Est. Length (m)	Actual Length (m)	Error %
S1	2.15	1.6	34.4
S2	1.6	1.4	14.3
S3	1.32	1.2	10

Figure 5.58 shows the results of the SKM with the 760 Hz seed frequency in S1, S2, and S3. In Figure 5.59, the SKM plots of all of the sensors are also plotted on top of each other for comparison and better understanding.

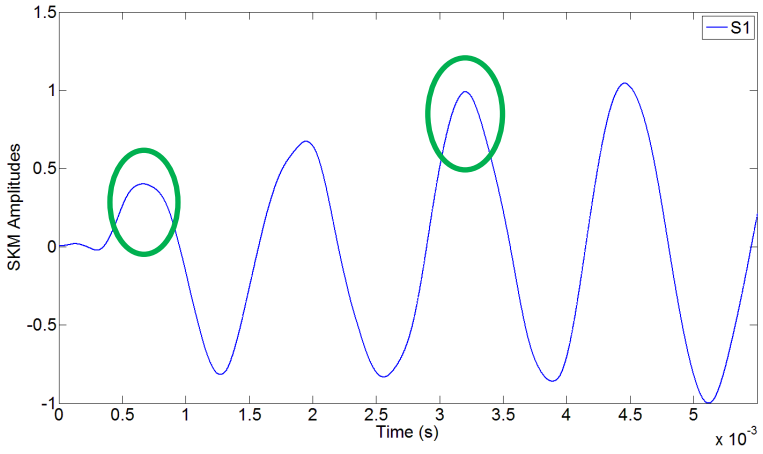

(a)

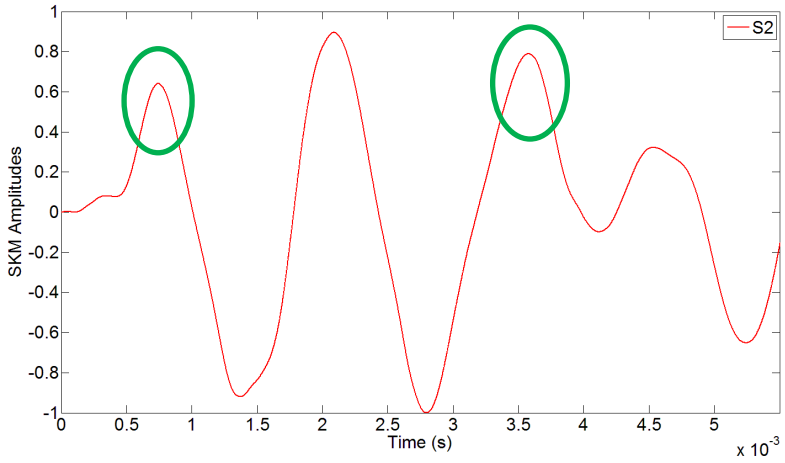

(b)

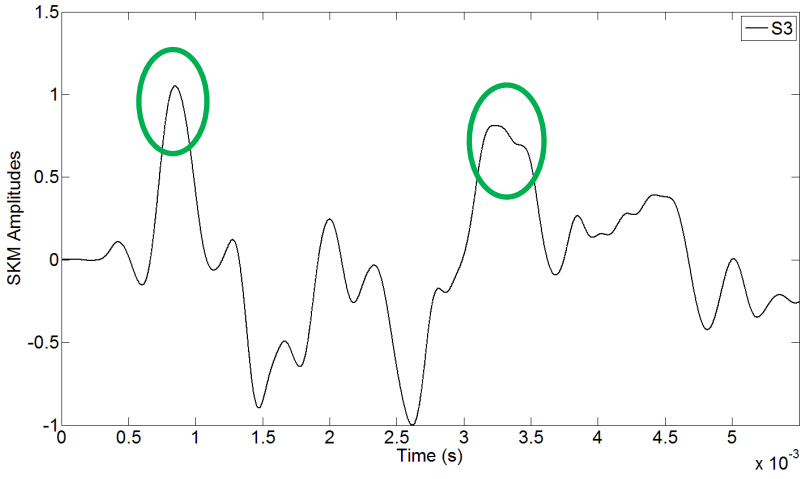

(c)

Figure 5.58: 760 Hz seed frequency SKM results in (a) S1, (b) S2, and (c) S3

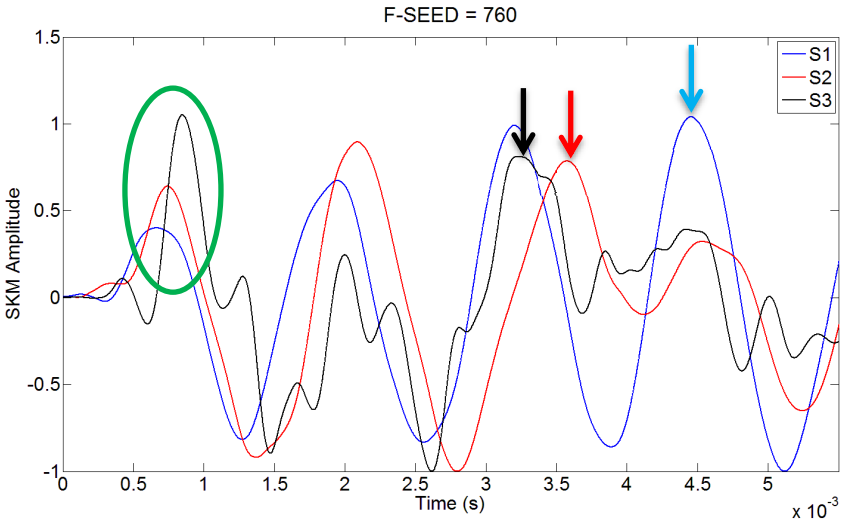

Figure 5.59: 760 Hz seed frequency SKM results of S1, S2, and S3 comparison

As can be seen in Figure 5.59, the reflection peak detection is not an easy and straightforward task in the embedded case especially in the S1 and S2 since in both sensors the reflection peak can easily be mistaken for its adjacent peak. In the real world applications, where in most of the cases there is no prior information available about the timber pole, the reflection peak detection is almost impossible. Only in the S3, the reflection peak can be detected relatively easier, which can be used as a benchmark for peak detection in the other sensors. It is also worth paying attention to the level of distortion occurred to the reflection peak in S1, which repositioned the peak to almost out of the range of the other sensors and leads to the very high estimation error.

5.8.3 Ultraseismic

Figure 5.60 shows the test setup for the Ultraseismic method.

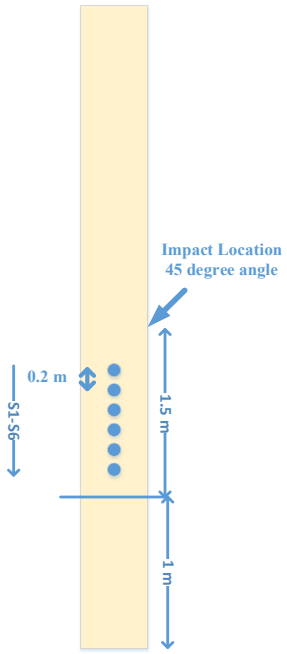

Figure 5.60: Ultraseismic laboratory test set up

Impacting the pole on the side at a 45º angle creates the longitudinal and the bending wave simultaneously. Figure 5.61 and Figure 5.62 show the velocity analysis and the length estimation procedure on the laboratory data in the standing-on-soil and the embedded conditions.

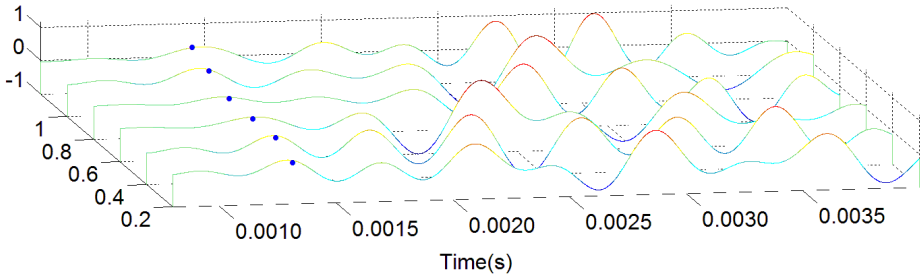

summary

Peaks 1 slope=-7900

R^2=0.96

Low-Pass Filter, Fpass=3500

(a)

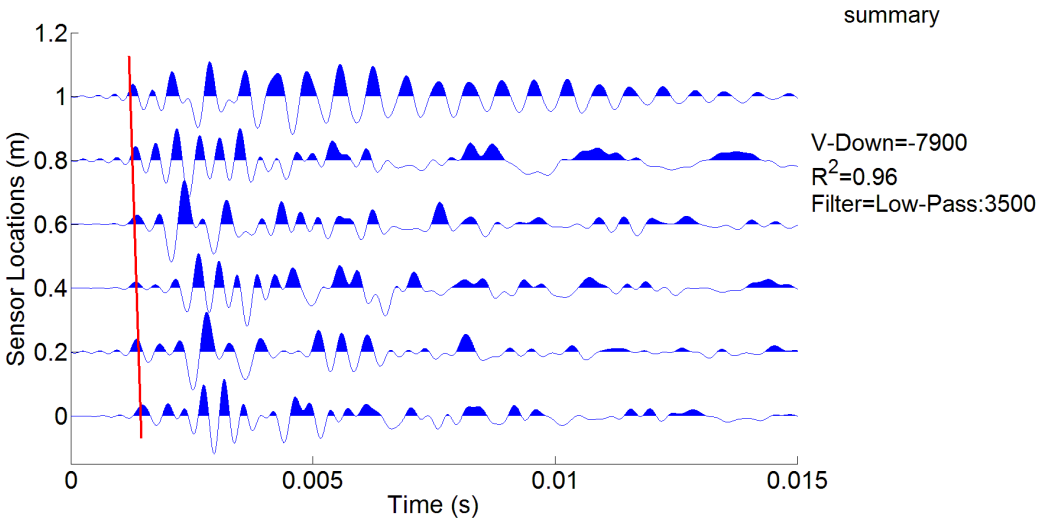

(b)

Figure 5.61: Velocity analysis and the length estimation procedure on the laboratory Ultraseismic test data in the standing-on-soil condition

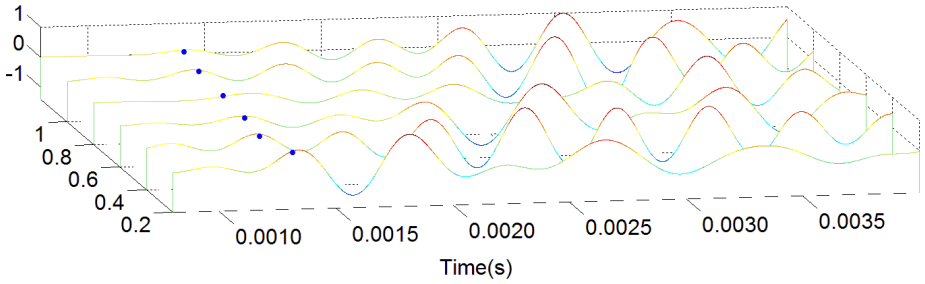

summary

Peaks 1 slope=-7600
R^2=0.83
Low-Pass Filter, Fpass=3500

(a)

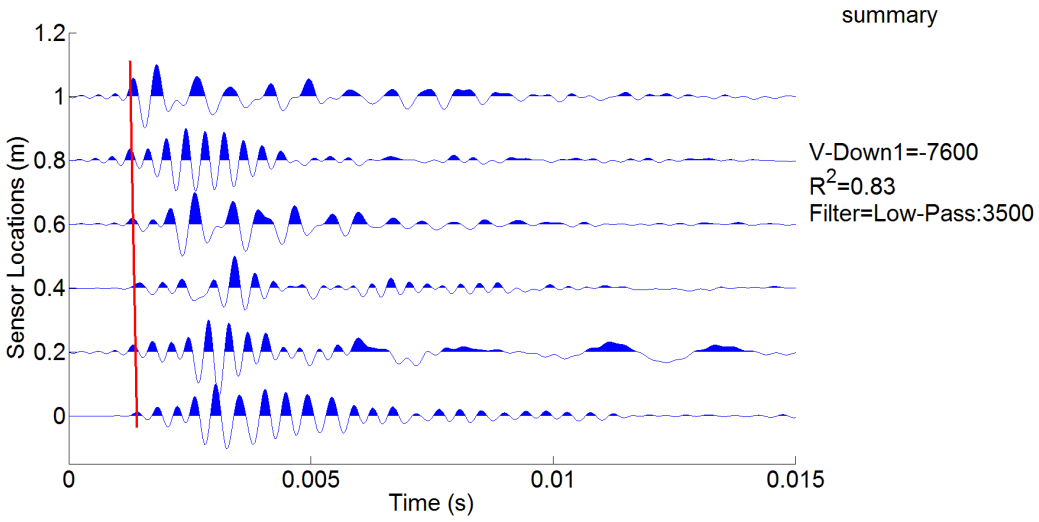

(b)

Figure 5.62: (a) Velocity analysis and (b) the length estimation procedure on the laboratory Ultraseismic test data in the embedded condition

Figure 5.63 shows the velocity analysis and the length estimation procedures for the data captured from the in-field test of the in-service timber pole.

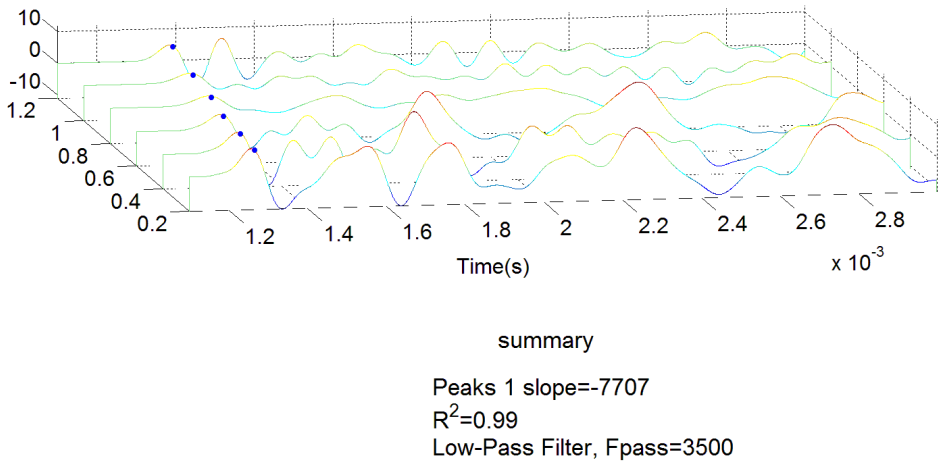

(a)

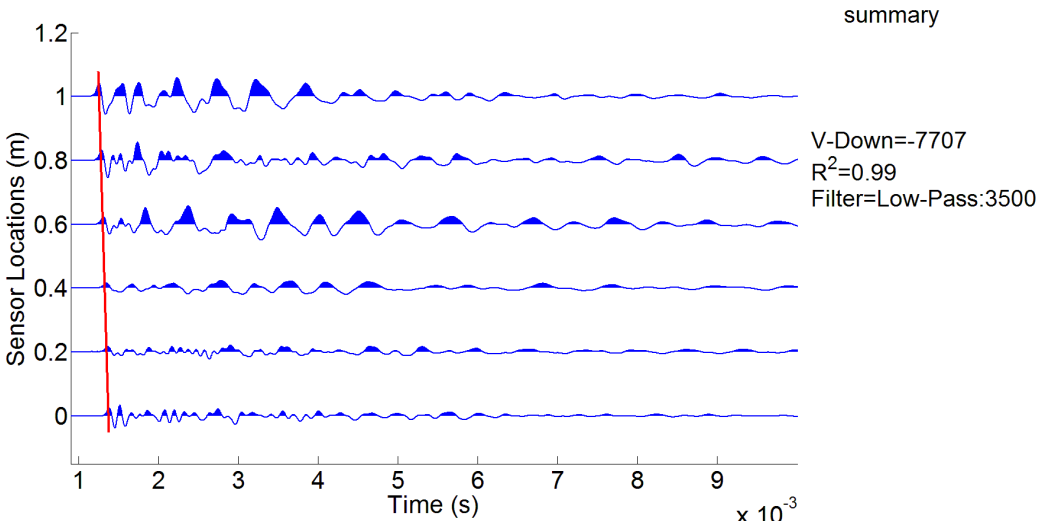

(b)

Figure 5.63: Velocity analysis and the length estimation procedure on the Field-test data for the Ultraseismic test

As can be seen in all of the figures in this section, the down-going wave velocities vary from 7000 to almost 8000 m/s. This phenomenon can be the effect of the second and third branches of the bending wave that exist in the frequency range of 0-3500 Hz and have very high energy at the beginning.

5.9 Conclusions

In this chapter firstly the digital filters, and then the application of the current surface stress-wave-based NDTs on the condition assessment of the timber pole have been investigated.

Conclusion 1: The digital filters investigation results reveal that the best digital filter to be used for the in-situ timber pole condition assessment test is the Equiripple FIR filter.

The FIR filters are chosen since their phase distortion is linear and can easily be amended by applying the zero-phase filtering process. Amongst all of the FIR filter design methods, the Equiripple method is the best option to be used for the embedded NDT system in this project since it is more efficient in terms of the energy consumption and the processing time.

In the next section of this chapter, the Sonic-Echo method utilizing the longitudinal wave; the Short Kernel Method utilizing the bending wave; and the Ultraseismic

method utilizing both of the longitudinal and the bending waves were investigated for determining the stress wave velocity and the length of poles. These methods were investigated on the different types of data (Numerical, laboratory, and the field tests) with both of the standing-on-soil and the embedded conditions.

Conclusion 2: In the Sonic-Echo method, it was shown that the conventional method output (in which a constant value is assumed for the wave velocity, and the length estimation relies on a single sensor) is reliant on the sensor location.

The length estimation error for the different sensor locations varies from 7% to 22%. Assuming a constant value for the wave velocity has the effect of different estimation errors for sensors in different locations since firstly the wave velocity varies from pole to pole and secondly the down-going and the reflection waves have different wave velocities. This shows the importance of using the multi-sensors array, which estimates the velocities of the both down-going and the reflection waves separately. Moreover, the length estimation errors in all of the sensors strongly depend on the assumed value of the wave velocity, and the constant value assumption for all poles will lead to faulty and unreliable results. In fact, the wave velocity needs to be calculated for each pole separately. In this regard, in the next subsection of the Sonic-Echo method the multi-sensors array has been employed in order to make the velocity analysis feasible, and consequently obtain more accurate and reliable length estimation results. The velocity analysis results reveal that the down-going and the reflection waves have not exactly the same velocities. Length of the pole can be estimated by crossing the two lines that are related to the down-going and the reflection waves. However, for the embedded conditions, the wave velocity under the soil decreases to 90% of its value above the soil due to the energy absorption by the soil. For this reason, the decrement factor has been considered and the lengths are estimated by using the equation (5.1). Results of this subsection have shown that the length can be estimated by crossing the two lines with almost 12% error while in the embedded conditions, considering the decrement factor can reduce the length estimation error to almost half of the line crossing method. Application of the Sonic-Echo method utilizing the multi-sensors array on the laboratory test in the standing-on-soil condition revealed that although the reflection peaks can be detected and the length can be estimated, the low fitting accuracy (60%)

shows the level of the distortion that has occurred to the reflection peaks and can bring question into the reliability of the results. This situation is worse in the embedded condition where no clear pattern of the reflection peaks can be detected.

Conclusion 3: Application of the Short Kernel Method (SKM) utilizing the bending wave on the numerical data shows that in the standing-on-soil condition, although choosing a correct seed frequency is tricky and vital, the reflection peaks detection is a straightforward and easy task and the length can be estimated with 20% error on average. While in the embedded conditions, both of the seed frequency determination and the reflection peaks detection are not easy tasks and heavily depend on the experience of the test performer or the signal processor, and availability of the prior knowledge about the pole.

It has also been shown that in the embedded situations, the reflection peaks can easily be mistaken for their adjacent peaks due to the considerably large attenuation that is imposed on the captured signal by the soil. Applications of SKM on the laboratory tests also show that even in the standing-on-soil condition, the reflection peak detection is not a very easy task and the reflection peaks can easily be mistaken for their adjacent peaks. The situation is worse when the pole is embedded in the soil in which the reflection peaks are subjected to more severe distortion.

In the last section, the Ultraseismic method utilizing both of the longitudinal and the bending waves has been investigated for determining the stress wave velocity and the length of the poles. The longitudinal and the bending waves can be applied to the pole simultaneously by the 45° angle impact. It is also necessary to mention that due to the limitations of the in-field tests (where access to the top or near top of the structure is prohibited due to the presence of the electrical and the communication wires), the impact is applied on the side of the structure in 1.5 m above the ground level. The velocity analysis results have shown that due to the presence of the second branch of the bending wave (which started with the considerable high energy), the estimated velocity of the down-going wave is considerably high.

Conclusion 4: The velocity of the down-going waves are estimated relatively higher that the analytical results. Furthermore, all of the aforementioned factors (i.e. the impact excitation type and location, the timber pole material and the soil effects) create a complicated dispersive behaviour as shown in Figure 5.64.

It is vital to consider that the hammer impact is a broadband low frequency excitation type. In another words, the hammer impact can excite the timber pole in a very broad range of low frequencies from zero to almost 5 kHz. The 45° angle impact creates both of the longitudinal and the bending waves that propagate simultaneously in the timber pole.

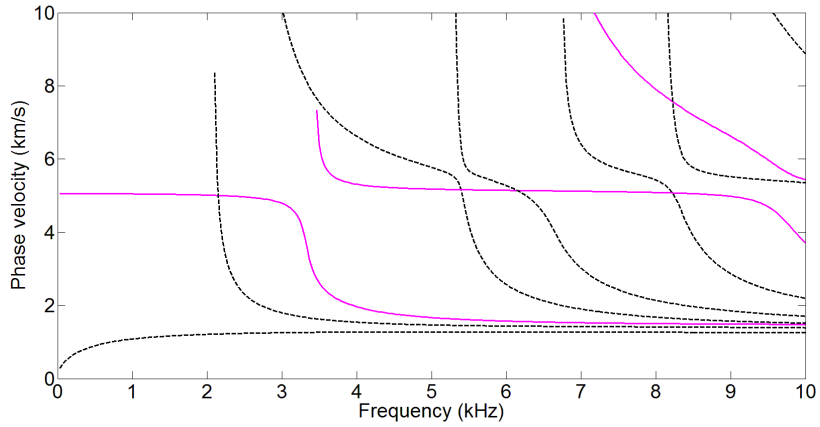

Figure 5.64: Spectrum curves of the cylindrical timber poles with orthotropic material properties. Dashed lines represent the flexural wave branches and the hard lines represent the longitudinal wave branches [52]

As shown in Figure 5.64, in the range of 0-5 kHz not only both of the longitudinal and the bending waves exist, but also each has at least two branches (modes). Furthermore, because of the aforesaid in-field test limitations, the impact is needed to be applied on the side of the pole, which itself increases the complications of the situation by creating the simultaneous up and down travelling waves in the timber pole (while each of them includes both of the longitudinal and the bending waves with their branches). Interference between the aforementioned patterns (up-travelling, down-travelling, the longitudinal, and the bending waves' branches) all together create a very complicated wave propagation pattern. In this regard, and in order to be able to detect the reflection

peaks, advanced digital signal processing is needed to separate these pattern from each other.

6 Chapter 6: Application of the advanced Digital Signal Processing on the Condition assessment of the timber poles

6.1 Introduction

In this chapter, applications of the advanced digital signal processing methodologies (which were explained in Chapter 3) on the condition assessment of the timber pole are investigated. All of the methodologies are applied on the numerical, experimental, and the field tests data. The proposed advanced digital signal processing methodologies can be categorized into three main groups of deterministic signal separation methods (i.e. the predictive deconvolution), the blind signal separation methods (i.e. Principal Component Analysis, Singular Value Decomposition, and the *K*-mean clustering), and finally the Frequency-Wavenumber analysis and filtering. The overall structure of this chapter is applying these methodologies on the numerical data followed by the experimental and the field tests data. It is also essential to consider that all types of the data are low-pass filtered before the applications of the predictive deconvolution.

6.2 Applications of the Deterministic signal separation and the Frequency-Wavenumber analysis on the Finite Element modeled timber pole

In this section, application of the predictive deconvolution, and the Frequency-Wavenumber (F-K) analysis on the timber pole condition assessment using the numerical data are investigated. Figure 6.1 shows the test setup for both of the standing-on-soil and the embedded conditions. The test setup in this chapter is mostly like the Ultraseismic test setup, which is explained in Chapter 5. The only difference is in this simulation, 241 sensors have been used instead of the eight sensors for the better

illustration of the wave propagation and the effectiveness of the proposed methods. The sensors are placed from the bottom of the pole (S1) to the top (S241) in 0.05 m distance. The length of the pole is 12 m, and the hammer impact at a 45° angle is applied on the side 3 m above the bottom of the pole.

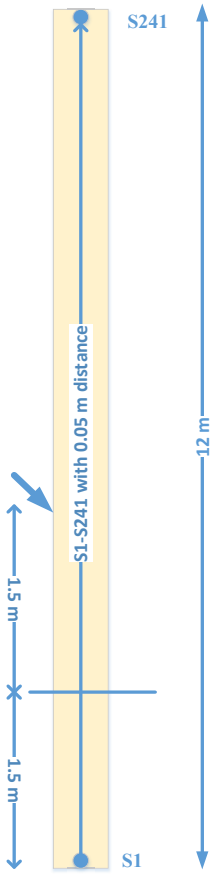

Figure 6.1: Simulated timber pole test setup for both of the standing-on-soil and the embedded conditions

6.2.1 Isotropic Standing-on-soil

Figure 6.2 shows the Ultraseismic plots before and after the low-pass digital filtering using the signals captured from all of the 241 sensors. The horizontal axis represents the time while the vertical axis represents the sensors location.

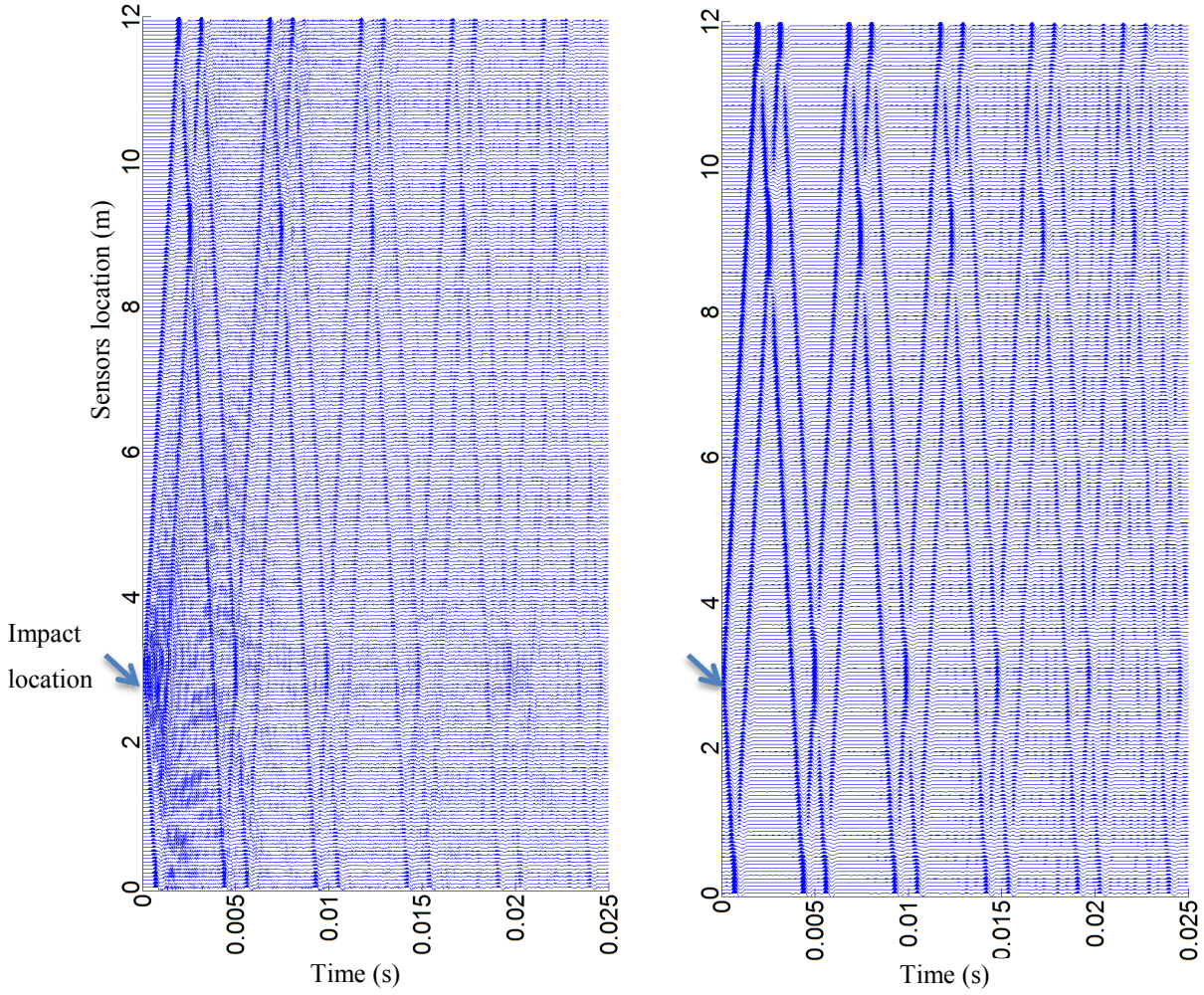

Figure 6.2: Ultraseismic plots for the simulated timber pole with the standing-on-soil condition (a) before the low-pass filtering, and (b) after the low-pass filtering

For better illustration of the effects of the digital filter, the original signal in a single sensor vs. the filtered one are presented in both time and frequency domain in Figure 6.2.

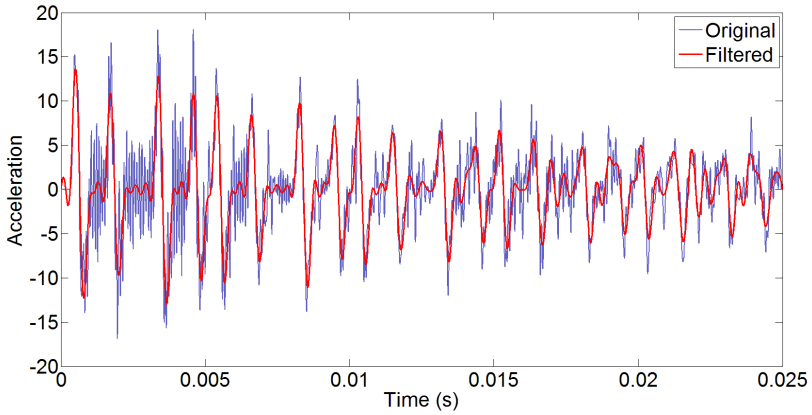

(a)

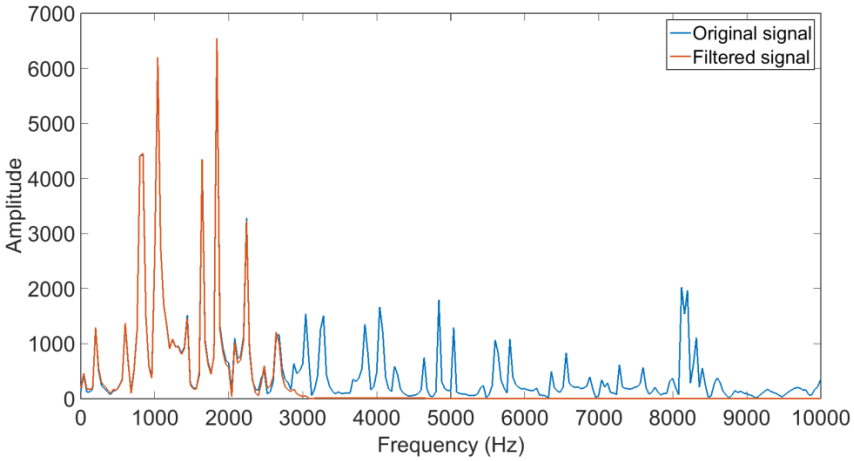

(b)

Figure 6.3: A comparison of the original and the filtered signal with 2.5 KHz cut-off frequency in a single sensor in (a) time domain, and (b) frequency domain

It can be easily seen in Figure 6.3 how very effectively the low-pass digital filter can clean the signal and preserve the main patterns of the signal. It is also worth mentioning that the high frequency components in the signal are due to the calculation error. This error occurs because in the FEM the sensors are actually measure displacement, converting the displacement into acceleration added some high frequency components to the signals, which are useless.

The patterns of the up and downward travelling waves that were explained previously in Chapter 5 can be seen in Figure 6.2. Presence of the up and downward travelling waves can make the reflection peaks detection a challenging task. It should be considered that in the tests of the in-service timber pole, only eight sensors can be attached to the pole, and the clear patterns that can be seen with the 241 sensors in Figure 6.2 are not clearly observable especially in the orthotropic embedded case. For better illustration of this

situation, a group of the eight sensors with exactly the same locations as the field test have been chosen from the set of the 241 sensors. Figure 6.4 shows the captured signals by these sensors before and after the low-pass digital filtering.

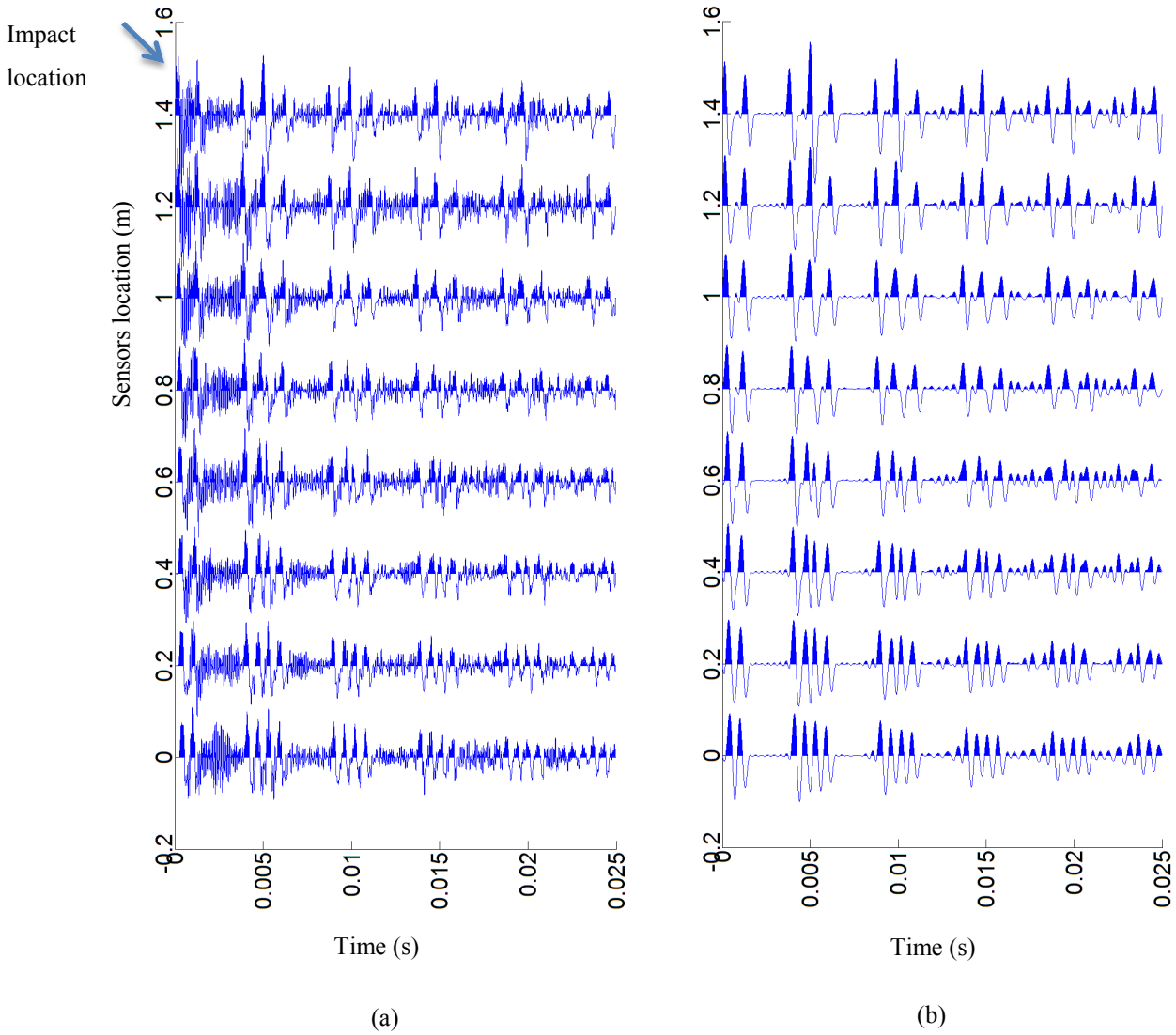

Figure 6.4: Captured signals by eight in-field sensors (a) before and (b) after low-pass digital filtering

As can be seen, the reflection peaks detection is almost impossible especially in the area that is highlighted with a green oval. It is also worth considering that in some cases because of the presence of the bending wave at the beginning of the signal with considerably large energy and amplitude, it is more suitable to use the second set of the first arrivals and the reflection peaks for the velocity analysis and the length estimation procedures.

As mentioned and explained earlier in Chapter 3, the predictive deconvolution assumes that the captured signal is wide-sense stationary. This means that the statistical

properties of the wavelets (caused by the hammer impact) that are propagating in the timber pole in both the up and downward travelling waves do not change during the capturing time. In the predictive deconvolution, the main goal is to remove the unwanted patterns from the captured signals in order to obtain purely the first arrivals and the reflection peaks from the bottom of the pole. The processing steps of the predictive deconvolution are as follows. First, the captured signal is divided into same size windows (which contains firstly the desired and then the unwanted patterns). Second, the pattern at the beginning of each window is assumed to have the main statistical properties of the desired pattern to be kept and every similar statistical property is removed from the rest of the window (i.e. the original wavelet related to the upward travelling wave is needed to be kept, and the rest of the patterns related to the downward travelling waves can be removed as they have the same statistical properties). It is also worth mentioning that since only first larger positive peaks of the down-going and reflection waves are needed for the length estimation, only half of the first sinusoidal single pulse wave is used as a pattern to be kept in each window. Based on application, one can also use a whole pulse as a desirable pattern in each window. Figure 6.5 shows the procedure of applying the predictive deconvolution on the signal captured by one sensor.

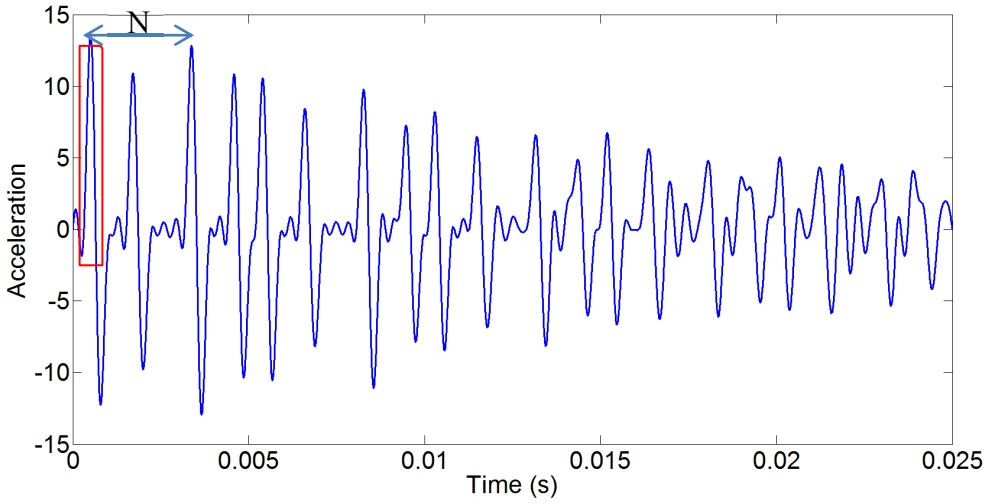

Figure 6.5: Predictive deconvolution procedures in a single sensor.

In Figure 6.5, the red rectangle shows the length of the desired output and N is the length of each window. Since both of the upward and downward travelling waves have the same statistical properties and the signal is wide-sense stationary, the upward travelling wave can be separated from the downward travelling one utilizing the

predictive deconvolution. Figure 6.6 shows the low-pas filtered data before and after applying the predictive deconvolution in a single sensor.

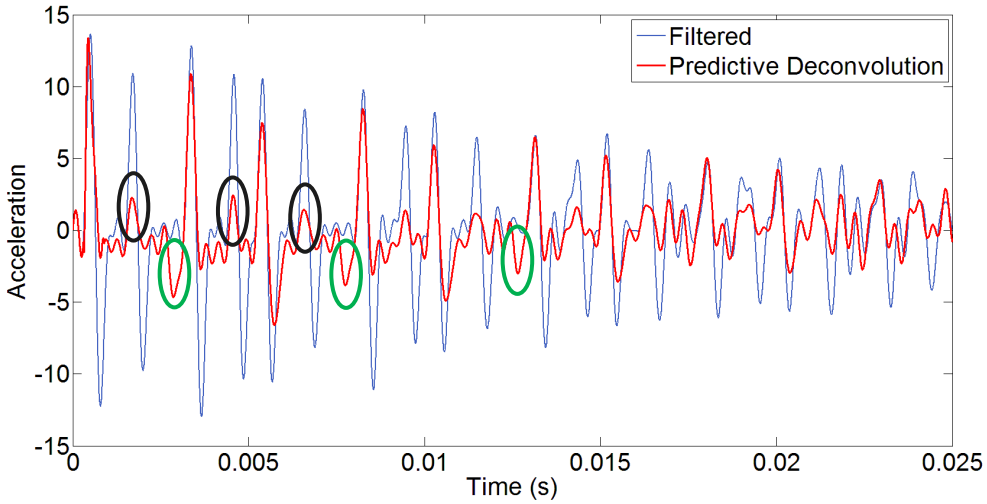

Figure 6.6: Low-pas filtered data before and after applying the predictive deconvolution in a single sensor for the simulated isotropic timber pole with the standing-on-soil condition

In Figure 6.6 the low-pass filtered signal is shown with light blue colour, while the predictive deconvolution output is shown in red. As can be seen in Figure 6.6, the predictive deconvolution could remove any pattern that has same statistical properties with the desirable pattern (see red rectangular in Figure 6.5) in each window. In other words, it can remove any unwanted similar pattern to the desirable one in the signal, although not completely as shown with the black ovals. It also created some faulty peaks as shown with the green ovals. Figure 6.6 illustrates the Ultraseismic plot of the outputs of the predictive deconvolution on all of the 241 sensors.

As can be seen in Figure 6.7, although the predictive deconvolution can separate the upward travelling wave from the downward travelling one, it cannot remove the patterns related to the downward travelling wave in the beginning of the signal. Furthermore, it created some unwanted patterns in the beginning of the signals near the impact location (see Figure 6.7 (b)).

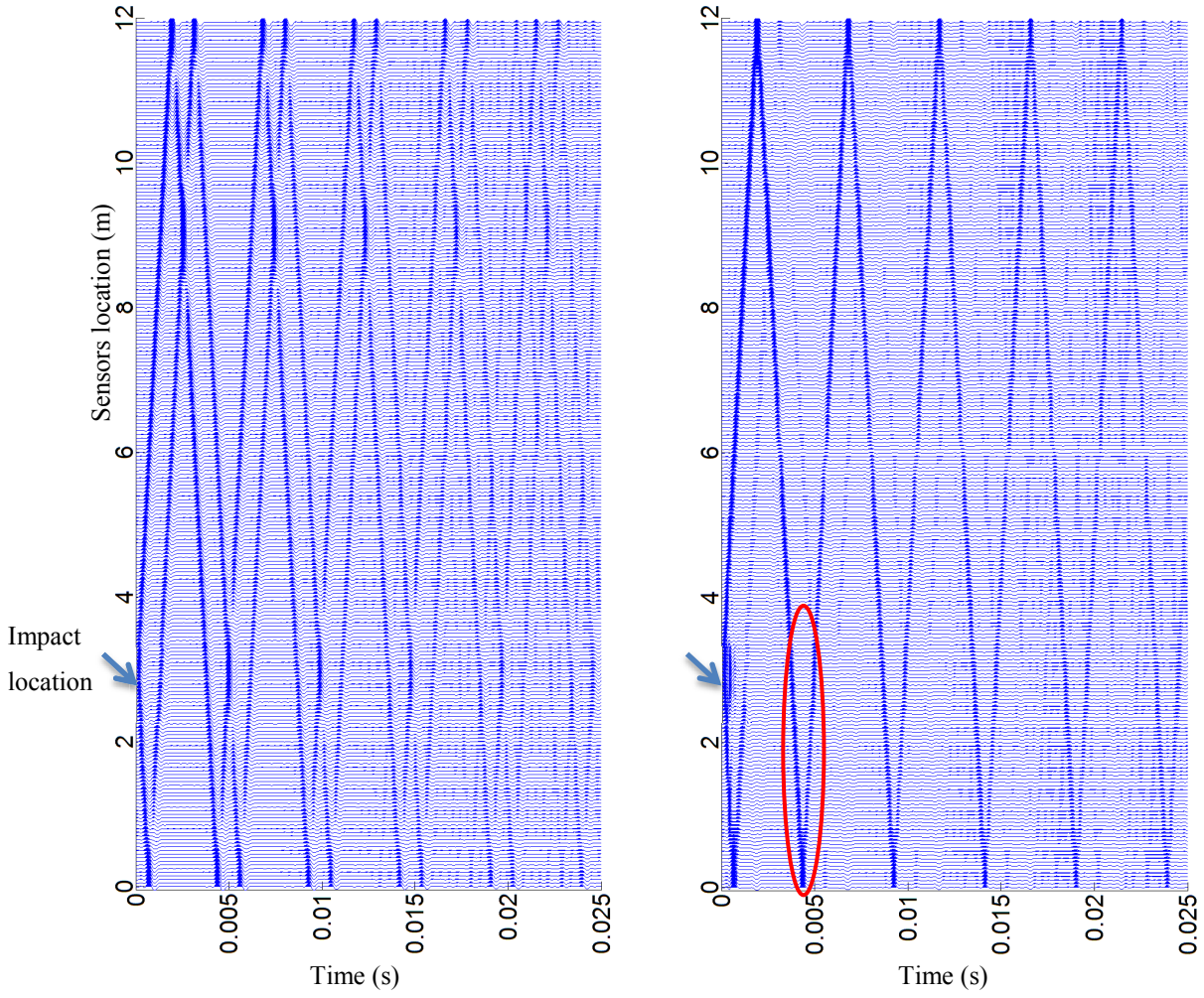

(a) (b)

Figure 6.7: Ultraseismic plot of (a) the low-pass filtered data, and (b) the outputs of the predictive deconvolution on 241 sensors for the simulated isotropic timber pole with the standing-on-soil condition

Peaks that are highlighted with the red oval are used for the length estimation. Figure 6.7 shows the signals of the in-field sensors before and after applying the predictive deconvolution.

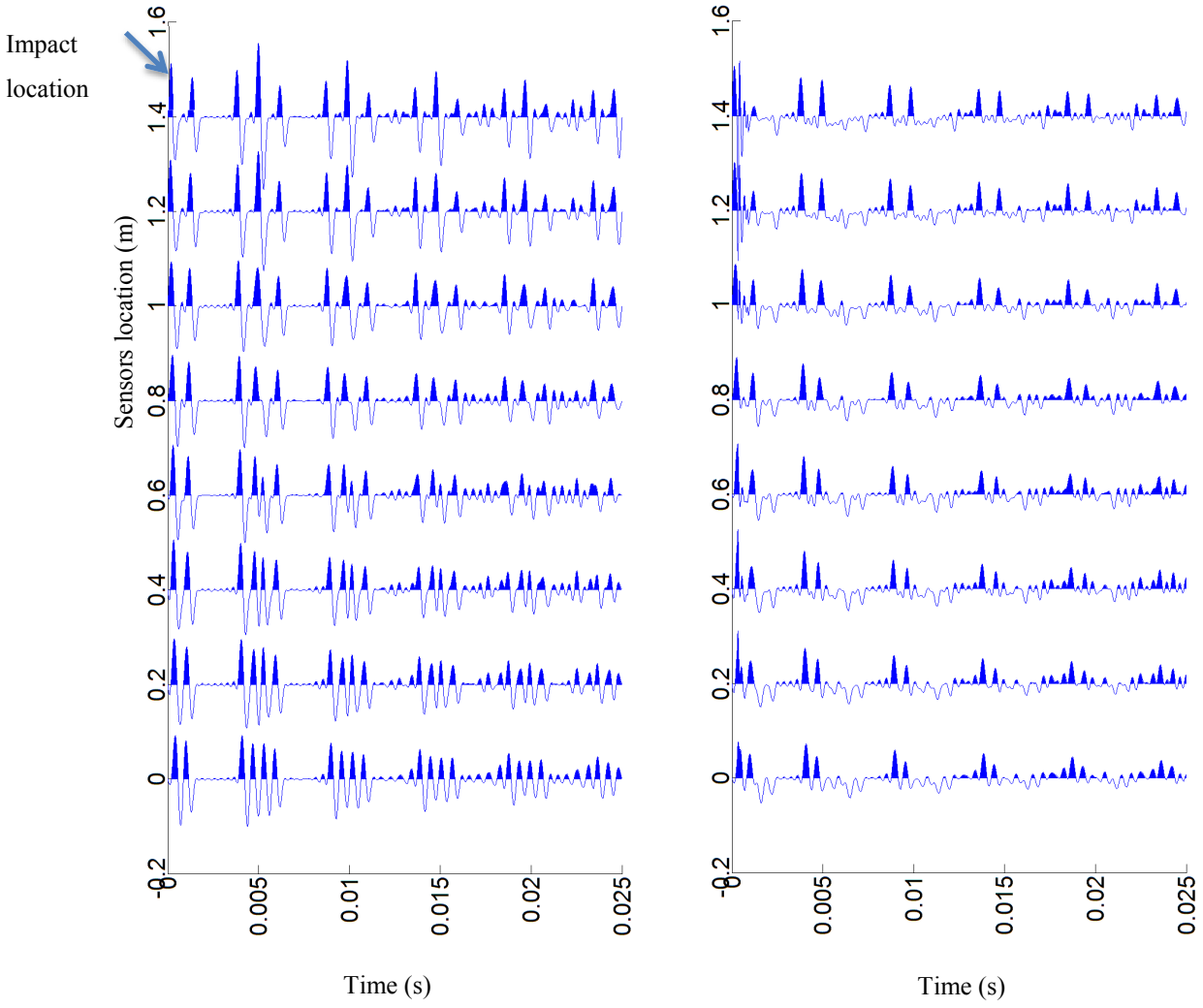

Figure 6.8: In-field sensors signals after (a) low-pass filtering, and (b) applying the predictive deconvolution for the simulated isotropic timber pole with standing-on-soil condition

The predictive deconvolution effectiveness in cleaning the unwanted patterns from the signal can easily be seen in this figure. The output of the predictive deconvolution can directly be used for the velocity analysis and the length estimation. Figure 6.9 and Figure 6.10 illustrate the velocity analysis and the length estimation procedures.

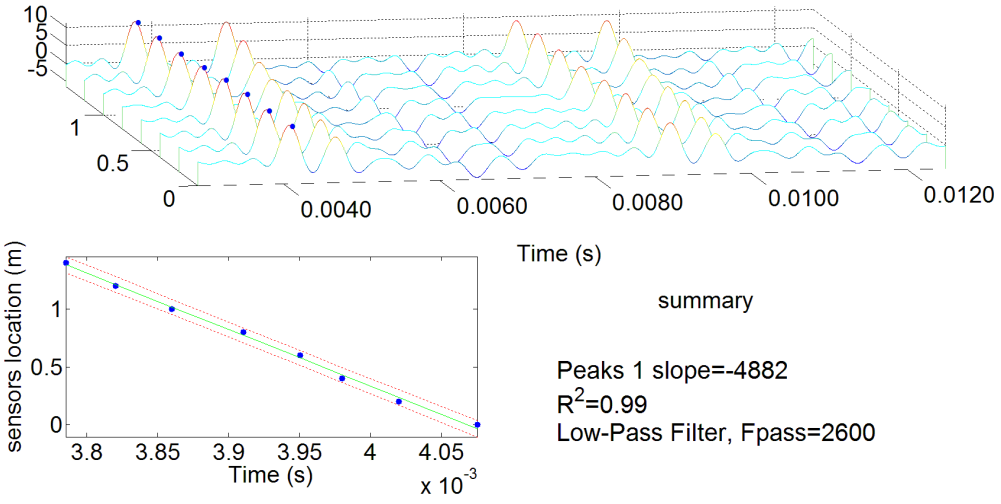

(a)

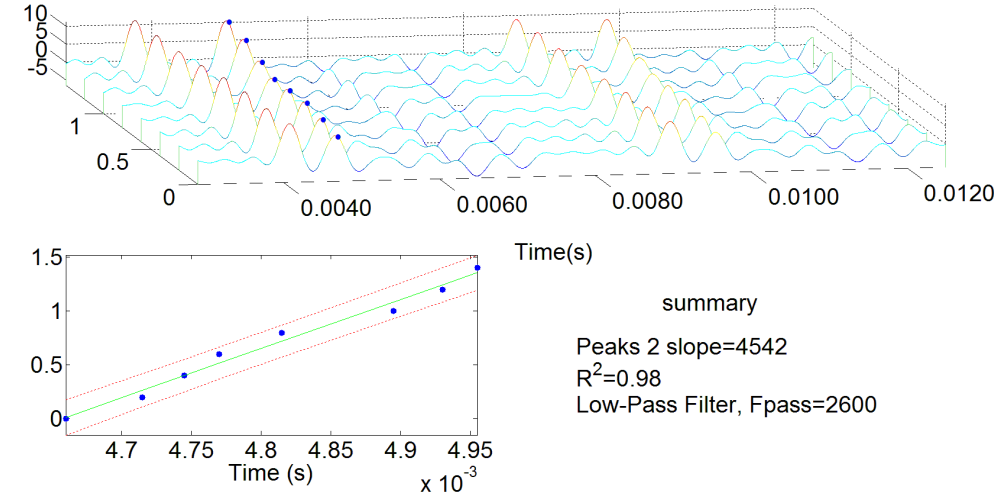

(b)

Figure 6.9: Velocity analysis procedures for (a) the first arrivals, and (b) the reflection peaks for the simulated isotropic timber pole with the standing-on-soil condition

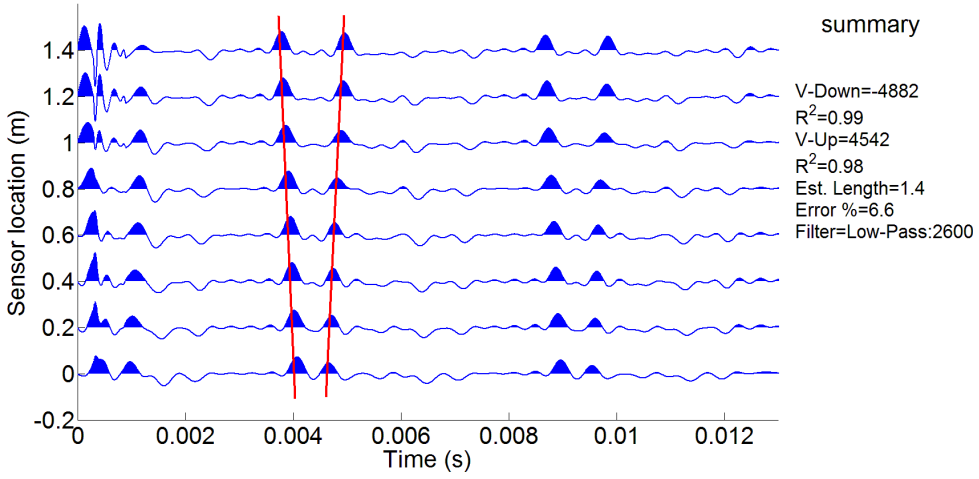

Figure 6.10: Length estimation procedures for the simulated isotropic timber pole with standing-on-soil condition

The down-going and the reflection waves' velocities are estimated with 99% and 98% fitting accuracies. The length of the pole is also estimated by crossing the two lines related to the down-going and the reflection waves with 6.6% error.

Figure 6.11 is the Frequency-Wavenumber (F-K) domain illustration of the low-pass filtered signals. The F-K domain illustration of the predictive deconvolution outputs has not been provided here because of its similarities with the low-pass filtered signals F-K domain illustration. It is worth mentioning that the F-K domain analysis is actually a velocity filter. In this regard, since both of the filter and the predictive deconvolution outputs have the same velocities, their F-K domain illustrations are also the same.

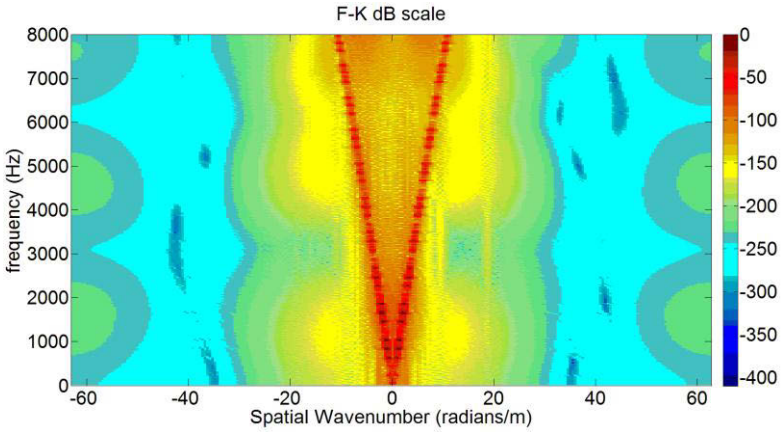

Figure 6.11: Frequency-Wavenumber (F-K) domain illustration of the low-pass filtered signals for the simulated isotropic timber pole with the standing-on-soil condition

As can be seen in Figure 6.11, only one velocity exists as expected. Based on the analytical solutions of the wave-guide theory in the cylindrical timber poles with the isotropic material properties, both of the longitudinal and the bending waves in the frequency range of 0-8 kHz have only one branch. Furthermore, since the bending wave's velocity is noticeably lower than the longitudinal one and attenuation in the bending wave is considerably large, only one velocity is observable in the F-K domain. It should be considered that the hammer excites the timber pole in the frequency range of 0-5 kHz.

6.2.2 Isotropic Embedded in soil

Figure 6.12 shows the captured signals in all of the 241 sensors before and after low-pass filtering.

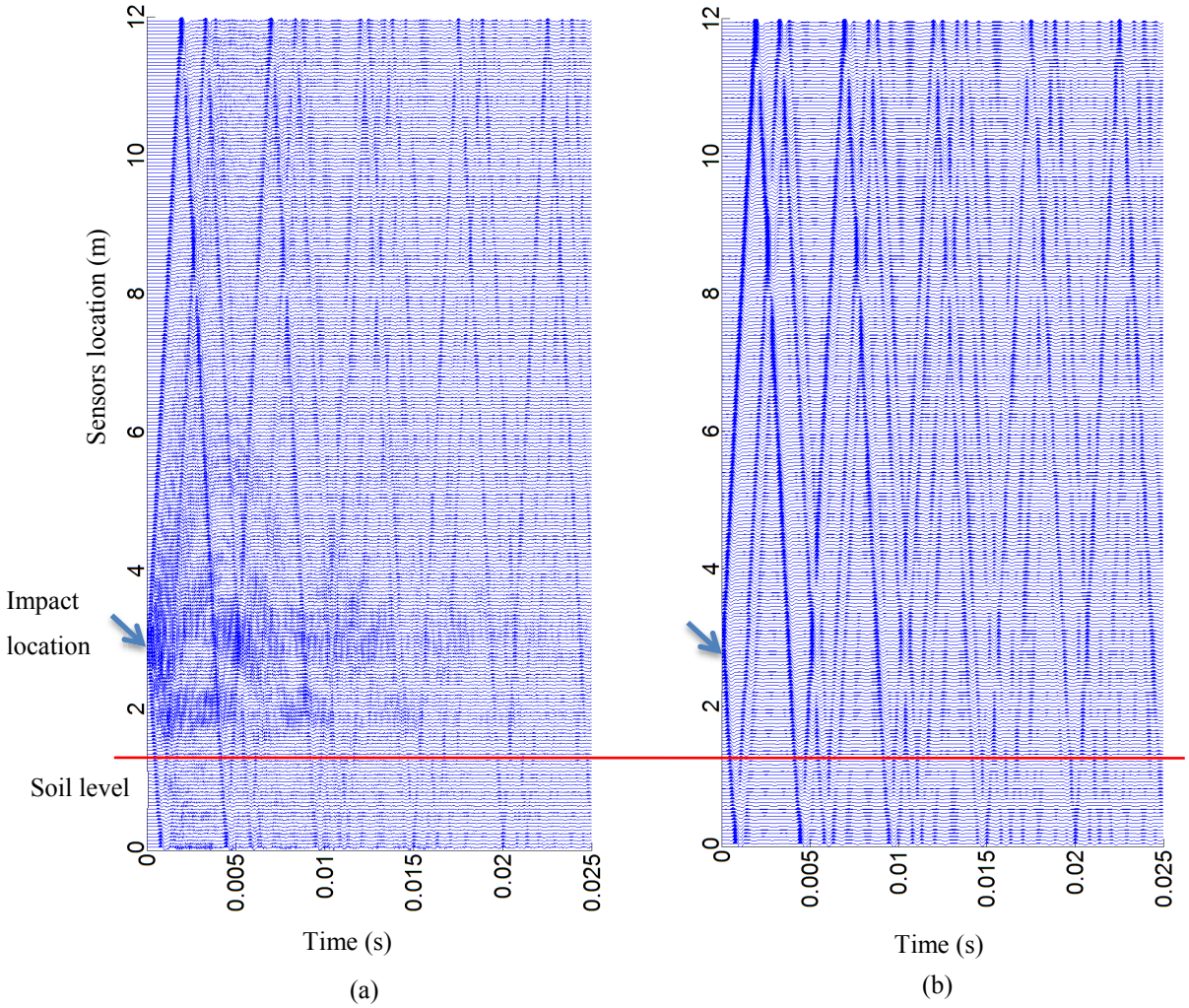

Figure 6.12: Captured signal in all of the 241 sensors (a) before and, (b) after the low-pass filtering for the simulated isotropic timber pole with the embedded condition

Although the upward and downward travelling waves' patterns are relatively observable in Figure 6.12(a), applying the low-pass filter could considerably clear the signals. Figure 6.13 also illustrates the captured signals by the in-field sensors before and after the low-pass filtering.

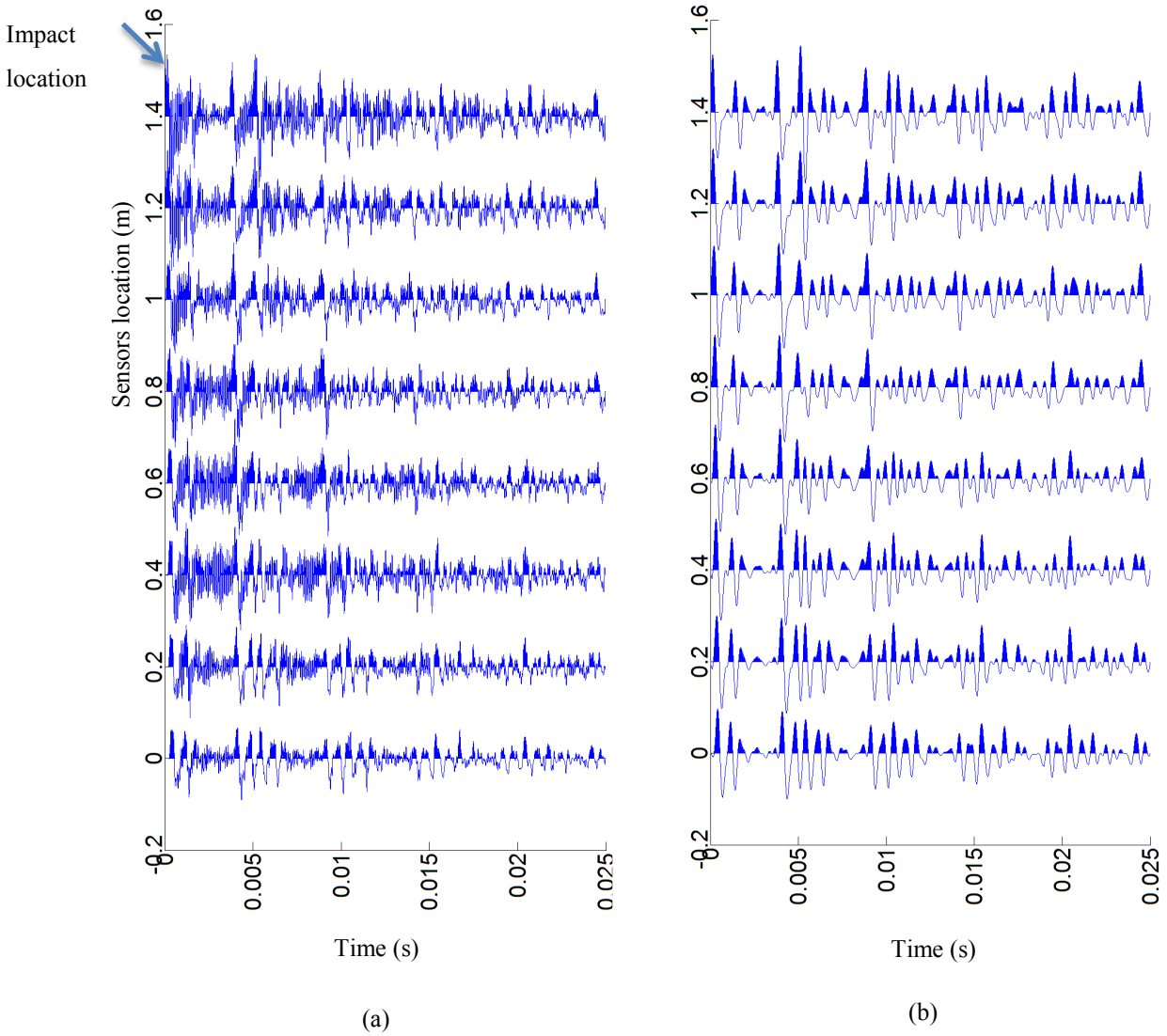

Figure 6.13: Captured signals by the in-field sensors (a) before, and (b) after the low-pass filtering for the simulated isotropic timber pole with the embedded condition

Figure 6.14 and Figure 6.15 demonstrate the predictive deconvolution outputs in all of the 241 sensors and the in-field sensors.

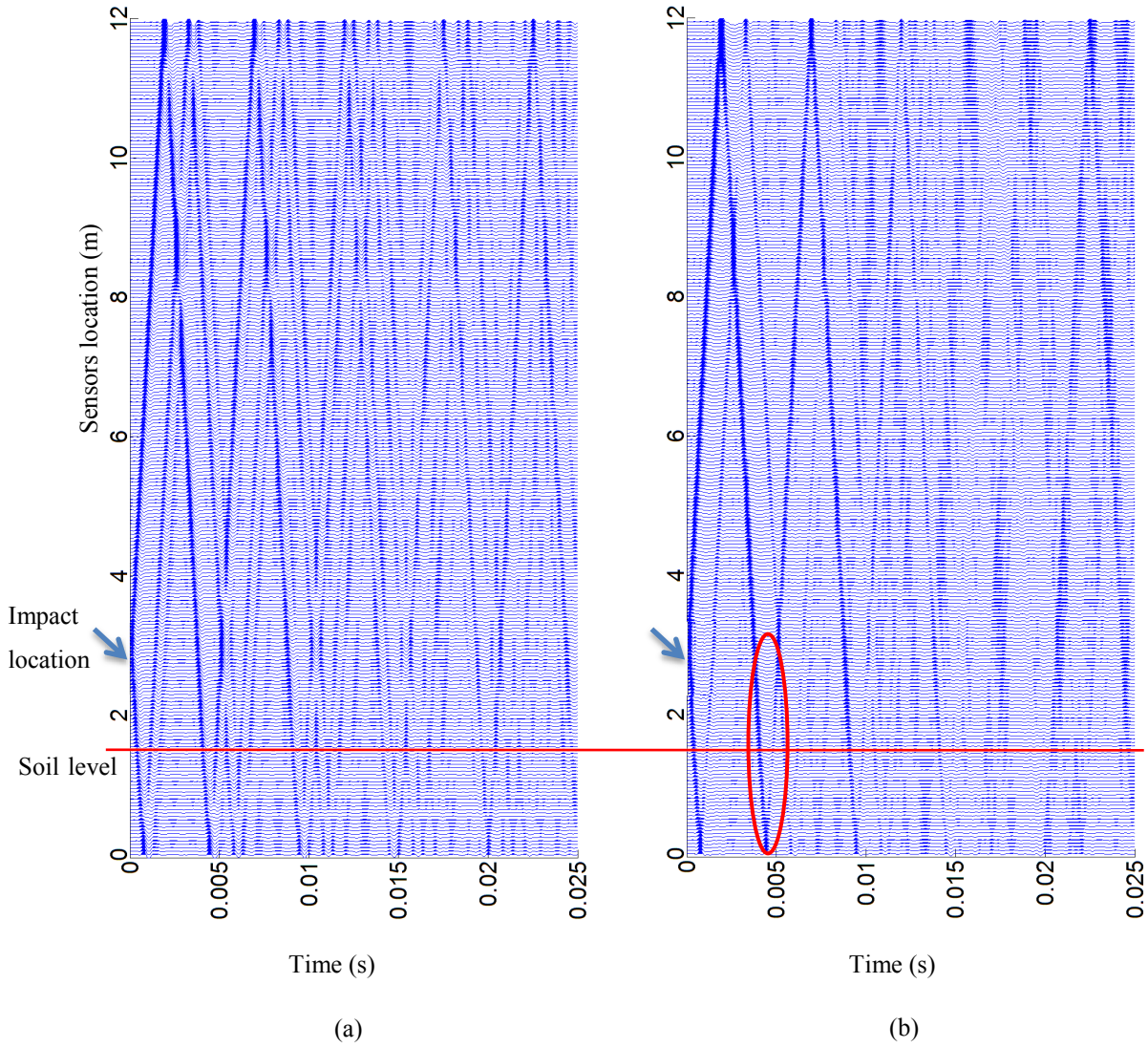

Figure 6.14: Ultraseismic plot of (a) the low-pass filtered data, and (b) the outputs of the predictive deconvolution on the 241 sensors for the simulated isotropic timber pole with the embedded condition

It can be seen in Figure 6.14 that the predictive deconvolution algorithm was able to reduce the signal of the downward travelling wave but was not able to remove it completely. Furthermore, only a weak pattern of bottom reflection is obtained (see the red oval in Figure 6.14). This is due to the presence of the soil embedment, which weakens the main bottom reflections. For better illustration the output of the predictive deconvolution vs. the filtered signal are also provided in Figure 6.16.

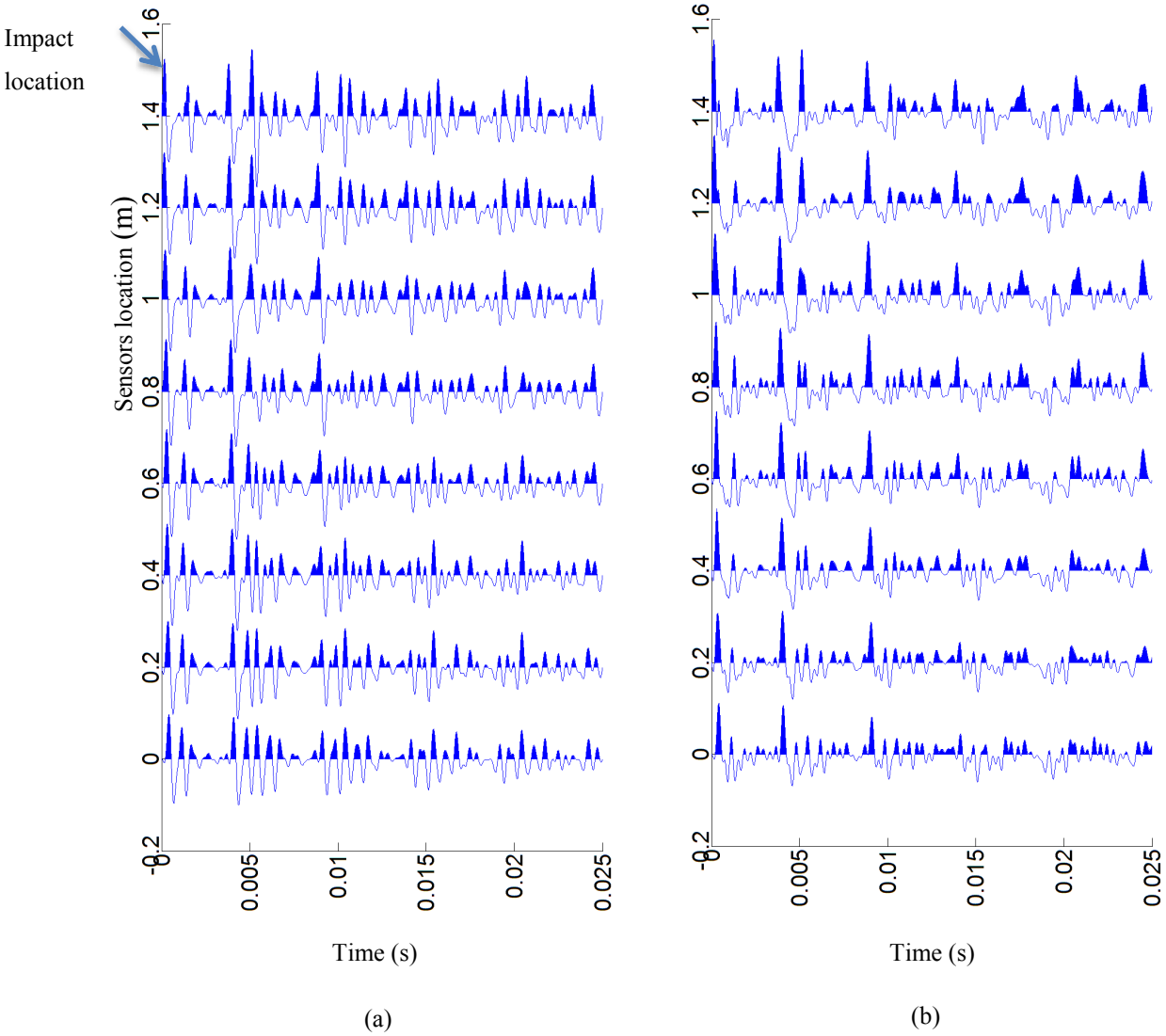

Figure 6.15: In-field sensors signals after (a) the low-pass filtering, and (b) applying the predictive deconvolution for the simulated isotropic timber pole with the embedded condition

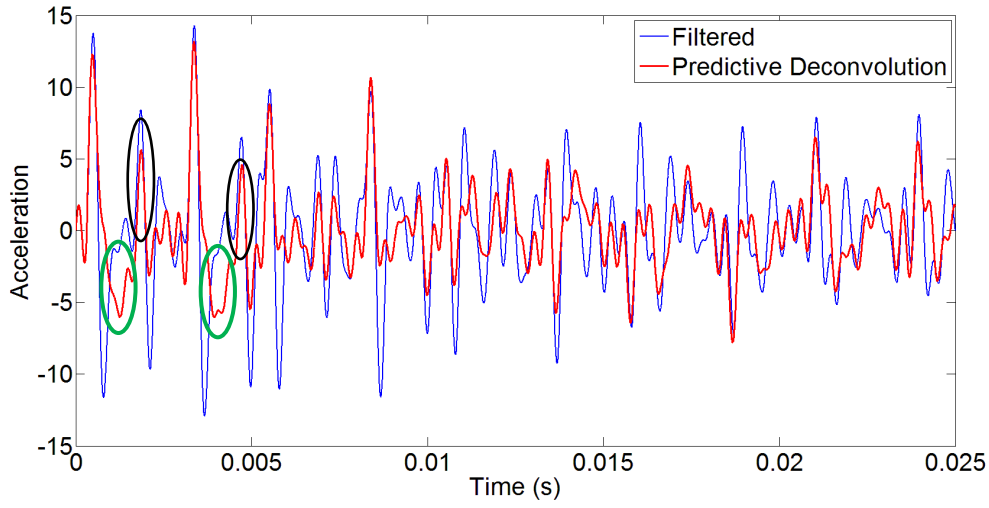

Figure 6.16: Low-pas filtered data before and after applying the predictive deconvolution in a single sensor for the simulated isotropic timber pole with the embedded condition

Comparing Figure 6.6 and Figure 6.16, one can simply see the amplitudes of the peaks related to the downward travelling (which was supposed to be removed completely) wave are relatively larger in the embedded condition. This means that the effectiveness of the predictive deconvolution has decreased in comparison to the isotropic standing-on-soil condition. The faulty peaks are also observable in Figure 6.16 (see the green ovals).

The velocity analysis and the embedment length estimation are provided in Figure 6.17 and Figure 6.18.

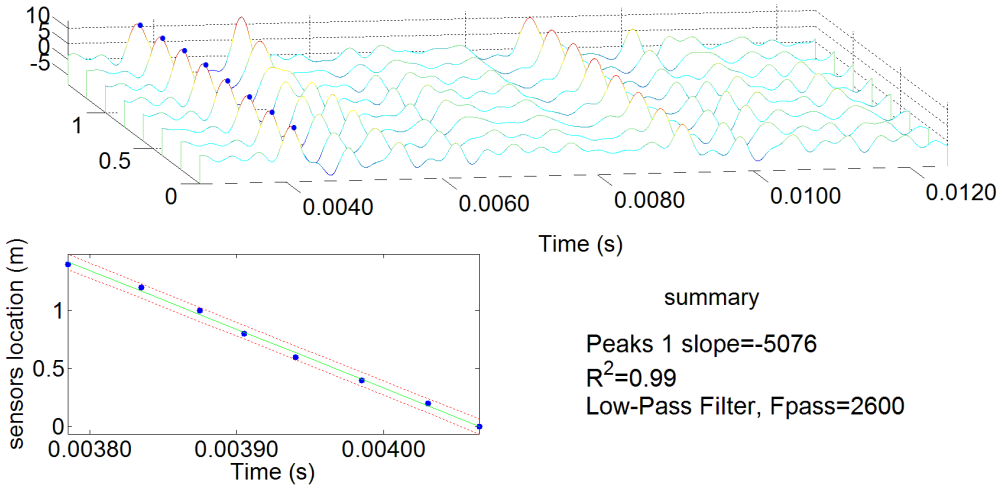

(a)

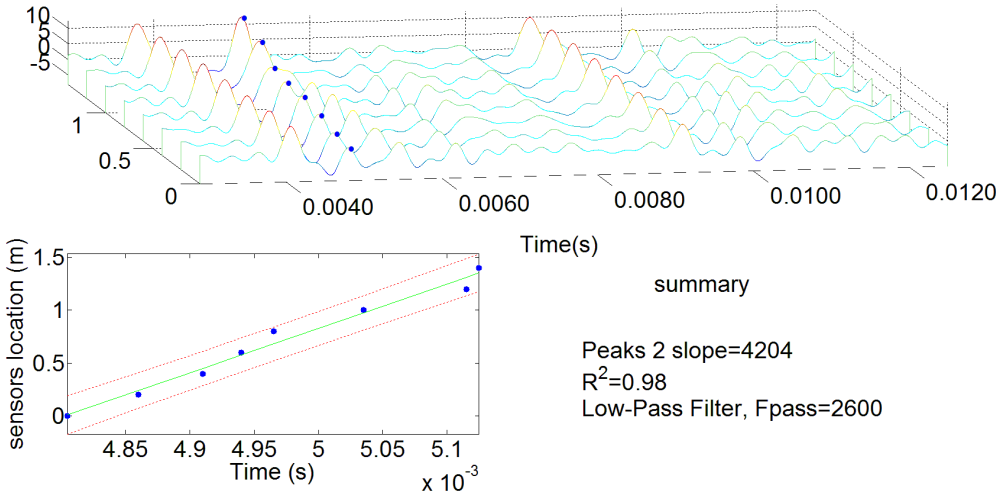

(b)

Figure 6.17: The velocity analysis procedure for (a): the first arrivals, and (b): the reflection peaks for the simulated isotropic timber pole with the standing-on-soil condition

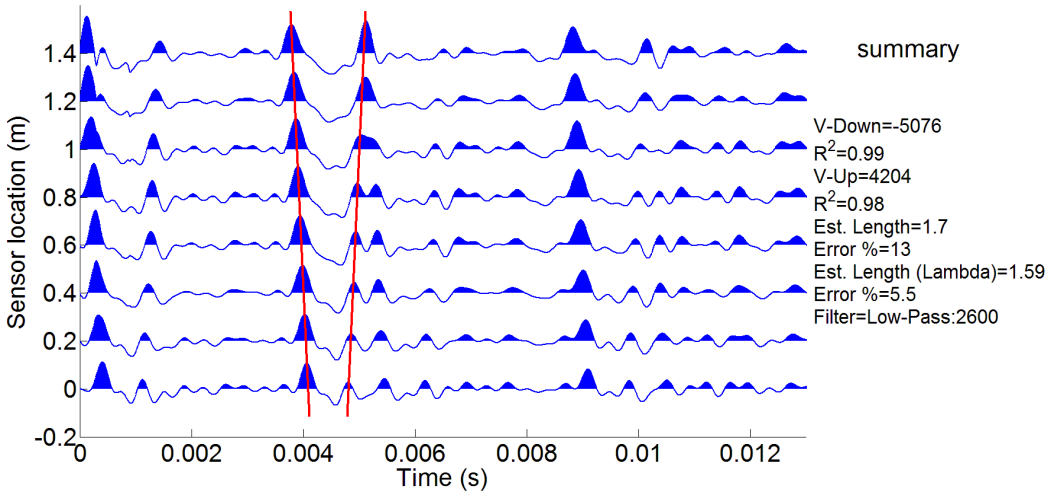

Figure 6.18: Length estimation procedure for the simulated isotropic timber pole with the embedded condition

As can be seen in Figure 6.17, the first arrivals and the reflection peaks' velocities are estimated with the 99% and 98% fitting accuracies. The embedment length is estimated with 13% error by using the two lines crossing method, while applying the decrement factor reduced the embedment length estimation error to 5.5%, which is less than half the earlier error.

The F-K domain illustration of this case is also provided in Figure 6.19. Once again, since the timber pole is simulated with the isotropic material properties only one velocity is observable in the F-K domain plot.

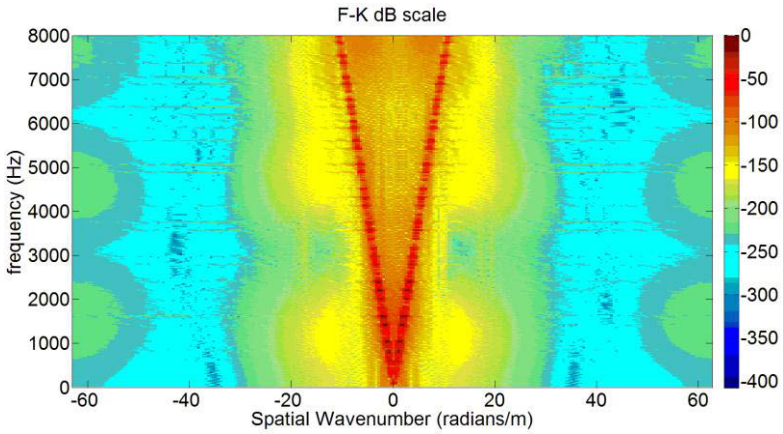

Figure 6.19: Frequency-Wavenumber (F-K) domain illustration of the low-pass filtered signals for the simulated isotropic timber pole with the embedded condition

6.2.3 Orthotropic embedded in soil

Figure 6.20 shows the captured signal in all of the 241 sensors before and after the low-pass filtering.

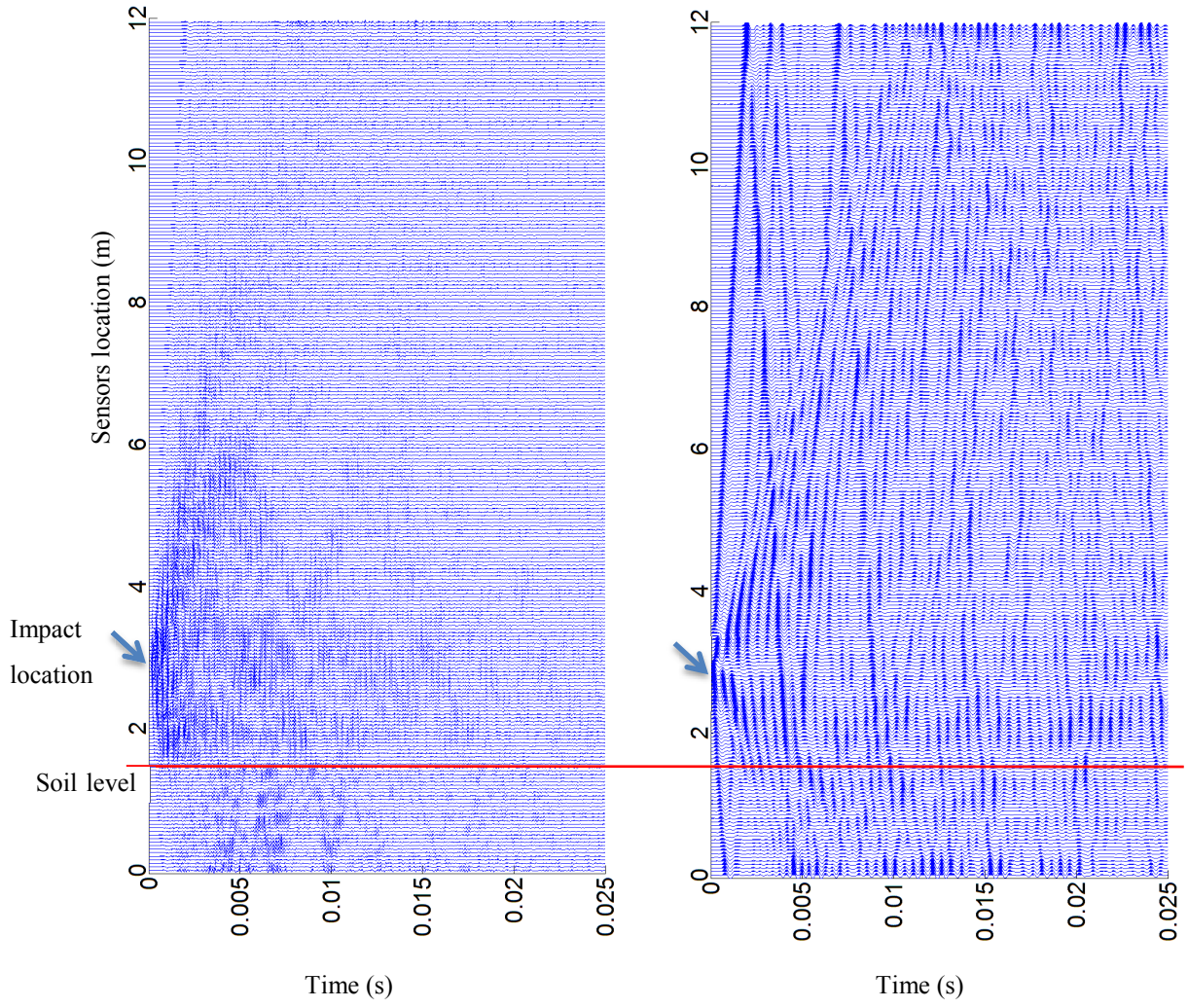

Figure 6.20 : Captured signal in all of the 241 sensors (a) before and, (b) after the low-pass filtering for the simulated orthotropic timber pole with the embedded condition

As can be seen in Figure 6.23 in the original signals, no clear pattern is recognizable, however applying the low-pass filter can clear the signals and reveals the patterns existing in them. It can also be seen that rather than the longitudinal waves' patterns, other patterns related to the bending waves also exist. Figure 6.23 illustrates the signals of the in-field sensors before and after the low-pass filtering.

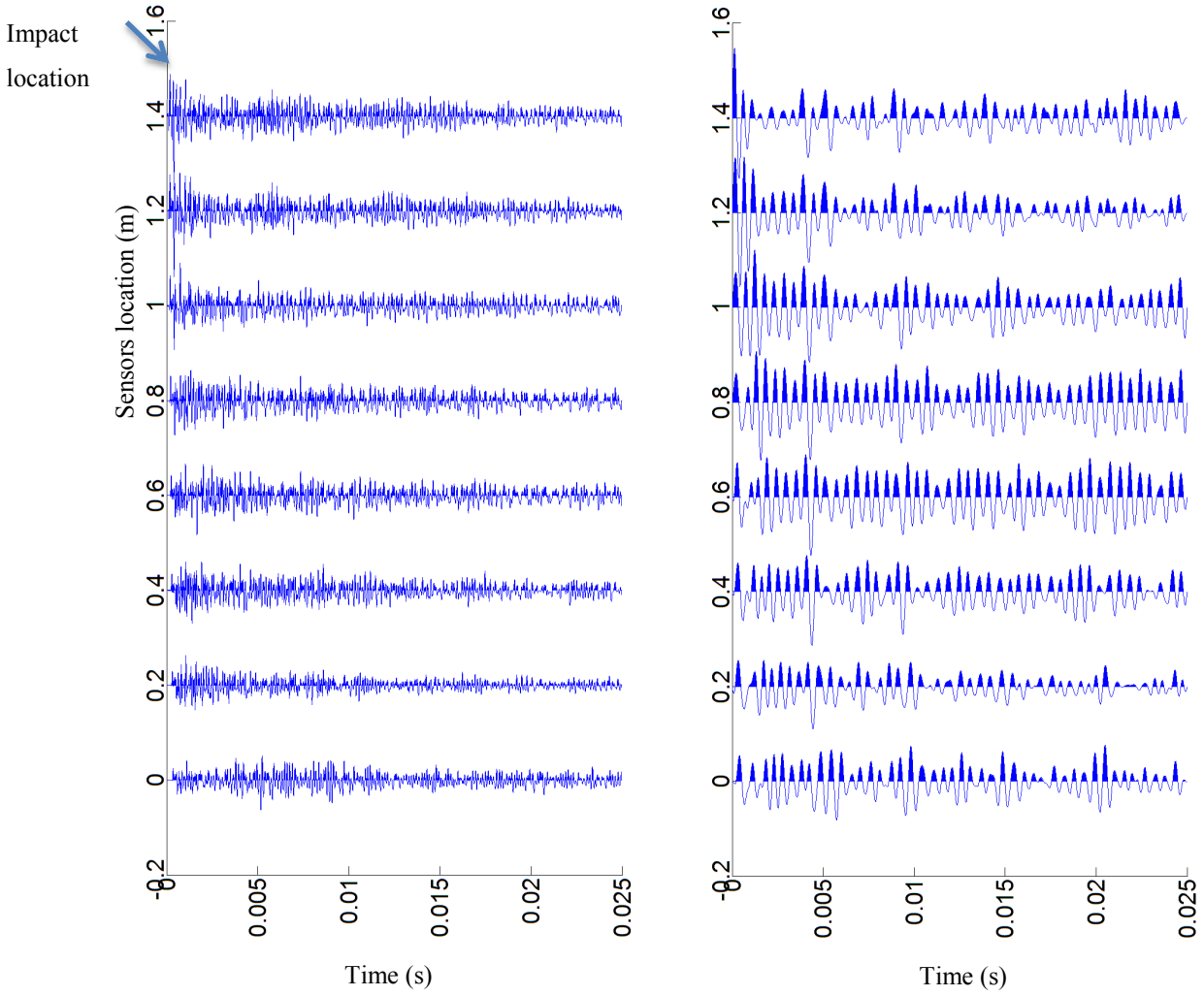

Figure 6.21 : Captured signals by the in-field sensors (a) before, and (b) after the low-pass filtering for the simulated orthotropic timber pole with the embedded condition

Figure 6.22 and Figure 6.23 demonstrate the predictive deconvolution outputs in all of the 241 sensors and in the in-field sensors.

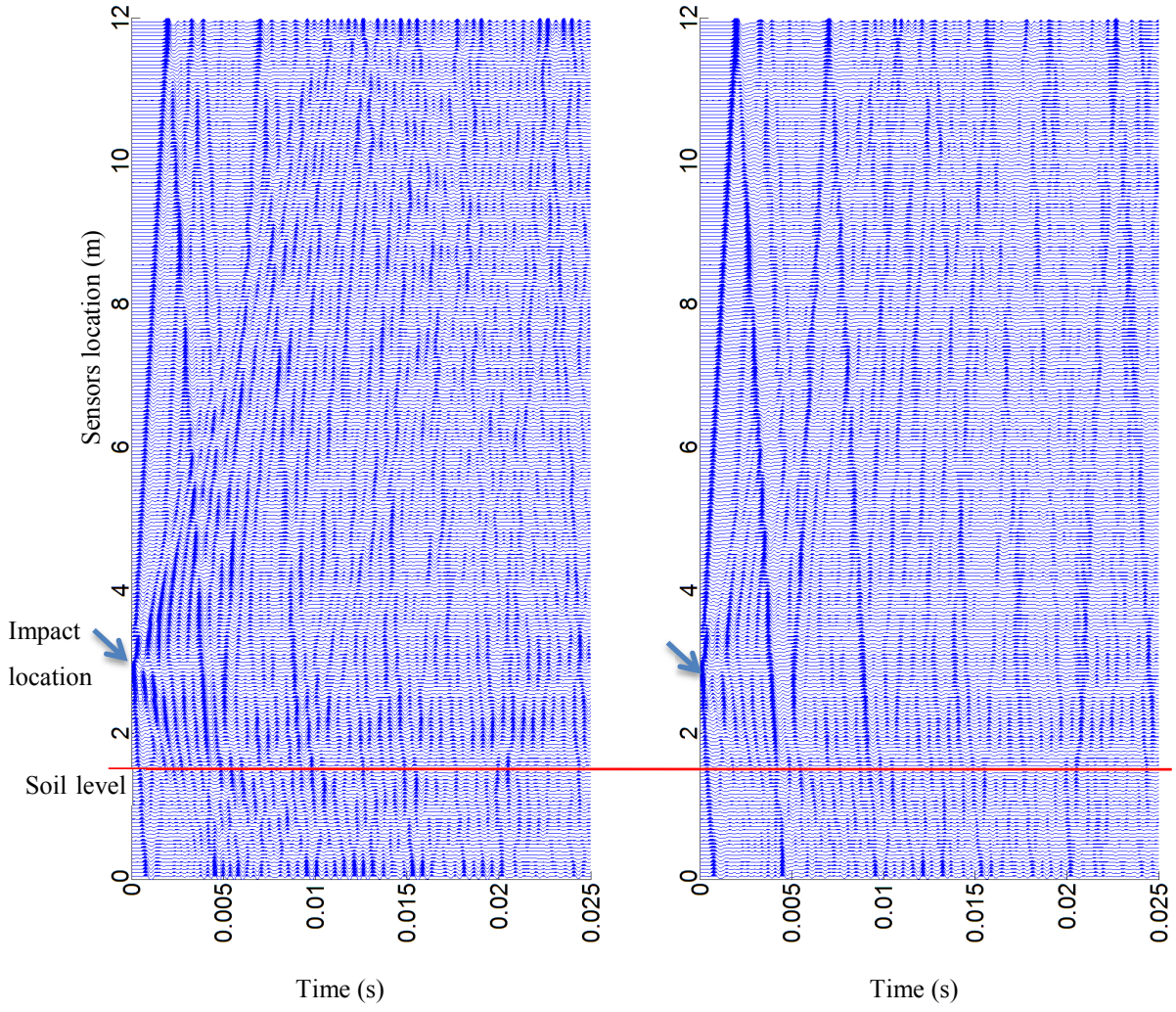

Figure 6.22: Ultraseismic plot of (a) the low-pass filtered data, and (b) the outputs of the predictive deconvolution on the 241 sensors for the simulated orthotropic timber pole with the embedded condition

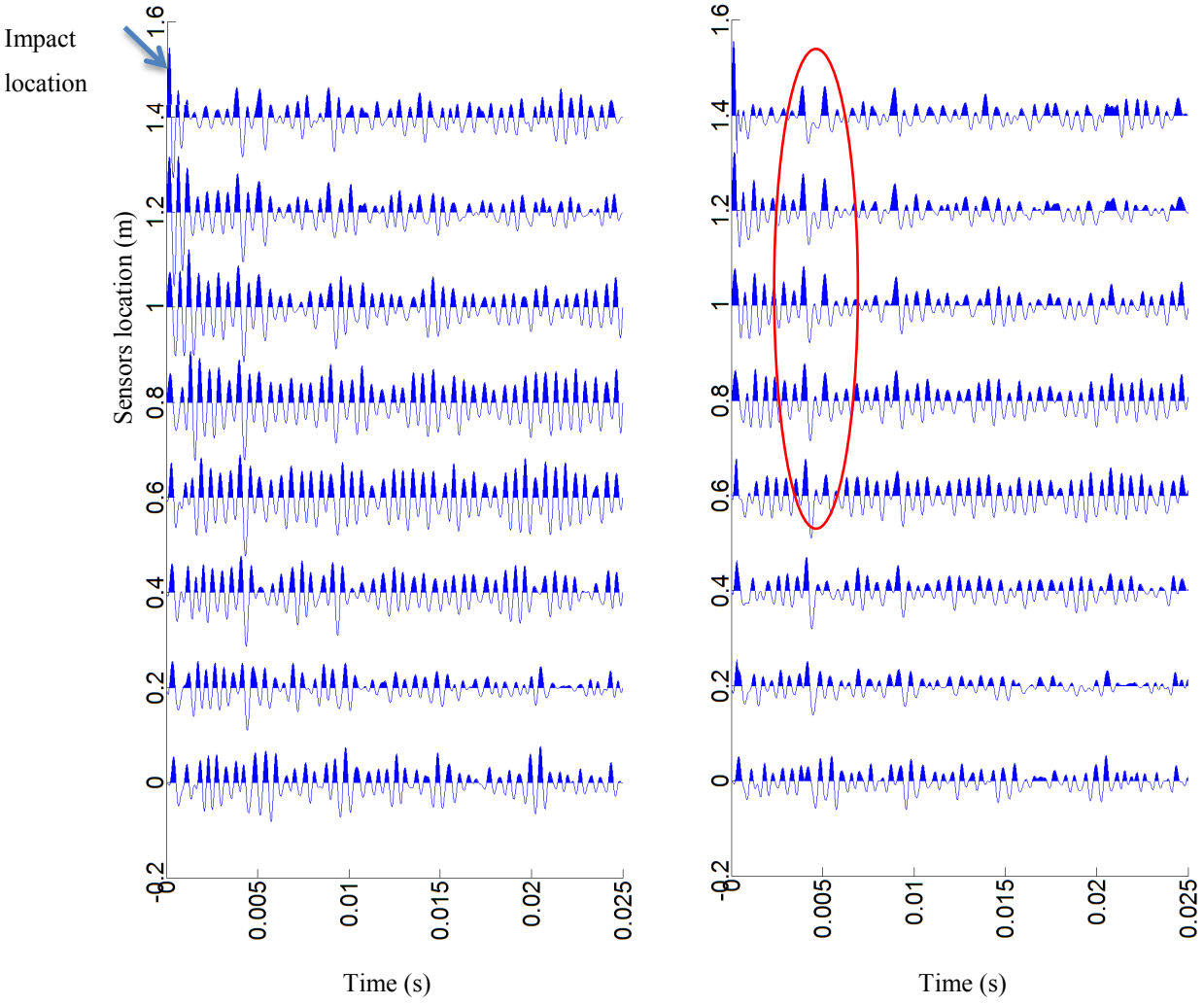

Figure 6.23: In-field sensors' signals after (a) the low-pass filtering, and (b) applying the predictive deconvolution for the simulated orthotropic timber pole with standing-on-soil condition

The pair of the peaks as is shown by the red oval in Figure 6.23 seems to be the first arrivals and the reflection peaks. The velocity analysis procedures of these set of the peaks are provided in Figure 6.24.

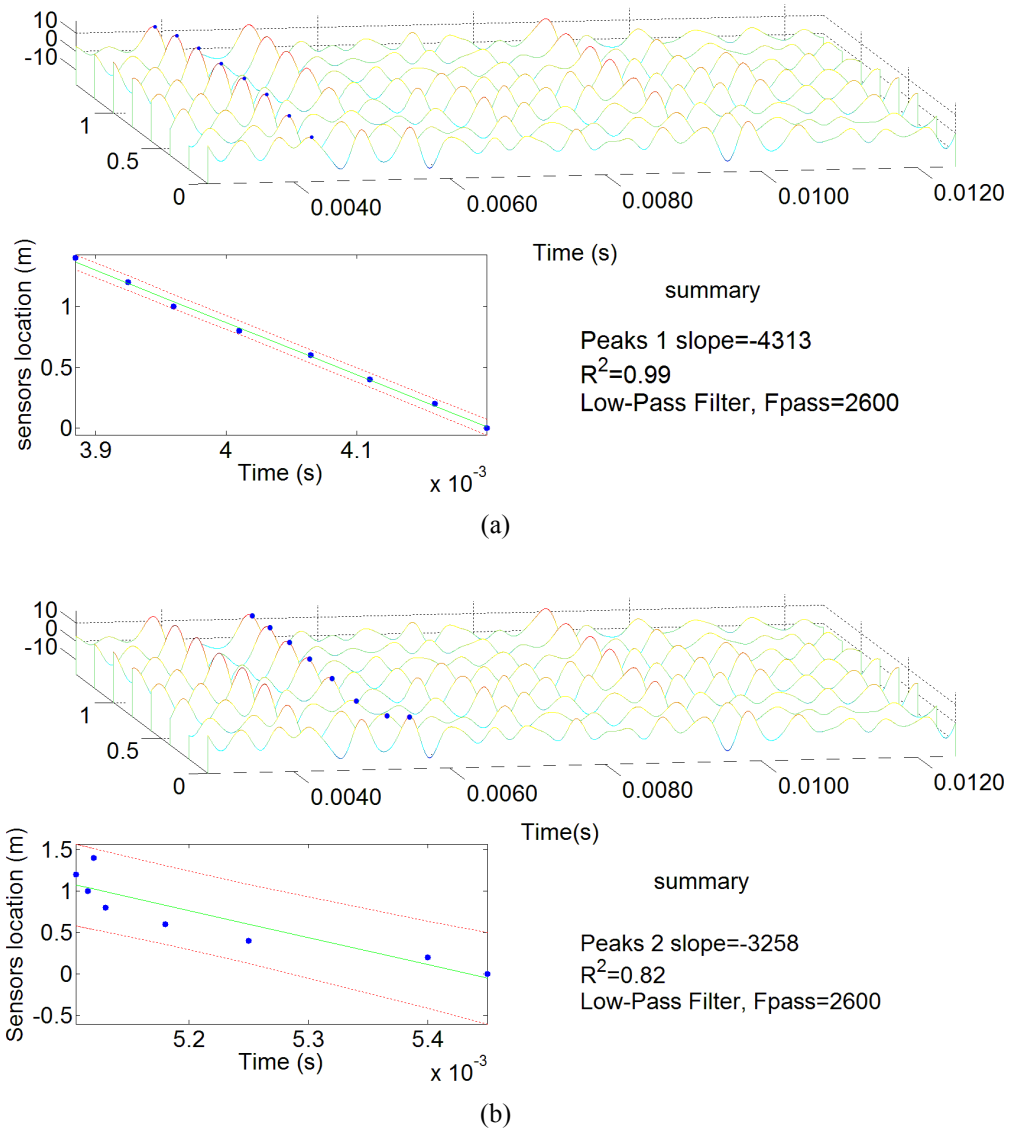

Figure 6.24: Velocity analysis procedures of the detected (a) first arrivals peaks, and (b) the reflection peaks after applying the predictive deconvolution for the simulated orthotropic timber pole with the embedded condition

As can be seen in Figure 6.24, since both of the velocities are negative, both sets of the peaks are related to the down-going waves and the detected second sets of the peaks are not related to the reflection from the bottom of the pole. By looking at the Figure 6.24, one can realize that the predictive deconvolution could only reduce the unwanted patterns and was not able to remove them completely. As mentioned earlier in Chapter 3, the predictive deconvolution assumes that the captured signal is wide-sense stationary while the captured signals from the simulated timber pole with the orthotropic material properties are non-stationary signals. This means that the statistical properties of the

original wavelets change as the waves are propagating through the pole. This is completely in concordance with the highly dispersive behaviour of the timber pole.

Figure 6.25 is the F-K illustration of the simulated orthotropic timber pole with the embedded condition.

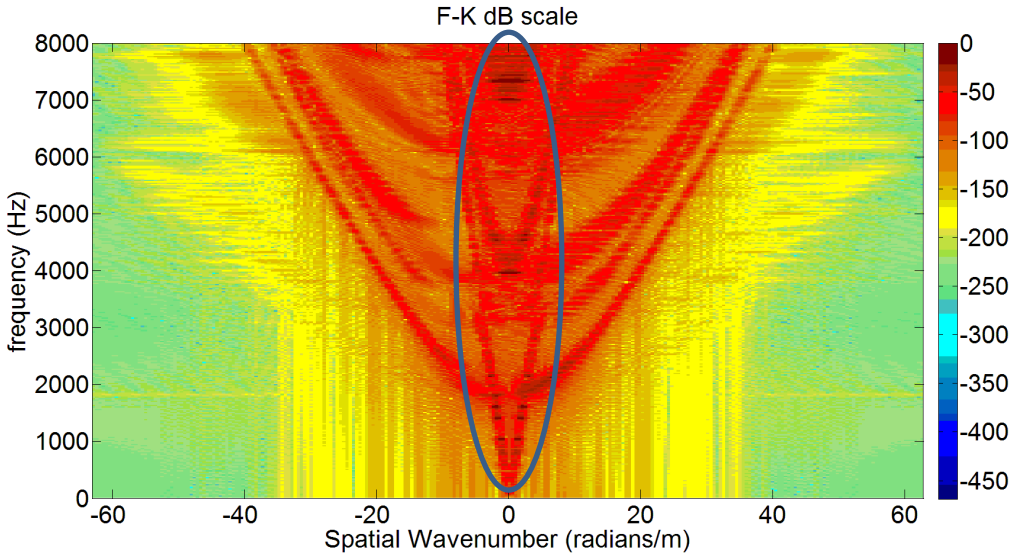

Figure 6.25: F-K illustration of the original data captured from the simulated orthotropic timber pole with embedded condition (the blue oval refers to the desired area to be preserved by the F-K velocity filter)

In Figure 6.25, velocities that are shown in the blue oval are related to the longitudinal waves. It can be seen that the second branch of the longitudinal wave has started from almost 4 kHz, and the third one has started from almost 7 kHz. The second branch of the bending wave is also started from almost 2 kHz (see Figure 2.12).

As previously mentioned, velocity filtering can be applied on the F-K domain. Based on the dispersion curves for the simulated orthotropic timber pole, the velocity of the longitudinal waves are around 5000 m/s. In this regard, a velocity filter is designed in a way to keep any existing velocities between 0-5000 (m/s) and remove the rest. Since the bandwidth of the desired region (the blue oval in Figure 6.25) is changing with the frequency, for each frequency component a Tucky window has been designed. Design procedure of the velocity filter is shown in Figure 6.26.

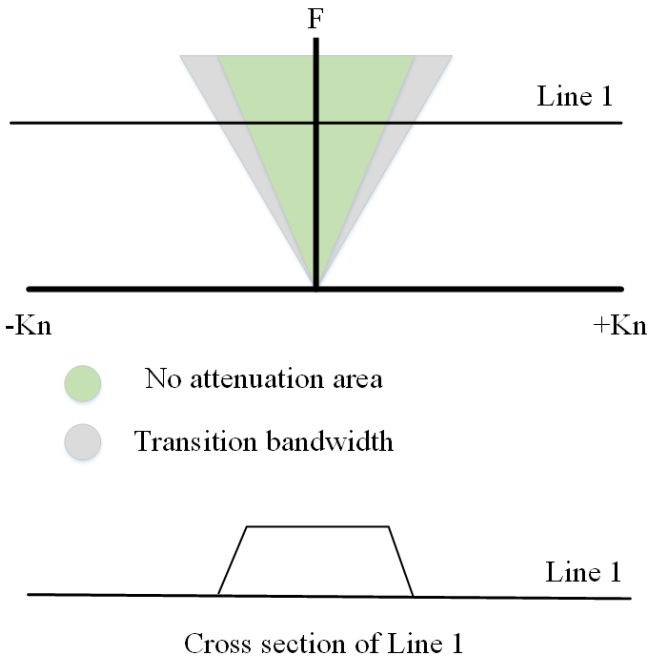

Figure 6.26 : Illustration of the Tucky windows design in the F-K domain velocity filtering

Figure 6.27 illustrates the results of the F-K velocity filter on the simulated orthotropic timber pole with the embedded condition. It can be seen that most of the undesired velocities in the F-K domain were removed. However, the second and the third branches of the longitudinal wave still exist.

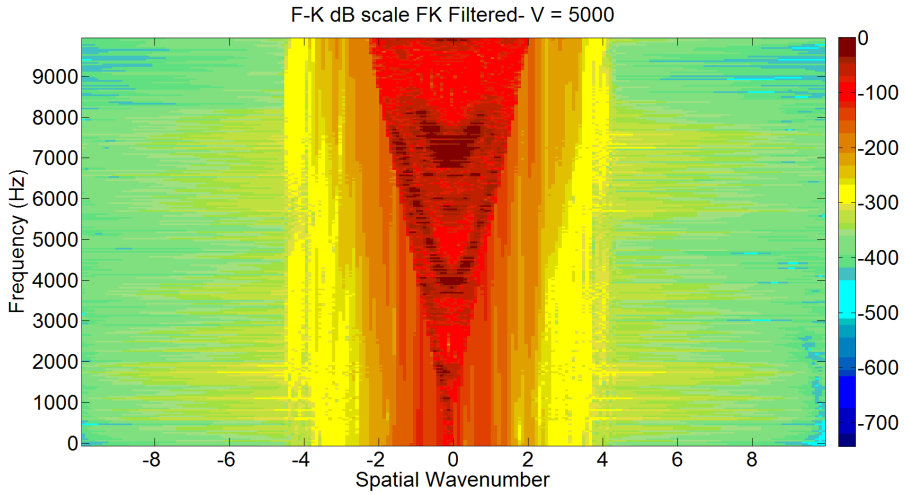

Figure 6.27: Results of the F-K velocity filter on the simulated orthotropic timber pole with the embedded condition

Figure 6.28 illustrates the outputs of the low-pass filtering and the velocity filtering outputs followed by the low-pass filtering. It can be seen in Figure 6.28 that only the

velocity components related to the longitudinal wave's branches exist as expected. For this reason, the low-pass filter in order to remove any unwanted high frequency components also filtered the outputs of the velocity filter.

Figure 6.28 demonstrates the outputs of the low-pass filter and the velocity filter followed by the low-pass filtering in the in-field sensors.

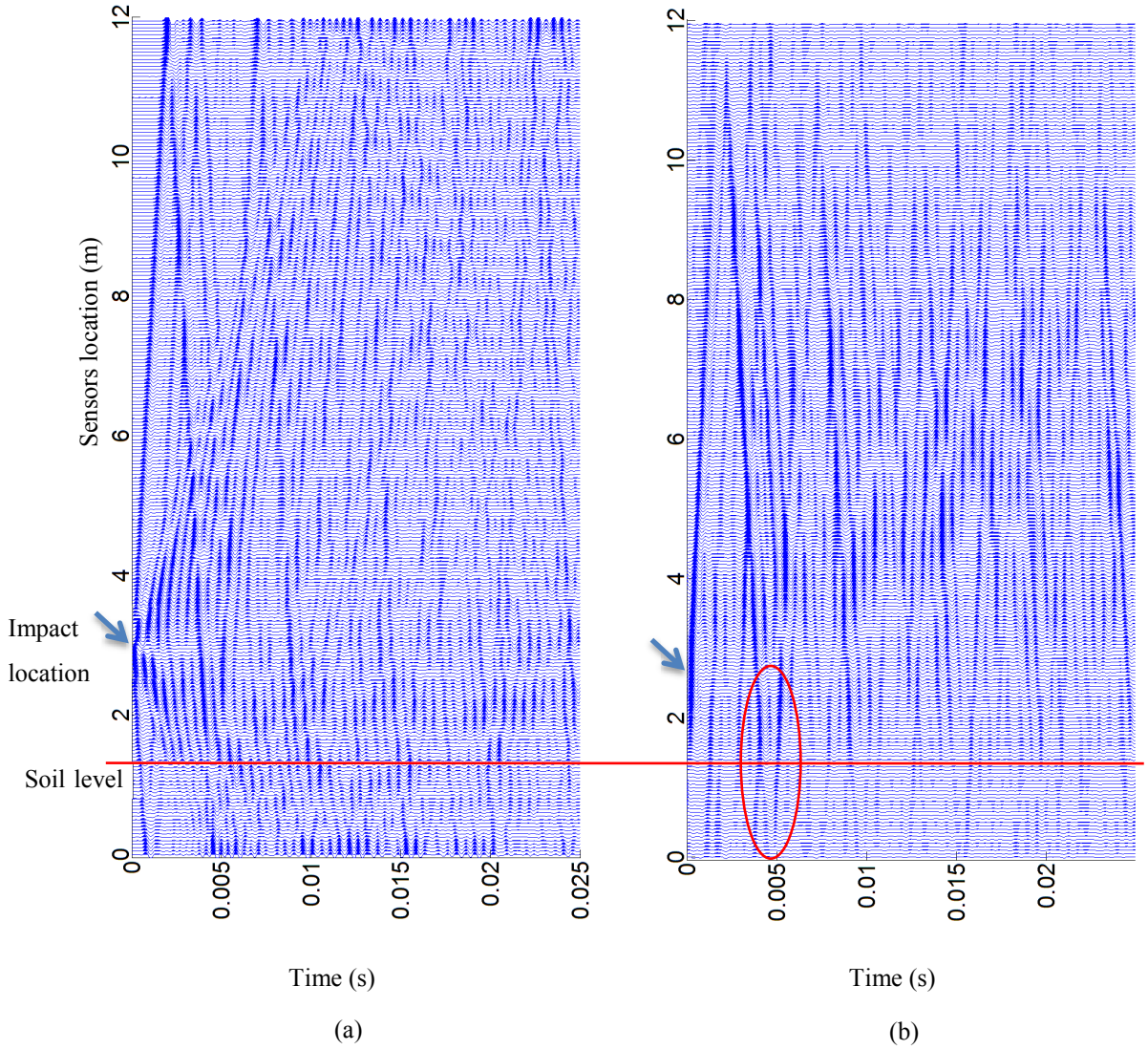

Figure 6.28: Outputs of (a) the low-pass filtering and (b) the velocity filtering outputs followed by the low-pass filtering in all 241 sensors for the simulated orthotropic timber pole with the embedded condition

As can be seen in Figure 6.28, although the velocity filter could remove all of the unwanted velocity components, it actually could not preserve the upward and downward travelling waves' patterns. It seems that the output of the velocity filter is the combination of the patterns of both of the upward and downward travelling waves. This

can be seen in the section highlighted by the red oval, where the reflection peaks belongs to one of the waves are interfering with the first arrivals of the other.

One alternative simple solution for removing all of the unwanted frequency and velocity components is applying the low-pass filter with 1.5 kHz cut-off frequency (see Figure 6.25). The outputs of the low-pass filtering with 1.5 kHz cut-off frequency in all of the 241 sensors are provided in Figure 6.29.

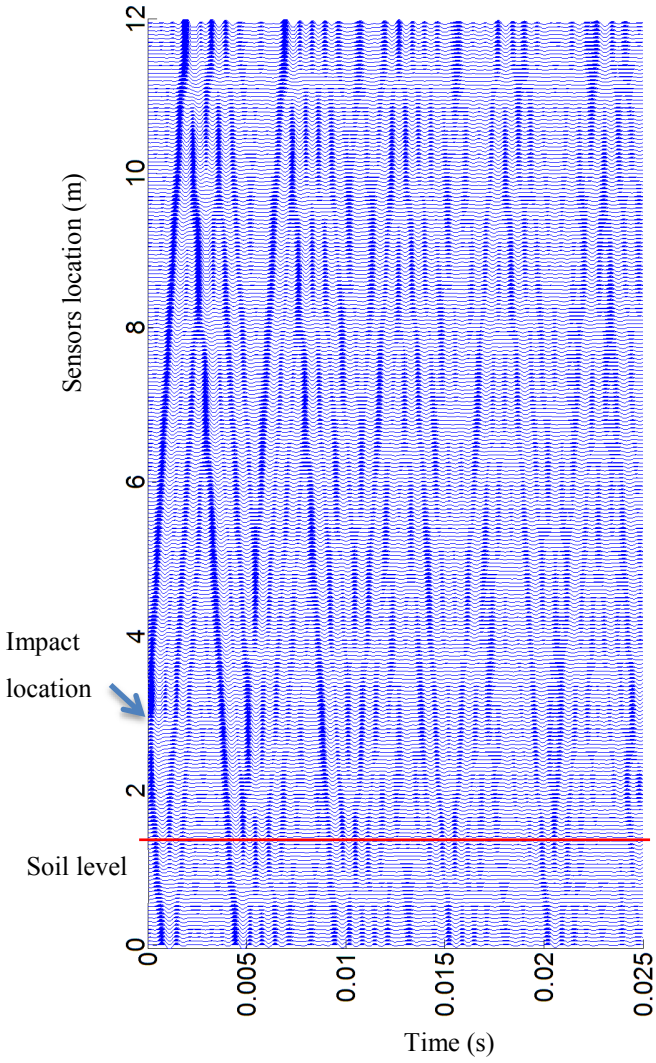

Figure 6.29: Outputs of the low-pass filtering with 1.5 kHz cut-off frequency in all of the 241 sensors for the simulated orthotropic timber pole with the embedded condition

As can be seen in Figure 6.29, this situation is very similar to the isotropic embedded case, of course as expected since only one velocity exists in the signals. Figure 6.30 shows the outputs of the 1.5 kHz low-pass filtering followed by the predictive

deconvolution. It can be seen in this figure that although the predictive deconvolution could remove the downward travelling wave, it weakened or in some sensors removed the reflection peaks (especially in sensors near the soil). The very weak detected reflection peaks are used for the velocity analysis and the embedment length estimation.

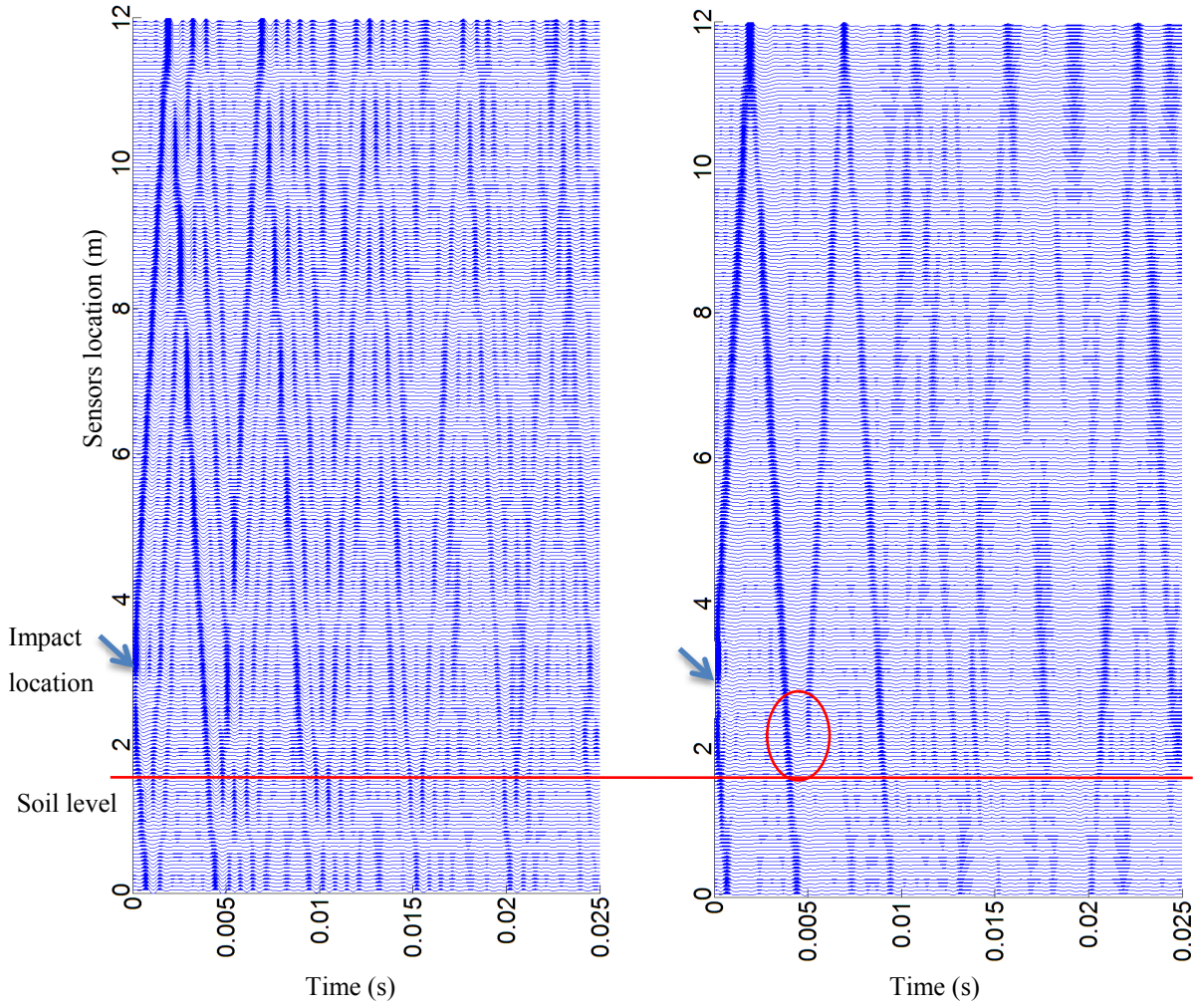

Figure 6.30: Outputs of (a) the 1.5 kHz low-pass filtering, and (b) the low-pass filtering followed by the predictive deconvolution for the simulated orthotropic timber pole with the embedded condition

The predictive deconvolution outputs in the range of the in-field tests are provided in Figure 6.31.

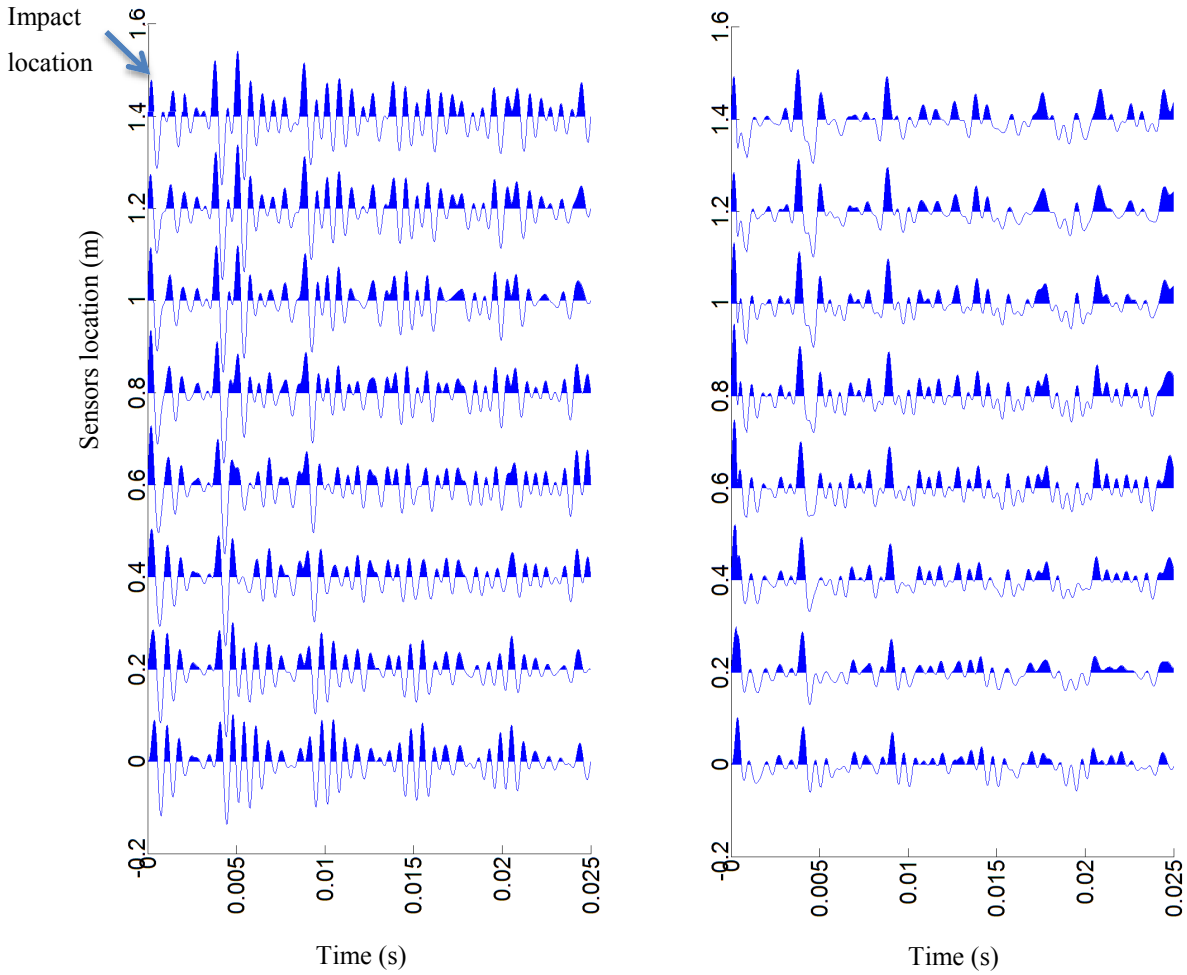

(a) (b)

Figure 6.31: Outputs of (a) the 1.5 kHz low-pass filter and (b) the predictive deconvolution in the range of the in-field tests for the simulated orthotropic timber pole with the embedded condition

The velocity analysis procedure is also illustrated in Figure 6.32.

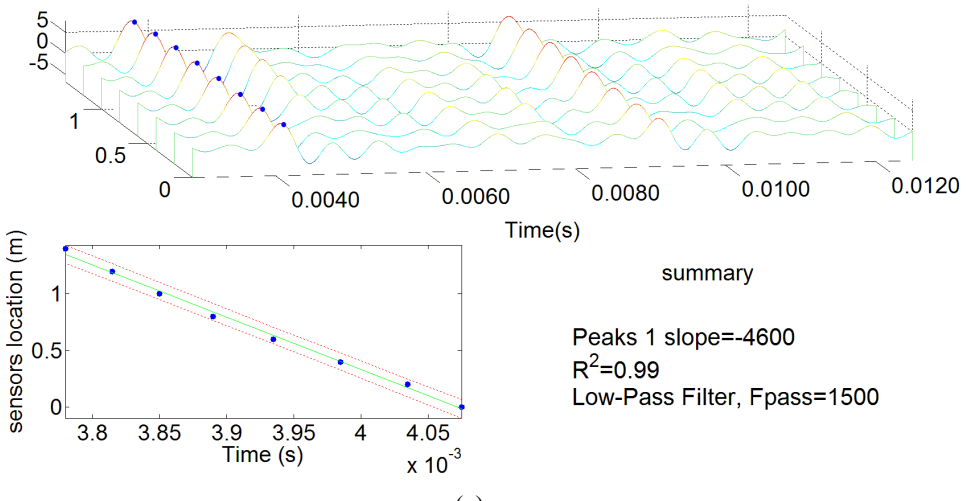

(a)

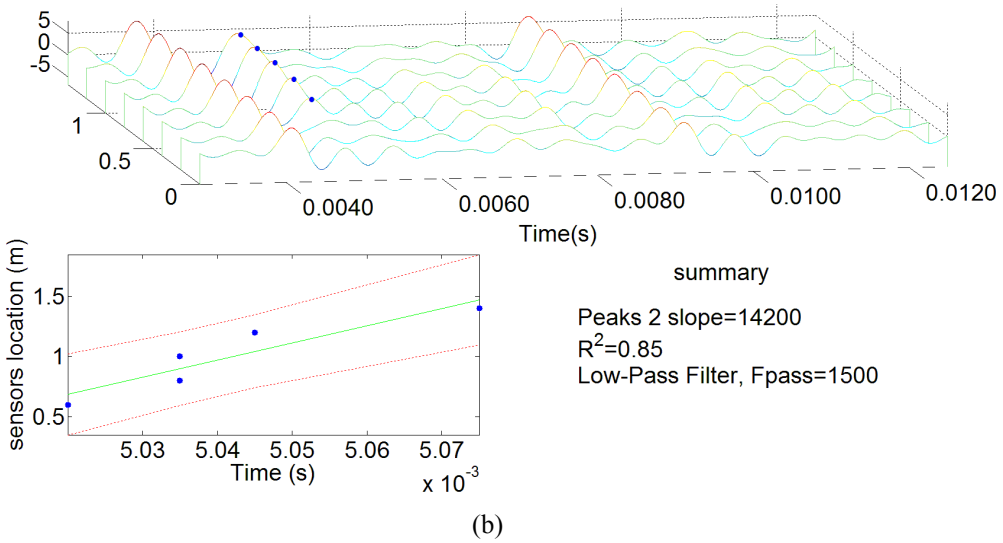

(b)

Figure 6.32: Velocity analysis procedure after the 1.5 kHz low-pass filtering followed by the predictive deconvolution for (a) the first arrivals, and (b) the reflection peaks for the simulated orthotropic timber pole with the embedded condition

It can be seen in Figure 6.32 that although the estimated velocity of the down-going wave is in the expected range, the velocity of the reflection wave is very considerably higher than usual. In the following, the possible reasons of this phenomenon are explained.

As mentioned earlier in Chapter 3, the timber pole is defined as a Linear Time-Invariant (LTI) system from the signal processing point of view. In this system, the excitation impact is the input and captured signals are the outputs. The outputs are related to the input through the transfer function of the system. Like any other LTI system, the transfer function can be studied in terms of its distortions. Defining the timber pole as the LTI system, amplitude and phase distortions are related to the damping of the system, and dispersion characteristics of the timber pole. In the following for a better understanding of the concept of dispersion, two very simple examples are presented. Firstly, one synthetic signal, which includes a broad range of frequencies from 1 Hz to more than 5 kHz is created and fed to one simple LTI system as an input (this LTI system can be a medium like steel, concrete or the timber pole). All of the frequency components of the synthetic signal are delayed when passed through this simple LTI system. This delay is different for different frequencies and is not amendable unless the LTI system has the property of causing a linear phase distortion. This means that the synthetic signal as a whole wave packet is delayed with a specific value while its shape

does not change. This is exactly the definition of the non-dispersive medium, in which the group velocity and the phase velocities are the same. On the other hand, in order to preserve the shape of the wave packet, all of the frequency components of the signal should travel the same distance in the same time. This is shown in Table 6.1. Only small ranges of frequencies are provided in this table.

Table 6.1: Illustration of the non-dispersive simple LTI system with the linear phase change property

Frequency (C/s)	Travel time (ms)	Velocity (m/s)	Travel distance (m)	Travel distance in 1 Cycle (m)	Phase delay as prop of a cycle
1	1	340	0.34	340	0.001
100	1	340	0.34	3.4	0.1
200	1	340	0.34	1.7	0.2
300	1	340	0.34	1.13	0.3
400	1	340	0.34	0.85	0.4
500	1	340	0.34	0.68	0.5
600	1	340	0.34	0.56	0.6
700	1	340	0.34	0.48	0.7
800	1	340	0.34	0.42	0.8
900	1	340	0.34	0.37	0.9
1000	1	340	0.34	0.34	1
1100	1	340	0.34	0.31	1.1
1200	1	340	0.34	0.28	1.2
1300	1	340	0.34	0.26	1.3
1400	1	340	0.34	0.24	1.4
1500	1	340	0.34	0.22	1.5
1600	1	340	0.34	0.21	1.6
1700	1	340	0.34	0.2	1.7
1800	1	340	0.34	0.18	1.8

If it is assumed that the assumed synthetic signal's group velocity is 340 m/s and travel time is 1 ms, then the wave packet travels 0.34 m. On the other hand, the travelled distance in one cycle for each frequency component is the velocity of that frequency

(i.e. 340 m/s) divided by the frequency itself (see "travelled distance in 1 cycle" column in Table 6.1). Finally, the phase delay that occurs to each frequency component can be calculated by dividing the total travelled distance (i.e. 0.34 m) to the travelled distance by one cycle, which is shown in the last column of the Table 6.1.

Figure 6.33 plots the phase changes vs. the frequency components. It can be seen that the phase change is linear.

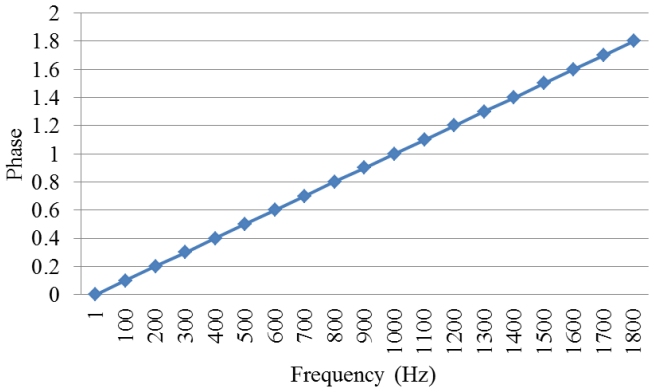

Figure 6.33: Phase changes vs. the frequency components in a simple non-dispersive LTI system

One of the simplest LTI systems that can cause the linear phase shift is the well-known FIR digital filter, which is fully explained in Chapter 3.

To continue of this simple example, one LTI system includes two FIR digital filters, where one causes linear and the other causes nonlinear phase shift, and the output of the overall system is the summation of these filters. This system is shown in Figure 6.34.

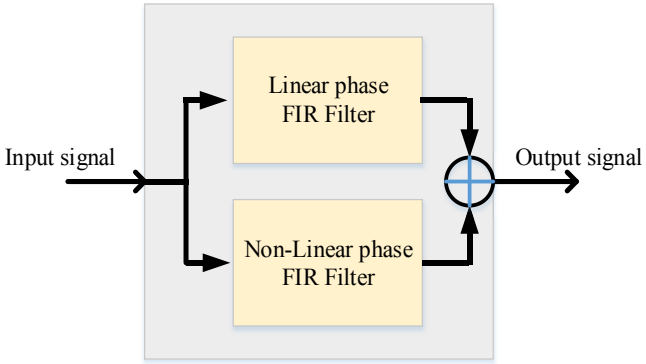

Figure 6.34: Simple LTI system includes one LTI system with the linear phase and the other with the nonlinear phase distortions

Considering the assumed LTI system, a single frequency sinusoidal signal is fed to the system as an input. Magnitude and Phase responses of both filters of the LTI system are shown in Figure 6.35.

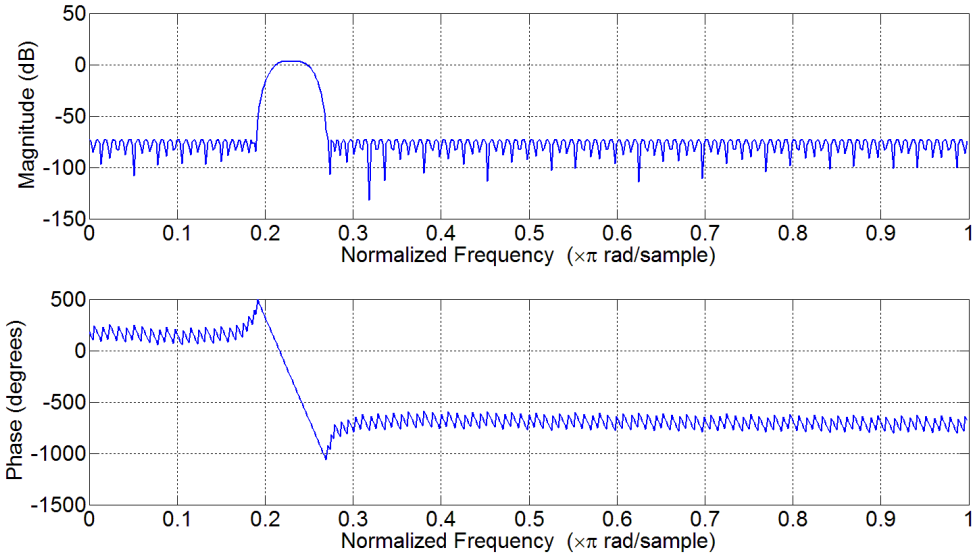

(a)

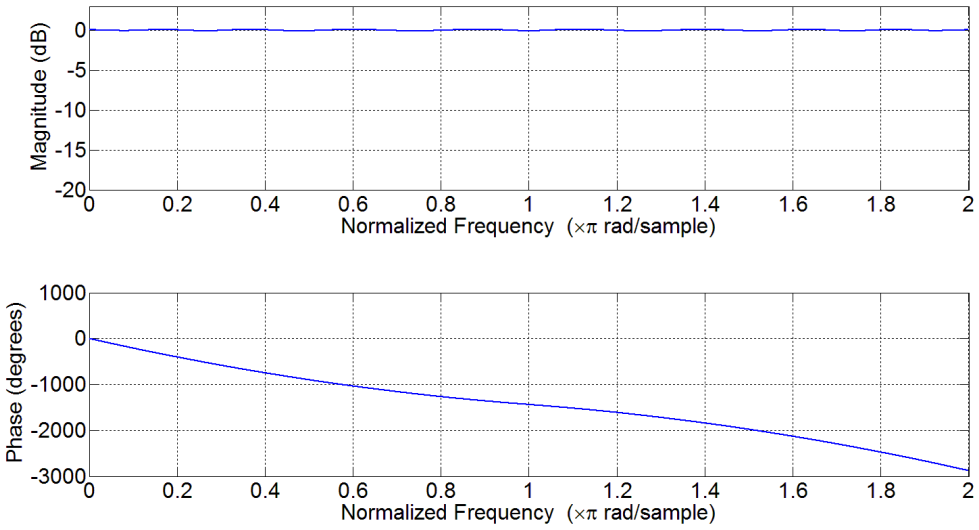

(b)

Figure 6.35: Magnitude and the phase responses of (a) the FIR filter with non-linear phase shift, and (b) the FIR filter with linear phase shift

As mentioned earlier, each of the FIR filters will cause a phase shift. Figure 6.36 and Figure 6.37 show the sensitivity of the overall LTI system output to the both filters' phase changes. Figure 6.36 shows the case where phase changes caused by both of the systems are not completely overlapping but weakening each other. Figure 6.37 shows

the situation where almost full overlapping occurs, and as a result, no signal can be seen in the output after a specific time. It can be seen in both of the figures that in the case of the simultaneous phase changes (even linear and non-dispersive system), phase changes can jeopardize the results when two signals weaken or completely remove each other and as a consequence, some peaks will be lost. Furthermore, the situation is worse when one or more of the phase changes are nonlinear (system is dispersive).

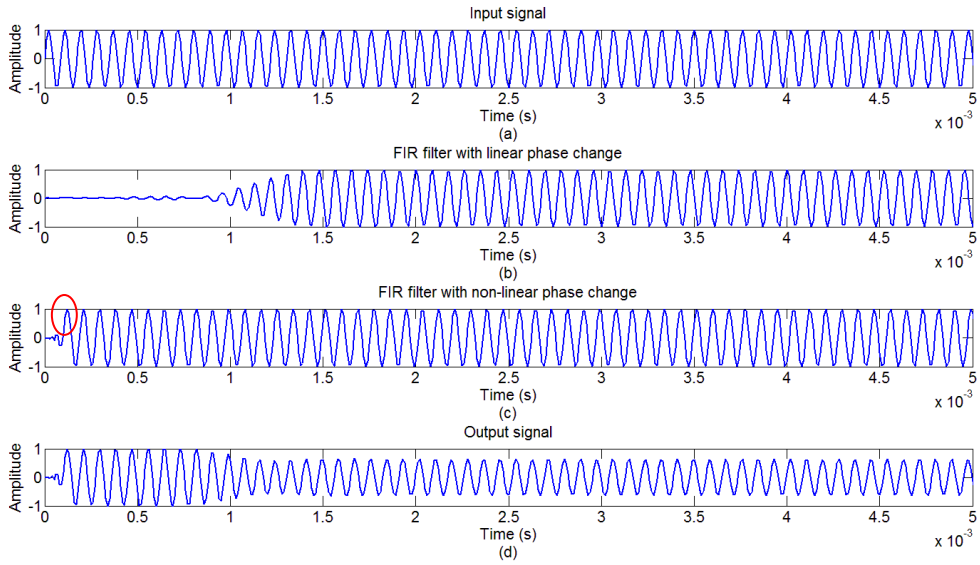

Figure 6.36: Illustration of (a) the LTI system input, the outputs of the FIR filter with (a) linear, and (b) non-linear phase shifts, and (d) the overall output of the LTI system

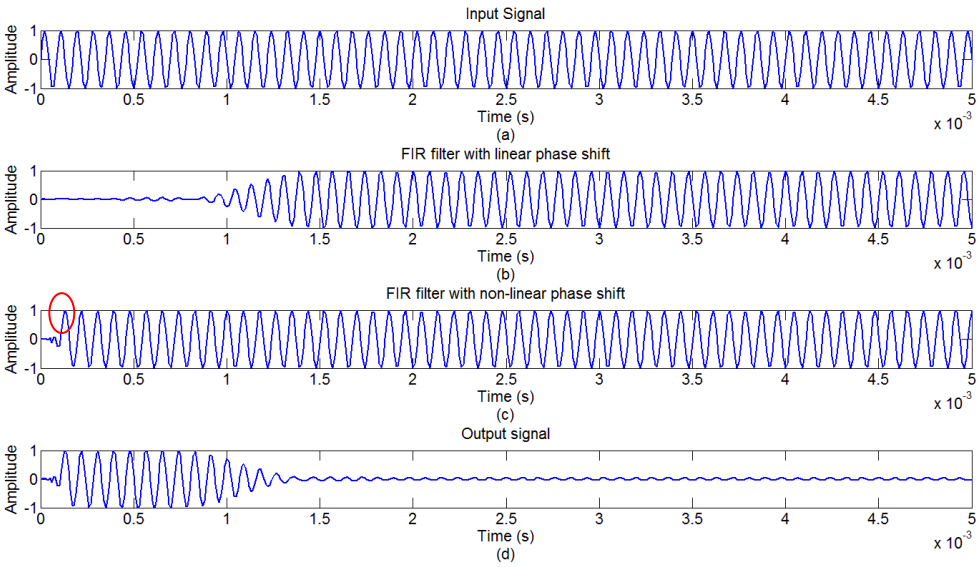

Figure 6.37: Illustration of (a) the LTI system input, the outputs of the FIR filter with (a) linear, and (b) non-linear phase shifts, and (d) the overall output of the LTI system

In this case, phase changes cannot only cause a signal removal, but their nonlinearity also can shift the position of the peaks in time (see the red ovals in Figure 6.36 and Figure 6.37). As the higher the nonlinearity is, the effects are more severe and destructive to the output signal.

Considering the cylindrical timber pole, dispersion relations for the simulated isotropic and orthotropic timber poles are shown in Figure 6.38. As can be seen in Figure 6.38 (a), the simulated isotropic timber pole acts as the non-dispersive LTI system in the frequency range of 0-7 kHz (i.e. in this frequency range the group velocity and the phase velocities are relatively the same). On the other hand, the hammer impact excites the timber pole in a frequency range of zero to almost 5 kHz. Consequently, the simulated isotropic timber pole acts as a non-dispersive medium under the hammer impact load. This is the main reason that reflection peaks can easily be detected in the isotropic cases. It is also worth noting that the captured signals by the sensors are called non-stationary when the medium is dispersive, and they are called stationary when the medium is non-dispersive.

On the other hand, the simulated orthotropic timber pole (which is more similar to the reality) is a highly dispersive material in the frequency range of zero - 5 kHz (the hammer impact frequency range). Furthermore and as mentioned earlier, lateral hammer impact at a 45° angle excitation creates both of the longitudinal and the bending waves simultaneously, while each of them has at least two branches. It is worth mentioning that each of the branches related to the longitudinal or bending waves acts as a dispersive LTI system with high nonlinearity. Considering the simple example that was explained earlier in this section and by looking at the Figure 6.38 (b), if the timber pole is excited with the broadband frequency impact (i.e. hammer), the captured signals (i.e. the response of the timber pole as a LTI system) suffer from severe and non-amendable distortions. It is worth considering that the different phase velocities mean firstly that the overall shape of the wave packet cannot be preserved (i.e. the reflection peaks are repositioned in time). Secondly, each of the frequency components has its own reflection (e.g. from the bottom of the pole), while the interference between the reflections created by the single and the same frequency but from the different modes can result in the peaks removal in the captured signal (as illustrated in the second simple

example). If this level of the distortion does not make it impossible to detect the reflections even from the bottom of the pole, it makes the task very difficult.

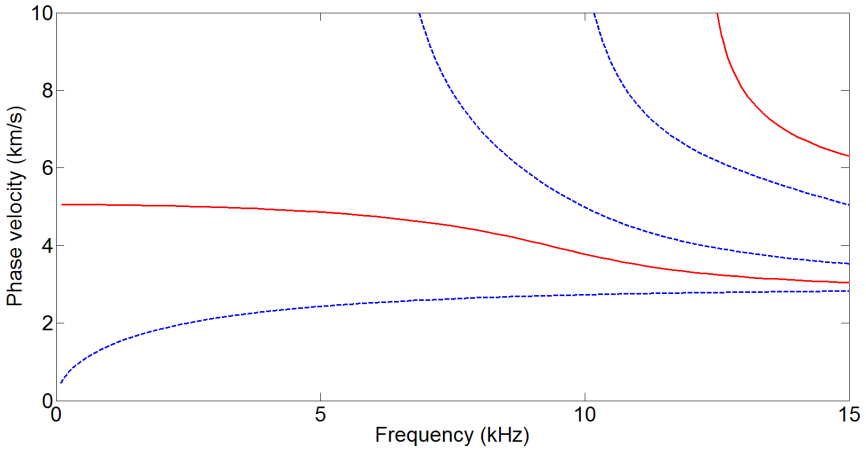

(a)

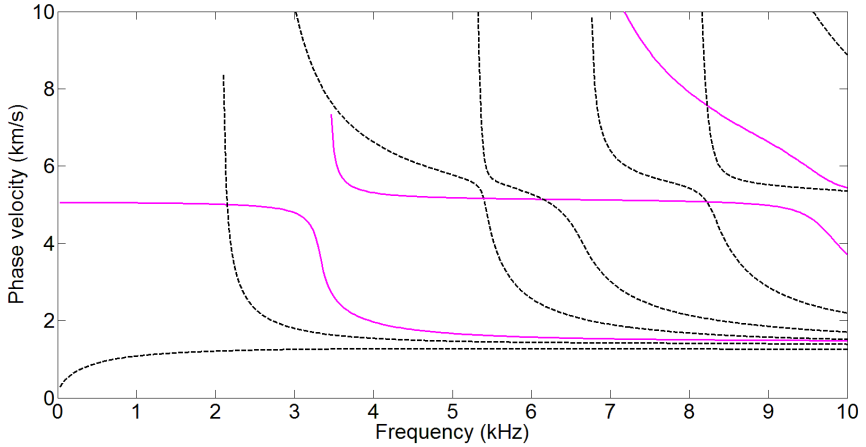

(b)

Figure 6.38: Dispersion curves of the cylindrical timber poles in (a) the isotropic; and (b) the orthotropic cases. Dashed lines represent the flexural wave branches and hard lines represent the longitudinal branches [52]

6.3 Applications of the blind signal separation methods on the Finite Element modeled timber pole

6.3.1 Principal Component Analysis (PCA)

In this section, the PCA is applied on the simulated timber pole with the isotropic and orthotropic material properties with the standing-on-soil and embedded conditions.

Figure 6.39 shows the principal components that were calculated from the simulated isotropic timber pole with the standing-on-soil condition. The captured signals from all of the 241 sensors are transferred back from the principal components domain to the time domain using the first 10 important principal components.

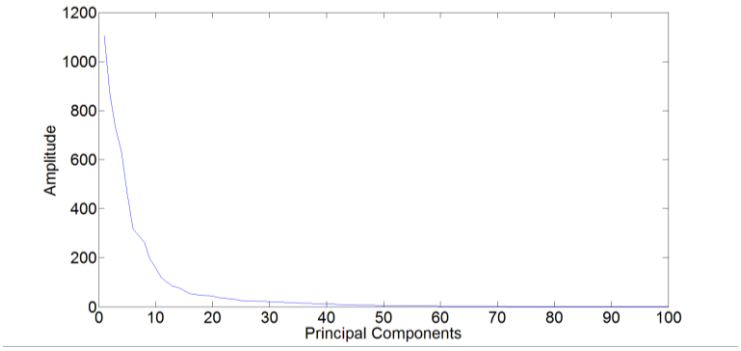

Figure 6.39: Principal components of the simulated isotropic timber pole with the standing-on-soil condition

Figure 6.40 shows the original signals, the signals that transferred back to time domain by using the first 10 principal components, and the signals that transferred back to the time domain by using the rest of the principal components.

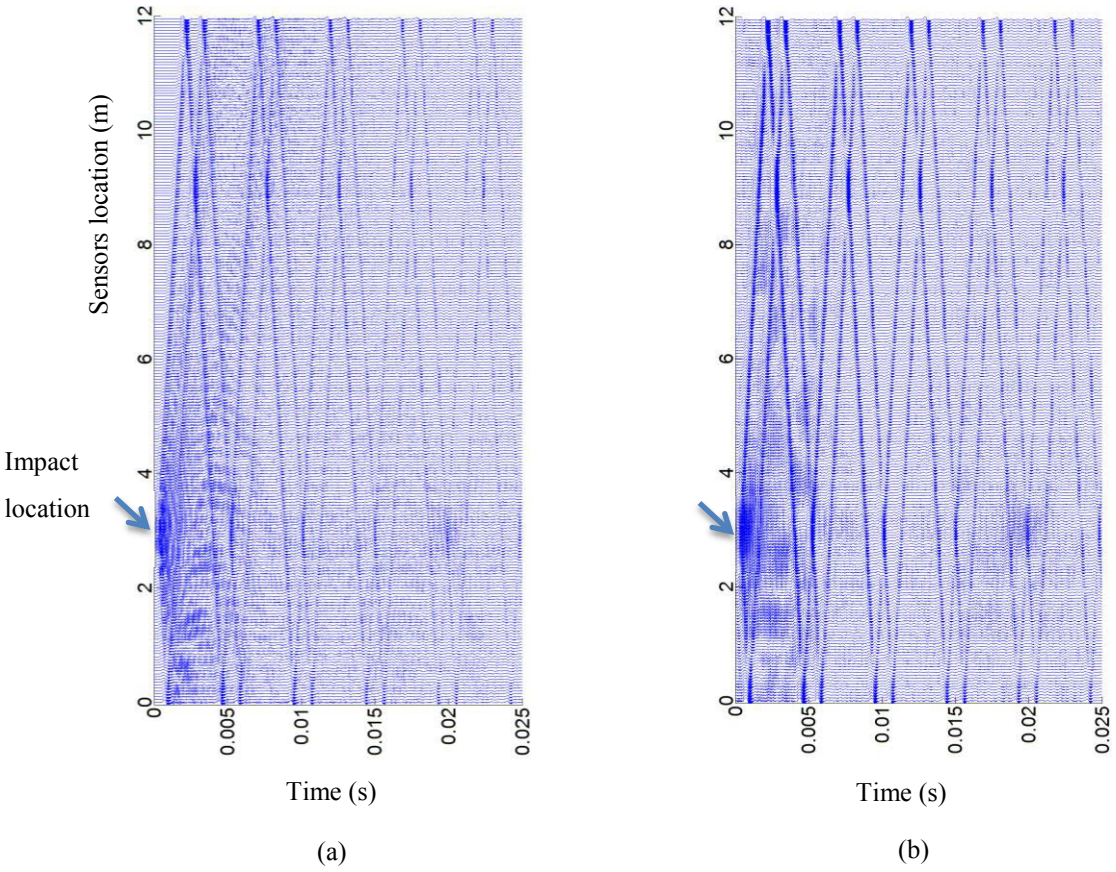

(a) (b)

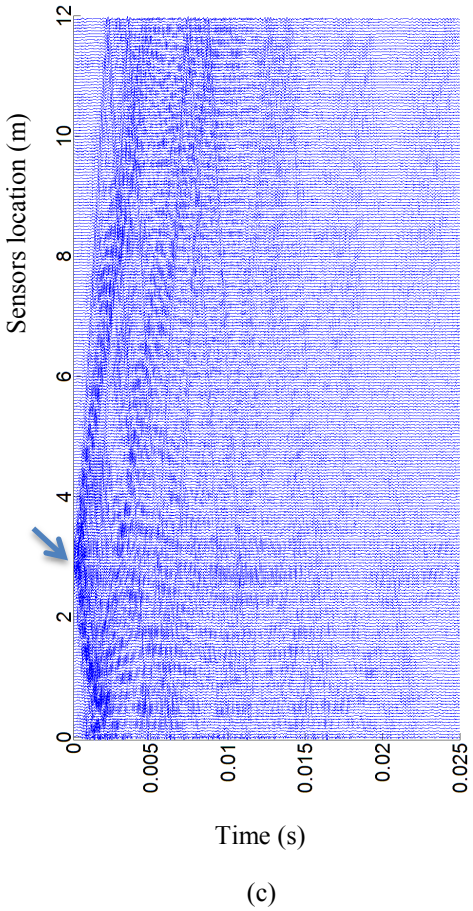

(c)

Figure 6.40: (a): Original captured signals; and the signals that transferred back to the time domain using (b): the first 10 most important principal components, and (c) the rest of the principal components for the simulated isotropic timber pole with the standing-on-soil condition

As can be seen in Figure 6.40, the PCA could noticeably clear the signal and highlight the main patterns of the signal. It is essential to consider that since the statistical properties of both of the upward and downward travelling waves are the same, and the PCA is based on the covariance matrix, both of these waves are categorized in the same group in the principal components domain. In other words, the PCA is not able to separate the upward and downward travelling waves from each other, but it can clear the signals from the rest of the unwanted patterns.

Figure 6.41 illustrates the principal components of the simulated isotropic timber pole with the embedded in 1.5 m soil condition. In this case, the first eight most important principal components are used for the signals transformation. Figure 6.40 shows the original signals, the signals that transferred back to the time domain by using the first eight most important principal components, and the signals that transferred back to the time domain by using the rest of the principal components.

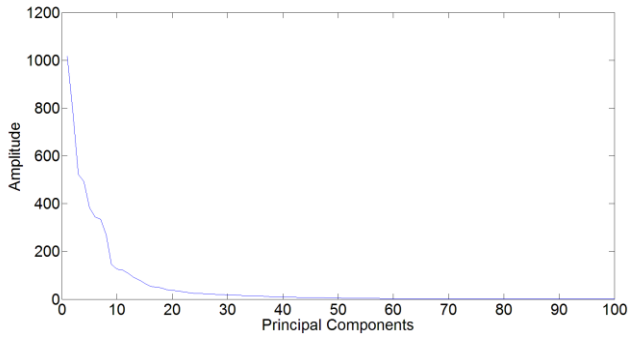

Figure 6.41: Principal components of the simulated isotropic timber pole with the embedded in 1.5 m soil condition

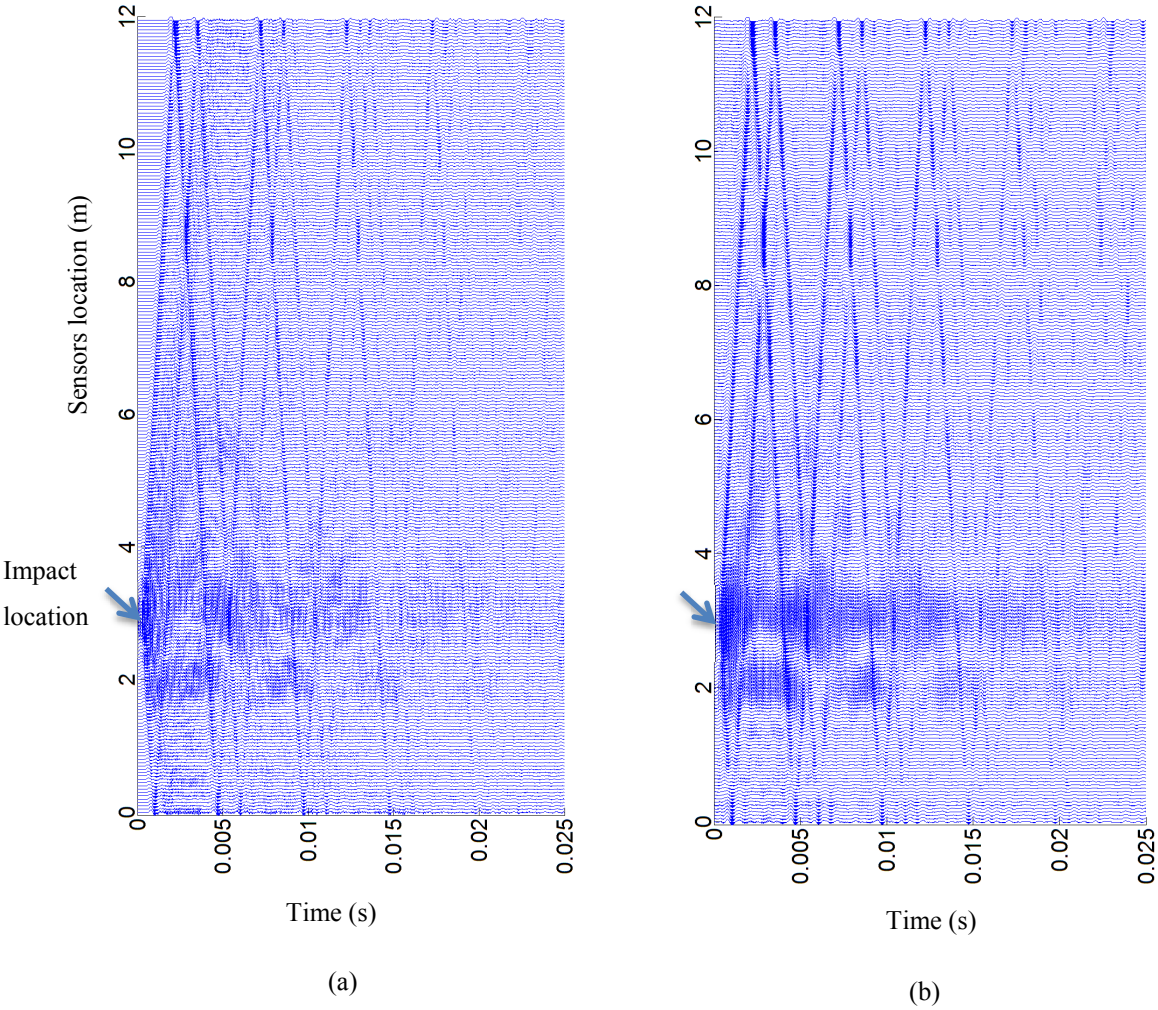

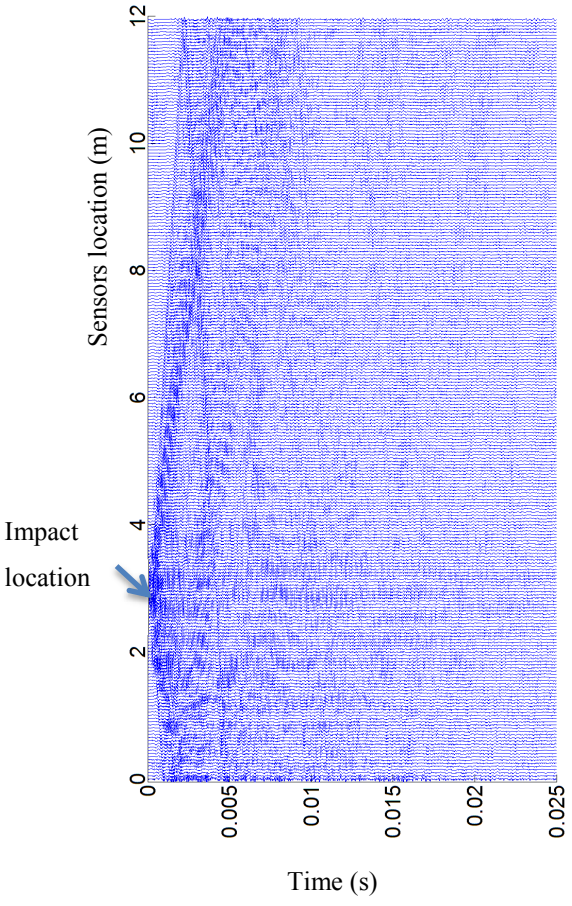

(c)

Figure 6.42: (a): Original captured signals; and the signals that transferred back to the time domain using (b): the first 10 most important principal components, and (c) the rest of the principal components for simulated isotropic timber pole with the embedded condition

Figure 6.43 shows the principal components of the simulated orthotropic timber pole with the embedded condition.

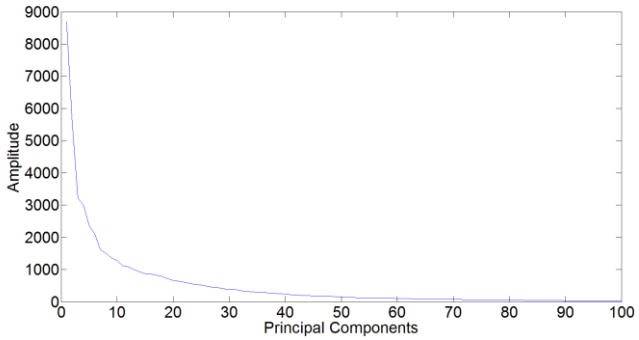

Figure 6.43: Principal components of the simulated orthotropic timber pole with the embedded condition

The first eight principal components have been used to transfer the signal back to the time domain, which are shown in Figure 6.44.

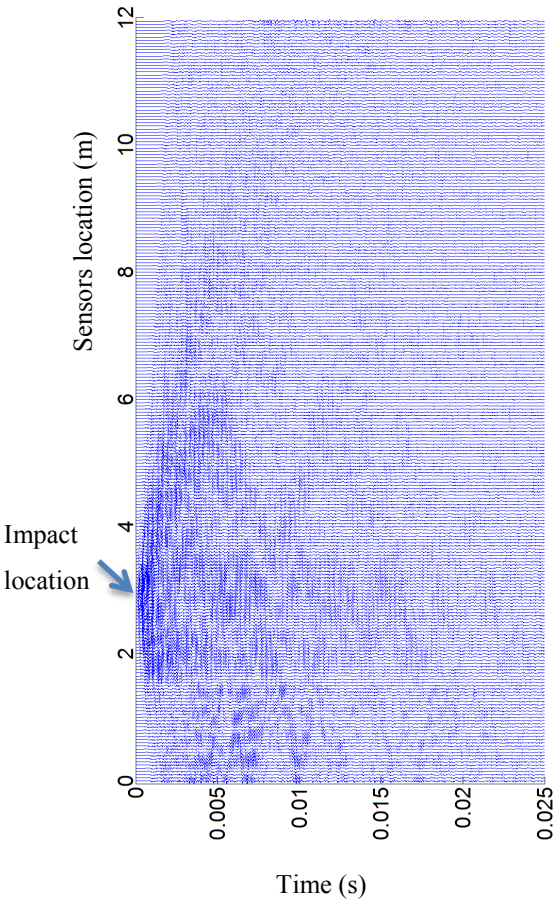
Sensors location (m)
Impact
location
0
2
4
6
8
10
12
0
0.005
0.01
0.015
0.02
0.025
Time (s)

(a)

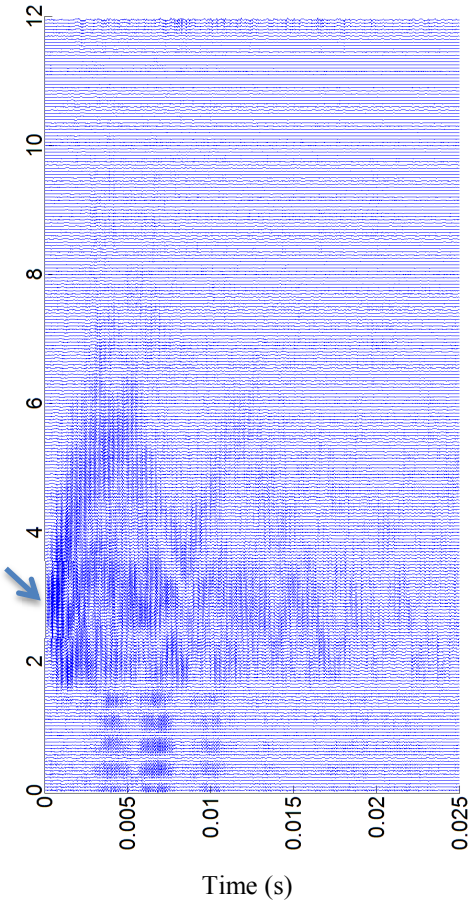
0
2
4
6
8
10
12
0
0.005
0.01
0.015
0.02
0.025
Time (s)

(b)

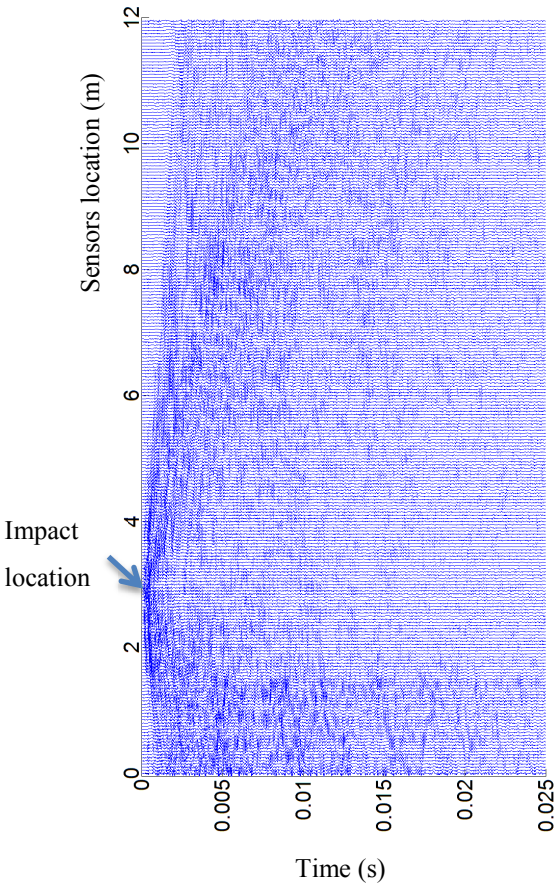

(c)

Figure 6.44: (a): Original captured signals; and the signals that transferred back to the time domain (b): using the first eight most important principal components, and (c) using the rest of the principal components for the simulated orthotropic timber pole with the embedded condition

It can be seen in Figure 6.44 that for the simulated orthotropic timber pole with the embedded condition, the PCA cannot clear the signals. This is due to the effects of the dispersion caused by the timber pole. In other words, this means that the statistical properties of the existing patterns not only change during the capturing time, but also interfere with each other.

6.3.2 Singular Value Decomposition (SVD)

Figure 6.45 shows the singular values obtained from the simulated isotropic timber pole with the standing-on-soil condition.

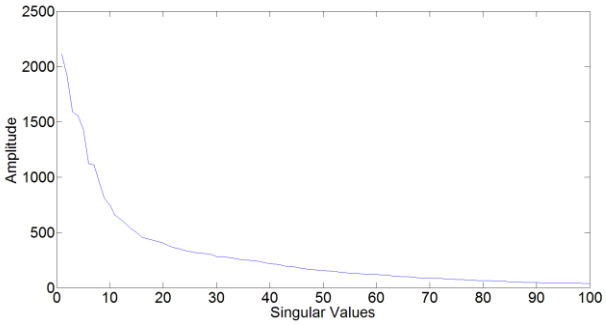

Figure 6.45: Singular values of the simulated isotropic timber pole with the standing-on-soil condition

In the SVD, the singular values can be separated in three groups of low, medium, and large. The most important singular values are grouped in the low, while the less important ones are grouped as the high, and the ones in the middle are grouped as the medium. In Figure 6.45, the first eight singular values are grouped as the low ones, from eight to thirty are grouped as the medium, and the remains are grouped as the high. The results of the reconstructed signals in all of the sensors using the singular values in each of these groups are shown in Figure 6.46.

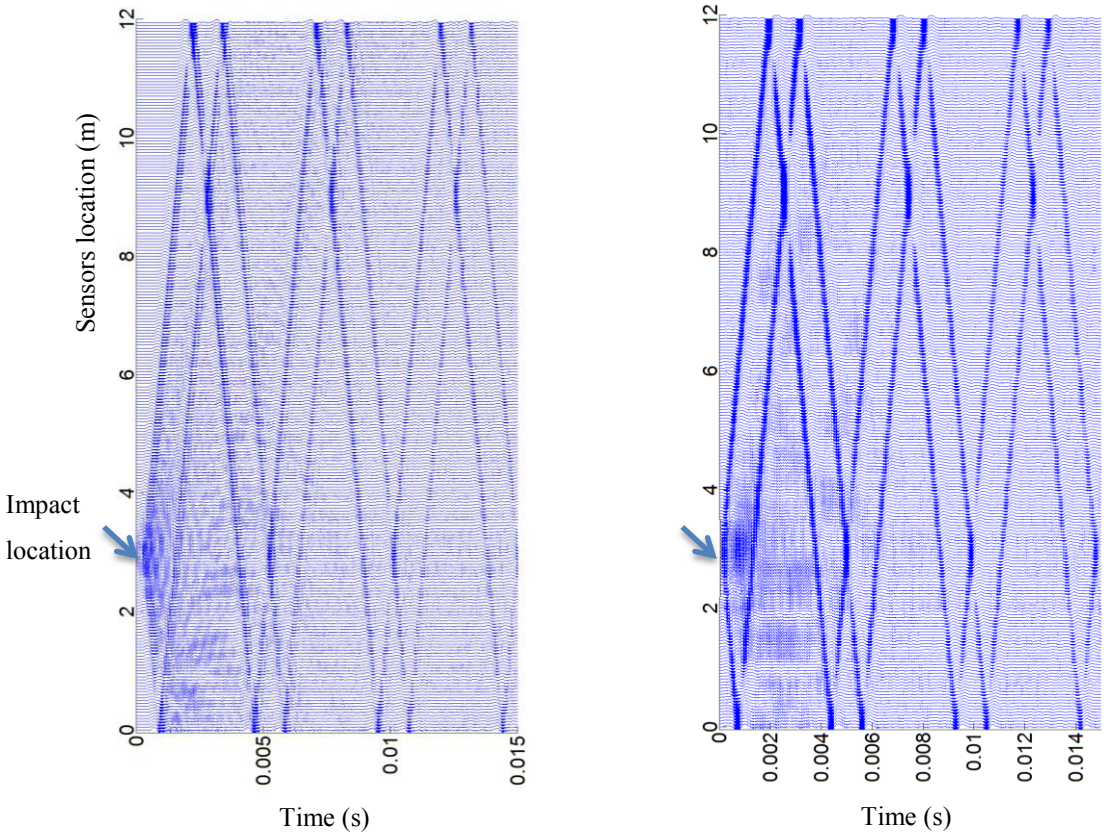

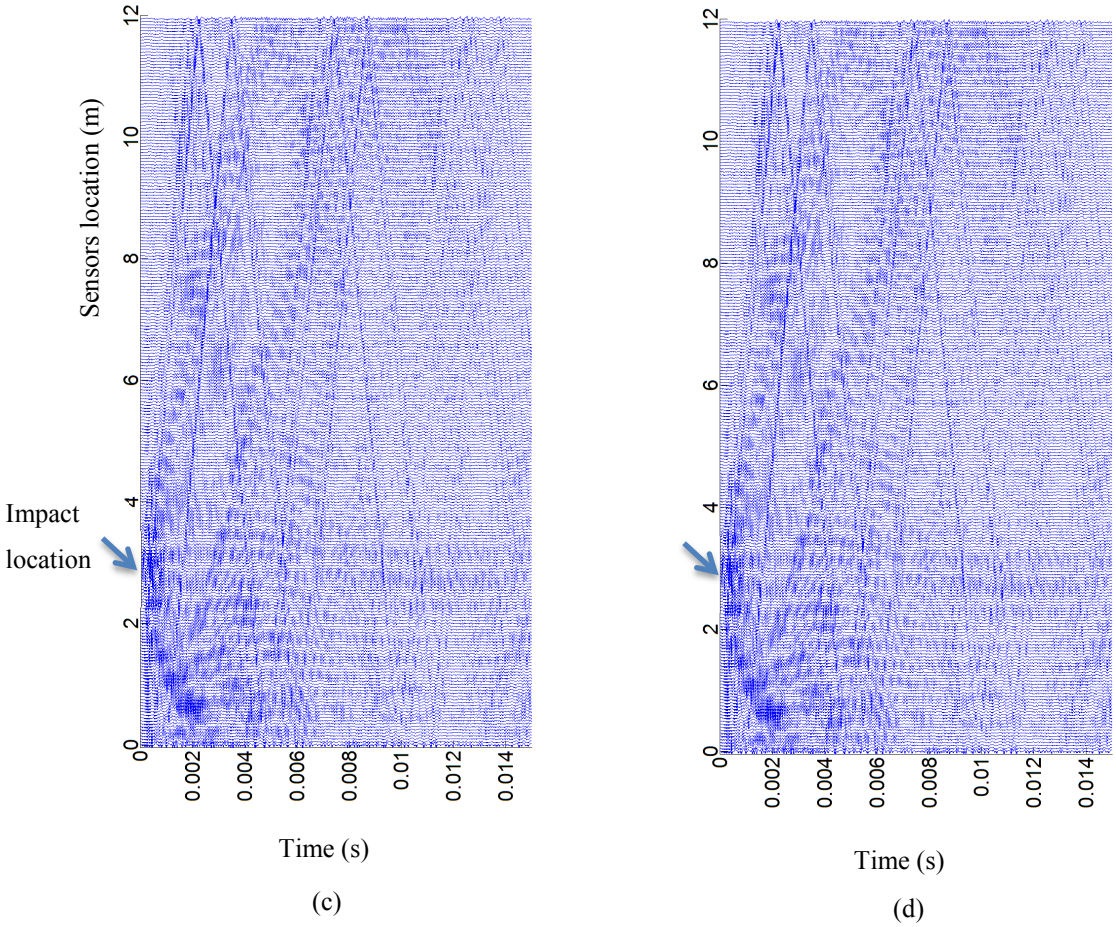

Figure 6.46: (a) Original signals, and the transferred signals to the time domain (b): using the low singular values, (c): using the medium singular values, and (d): using the high singular values for the simulated isotropic timber pole with the standing-on-soil condition

As can be seen in Figure 6.46, the SVD can mostly remove the noise or unwanted patterns in the signal, and preserve the main patterns that are related to the upward and downward travelling waves. Figure 6.47 shows the Singular values of the simulated isotropic timber pole with the embedded condition.

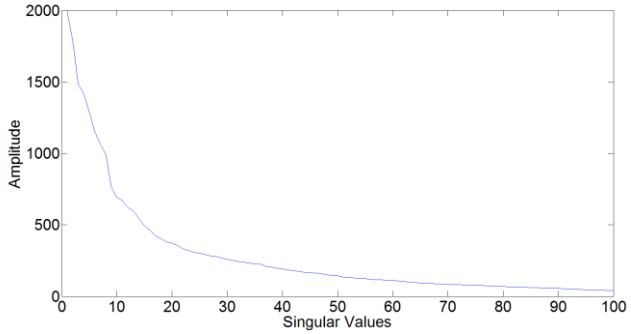

Figure 6.47: Singular values of the simulated isotropic timber pole with the embedded condition

The first ten singular values are grouped as the low, ten to thirty are grouped as the medium, and the rest are in the high group. Figure 6.48 illustrate the time signals obtained from each of these groups of the singular values.

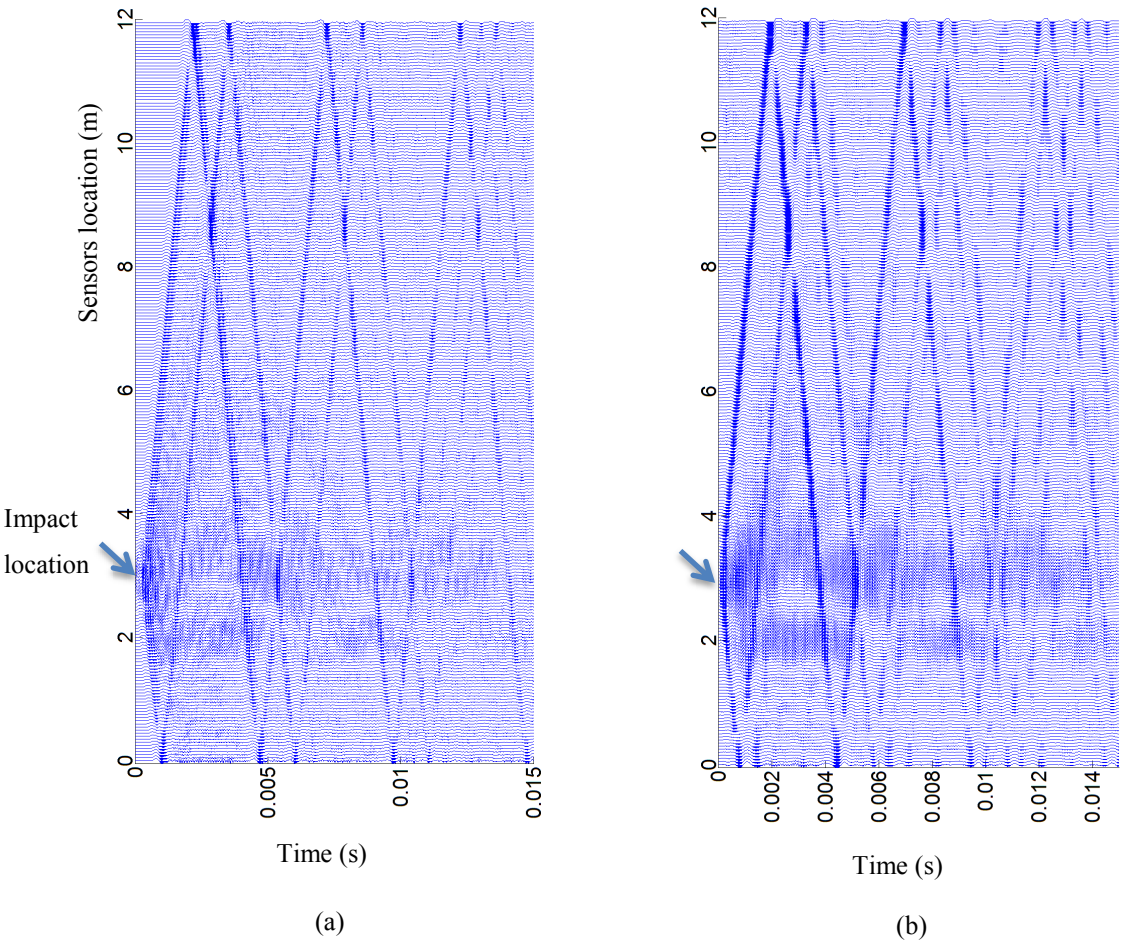

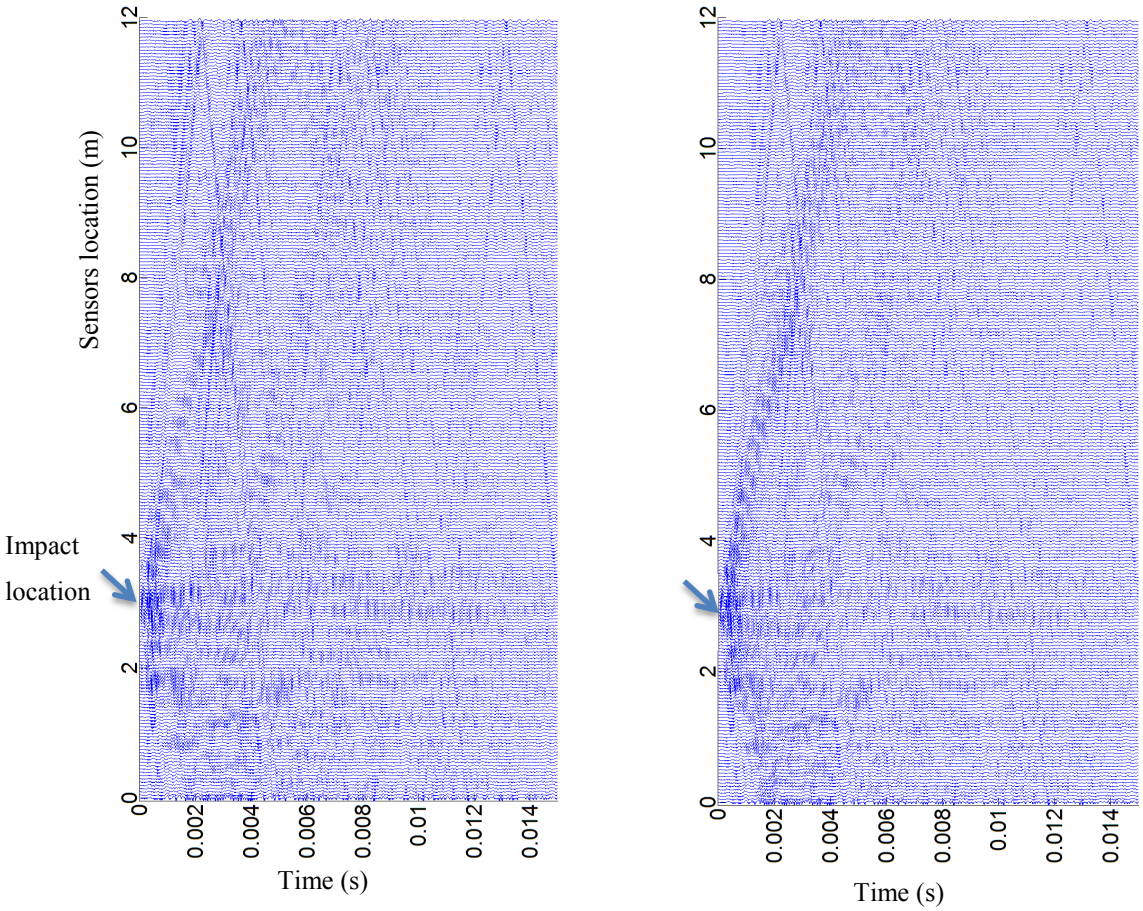

(c) (d)

Figure 6.48: (a) Original signals, and the transferred signals to the time domain (b): using the low singular values, (c): using the medium singular values, and (d): using the high singular values for the simulated isotropic timber pole with the embedded in 1.5 m soil condition

It can be seen in Figure 6.48 that although the SVD could highlight the main patterns and remove the noise, its effectiveness has decreased in comparison with the isotropic standing-on-soil results.

Figure 6.49 demonstrates the singular values of the simulated orthotropic timber pole with the embedded condition.

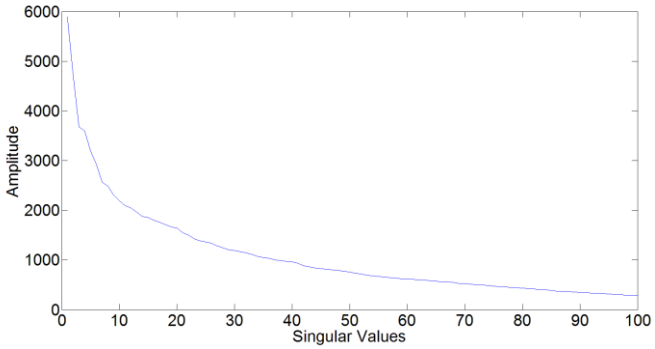

Figure 6.49: Singular values of the simulated orthotropic timber pole with the embedded condition

In this case, only the first five singular values are grouped as low, from five to thirty are grouped as medium, and the remaining are grouped as the high ones. Figure 6.50 illustrates the time signals obtained from each of these groups of the singular values.

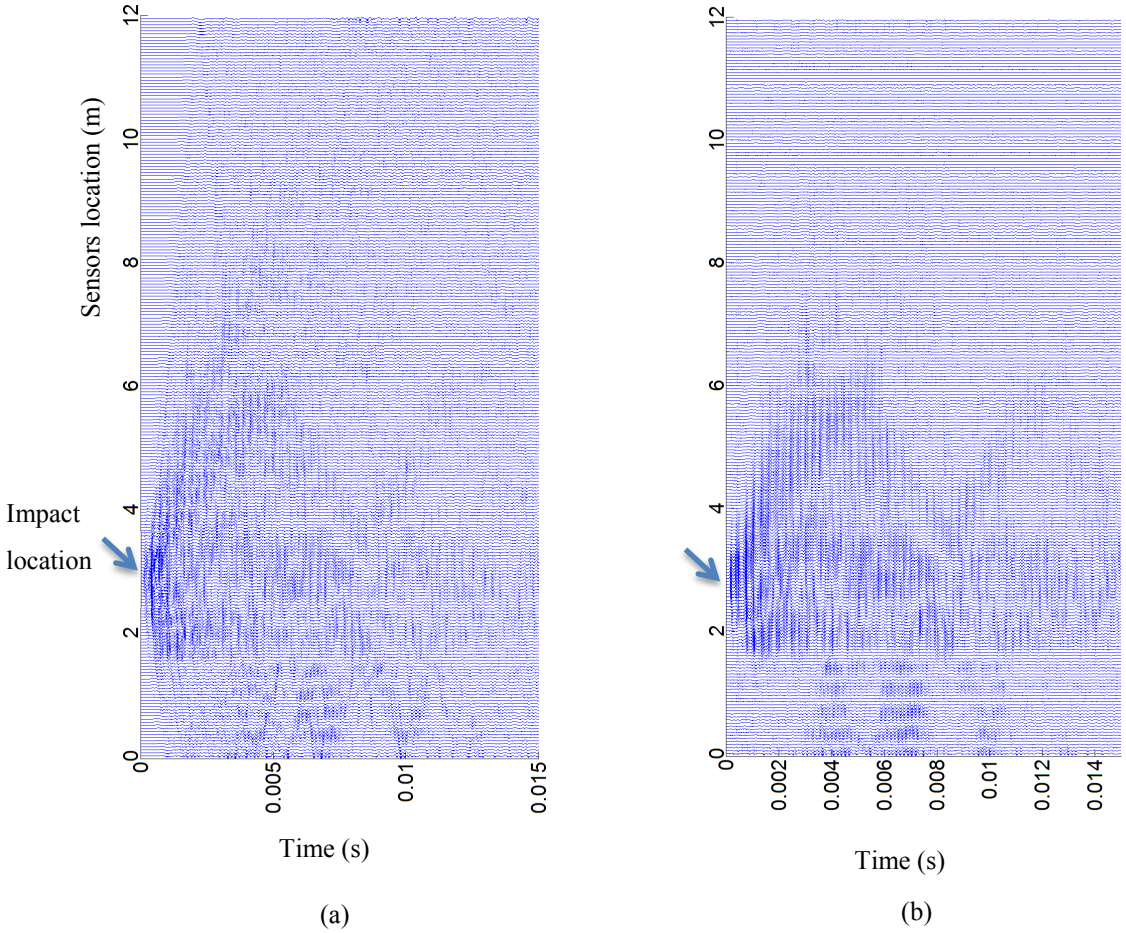

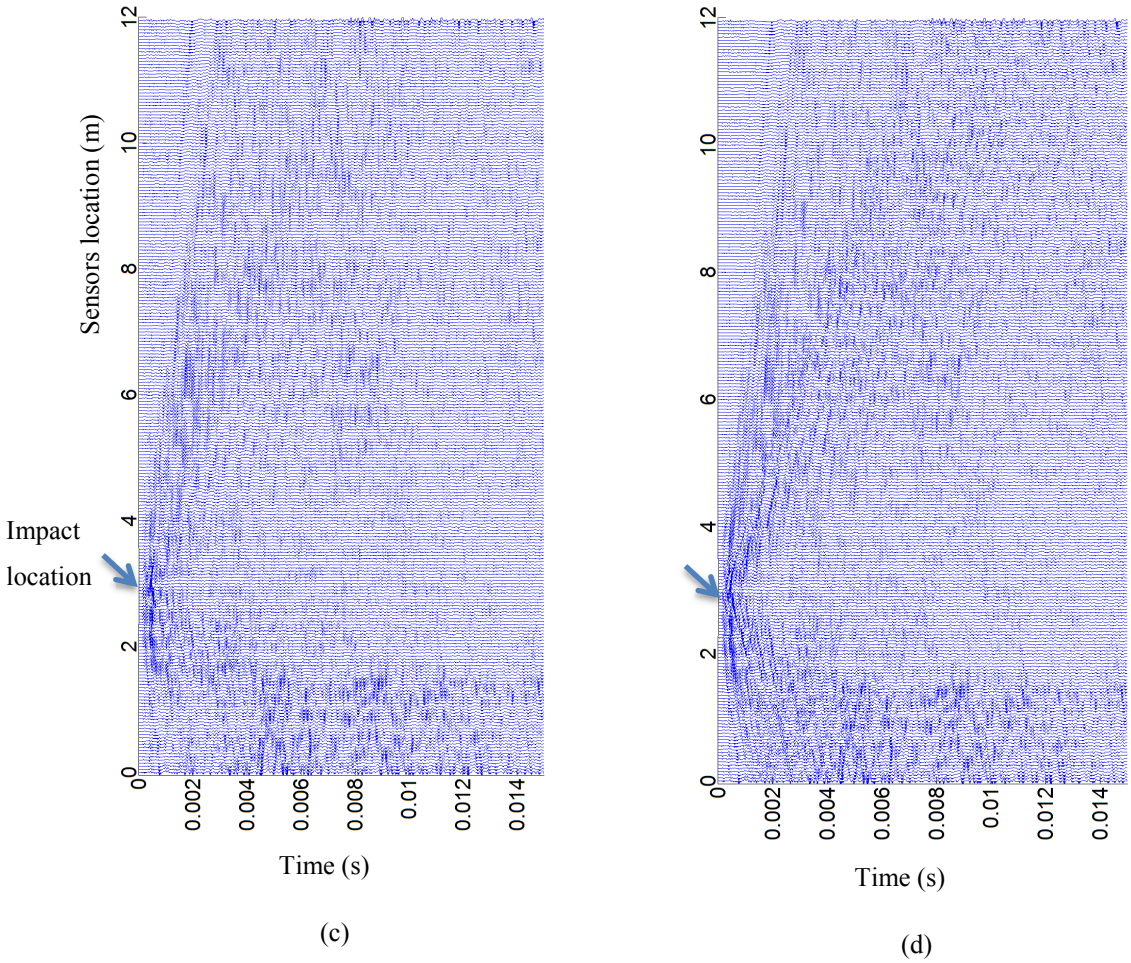

Figure 6.50: (a) Original signals, and the transferred signals to the time domain using (b): the low singular values, (c): the medium singular values, and (d): the high singular values for the simulated orthotropic timber pole with the standing-on-soil condition

It can be seen in Figure 6.50 that the SVD could not preserve the main patterns as it did in the isotropic cases. The SVD and the PCA are both based on second order statistics. On the other hand and as explained earlier in this chapter, the distortion caused by the timber pole with the orthotropic material properties makes it impossible for the algorithms like PCA and SVD to separate the patterns, which exist in the signal from each other. In the best situation where the timber pole is simulated with the isotropic material properties with the standing-on-soil condition, these algorithms can only remove the noise and are not able to separate the patterns with the similar statistical properties like the upward and downward travelling waves from each other.

6.3.3 *K*-mean clustering

In this section, *K*-mean clustering, which is the iterative and learning algorithm, is applied on the data captured from the simulated orthotropic timber pole in order to deal with the intrinsic complexities, which exist in the data and to separate the different patterns (related to the different branches of the waves) from each other. One of the major steps in the learning algorithms is a feature extraction. Feature extraction is needed to be done in a way that assumes that the most convenient features of the data are fed into the learning algorithm. As mentioned earlier, the captured signals from the simulated orthotropic timber pole as well as the real timber pole suffer heavily from the dispersion. On the other hand, the dispersion relation can be obtained from the temporal and the spatial frequency relations. As also explained earlier in the F-K filtering section in this chapter and also Chapter 3, two dimensional Fast Fourier Transform (FFT) of the two dimensional data (captured signals from 241 sensors) can obtain the data in the two dimensions of the temporal and spatial frequency domains. Since the dispersion relation is obtained directly from the aforementioned transferred data, this data is also used to feed to the *K*-mean clustering algorithm. Original data (that is going to be fed into the algorithm) is shown in Figure 6.51.

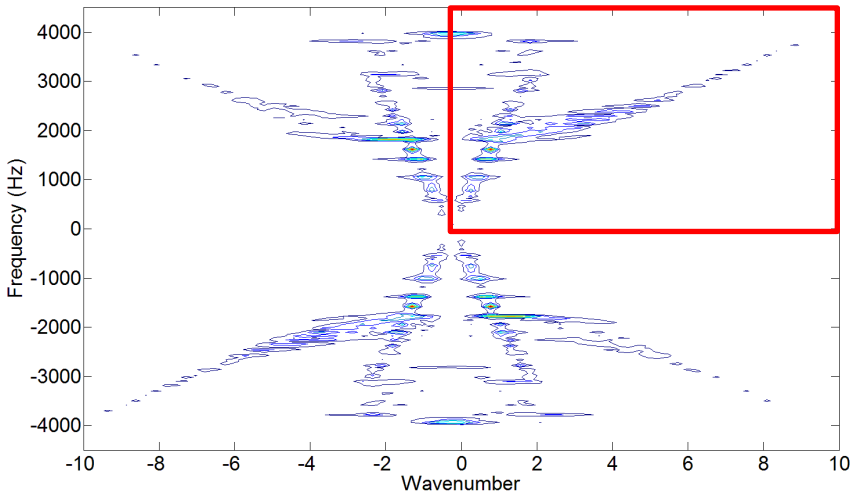

Figure 6.51: Two-dimensional FFT of the original data, which is going to be fed into the *K*-mean clustering algorithm

It is necessary to consider that since one-dimensional FFT is mirrored in the frequency domain, two-dimensional FFT has four mirrored sections. For this reason, only one

quarter of the transferred data (shown with the red rectangular in Figure 6.51) has fed into the *K*-mean algorithm, and the outputs are generalized into the other three sections. By looking at Figure 6.38 (b), one can simply see that five branches exist in the frequency range of the hammer impact. In this regard, the *K*-mean algorithm is set in a way that separates its input dataset into the five clusters. The result of the *K*-mean clustering is shown in Figure 6.52.

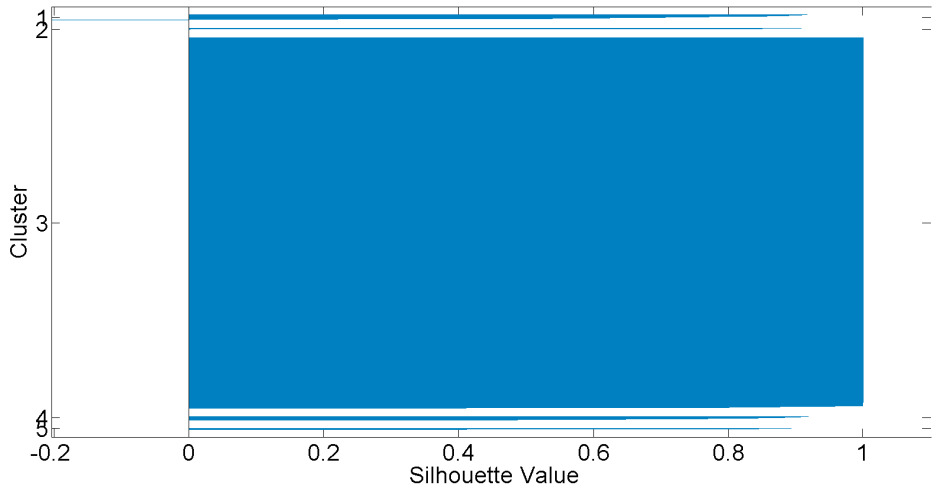

Figure 6.52: Silhouette plot of the output of the *K*-mean clustering algorithm

Figure 6.52 demonstrates the Silhouette value of each cluster vs. the related cluster. As can be seen, the third cluster is the most important cluster amongst all five and its silhouette value is one. The related data of the third cluster in the F-K domain (which is obtained from the *K*-mean algorithm) that contains the desired output is shown in Figure 6.53.

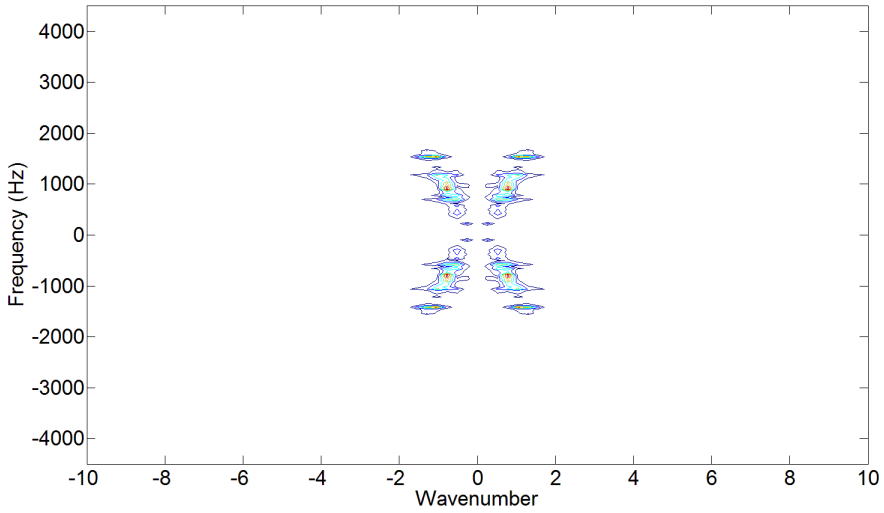

Figure 6.53: Third cluster of the *K*-mean algorithm, which contains the desired output (The longitudinal wave)

Figure 6.54 illustrates the original signals and the *K*-mean clustering outputs in the original dimensions. As can be seen in Figure 6.54 (b), the *K*-mean clustering could successfully separate the longitudinal and the bending waves from each other. However, by looking at the Figure 6.53, one can simply see that the data obtained of the third cluster is limited to the frequency range of -2 to 2 kHz, which makes it very similar to the results of the low-pass filtering with 1.5 kHz cut-off frequency. A better demonstration can be found in Figure 6.55.

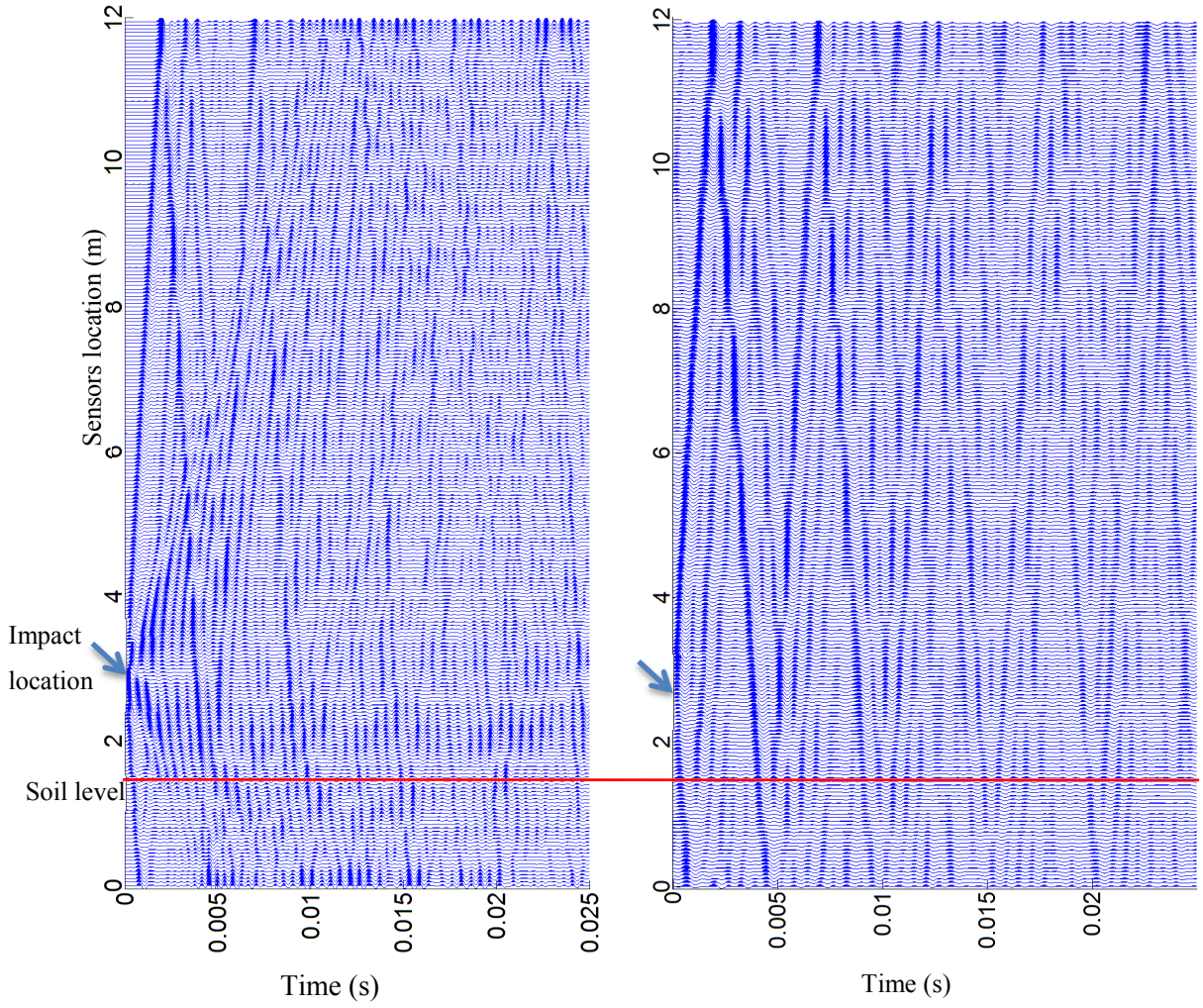

(a) (b)

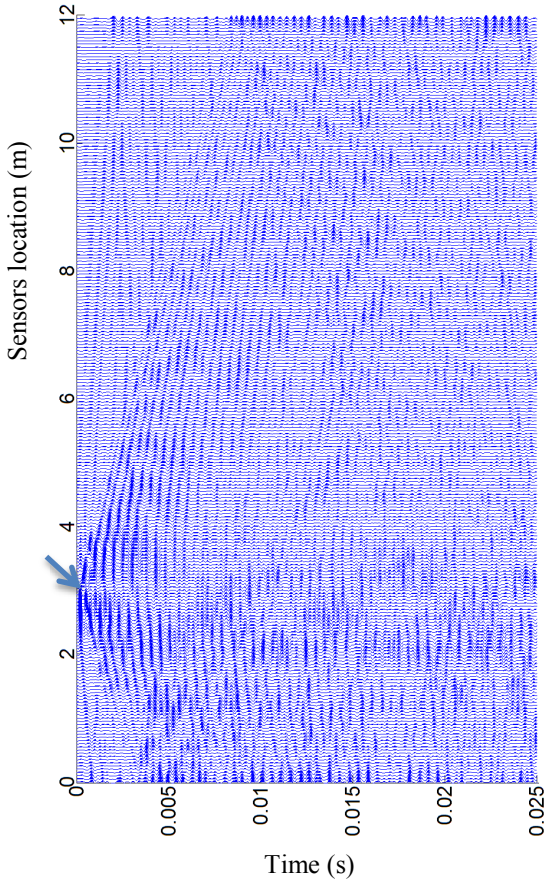

(c)

Figure 6.54: (a) original data captured from the simulated orthotropic timber pole after low-pass filtering with 4500 Hz (Hammer impact frequency range), (b): the data of the third cluster which is transferred back to the time-space domain, and (c): The data obtained from the rest of the clusters which is transferred back to the time-space domain

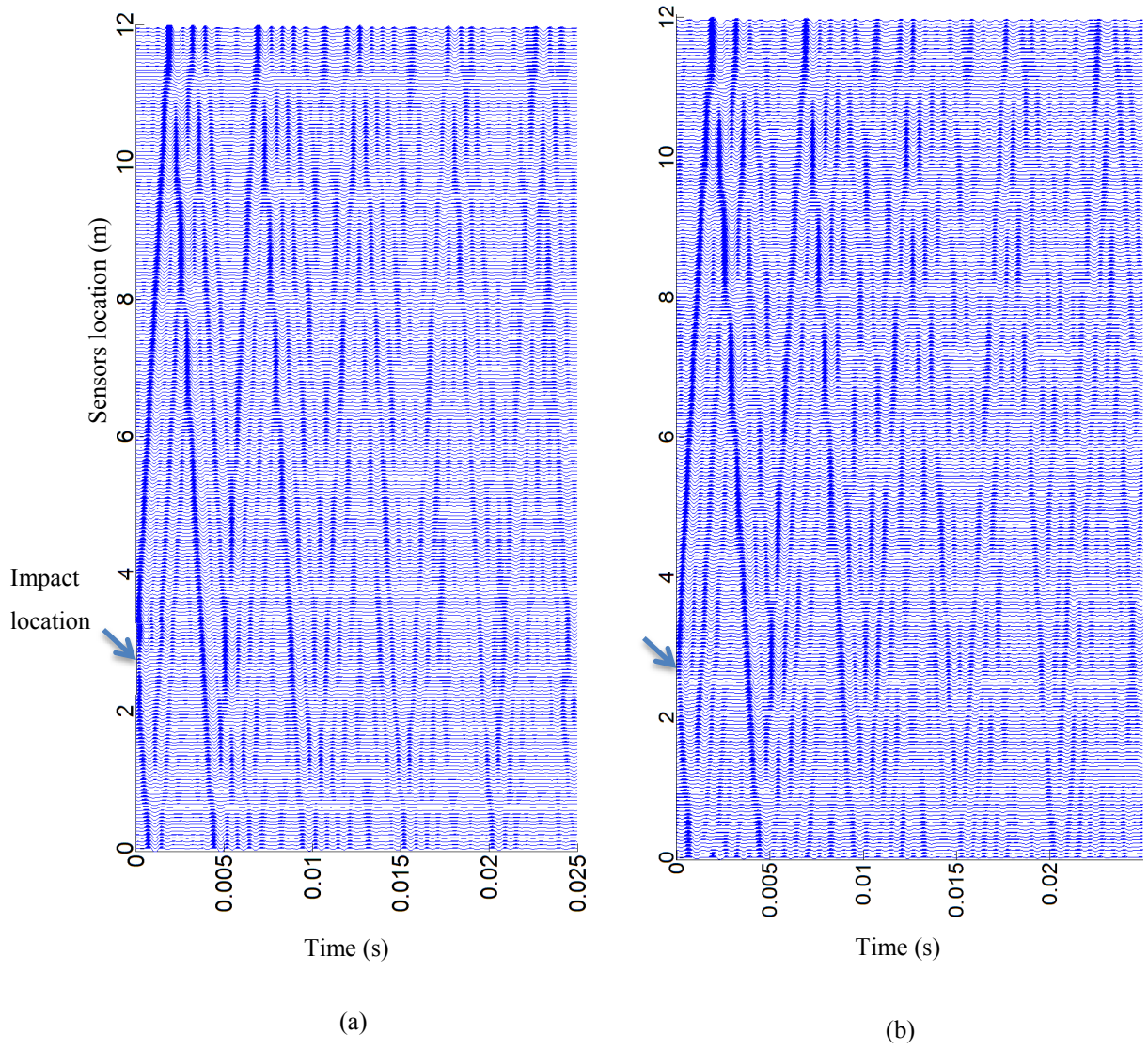

Figure 6.55: (a) low-pass filtered data with 1.5 kHz cut-off frequency, and (b): output of the third cluster of the *K*-mean clustering algorithm

As can be seen in Figure 6.55, there is a considerably large similarity between the output of the low-pass filter with 1.5 kHz cut-off frequency, and the output of the K-mean clustering. In fact, although the *K*-mean algorithm could successfully separate the longitudinal waves and the bending waves from each other, due to the interference between the existing branches, results of the velocity analysis are not reliable. It can be seen that the estimated velocity after applying the predictive deconvolution will be around the unacceptable value of 14000 m/s.

6.4 Experimental tests data analysis

In this section, the applications of the digital filters followed by the deterministic signal separation (i.e. predictive deconvolution), and the blind signal separation (PCA and SVD) on the timber pole condition assessment using the experimental data are investigated. It is essential to consider that the Frequency-Wavenumber analysis as well as the *K*-mean clustering cannot be applied on the experimental signals due to very low resolution in the spatial domain (i.e. only eight sensors are used in the real in-field and laboratory tests). All experimental tests are performed on a 5m timber pole with a 30cm diameter in the cross-section. Two types of tests have been performed, one while the timber pole is standing on soil, and the other when it is embedded in the soil. Hammer impact is also applied 2.5 m from the bottom of the pole. Figure 6.56 and Figure 6.57 illustrate the outputs from the FIR filter and the predictive deconvolution using the signals captured from the timber pole with the standing-on-soil condition. It is necessary to mention that the sensor 1 is not considered in the analysis since its output is out of the range of the others.

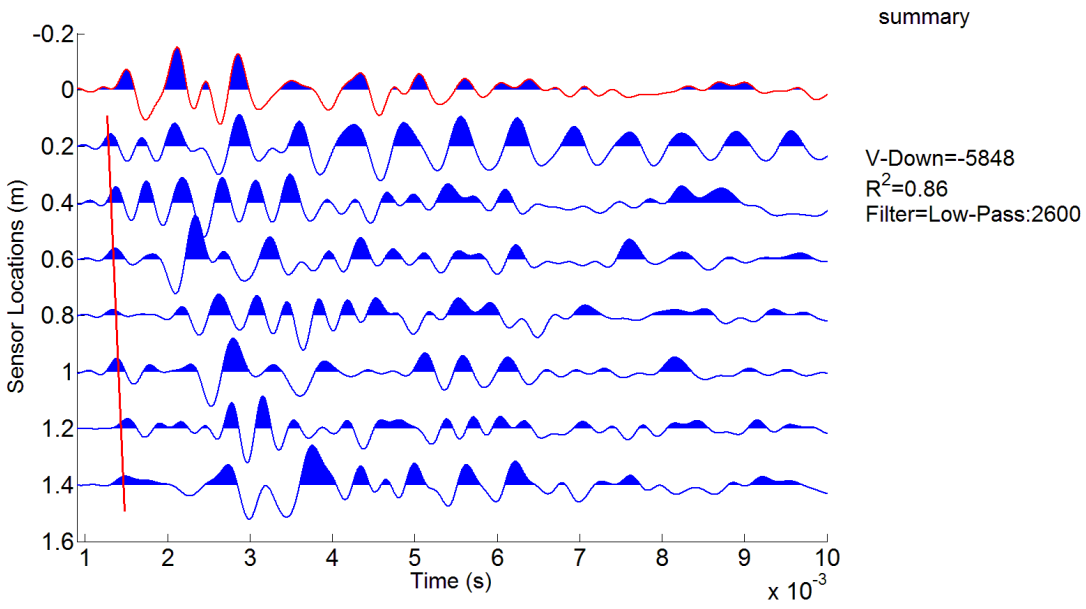

Figure 6.56: Outputs of the digital FIR filter on the experimental data captured from the timber pole with the standing-on-soil condition

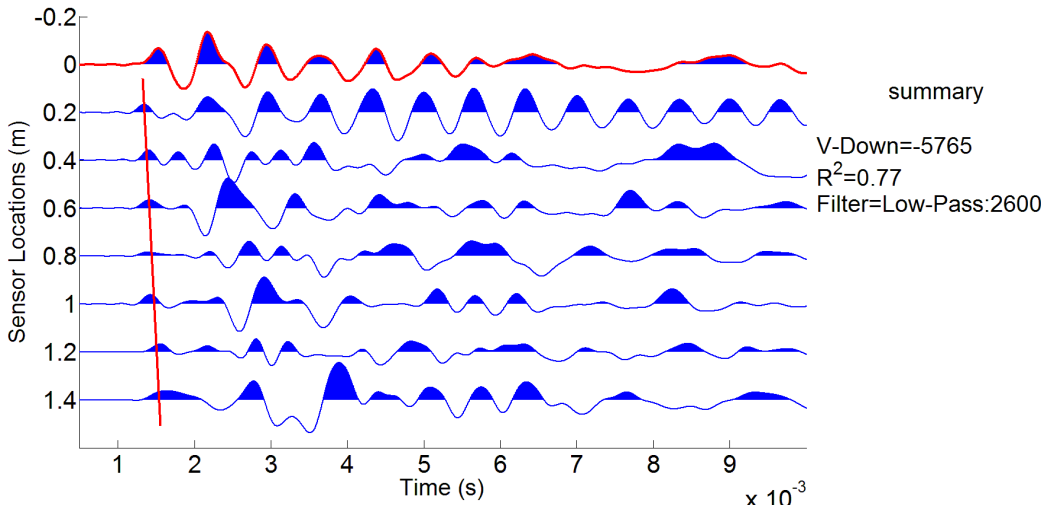

Figure 6.57: Outputs of the digital FIR filter followed by the predictive deconvolution on the experimental data captured from the timber pole with the standing-on-soil condition

It can be seen in Figure 6.57 that no patterns of the reflections can be detected as expected. Figure 6.58 shows the output signals of the low-pass filtering with 1.5 kHz cut-off frequency.

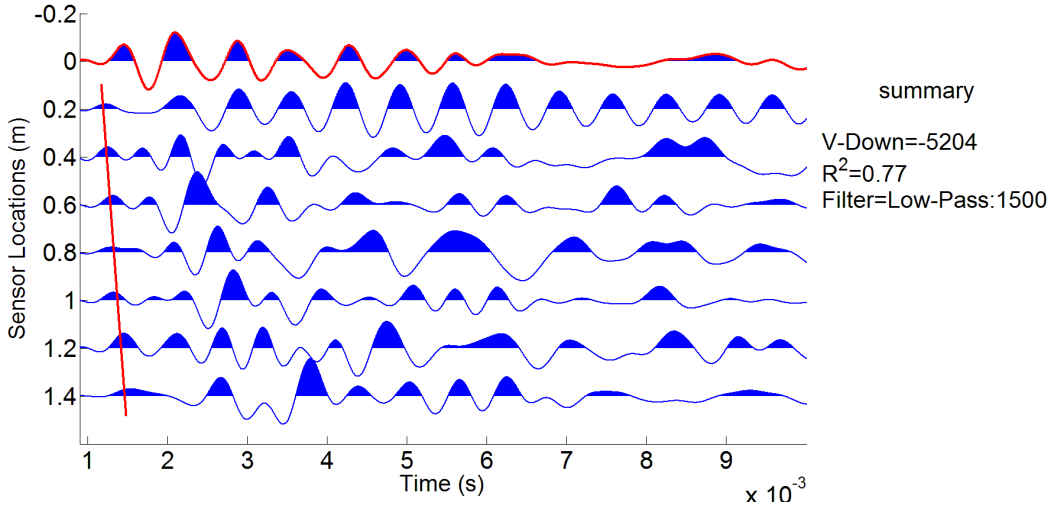

Figure 6.58: Output signals of the low-pass filtering with 1.5 kHz cut-off frequency on the experimental data captured from the timber pole with the standing-on-soil condition

Figure 6.59 and Figure 6.60 demonstrate the output signals of the low-pass digital filter and the predictive deconvolution applied on the experimental captured signals from the timber pole with the embedded condition.

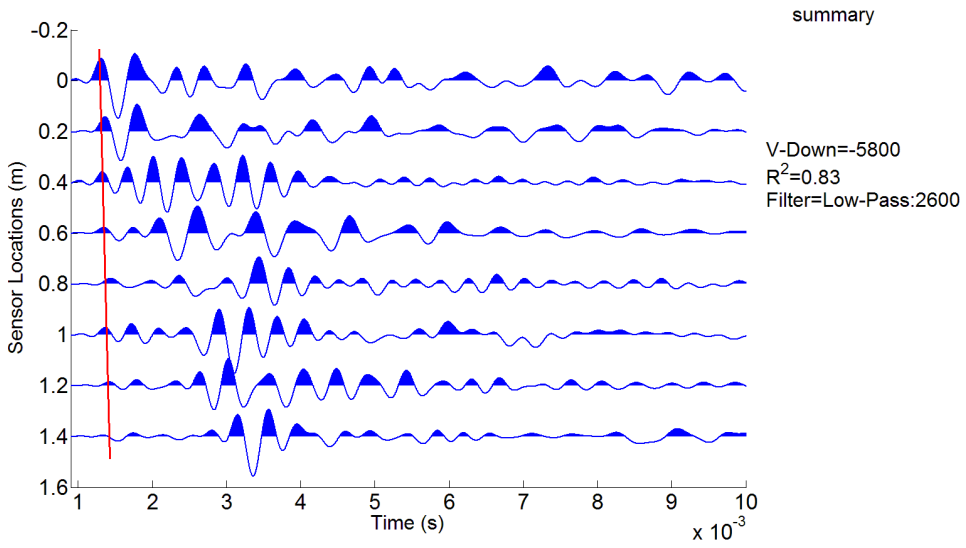

Figure 6.59: Outputs of the digital FIR filter on the experimental data captured from the timber pole with the embedded condition

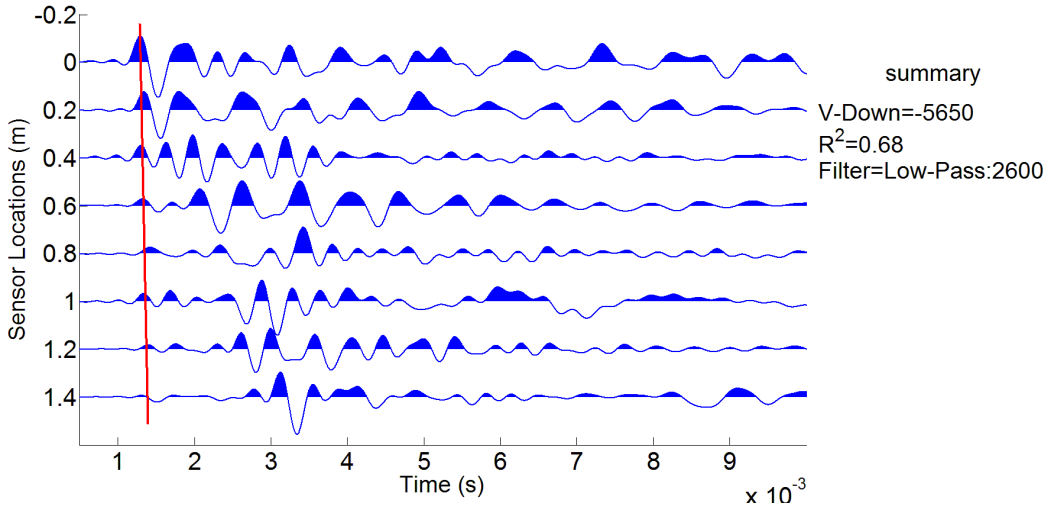

Figure 6.60: Outputs of the digital FIR filter followed by the predictive deconvolution on the experimental data captured from the timber pole with the embedded condition

The output of applying the low-pass filter with the cut-off frequency of 1.5 kHz is shown in Figure 6.61.

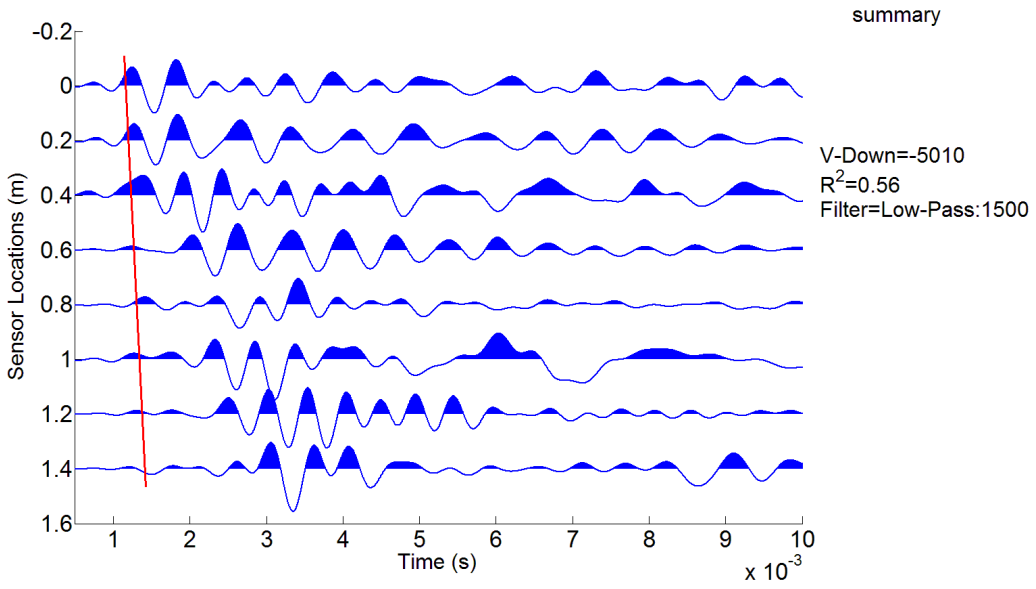

Figure 6.61: Output signals of the low-pass filtering with 1.5 kHz cut-off frequency on the experimental data captured from the timber pole with the embedded condition

The frequency spectrum of the captured signal in the sensor 4 is shown in Figure 6.62. As can be seen, the signal has a considerable energy after 2 kHz. This is the possible reason for the very weak first arrivals peaks in Figure 6.61.

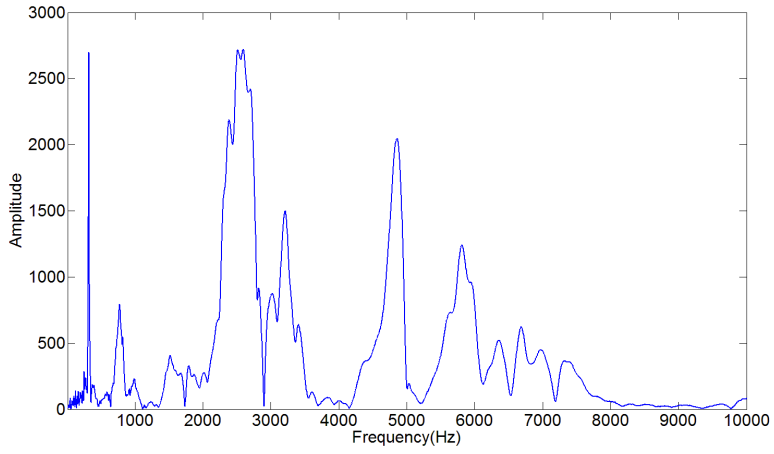

Figure 6.62: Frequency spectrum of the experimental data captured from the timber pole with the embedded condition

The frequency spectrum of the standing-on-soil condition is also provided in Figure 6.63. As can be seen, the most considerable energy of the signal is in the low frequency range of 0 to 1 kHz. This is the reason that the first arrival peaks in the output of the low-pass filter with 1.5 kHz cut-off frequency have more energy in the standing-on-soil

condition rather than the embedded one. It is also essential to consider the level of the energy in the embedded case is almost one third of the one in the standing-on-soil case.

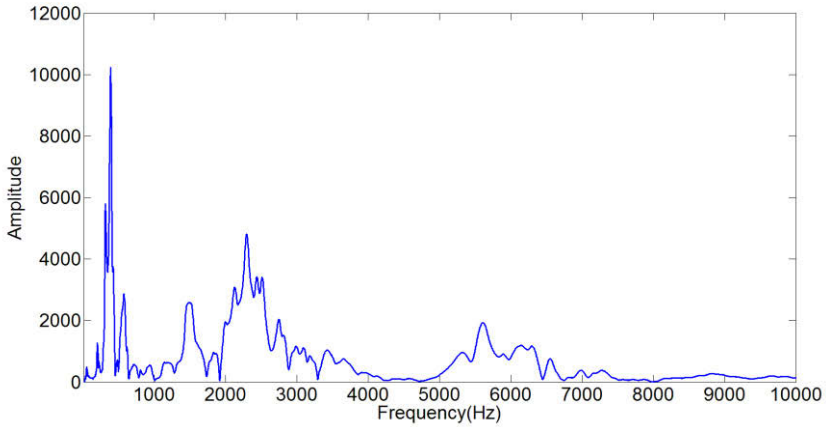

Figure 6.63: Frequency spectrum of the experimental data captured from the timber pole with the standing-on-soil condition

In the following, the results of applying the SVD and PCA on the experimental signals captured from the timber pole with the standing-on-soil condition are provided. The embedded condition results are not illustrated because of their similarity to the standing-on-soil. Figure 6.64 shows the singular values obtained from the standing-on-soil condition.

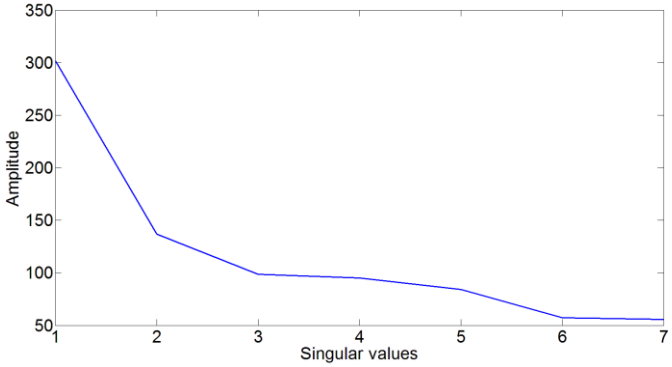

Figure 6.64: Singular values obtained from the experimental signals captured from the timber pole with the standing-on-soil condition

Similar to the application of the SVD on the numerical data, the singular values are categorized into the three groups of the low (the first and the second singular values), the medium (3rd, 4th, and 5th singular values), and the high (6th and 7th singular values).

Figure 6.64 shows the original captured signals and the time signals obtained from each of these groups of the singular values.

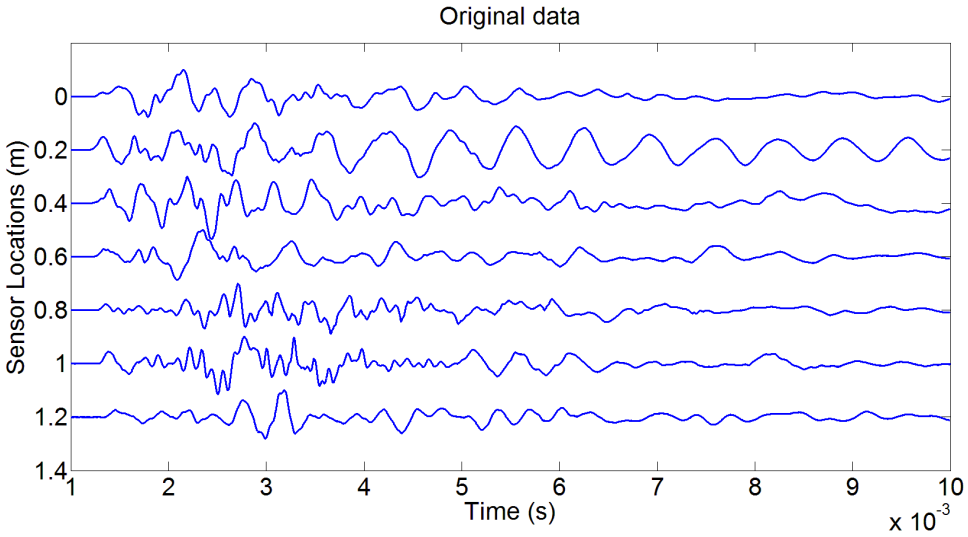

(a)

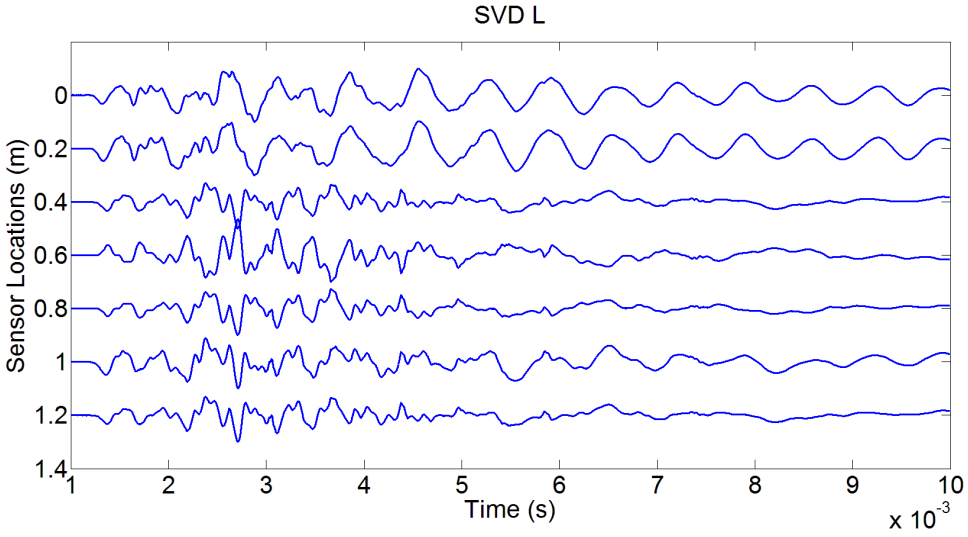

(b)

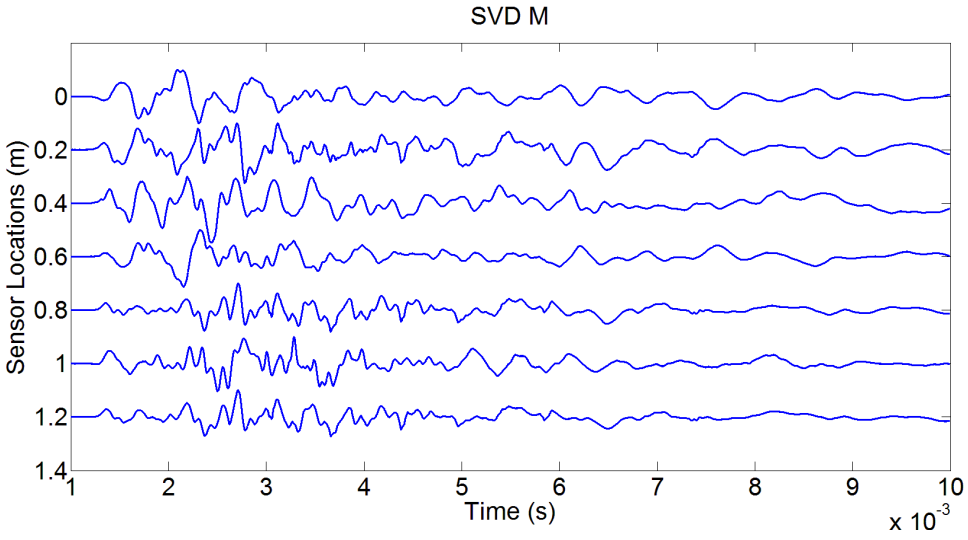

(c)

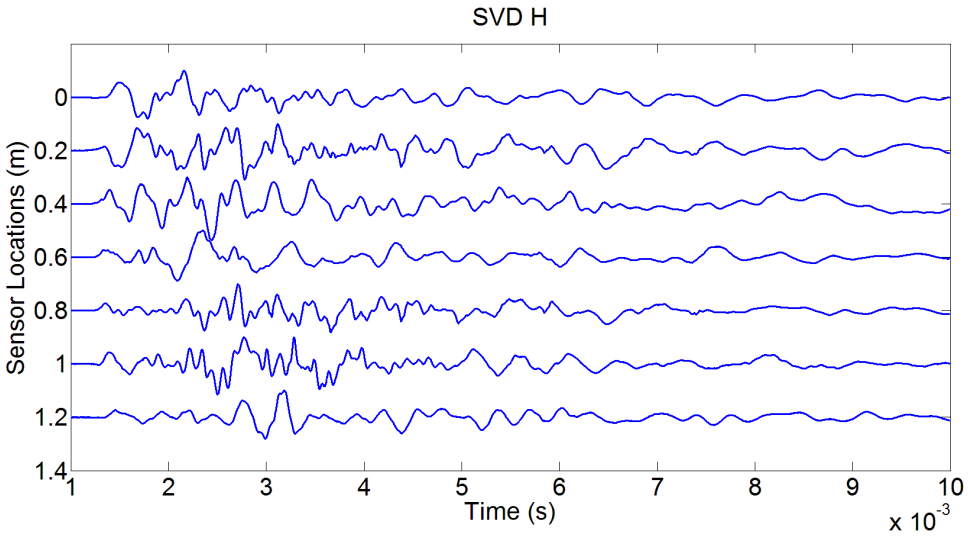

(d)

Figure 6.65: (a) Original captured signals, and the time signals obtained from (a) the 1st and 2nd, (b) the 3rd, 4th, and 5th, and (c) the 6th and 7th singular values obtained from the captured experimental signals from the timber pole with the standing-on-soil condition

As can be seen in Figure 6.65, the SVD could separate the signals into the groups of the patterns with the same statistical properties, but it could not preserve the down-going and the reflection peaks' patterns as expected.

Figure 6.66 illustrates the principal components of the experimental signals captured from the timber pole with the standing-on-soil condition.

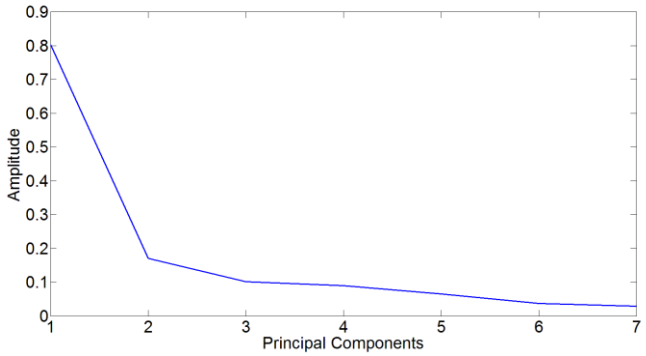

Figure 6.66: Principal components of the captured signals from the timber pole with the standing-on-soil condition

Figure 6.67 demonstrates the original signals captured from the timber pole with the standing-on-soil condition in the laboratory test. It can be seen that although the PCA could separate the similar patterns in the signals, no clear pattern is observable in the results.

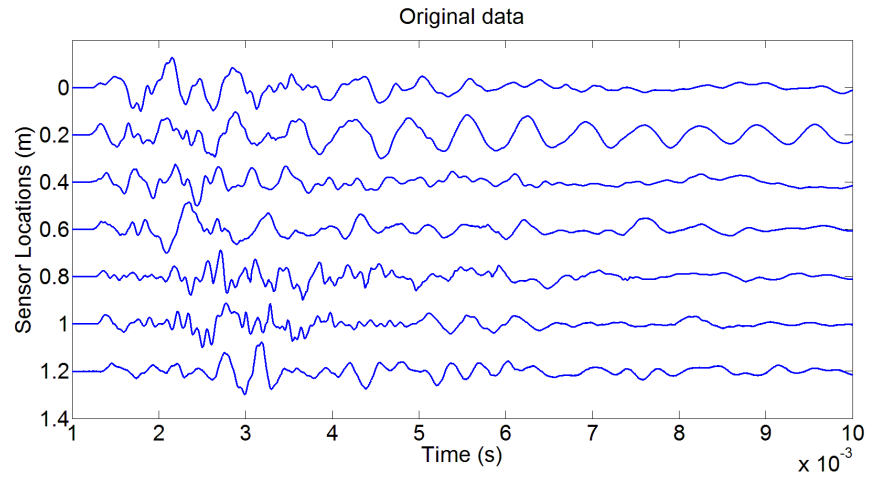

(a)

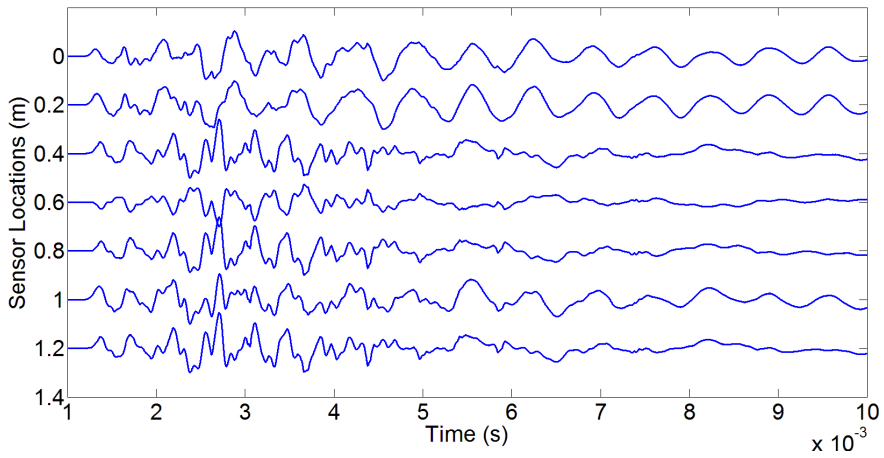

(b)

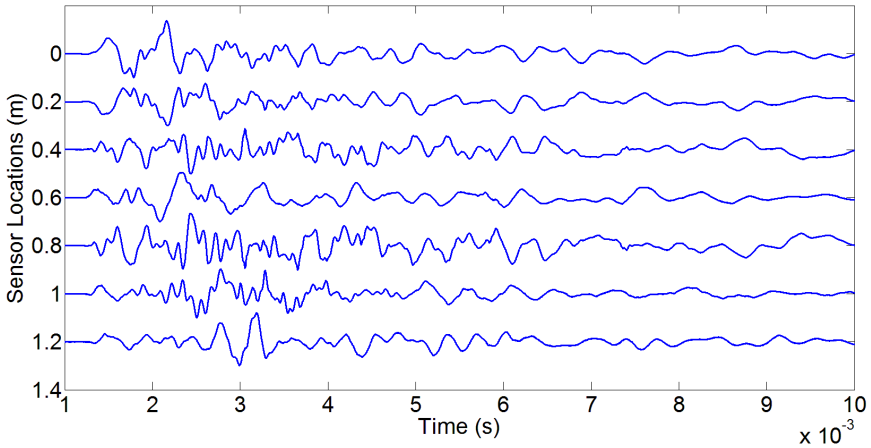

(c)

Figure 6.67: (a): Original captured signals; and the signals that transferred back to the time domain (b): using the first two most important principal components, and (c) using the rest of the principal components for the timber pole with the standing-on-soil condition

6.5 Conclusions

In this chapter, some modified advanced digital signal processing methodologies including the deterministic, blind signal separation methods, and frequency-wavenumber velocity filter are employed in order to overcome the intrinsic existing complexities (explained earlier in Chapter 2) in the captured signals from the timber utility poles. Since the phase and group velocities can be obtained from the dispersion relation of the timber pole, Frequency-Wavenumber analysis (velocity filtering) is also investigated on the captured signals from the timber poles.

The predictive deconvolution is the main deterministic signal separation method, while the PCA, the SVD, and the *K*-mean clustering are the blind signal separation methods that are employed in the second phase of this research. All of the proposed methodologies are applied on the data captured from the simulated timber poles with the isotropic and orthotropic material properties with the both standing-on-soil and embedded conditions. The results of applying the deterministic signal separation methodologies on the simulated timber poles with the isotropic material properties illustrated that the down-going and the reflection peaks' patterns can be preserved and the velocities of both patterns (the up- and down-going waves) can be estimated with high fitting accuracies. The length of the pole can also be estimated with the acceptable

accuracy of less than 10% error. In the embedded condition applying the decrement factor (which refers to the velocity decrement in the soil section due to the energy absorption), the embedment length can be estimated more accurately.

The results of applying the deterministic signal separation methodologies on the simulated timber pole with the orthotropic material properties demonstrated that although the first arrivals peaks' pattern is detectable and the down-going wave velocity can be estimated with acceptable fitting accuracy, the reflection peaks' pattern cannot be preserved. In the following, the possible reasons of this phenomenon are explained.

One of the main assumptions in the deterministic signal separation methods is that the statistical properties of the different patterns that exist in the captured signal are not changing during the capturing time, which means that the captured signals are stationary or wide-sense stationary.

Conclusion 1: Considering the dispersion relation and the spectrum curves, the timber pole with the isotropic material properties behaves as a non-dispersive material in the frequency range of the hammer excitation impact, while the timber pole with the orthotropic material properties behaves as a highly dispersive medium. This is due to the presence of the two waves (i.e. longitudinal and bending) and their branches in the frequency range of the hammer excitation impact (see Figure 6.38).

Two very simple examples were also provided in this chapter. In the first example the concept of the dispersion in the Linear Time-Invariant (LTI) system and its effects on the captured signals was explained simply. In the second simple example, one LTI system, which includes two different LTI systems was assumed, where one was a non-dispersive, and the other was a dispersive systems, and the output of the overall system was the summation of both of the LTI systems (Figure 6.34). In this example, the effects of the presence of two different LTI systems on the overall output are shown in the simplest approach. In the case of the orthotropic timber pole, each branch can be assumed as a highly dispersive LTI system. Each of these LTI systems based on their dispersion behaviours produces different outputs, and the overall output of the timber pole (i.e. the captured signal by the sensor) is the summation of all of the LTI systems' outputs. It is essential to consider that the hammer impact at a 45 degree angle excites

the timber pole in the broadband frequency range of 0 to almost 5 kHz. Based on the spectrum curves (Figure 6.38), changes of the phase velocities in each branch is highly non-linear in the broadband frequency range. Thus, even assuming a single branch in the hammer impact frequency range, the overall shape of the propagating wave changes and is not amendable. This means that the captured signal is non-stationary. Furthermore, considering the presence of all of the several branches with highly dispersive behaviour in the hammer excitation impact frequency range (i.e. all of the longitudinal and the bending waves' branches in the frequency range of 0 to almost 5 kHz), the interference between them is unamendable in the captured signal.

Conclusion 2 (a): Because the simulated isotropic timber pole acts as a non-dispersive medium in the frequency range of the hammer excitation, utilizing deterministic signal separation methods could obtain the reflection peaks from the bottom of the pole, and the length could be estimated with an acceptable accuracy.

Conclusion 2 (b): Since the simulated orthotropic timber pole acts a highly dispersive medium in the frequency range of the hammer excitation, and due to the interference between existing branches in this frequency range, deterministic signal separation methods were not effective and could not preserve the reflection peaks.

Conclusion 2 (c): Although applying the frequency-wavenumber velocity filtering could separate the longitudinal waves from the bending ones, the interference between the branches makes the reflection peaks detection impossible. This was explained in a very simple approach by two examples in this chapter.

In the simulated isotropic timber pole, since for both of the longitudinal and the bending wave only one branch exists and the longitudinal wave is the dominant wave, only one velocity can be observed in the F-K domain. Furthermore, for the longitudinal wave all of the frequency components travel with constant velocity (i.e. phase velocities and group velocities are the same) in the frequency range of the hammer impact. In this situation, not only the captured signals are stationary or wide sense stationary, but also the interference between the existing two branches is ignorable. This is the main reason that by employing the modified advanced digital signal processing methodologies and the conventional stress-wave-based methods, the pattern of the reflection peaks were detectable. While in the simulated orthotropic timber pole, the experimental and the

field-tests' data, the aforementioned methodologies were not effective and the reflection peaks' pattern could not be preserved.

Applications of the blind signal separation methods revealed that PCA and SVD can preserve the main patterns (related to the up- and down-travelling waves) of the signal. In fact, they can be applied to remove the noise from the signal. These methods are based on the second order statistics and since the up- and down-travelling waves have the same statistical properties, they cannot be separated by these methods. This situation became worse when they are applied to the data captured from the simulated orthotropic timber pole, in which the statistical properties change during the capturing time. Application of the *K*-mean clustering demonstrated that although this method can separate the longitudinal and the bending waves from each other, the reflection peaks from the bottom of the pole could not be detected due to the interference between the waves' branches.

Conclusion 3 (a): Applications of the blind signal separation methods revealed that, PCA and SVD can preserve the main patterns (related to the up- and down-travelling waves) of the signal. In fact, they can be applied to remove the noise from the signal.

Conclusion 3 (b): Application of the *K*-mean clustering demonstrated that although this method can separate the longitudinal and the bending waves from each other, the reflection peaks from the bottom of the pole could not be detected due to the interference between waves' branches.

Main conclusion of this chapter

As a main conclusion of this chapter, considering the fact that the behaviour of the timber pole under the lateral and angled broadband low frequency excitation (i.e. the hammer impact on side of the timber pole at a 45° angle) is very complicated. Dealing with this high level of the complexities is not impossible; it is a very difficult task. In this regard, the author strongly recommends exciting the timber pole with a narrowband frequency input in order to minimize the dispersion effects on the captured signals.

It is also necessary to consider that for future work on damage detection, low frequency excitation (hammer impact- i.e. 0to 5 kHz) is not suitable especially for small damages due to the relatively large wavelengths of the low frequencies. In this regard, in the next chapter firstly applications of an ultrasonic single frequency excitation will be investigated. Secondly based on the limitation of the ultrasonic single frequency excitation, a specific type of narrowband ultrasonic excitation along with a very fast signal processing procedure will be proposed, and investigated.

It is also worth mentioning that one conference paper have been written and submitted based on the work of chapter 6.

7 Chapter 7: Ultrasonic narrowband chirped pulse: an alternative proposition

7.1 Introduction

Ultrasonic Non-Destructive Testing (NDT) techniques have been widely used in the Civil engineering field for both structure condition assessment and material characterization without causing any damage. Pulse based methods are amongst the most commonly applied ultrasonic NDTs in the Civil engineering field [22]. As a part of the development process, limitations of the pulse NDT methods were discovered. In many cases, these are set by the tested specimen's material, its geometry, its defects, and the wave propagation theory in the specific related material [110]. Major limitations of these methods are due to the dispersion properties of tested specimens and wave attenuation in materials such as timber in which the attenuation can be very severe. Pulse methods can be categorized into three main groups: pulse-echo, pitch-patch or time-of-flight diffraction, and transmission through or time-of-flight methods [22].

In the pulse-echo methods an ultrasonic transducer is used firstly to transmit the signal through the media and then to capture the response. Major shortcomings of this method are firstly that limited thickness can be measured because of wave attenuation, and secondly, in the presence of a significant damage no reflection can be detected from the bottom or other side of the specimen. As a result, determining the specimen thickness is impossible.

Pitch-patch or time-of-flight diffraction methods were developed to overcome the second shortcoming of the pulse-echo method. However, the first shortcoming due to the attenuation remains unsolved. In this method, two ultrasonic transducers are used on the same side of the specimen, one as a transmitter and other as a receiver. In the presence of damage, mainly four wave packets will be received. The direct transmission or cross-talk between the transmitter and the receiver, the first reflection from the top of the defect, the second reflection from the bottom of the defect, and the final reflection from the bottom of the specimen. Pulse-echo and pitch-patch tests are ideal in cases

where accessibility to both sides of the structure is not possible (such as bridge piles). Figure 7.1 shows the time-of-flight diffraction test setup.

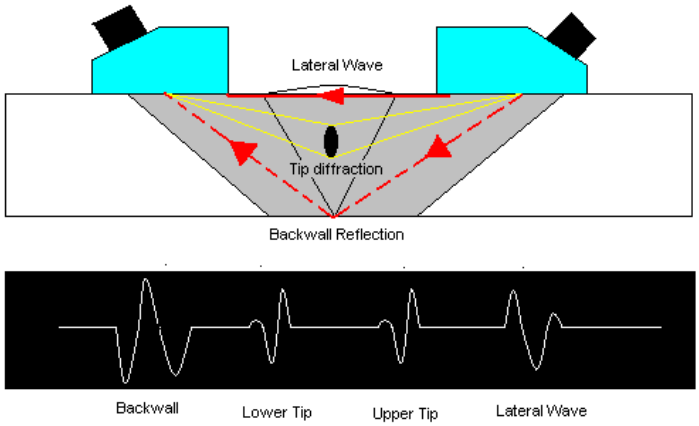

Figure 7.1: The Ultrasonic time-of-flight diffraction test setup

Finally, in the third group of the pulse methods known as transmission-through or time-of-flight (TOF) tests, like the pitch-patch method, two ultrasonic transducers are used but on opposite sides of the tested specimen. These methods are used for material characterization and tomography.

Several researchers have utilized the ultrasonic pulse methods for several applications. Fritsch and Veca used the pulse-echo method to detect small and near surface defects in aluminium specimens [111]. Tartnik and Gams used both ultrasonic pulse transmission-through and pulse-echo methods to monitor cement based materials in their early age and hydration process [112]. Praveen et al also improved the signal to noise ratio of ultrasonic pitch-path or time-of-flight diffraction test signals captured from stainless steel welds by applying wavelet analysis [113]. Bogas et al also utilized ultrasonic pulse velocity methods to evaluate the compressive strength (one of the material properties) of light weight concretes with different mixture parameters [114]. Some other applications of ultrasonic pulse methods in the material characterization or condition assessment can be found in [115], [116], [117], [118], [119], [120].

Timbers are well known as being highly dispersive and attenuating materials. Their condition assessment has been one of the major challenges in the structure health-monitoring field. Due to considerably high attenuation of the ultrasonic waves in wood, effective and industrial ultrasonic pulse NDT inspection is usually limited to only

transmission-through tests. In fact, high attenuation limits the applicability of even transmission through ultrasonic tests to timbers with relatively small cross-section areas [121], [122]. This means that they cannot be applied to timbers with large cross sections in heavy timber structures. Another factor which is worth noting is that in most cases of the pulse-echo or pitch-patch methods, captured signals cannot be analysed directly in the time domain. If the transmitting pulse duration in these methods exceeds a specific threshold, interference between transmitted and captured signals is unavoidable. This makes it impossible to detect the reflected signals in the time domain. Several signal processing methodologies such as the Wiener filter or deconvolution have been applied by many researchers and also in industry to overcome this limitation [123]. In this situation, it is necessary to create narrowband transmission pulses otherwise results will be unreliable and faulty due to the dispersion effects. Normally the centre frequency and number of cycles are determined in a way to assure minimum dispersion effects [124].

Another way to overcome the attenuation problem or improve the signal to noise ratio is by using broadband coded excitation signals like chirp, or white noise in a relatively long time. In these situations, the energy of the excitation is considerably increased. Signal processing of this method usually includes pulse compression techniques [125], [126].

In this chapter, an ultrasonic narrowband chirped pulse excitation was utilized in order to overcome the shortcomings of the conventional and current ultrasonic pulse NDTs in the condition assessment of timber structures. Narrowband excitation was chosen in order to minimize the effect of dispersion. Results were calculated directly from the chirped pulse response by simple and fast signal processing procedures. Experimental investigations in this chapter proceeded as follows. Firstly, an ultrasonic pulse (centred at 40 kHz) testing system was designed and implemented. Then two sets of experiments were performed. The first set relates to the transmission-through tests utilizing conventional single frequency ultrasonic pulse methods. They were performed on a 1 m timber beam with the intention of achieving the required accuracy of the implemented ultrasonic system in a single frequency pulse method. The second sets of tests, which relate to the proposed ultrasonic chirped pulse method, were performed firstly on the air (as the tested medium), and then on a 4 m timber beam for transmission-through tests. The proposed signal processing procedure did not need powerful computers for

processing and results could obtained in a short time. Furthermore, by utilizing the proposed methodology in this chapter, considerably longer timber specimens could be inspected in the transmission-through tests. Finally, the accuracy of the transmission-through or time-of-flight test has been considerably improved utilizing the proposed chirped pulse method.

7.2 Review of the Theory

A chirp is a signal in which frequency changes over time and, based on the application, this change can be linear on non-linear. In a simple chirped signal, frequency increases or decreases linearly with time. The chirped pulse is obtained by equation (7.1).

$$Y_{Chirp}(t) = Cos[2\pi * f(t) * t] \tag{7. 1}$$

where $f(t)$ is a frequency increment function, and obtained by the equation:

$$f(t) = f_0 + \frac{kt}{2} \tag{7. 2}$$

where $k = \frac{f_1 - f_0}{t_{Chirp}}$

here k is the frequency increment factor, and f_0 is the initial frequency. Many researchers have utilized the chirped pulse compression technique in a broadband frequency range (which varies from a couple of hundred kHz to a couple of MHz) in the ultrasonic NDT mostly with the intension of improving the signal to noise ratio [125]. Michaels et al proposed an effective method for extracting ultrasonic single frequency response from a single broadband chirped excitation. They transmitted a chirped broadband pulse signal through an aluminium plate to obtain multi-modal (broadband) response by a single excitation, next they successfully calculated the specimen single frequency excitation response from the chirped pulse response, and then they used the calculated responses to image the damage [127]. In their follow up work in [128], high signal to noise ratio was achieved by combining chirped excitation and efficient guided-wave implementation data acquisition. In this research, linear frequency increment or "up-chirp" is used with different chirp time starting from 6 ms and ends to up at 14 ms

(where maximum transmission time is less than 2 ms). Figure 7.2 shows a sample of chirped pulse before modulation and its related spectrogram.

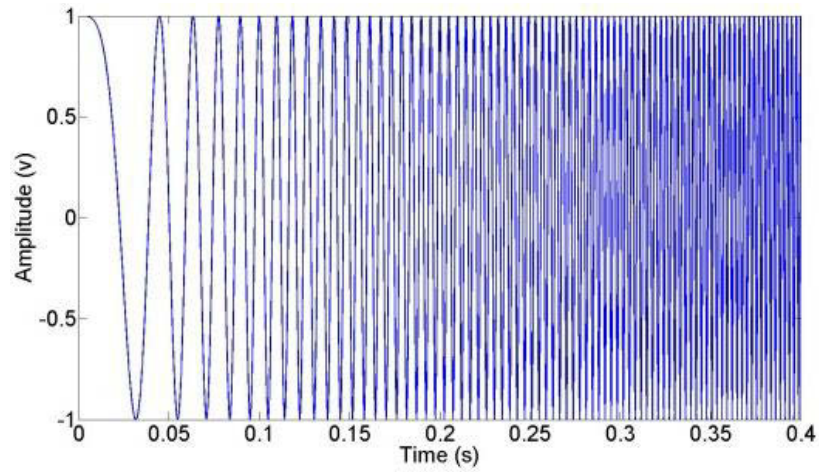

(a)

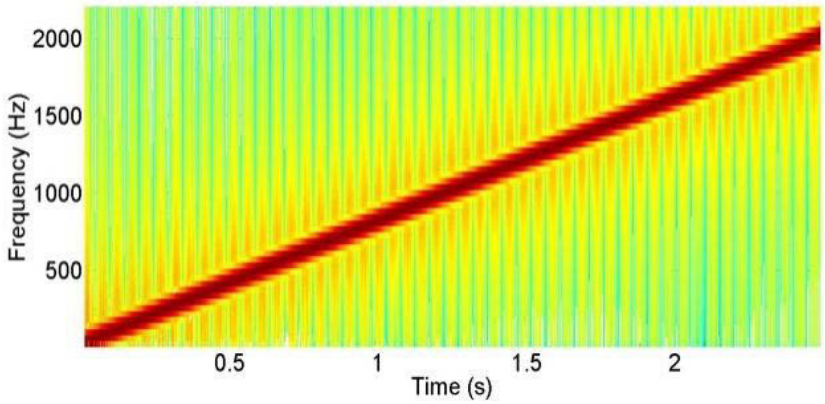

(b)

Figure 7.2: utilized simple linear chirp signal with 2 kHz bandwidth (a) time domain, signal is zoomed in up to 0.4 s for better illustration, and (b) spectrogram.

The transmitted chirped pulse will travel through the media as a wave packet with a defined frequency spectrum. Consider the chirped pulse for the transmission-through (time-of-flight) test. The transmitted pulse (wave packet) will arrive at the receiver with delays in time. Figure 7.3 illustrates this situation (for the sake of simple illustration and explanation, attenuation is not considered in Figure 7.3).

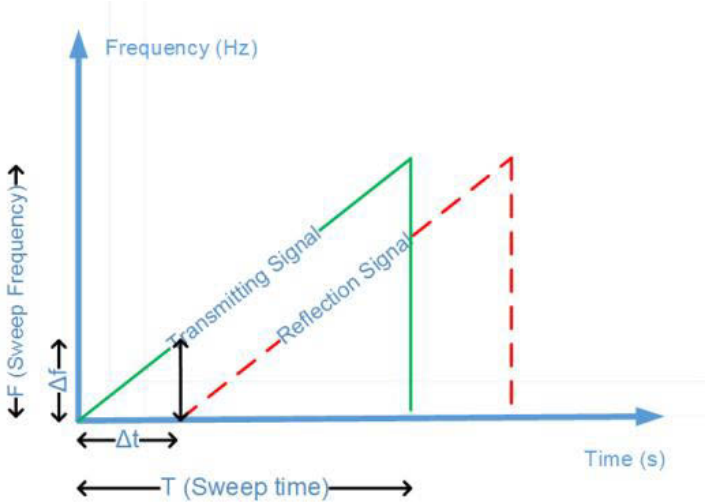

Figure 7.3: Illustration of transmitting (green line) and receiving (dashed red line) chirped pulse in transmission through ultrasonic NDT

In Figure 7.3, Δt is the time difference between transmitted and received signals which in fact is the required transmission time in the time-of-flight test and is twice the required time in pitch-patch or pulse-echo tests. Δf (frequency difference between transmitted and received signal) and Δt are related through Equation (7. 3).

$$\Delta t / T = \Delta f / F \tag{7. 3}$$

Chirped time (T), and chirped bandwidth (F) are known, the Δf is obtained by the signal processing procedure (explained in section 7.3), Δt can be calculated. Knowing the wave velocity, length also can be estimated in the transmission-through test; see Equation (7. 4)

$$L_{TOF} = Velocity * \Delta t \tag{7. 4}$$

7.3 Signal processing procedure

Figure 7.4 shows the proposed signal processing procedure. Firstly, the created chirped pulse should be modulated to the ultrasonic range. In this regard, a sinusoidal 40 kHz wave is used as a carrier signal. The final transmitting signal can be described as a wave packet centred in the ultrasonic range of 40 kHz (carrier signal), and the chirped pulse as an information signal (with 2 kHz of bandwidth). A 40 kHz is chosen since in the

range of ultrasonic frequencies (39 to 41 KHz), dispersion in longitudinal waves is minimum [47].

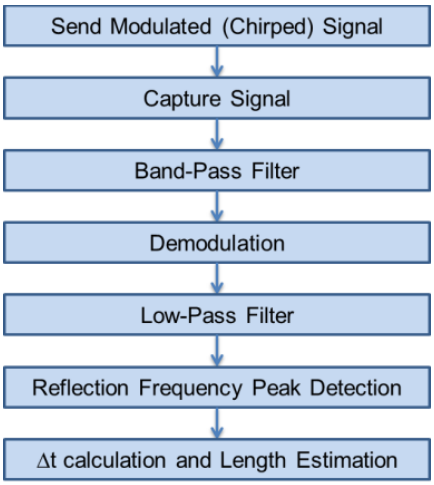

Figure 7.4: proposed signal processing procedure for fast and accurate ultrasonic chirped pulse NDT

It should be considered that the dispersion relation is obtained from wave guide theory in which the curves depend on the dimensions, shape, and material properties of the structure. In this regard, the bandwidth for the chirped pulse should be determined based on new calculations if the characteristics of the timber structure change significantly. In this work, longitudinal wave velocity was assumed to be 5000 m/s [47], and the bandwidth of the chirped pulse assumed to be 2 kHz for all experiments. After modulation, the timber specimen will be excited with the transmission signal, and the structure response will be captured afterwards. The next step is applying the band-pass filter to preserve the modulated signal frequency range and remove the rest. Demodulation is the following step in order to remove the effect of the 40 kHz carrier signal from the filtered captured signal. Since the chirped pulse bandwidth is 2 kHz, applying a low-pass filter will remove all other higher frequency components. Finally, transmission time (Δt) can be calculated as explained in section 7.2. It is also necessary to consider that the chirp pulse duration should be carefully determined. As can be seen in Figure 7.3, if the transmission signal time is much larger than the reflection time, the proportion of $\Delta t/T$ will be small and detecting the arrival peak will be more difficult. On the other hand, the energy of the transmission signal is directly proportional to its length. In connection with these points, the following factors should be considered in the chirp pulse length determination: approximate length of the tested specimen,

approximate wave velocity in the specimen, and the minimum energy required for the transmission signal.

7.4 Experimental test setup

The equipment necessary to perform the ultrasonic time-of-flight tests consists of two ultrasonic transducers, an amplifying circuit for a captured signal, a data acquisition system and a personal computer equipped with signal acquisition software. The block diagram of the implemented ultrasonic NDT system for the time-of-flight test is shown in Figure 7.5.

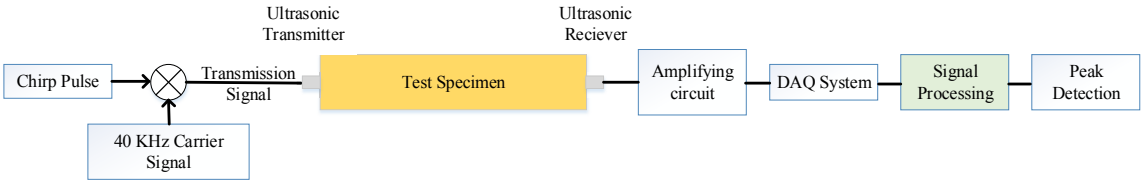

Figure 7.5: The block diagram of implemented ultrasonic NDT system

7.4.1 Ultrasonic Transducers

In this work, a pair of very cheap ultrasonic 40 kHz transducer (5 AUD each), as shown in Figure 7.6, has been used as transmitter and receiver. These transducers have a maximum of 4 kHz of transmission bandwidth (i.e. signals with less than 38 kHz and more than 42 kHz will not be transmitted).

Figure 7.6: The Ultrasonic 40 kHz transducer

7.4.2 Receiver signal amplifier circuit

The implemented circuit (shown in Figure 7.7 (a)) has been designed to amplify the captured signal 400 times. The commercial TL072 JFET Operational Amplifiers have

been used in this circuit. Figure 7.7 show the schematic and implemented circuit on the perfboard.

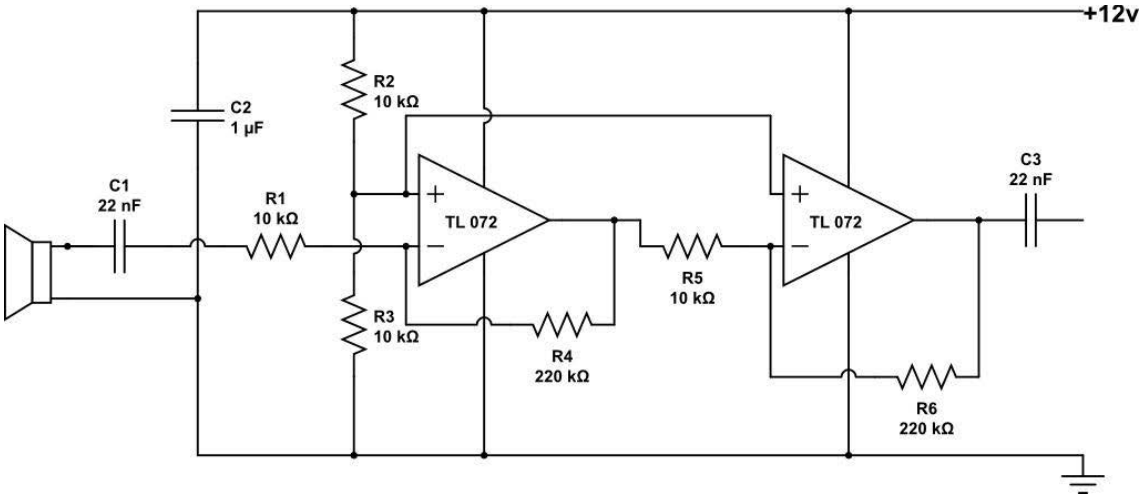

(a)

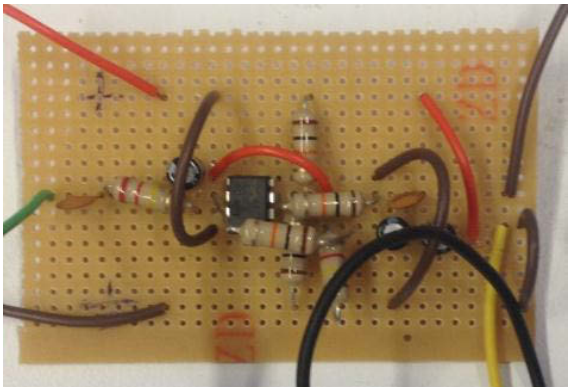

(b)

Figure 7.7: The receiver signal amplifying circuit (a) the schematics, and (b) implemented on the perfboard

7.4.3 Data Acquisition Systems

Two data acquisition systems were used as a transmitter and a receiver. One myDAQ data acquisition system from National Instrument and a Picoscope series 5000 from the Pico Technology were used as the transmitter and the receiver. Figure 7.8 shows both of the data acquisition systems.

(a) (b)

Figure 7.8: (a) the transmitter, and (b) the receiver data acquisition systems

7.4.4 Data Acquisition Software

Picoscope software version 6 was used as a data capturing software. This software was developed by Pico Technology to be used with the related data acquisition system. An Equiripple finite impulse response filter was applied by zero-phase filtering technique in order to minimize any phase shift effect that could be imposed to the captured signal by the digital filter. Sampling frequency was set on 2MHz in order to avoid any round up error.

7.5 Laboratory test setups

For both set of tests (i.e. single frequency and chirped) two timber specimens from the same species but different in length have been used. The reason for using specimens with different lengths is due to both methods limitations as the single frequency technique cannot be applied on specimens longer than almost 3 m and the proposed chirped method can be effectively applied on considerably longer specimen. For single frequency tests, a timber with the following dimensions has been used: 0.04 m width, 0.02 depth, and 1 m length. The aim of the tests was to obtain the accuracy of implemented ultrasonic NDT system in a single frequency excitation. Figure 7.9 shows the test set up for the transmission-through tests in the single frequency excitation.

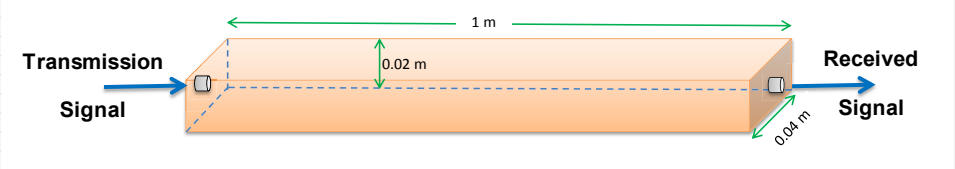

Figure 7.9: The transmission through or time-of-flight tests setup for the ultrasonic single frequency excitation

In the ultrasonic chirped pulse method, two sets of tests were performed. Firstly, to avoid the complexity of the timber structure and for the proof of the proposed methodology, the chirped pulse method was tested on the air. Figure 7.10 illustrates the air test setup.

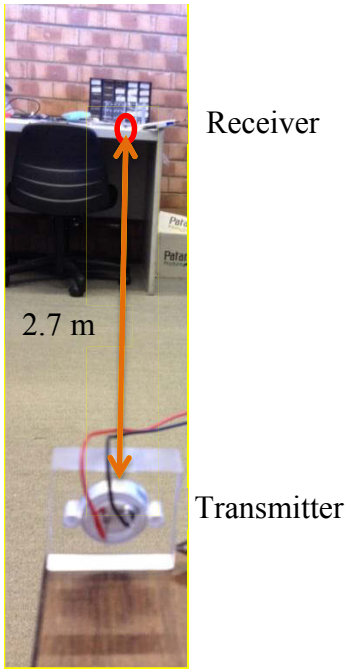

Figure 7.10: The Ultrasonic narrowband chirped pulse air test setup

Secondly, the proposed methodology was tested on the 4 m timber (0.04 m width, 0.02 depth, and 4 m length). Figure 7.11 show the test setup for the transmission-through tests in the 4 m timber. It is also worth mention that two beams with different lengths but from same species are chosen for the single frequency and chirped pulse tests because of the limitation of each method. Chirp pulse method cannot be used on the beams lower that 3 m in length because otherwise, the obtained reflection peak in the frequency domain after signal processing will be so close to zero and detecting it will be so much difficult. On the other hand due to the high attenuation of the stress waves in the ultrasonic range, single frequency pulse cannot be used on the 3 m or larger beams.

Figure 7.11: The Ultrasonic narrowband chirped pulse test setups in the 4 m timber for the transmission-through or the time-of-flight test (two transducers on both sides)

As mentioned earlier, two types of ultrasonic tests were performed. In both sets, the time-of-flight test was performed. In the first set, the length of the tested specimen was estimated using the ultrasonic single frequency pulse signal. The length of the pulse, or in other words, the number of cycles per pulse was changed from a single cycle to 100 cycles per pulse. In the next set of tests, firstly the ultrasonic chirp pulse signal was tested on the air (i.e. the air used as a tested medium) in order to verify the proposed theory and avoid the complexities of the timber; secondly the proposed methodology was utilized to estimate the length of the timber beam. It is also necessary to mention that the length of the specimen, time-of-flight, and the velocity of the wave in the specimen are directly related to each other. In fact, having two of these factors, the third can be calculated easily. Although in the typical condition assessment NDTs, changes in the time-of-flight was used as a measurement for the integrity of the specimen, in this work, length estimation was used in order to have a reliable measurement to compare the accuracy of the single frequency method with the proposed chirp method.

All of the previously mentioned tests were performed in the laboratory of the Centre of Real-Time Information Networks (CRIN) in the University of Technology Sydney (UTS).

7.6 Experimental Data Analysis

In this section, the results of the ultrasonic single frequency and the proposed chirp pulse tests are analysed and illustrated.

7.6.1 The Ultrasonic Single Frequency tests

In this section, the results of the time-of-flight (TOF) tests utilizing the single frequency pulse method are provided. It is essential to consider that the main goal of these tests was to obtain the accuracy of the implemented ultrasonic NDT system as a benchmark for later comparisons with the ultrasonic chirp pulse method results. The test setup for the time-of-flight tests is shown in Figure 7.9. As mentioned earlier, the centre frequency was set up at 40 kHz, and the sampling frequency was 2 MHz. Figure 7.12 shows the transmitted and the captured signals from TOF tests with several pulse durations in the 1 m timber beam specimen.

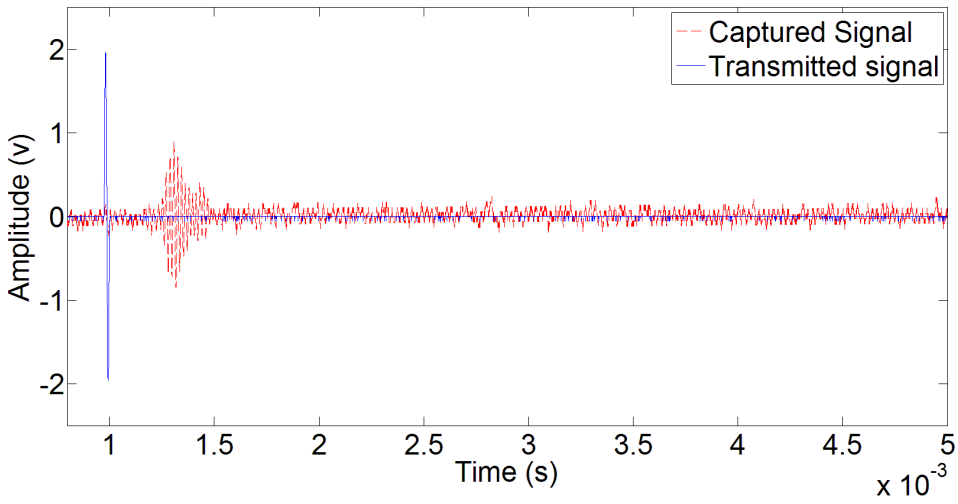

(a)

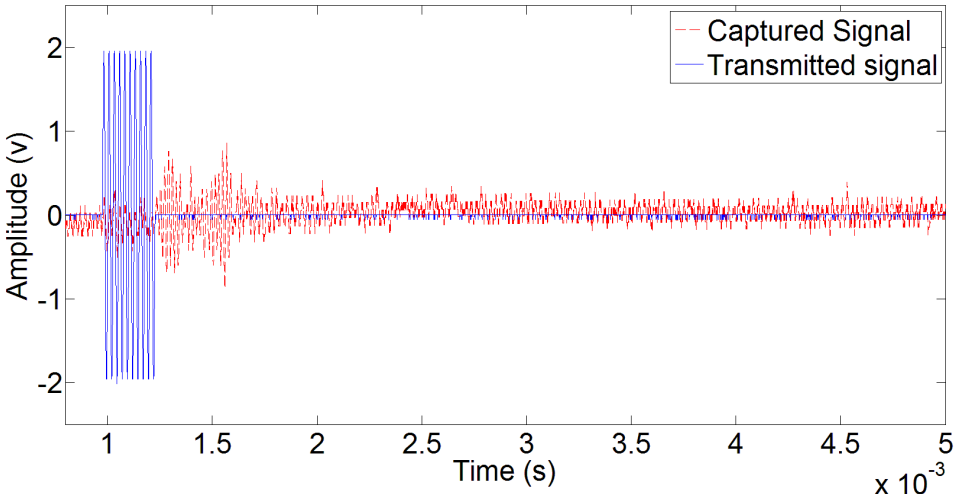
Captured Signal
Transmitted signal
Amplitude (v)
Time (s)
x 10^-3

(b)

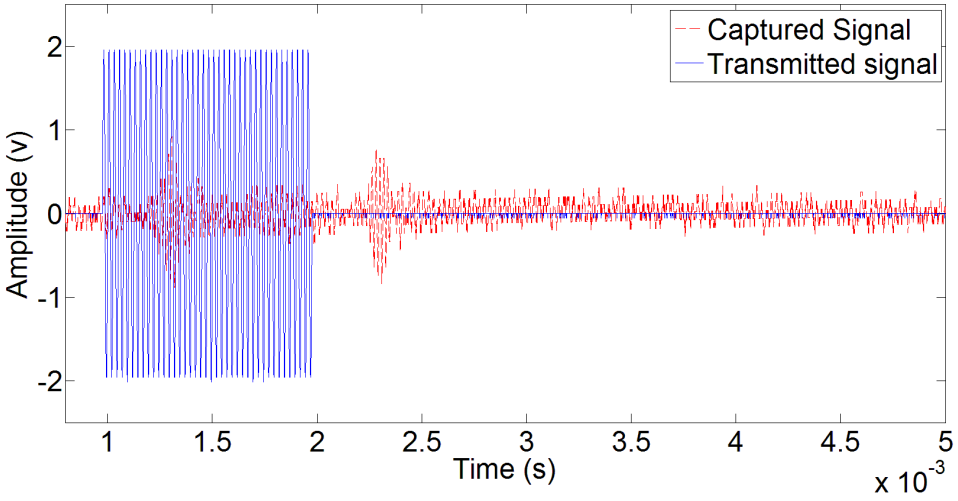
Captured Signal
Transmitted signal
Amplitude (v)
Time (s)
x 10^-3

(c)

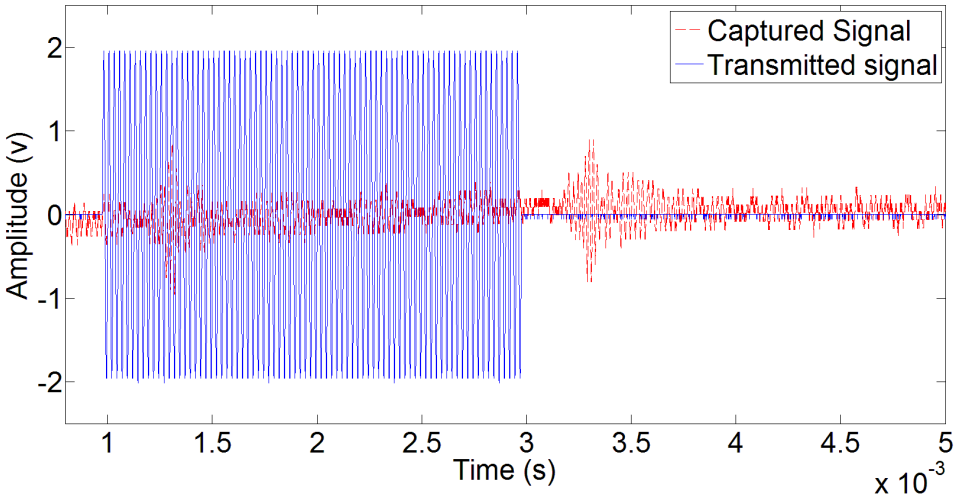
Captured Signal
Transmitted signal
Amplitude (v)
Time (s)
x 10^-3

(d)

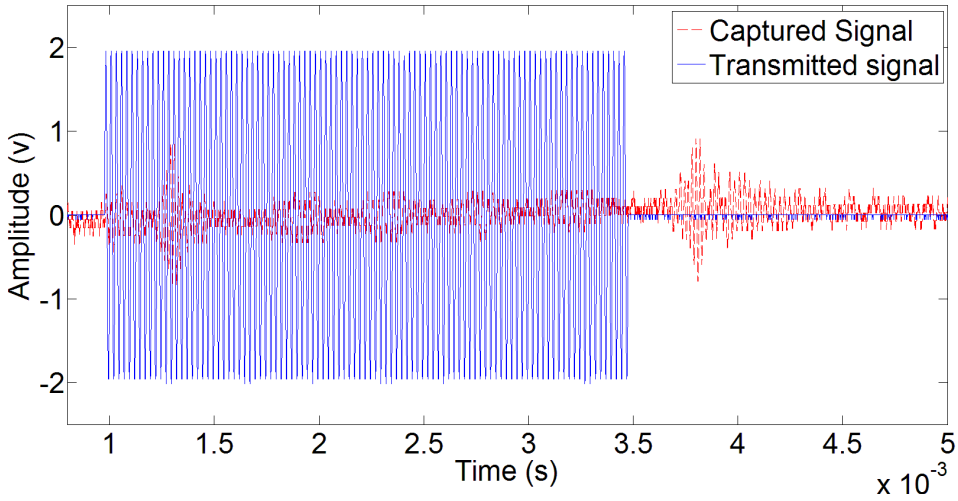

(e)

Figure 7.12: Transmitted and captured signals in the ultrasonic Single Frequency (40 kHz) time-of-flight tests with (a) one, (b) ten, (c) 40, (d) 80, and (e) 100 cycles per pulse

The length estimation results are also provided in Table 7.1. The length of the tested specimen is 1 m, and the wave velocity is assumed as 5000 m/s.

Table 7.1: Ultrasonic single frequency (40 kHz) time-of-flight tests' length estimation results with different pulse durations in the 1 m timber beam specimen

Cycles	Time-of-flight (μs)	Estimated length(m)	Error%
1	270	1.35	35
10	272	1.36	36
40	273	1.365	36.5
80	274	1.37	37
100	275	1.375	37.5

As can be seen in Table 7.1, the length estimation errors are relatively constant or fluctuating in a very small range. It is worth noting again that although the errors are relatively high, the main goal of these tests was to obtain a benchmark for the proposed chirp pulse methodology results. The length estimation errors are demonstrated in Figure 7.13.

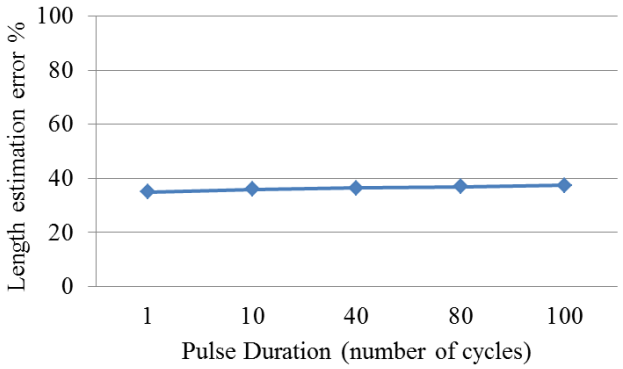

Figure 7.13: Ultrasonic single frequency (40 kHz) time-of-flight tests' length estimation errors for different pulse duration in the 1 m timber beam specimen

7.6.2 The Ultrasonic Narrowband Chirp pulse tests

This section's tests can be categorized into two groups. First, the proposed chirp methodology was utilized for TOF tests on the air in order to verify the effectiveness of the methodology and avoid the complexities of the timber material. The second set of tests was related to the TOF tests of a 4 m timber beam in a free-free condition. Length estimation errors were then compared to the single frequency test results from the previous section.

The Chirped pulse TOF tests for the length estimation in the air

The test setup is shown in Figure 7.10. The ultrasound wave's velocity in the air is 343 m/s, which was assumed here as well. The tests in this section were performed using the chirp pulses with different durations (T in Figure 7.3). Duration of the transmission signals are determined by considering the wave velocity in the medium (the air) and the distance between the transducers. In the real-world applications where no prior information is provided, the transmission signal duration can be set to the minimum at the beginning and it then increases linearly until the reflection peaks are detectable. The output signals (frequency domain) of the signal processing algorithm for the transmitting signals with different time lengths are shown in Figure 7.14.

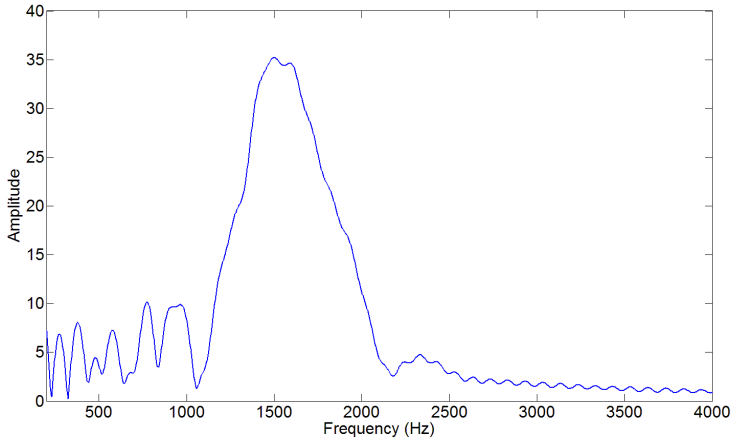

(a)

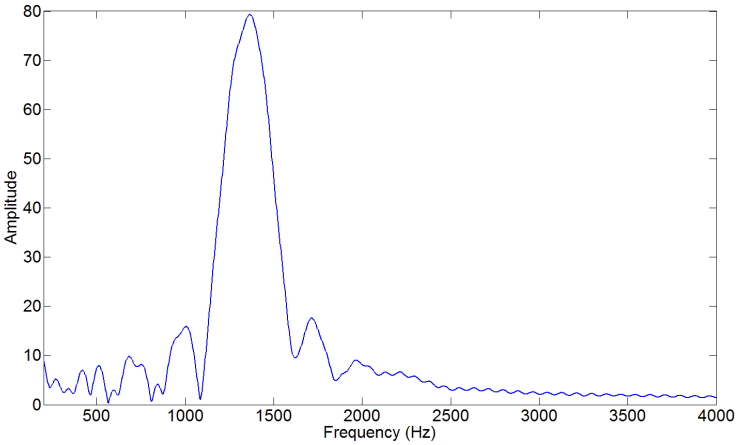

(b)

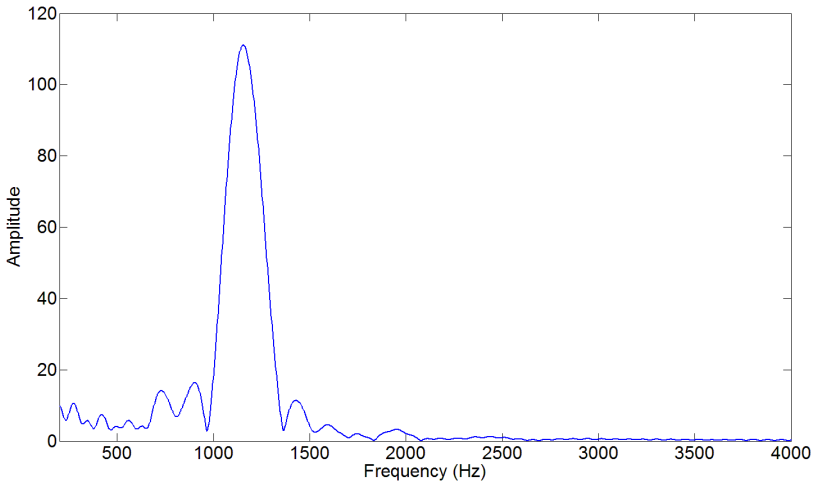

(c)

Figure 7.14: Output signals from the proposed chirp pulse signal processing algorithm for the transmitting signals with (a) 10 ms, (b) 12 ms, and (c) 14 ms duration in the TOF tests in the air

As can be seen in Figure 7.14 and as expected, the reflection peak is moving toward zero Hz as the transmission signal time length is increasing. The reflection time (Δt) can be calculated using equation (7.3). The length estimation results are also provided in Table 7.2.

Table 7.2: Length estimation results for the chirp pulse TOF tests on the air

Pulse duration (ms)	Δf (Hz)	Δt (s)	estimated length (m)	Error %
10	1530	0.00765	2.62	-2.8
12	1355	0.00813	2.78	3.28
14	1140	0.00798	2.73	1.37

As can be seen in Table 7.2, the distance between transducers can be estimated with very high accuracy (less than 4% error), which shows the effectiveness of the proposed methodology.

The Chirped pulse TOF tests for length estimation in the 4 m timber beam

The test setup is shown in Figure 7.11. In these tests, the transmission signal durations are 6, 8, 10, 12, and 14 ms. The length of the timber beam is 4 m, and the wave velocity is assumed as 5000 m/s as explained earlier in this chapter. Figure 7.15 shows the output signals of the signal processing algorithm for transmission signals with different time lengths.

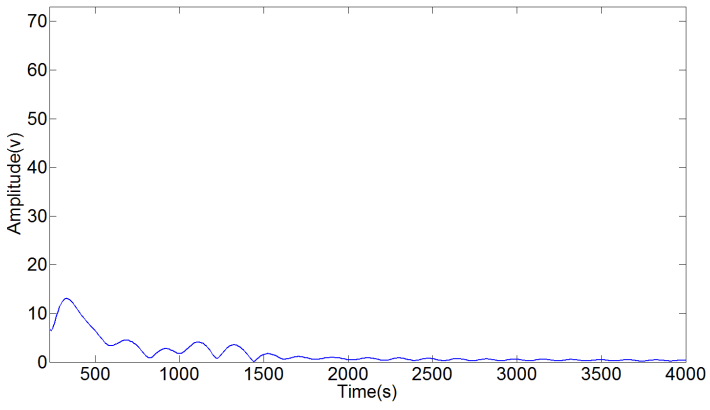

(a)

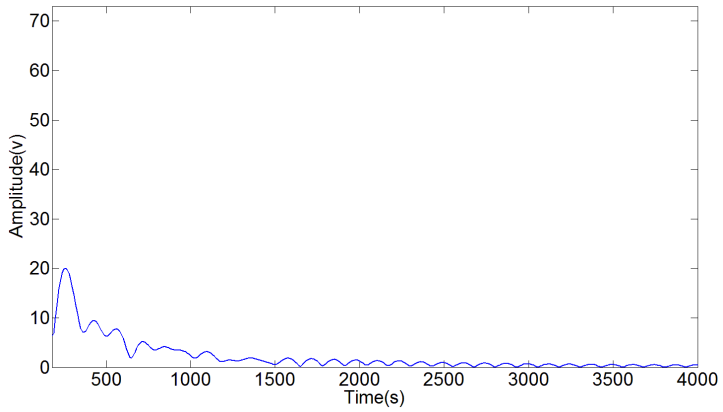
Amplitude(v)
Time(s)
0
10
20
30
40
50
60
70
500
1000
1500
2000
2500
3000
3500
4000

(b)

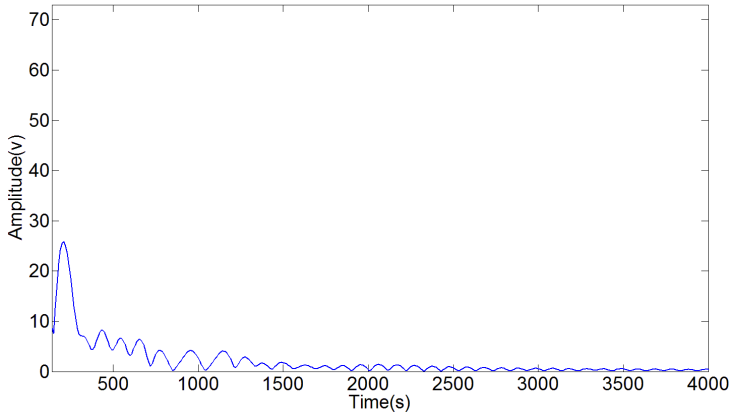
Amplitude(v)
Time(s)
0
10
20
30
40
50
60
70
500
1000
1500
2000
2500
3000
3500
4000

(c)

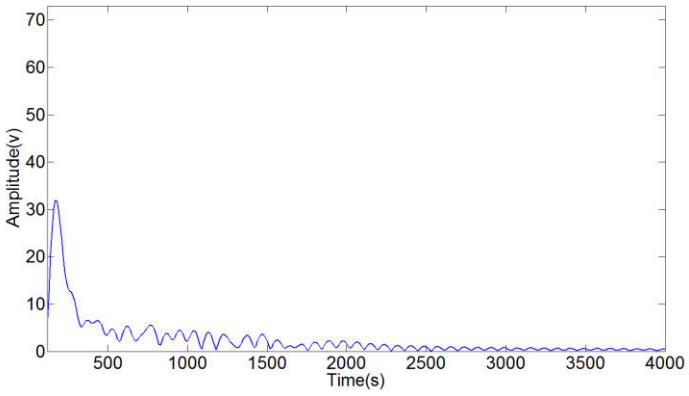
Amplitude(v)
Time(s)
0
10
20
30
40
50
60
70
500
1000
1500
2000
2500
3000
3500
4000

(d)

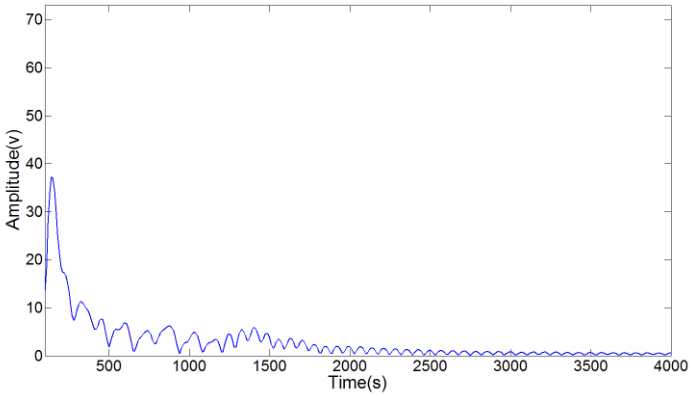

(e)

Figure 7.15: Output signals from the proposed chirp pulse signal processing algorithm for the transmitting signals with (a) 6 ms, (b) 8 ms, (c) 10, (d) 12, and (e) 14 ms duration in TOF tests on the 4 m timber beam

It can be seen in Figure 7.15 that not only the peak related to the arrival wave is moving toward zero as the transmission signal time length increases, but its amplitude is also increasing. This shows that as the longer the transmission signal is, more energy can be transmitted through the medium. The length estimation results are provided in Table 7.3.

Table 7.3: Length estimation results for the chirp pulse TOF tests on 4 m timber beam

Transmission chirp signal length (ms)	Δf (Hz)	Δt (s)	Estimated length (m)	Error %
6	320	0.00096	4.8	20
8	245	0.00098	4.9	22.5
10	195	0.000975	4.88	22
12	160	0.00096	4.8	20
14	140	0.00098	4.9	22.5

Figure 7.16 illustrates the length estimation errors for the transmission chirp signals with different time lengths.

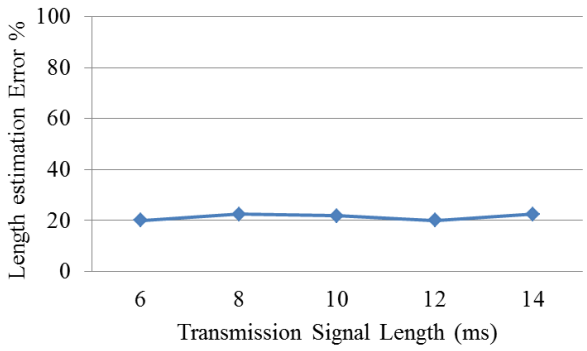

Figure 7.16: Ultrasonic chirp pulse TOF tests' length estimation errors for the different pulse duration

As can be seen in Figure 7.16, the average of the length estimation errors is around 20%. As can be seen, chirp pulse method could achieve better accuracy in comparison with the single frequency method. For a better illustration, the results of the single frequency tests and the proposed chirp pulse tests are compared in Figure 7.17.

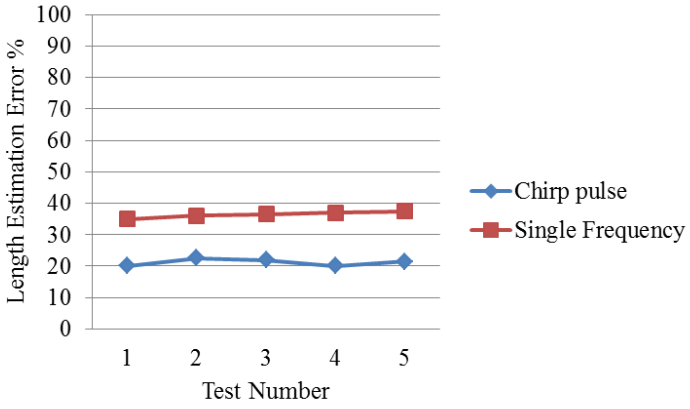

Figure 7.17: Comparison between the ultrasonic single frequency and the ultrasonic chirp pulse TOF tests on the timber beams

It can be seen that by utilizing the proposed chirp pulse methodology, not only are the accuracies of the length estimation considerably improved (the length estimation errors are dropped to almost half in the average), but also the time-of-flight tests are now possible for considerably longer timber specimens. It is worth mentioning that no signals could be detected in the 4 m timber beam when it was tested by the single frequency method. The proposed methodology has a significant potential to be used in industrial applications since it does not need powerful computers for the signal processing and results can be obtained in a short time.

7.7 Conclusions

Given the observation that the low broadband frequency excitation impact (i.e. hammer) creates a very difficult situation to deal with, in the condition assessment of the timber poles, in this chapter an alternative proposition and solution is proposed. The proposed methodology consists of an ultrasonic narrowband chirp pulse as a transmission signal, and a simple and fast signal processing procedure, in which the results can be calculated in almost 30 s. The concept of the frequency modulation (which has been used for many years in the telecommunication field) is being used in creating the ultrasonic chirp pulse transmission signal. Firstly, one low frequency chirp pulse signal is created with the specific bandwidth, and then a 40 kHz sinusoidal wave is used as a carrier signal. The final transmission signal is an ultrasonic wave packet centred at 40 kHz, and contains a chirp pulse as information of the message signal. It is also shown that several factors should be considered in designing the chirp pulse. Firstly, the bandwidth of the chirp pulse should be determined based on the dispersion relations of the tested specimen. For instance, since in this section the excitation is applied on top of the timber beam (which creates only the longitudinal wave), the bandwidth of the chirp pulse is determined as 2 kHz in order to avoid any dispersion in the high frequency range (i.e. 39-41 kHz). It is also shown that in the chirp pulse time length determination, the following factors should be considered: approximate length of the tested specimen and approximate wave velocity in the specimen.

For experimental investigations in this chapter, firstly a simple ultrasonic NDT system was designed and implemented. The accuracy of this system was obtained through the ultrasonic single frequency (40 kHz) time-of-flight tests on a 1 m timber beam. Then the proposed chirp pulse methodology was tested on the less complicated medium (i.e. the air) in order to verify its effectiveness, and finally the proposed methodology was tested on the 4 m timber beam in the time-of-flight tests. The main contributions of this chapter are firstly to propose a simple and fast signal processing procedure that uses chirped pulse response directly and produces accurate results. The proposed signal processing procedure has a significant potential to be used in industrial applications since it does not need powerful computers for processing and results can be obtained in a short time. Secondly, by utilizing the proposed methodology in this study, considerably longer timber specimens can be inspected in the transmission-through

tests, while in the single frequency pulse method, timber beams longer than 3 m cannot be inspected due to the high attenuation. Finally, the accuracy of the transmission-through or time-of-flight test has been considerably improved utilizing the proposed chirped pulse method. One journal paper has been written and submitted based on the results reported in this chapter.

8 Chapter 8: Conclusions and recommendations

8.1 Summary

Timber utility poles are a significant part of infrastructure in Australia. According to [19], there are nearly 5 million timber poles being used in the current power and communications distribution network in Australia. The utility pole industry in Australia spends approximately 40–50 million annually on maintenance and asset management to avoid failure of utility lines, which is very costly and may cause serious and not easily amendable consequences. Roughly 300,000 electricity poles are replaced in the eastern states of Australia each year, even though up to 80% of them are still in a very good serviceable condition [19].

Lack of accurate information concerning their past and current condition, such as embedment depth makes it very difficult to manage these assets and undertake reliable assessment with respect to safety. Furthermore, the current value of these assets exceeds $20 billion and as such, it is exigent that they remain in service as long as possible in order to optimise the balance between the costs associated with maintaining public safety and those incurred by premature replacement of these piles and poles.

Currently available surface stress wave based non-destructive testing (NDT) methods such as Sonic-Echo, Bending Waves and Ultraseismic methods have been considered over the past decade to be simple and cost-effective tools for identifying the condition and underground depth of embedded structures such as piles. Despite the wide spread use of these methods, the effectiveness and reliability of them on determination of the embedded length of poles, especially timber poles, are not addressed.

When it comes to field applications, these developed/to be developed NDTs face a significant challenge due to the presence of uncertainties such as complex material properties (e.g. timber), environmental conditions, interaction of soil and structure, defects and deteriorations, as well as the coupled nature of unknown length and condition. In this regard, an industrial supported research project was started in 2011 in

the University of Technology Sydney (UTS) in collaboration with the Electricity Network Association of Australia. This project aims at developing accurate and reliable non-destructive assessment tools for timber poles based on the stress wave techniques. It is necessary to mention that the project was started from the outset and with minimal information available about the timber pole including the effects of its orthotropic material properties, and wave propagation in the timber pole.

Considering the cost/benefit and inherent complications for applicability in the field:

In the first phase of this research (Chapters 2 and 5), currently available NDT methods such as Sonic-Echo, Bending waves and Ultraseismic methods were considered and employed for the condition assessment of the timber pole. Results (provided in Chapter 5) revealed the limitations of these methods on the condition assessment of the timber pole. However, some improvements were suggested, applied and tested on these methods (where applicable).

In the second phase (Chapters 3 and 6), given that currently available surface stress wave based NDTs are not mature enough to be used in this project, some advanced digital signal processing methodologies have been chosen, modified and applied in order to overcome the existing complexities imposed by the impact type (i.e. lateral and 45º angled broadband low frequency hammer excitation). The impact was applied on the side of the timber pole due to the limitations of the in-field tests (i.e. access to the top or near top surface of the timber pole is prohibitive due to the presence of the wires). The impact was also applied with the 45º angle in order to maximize the probability of creating the longitudinal wave (which is more appropriate for the length estimation). Three main groups of advanced digital signal processing tools that can be used are as follows. Deterministic signal separation methods can be used, in which statistical properties of the impact load or the impulse response of the timber pole are determined and provided. Blind signal separation methods can be used, in which no prior information is available about the impact load or the impulse response of the timber pole. The frequency-wavenumber analysis can be used, in which the data is filtered based on the existing velocities in the data. It is also necessary to mention that all methodologies referred to in the first and the second phase of this research were modified and employed on three distinct kinds of data encompassing Finite Element modelled data (also known as simulation or numerical data), laboratory experiments,

and field tests. Furthermore, both isotropic and orthotropic material properties were used in the simulation of the timber poles in order to investigate their effects on the wave propagation in the timber poles.

Finally, considering the fact that, although dealing with the complexities of the second phase (imposed by the impact type) may not be impossible, it is very difficult, in the third phase of this research (Chapter 7), a novel, fast, and accurate ultrasonic NDT methodology was proposed as an alternative solution for the timber structures condition assessment. The proposed methodology was verified through the experimental tests.

8.2 Concluding remarks

In this section a conclusions diagram, in which the conclusions of each phase of this research are explained briefly, is provided in Figure 8.1. Then comprehensive descriptions of the results are provided phase by phase.

In the first phase of this research, the Sonic-Echo, Bending Wave and Ultraseismic methods were investigated with different boundary conditions to evaluate the reliability and accuracy of the prediction of the stress wave velocity and embedded length of the timber poles under vertical and horizontal impact excitations.

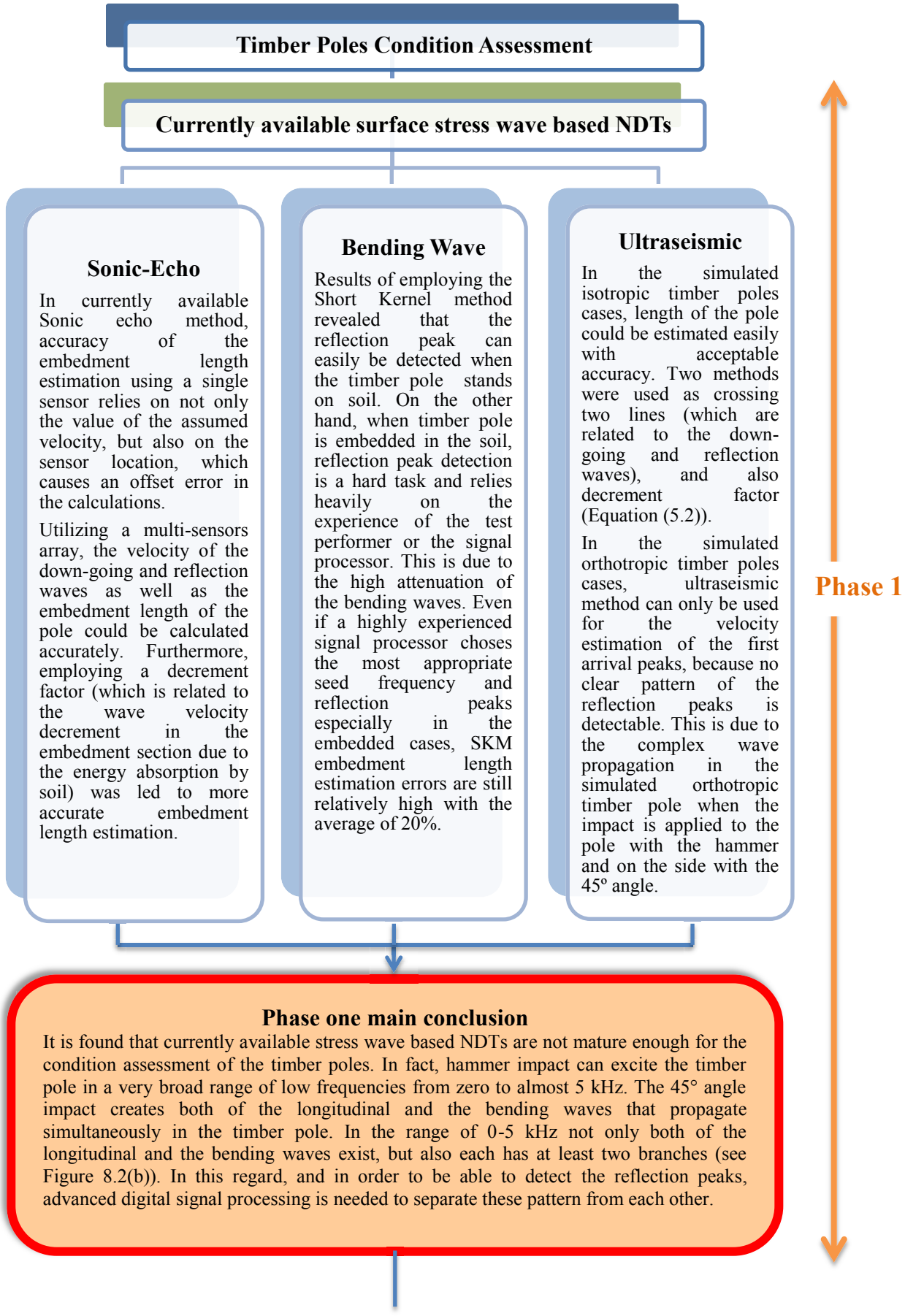
Timber Poles Condition Assessment
Currently available surface stress wave based NDTs
Sonic-Echo
In currently available Sonic echo method, accuracy of the embedment length estimation using a single sensor relies on not only the value of the assumed velocity, but also on the sensor location, which causes an offset error in the calculations.
Utilizing a multi-sensors array, the velocity of the down-going and reflection waves as well as the embedment length of the pole could be calculated accurately. Furthermore, employing a decrement factor (which is related to the wave velocity decrement in the embedment section due to the energy absorption by soil) was led to more accurate embedment length estimation.
Bending Wave
Results of employing the Short Kernel method revealed that the reflection peak can easily be detected when the timber pole stands on soil. On the other hand, when timber pole is embedded in the soil, reflection peak detection is a hard task and relies heavily on the experience of the test performer or the signal processor. This is due to the high attenuation of the bending waves. Even if a highly experienced signal processor choses the most appropriate seed frequency and reflection peaks especially in the embedded cases, SKM embedment length estimation errors are still relatively high with the average of 20%.
Ultraseismic
In the simulated isotropic timber poles cases, length of the pole could be estimated easily with acceptable accuracy. Two methods were used as crossing two lines (which are related to the down-going and reflection waves), and also decrement factor (Equation (5.2)).
In the simulated orthotropic timber poles cases, ultraseismic method can only be used for the velocity estimation of the first arrival peaks, because no clear pattern of the reflection peaks is detectable. This is due to the complex wave propagation in the simulated orthotropic timber pole when the impact is applied to the pole with the hammer and on the side with the 45° angle.
Phase one main conclusion
It is found that currently available stress wave based NDTs are not mature enough for the condition assessment of the timber poles. In fact, hammer impact can excite the timber pole in a very broad range of low frequencies from zero to almost 5 kHz. The 45° angle impact creates both of the longitudinal and the bending waves that propagate simultaneously in the timber pole. In the range of 0-5 kHz not only both of the longitudinal and the bending waves exist, but also each has at least two branches (see Figure 8.2(b)). In this regard, and in order to be able to detect the reflection peaks, advanced digital signal processing is needed to separate these pattern from each other.
Phase 1


Advanced Digital Signal Processing
Groups of possible solutions
Deterministic Signal Separation
Results of this section revealed that the predictive deconvolution is very effective on the signals obtained from the simulated isotropic timber poles, and it can clearly separate the first arrival and reflection peaks, while it cannot separate the reflection peaks in the data obtained from the simulated orthotropic timber poles. The main reason is due to the differences of the wave propagation in the simulated timber pole with the isotropic and orthotropic material properties. Simulated isotropic timber pole behaves as a non-dispersive medium in the hammer impact excitation frequency range (i.e. 0 to 5 kHz). While the simulated orthotropic one (which is more similar to the real timber pole) behaves as a highly dispersive medium in the frequency range of the hammer impact excitation. See Figure 8.2.
Blind Signal Separation
Results of employing PCA and SVD revealed that these methods can reduce the noise and preserve the main existing patterns in the signal (i.e. up- and down-travelling waves) in the isotropic simulated timber pole. While in the orthotropic case, since not only the statistical property of existing patterns change non-linearly, but also there is a severe interference between these patterns, although these methodologies can be used for a noise reduction, they are not able to preserve the main patterns. Furthermore, even in the isotropic case up- and down-travelling waves cannot be separated since both have same second order statistical property.
F-K Analysis
1. Results of applying a two dimensional velocity filter demonstrated that although this filter can separate the longitudinal and the bending waves from each other, the contributions or interference between two branches of the longitudinal waves is not amendable.
2. Application of the K-mean clustering algorithm, which includes iterations and learning, on the F-K domain data revealed that although this algorithm can successfully separate the longitudinal wave from the bending one, due to the interference between the wave's branches, the reflection peaks from the bottom of the pole cannot be detected correctly.
Phase 2

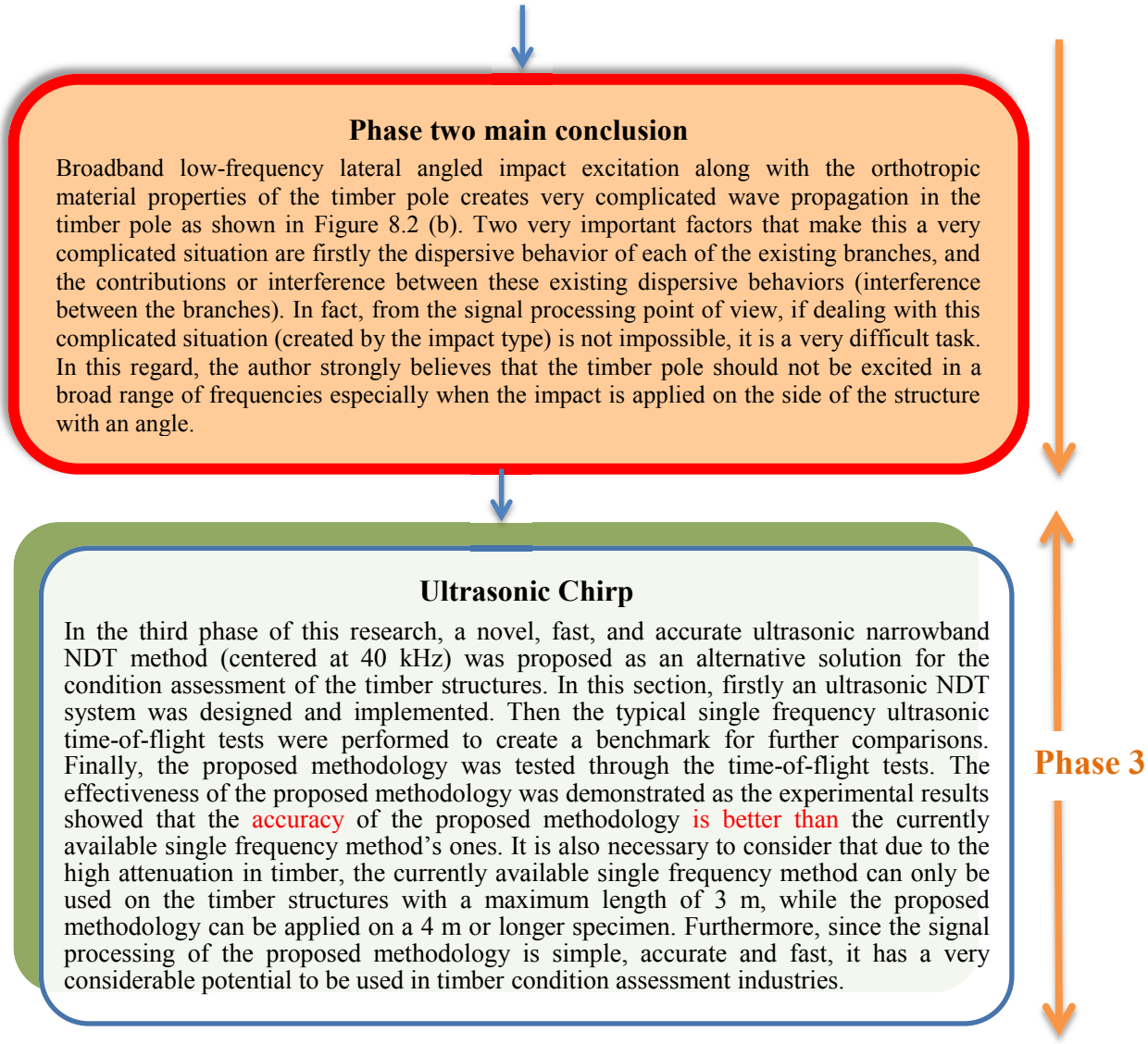

Figure 8.1: Conclusion diagram of this research

It should be mentioned that both the isotropic and orthotropic material properties were used in the FE model to investigate the effects of anisotropy in the results. The findings of numerical modelled data analysis are summarised as follows:

1.1. In the Sonic-Echo method for both the isotropic and orthotropic simulations, the reflected wave can be identified easily since peaks are very clear and calculation of the embedment length is relatively simple utilizing a single sensor. However in the Sonic-Echo method, it is shown that the accuracy of the embedment length estimation using a single sensor relies on not only the value of the assumed velocity, but also on the sensor location, which causes an offset error in the calculations. It is necessary to consider that in the conventional Sonic-Echo method, a value is pre-assumed for the velocity of the wave propagation. For these reasons, in the Sonic-Echo section, multi-sensors array was used to estimate the velocities of the down-going and reflection waves accurately, and

also to avoid the offset error. Furthermore, as the velocity will decrease inside the soil, the determination of the length is more complex under the embedded conditions and the velocity decrement factor should be considered when the waves travel inside the soil. Using multi-sensors array and considering the timber pole as an isotropic material, the maximum error of the length determination under embedded conditions was only 6%, while the maximum error for the orthotropic case was almost 8%. Using multi-sensors increased the accuracy of the stress wave calculations and indeed, it decreased the length determination error. Anyhow, due to the constraints imposed on the project because of the presence of the electrical or communication wires on top of the in-service timber utility pole, the Sonic-Echo method is not suitable to be used in the field tests.

1.2. In the Bending wave utilizing Short Kernel Method, as there are no guidelines available to select the most appropriate kernel frequency, different kernel frequencies were selected from the Frequency Response Functions to calculate the velocity and the embedded length. Results of the investigations revealed that the reflection peak can easily be detected when the timber pole has not been embedded and only stands on soil. It is also seen that although the estimated phase velocities are not exactly the same as the analytical results (i.e. results obtained from solving the mathematical equations of the wave propagation in the cylindrical timber pole), they show the same trend of increasing as frequency increases. When the timber pole is embedded in the soil, reflection peak detection is a hard task and relies heavily on the experience of the test performer or the signal processor as was shown in the results in Chapter 5. This is due to the high attenuation of the bending waves. Even if a highly experienced signal processor choses the most appropriate seed frequency and reflection peaks especially in the embedded cases, SKM embedment length estimation errors are still relatively high with the average of 20%.

1.3. Based on the Ultraseismic method, the length of the simulated isotropic timber pole could be estimated easily by crossing the two lines, which are related to the first arrival and the reflection waves. However, in the embedded case, the velocity is different above and below the soil and the decrement factor should be

considered in the length estimation procedure. As the results of the orthotropic cases in Chapter 5 revealed, the Ultraseismic method can only be used for the velocity estimation of the first arrival peaks, because no clear pattern of the reflection peaks is detectable. This is due to the complex wave propagation in the simulated orthotropic timber pole when the impact is applied to the pole with the hammer and on the side with the 45º angle.

In the first phase of this research, the Sonic-Echo, Bending Wave and Ultraseimic methods have been investigated for determining the stress wave velocity and the embedded length of the pole with different geotechnical conditions. A series of experimental tests have been conducted on the 5 m timber pole sectioned from a field pole in service. The results of the experimental studies of this phase of the research can be summarized as follows:

1.1. In the Sonic-Echo method utilizing multi-sensors array on the standing-on-soil condition, the velocity of the down-going wave can be estimated with a high fitting accuracy of 95%. Although a clear pattern of reflection peaks can be seen in this case, the fitting accuracy dropped to 60%, and the length of the specimen can be estimated with 21% error. The results in the embedded case were of little practical use as the pattern of reflection peaks was not detectable.

1.2. Based on the results of the SKM, the kernel frequency of between 400-2000 Hz was identified to be used for the phase velocity calculations. Using the SKM to estimate the length of the pole in the Bending Wave method for the 5m timber pole shows that the percentage of the error for all boundary conditions is between -12% and 34%. The average error for the length estimation is about 20% for most boundary conditions.

1.3. According to the Ultraseismic method with the lateral impact at a 45° angle results, using multi-sensors array resulted in estimation of the first arrival's velocity with a high fitting accuracy. However, the estimated velocity is much higher than it was expected to be (compared to the analytical results). This is due to the presence of the second and sometimes the third branches of the flexural waves in the signal. These branches have started with the very high level of energy (see Figure 8.2(b)). Furthermore, some sensors might need to be eliminated for the velocity calculations as they show large variations or are out

of the range compared to the rest of the sensors. It is believed that those variations are related to the uncertainties involved in wave generation in the timber materials such as anisotropy of the timber, location of the sensors with regards to annual growth ring orientation and slope of grain and possible existence of imperfections in the timber such as knots.

1.4. Length estimation and analysis in the Ultraseismic method is very complicated due to the lateral and angled impact. In fact, this impact type creates very complicated stress wave propagation in the timber pole. Due to the impact type, multiple wave types such as the longitudinal and the bending waves propagate through the timber. While in each, the wave travels in both up and down directions. Furthermore, these wave types propagate simultaneously in the timber pole with different branches and each branch has a non-linear behaviour. In addition, these branches contribute to each other, for instance the bending waves contribute to the longitudinal direction. Finally, the stress wave velocity will change inside the soil. In this regard, advanced digital signal processing techniques are needed to be employed.

2. Based on the results obtained from the first phase of this research, in the second phase several advanced digital signal processing techniques were selected, modified and applied on the timber pole. Firstly, from the signal processing point of view, the timber pole was defined as a Linear Time-Invariant (LTI) system, in which the output of the system (captured signal by sensor) can be mathematically expressed as the convolution of the input signal (i.e. hammer impact) with the transfer function or impulse response of the timber pole. Then possible types of solutions were nominated which can be categorized into deterministic signal separation, blind signal separation, and frequency-wavenumber analysis methods. In the deterministic signal separation methods, it was been assumed that prior information about the input signal or impulse response of the tested specimen (i.e. timber pole) is provided or can be extracted directly from the captured signal, while blind signal separation methods only rely on the statistical differences, which exist in the captured signal.

2.1. Wiener deconvolution is the most famous and widely applied deterministic signal separation methodology, in which the availability of prior information is necessary. On the other hand, predictive deconvolution is the generalized form

of the Wiener deconvolution, in which the necessary information can be extracted from the captured signal itself. It is vital for the captured signal to be stationary or wide-sense stationary, which means the statistical properties, which exist in the signal do not change during the capturing time. Results of this section revealed that the predictive deconvolution is very effective on the signals obtained from the simulated isotropic timber pole, and it can clearly separate the first arrival and reflection peaks, while it cannot separate the reflection peaks in the data obtained from the simulated orthotropic timber pole. The main reason is due to the differences of the wave propagation in the simulated timber pole with the isotropic and orthotropic material properties. As shown in Figure 8.2 (a), the simulated isotropic timber pole behaves as a non-dispersive medium in the hammer impact excitation frequency range (i.e. 0 to 5 kHz). The simulated orthotropic timber pole (which is more similar to the real timber pole) behaves as a highly dispersive medium in the frequency range of the hammer impact excitation as shown in Figure 8.2 (b). In simple words, even if the dispersion of one existing branch is considered and the rest of the complicating factors such as up- and down-travelling waves, and the contributions and interference between branches are ignored, this dispersion means that the statistical properties are changing during the capturing time, which makes these methods inefficient.

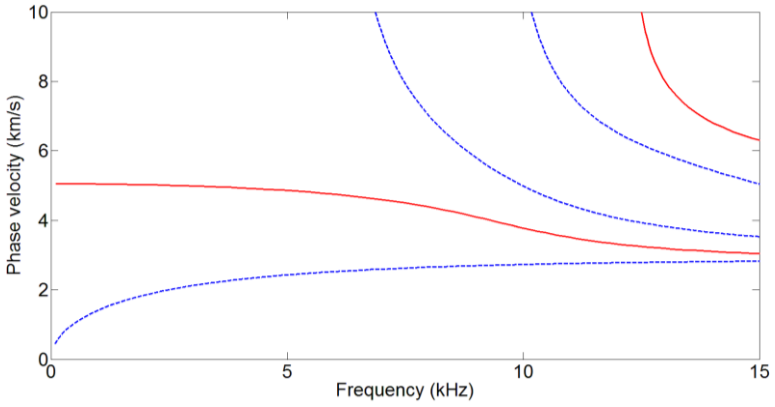

(a)

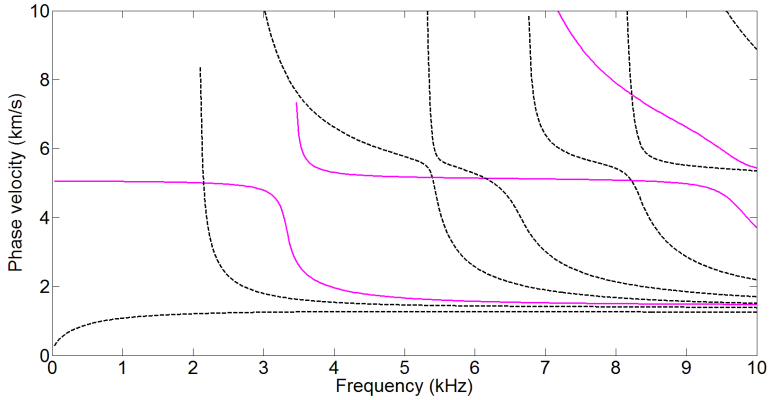

(b)

Figure 8.2: The spectrum curves of the cylindrical timber poles in (a) the isotropic; and (b) the orthotropic cases. The dashed lines represent the flexural wave branches and the hard lines represent the longitudinal branches [52]

2.2. Employing the most widely applied blind signal separation methodologies such as Principal Component Analysis (PCA), and Singular Value Decomposition (SVD) demonstrated that they are more useful for preserving the main patterns, which exist in the signal. For example, the results of their application on the simulated isotropic timber pole revealed that they can preserve the main patterns of the signal (the patterns related to the up- and down-travelling waves) and can remove the unwanted parts or noise. It is necessary to mention that since these methods separate the existing pattern in the signals based on the second order statistics and the up- and down-travelling waves have the same statistical properties, they cannot be used for the wave separation. Application of these methods on the simulated orthotropic timber pole demonstrated that these methods are not effective due the dispersion effects. In other words, not only the statistical properties of the several existing patterns (branches) in the signals are changing based on their dispersion curves shown in Figure 8.2(b), but also they contribute to each other as well.

2.3. In the second phase of this research, a two dimensional velocity filter was also designed and applied on the two dimensional data (It should be noted that the phase velocity can be obtained from the relation between the frequency and the real part of the wavenumber). The data was transferred from the time-space domain to the frequency-wavenumber domain. Results demonstrated that although this filter can separate the longitudinal and the bending waves from

each other, the contributions or interference between two branches of the longitudinal waves is not amendable. One alternative solution based on the F-K domain data illustration (see Figure 6.25) was to filter the data with the low-pass digital filter with the cut-off frequency of 1500 Hz. Results showed that the output of the digital filter was very similar to the isotropic case, but the velocity of the detected reflection peaks has the unacceptable value of almost 14000 m/s. This high velocity is due to the interference or contributions between several branches that exist in the captured signal.

2.4. In the last section of the second phase of this research, application of the *K*-mean clustering algorithm, which includes iterations and learning, on the F-K domain data revealed that although this algorithm can successfully separate the longitudinal wave from the bending one, due to the interference between the wave's branches, the reflection peaks from the bottom of the pole cannot be detected correctly. In fact, the results were very similar to the results of the low-pass filtering of the data with the 1.5 kHz cut-off frequency.

2.5. Broadband low-frequency lateral angled impact excitation along with the orthotropic material properties of the timber pole creates very complicated wave propagation in the timber pole as shown in Figure 8.2 (b). Two very important factors that make this a very complicated situation are firstly the dispersive behavior of each of the existing branches, and the contributions or interference between these existing dispersive behaviors (interference between the branches). Two simple examples were also provided to explain this situation in a simpler way. Finally, from the signal processing point of view, if dealing with this complicated situation (created by the impact type) is not impossible, it is a very difficult task.

3. In the third phase of this research and based on the results and understandings obtained from the broadband low-frequency lateral angled impact excitation analysis, a novel, fast, and accurate ultrasonic narrowband NDT method (centered at 40 kHz) was proposed as an alternative solution for the condition assessment of the timber structures. In this section, firstly an ultrasonic NDT system was designed and implemented. Then the typical single frequency ultrasonic time-of-flight tests were performed to create a benchmark for further comparisons. Finally, the proposed

methodology was tested through the time-of-flight tests. The effectiveness of the proposed methodology was demonstrated as the experimental results showed that the accuracy of the proposed methodology is better than the currently available single frequency method's ones. It is also necessary to consider that due to the high attenuation in timber, the currently available single frequency method can only be used on the timber structures with a maximum length of 3 m, while the proposed methodology can be applied on a 4 m or longer specimen. Furthermore, since the signal processing of the proposed methodology is simple, accurate and fast, it has a very considerable potential to be used in timber condition assessment industries.

8.3 Recommendations of the future studies

Based on the literature review and the research of this thesis, the following recommendations for future research work in the area of non-destructive testing methods of timber structures are given:

- More advanced digital signal processing such as probabilistic methodologies can be modified and applied on the data captured from the simulated orthotropic timber pole or real in-field timber poles in order to try to overcome the existing complexities of the broadband low frequency lateral angled impact excitation.

- Conducting further field-tests to prepare a large database to use other methods such as machine learning to identify the damage signatures in the timber poles.

- Excite the timber pole with a single low frequency impact excitation in order to minimize the dispersion. It is also necessary to consider that one of the shortcomings of the low frequency excitation is due to the large time length of the waves, which is not suitable for further damage detection applications.

- Utilize the theories such as phase array or Guided Wave theory in which a wave is transmitted through the pole/pipe with a specific angle (For instance, based on the system setups, mostly longitudinal waves can be applied), in order to minimize the interference between wave types when the impact is applied on the side of the specimen.

- Further study of temperature change in determining the condition of the timber poles.
- Performing more tests based on the proposed ultrasonic NDT methodology with the following setups:
    - Perform the tests on timber pole with several ultrasonic centre frequencies in order to obtain the best centre frequency for the condition assessment of the timber structures.
    - Use other advanced digital signal processing techniques such as match filter on both single frequency and chirped pulse tests in order to investigate the effectiveness of these techniques.
    - Perform the test on other materials such as steel, and concrete in order to investigate the possibility of employing the proposed methodology on the condition assessment of these materials.
    - Combine the proposed methodology with the phase array or Guided Wave theory to investigate other alternative impact locations rather than the top in the ultrasonic tests.

9 Appendices

9.1 Appendix-A: Guided wave equations for the cylindrical structures

GW propagation in the cylindrical coordinates is shown in Figure A. 1.

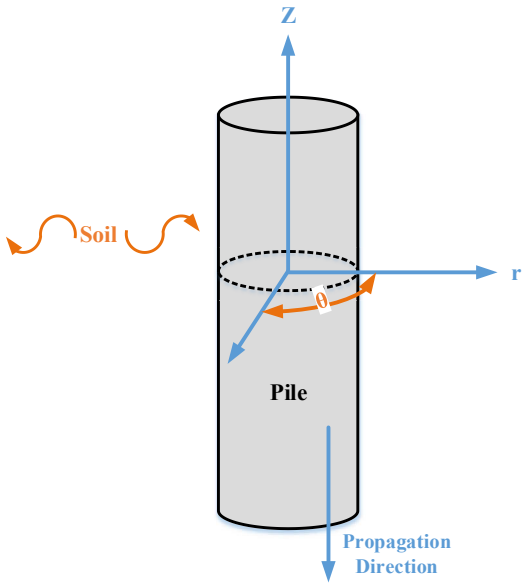

Figure A. 1: Guided wave propagation and coordinate directions for cylindrical pile/pole [51]

The Navier-Stokes equation for the displacements equations of motion in the cylindrical structure (pile/pole) can be written as:

$$(\lambda+\mu)\nabla\nabla\bullet \mathrm{u}+\mu\nabla^2\mathrm{u}=\rho\ddot{\mathrm{u}} \qquad \text{(A. 1)}$$

In equation (A.1) "u" is the vector of displacements, ρ is the pile/pole density, λ is the lame's constant, and μ is the shear modulus. ∇ is the derivative operator over spatial domain, and two dots over "u" is the derivative operation over time. Based on Helmholtz equation, "u" in equation (A.1) can be rewritten as a sum of scalar potential Φ (i.e. magnitude of displacement vector), and vector potential Ψ (i.e. direction of displacement vector) as shown in equation (A.2). [129]

$$\mathrm{u}=\nabla\Phi+\nabla\times\Psi,\nabla\bullet\Psi=0 \qquad \text{(A.2)}$$

Using the Helmholtz equation, compression waves can be separated from the Shear waves, i.e. the wave equation is decoupled. If the body force is zero, the decoupled equations become

$$\nabla^2\Phi = \frac{1}{c_L^2}\frac{\partial^2\Phi}{\partial t^2}$$
$$\nabla^2\Psi = \frac{1}{c_T^2}\frac{\partial^2\Psi}{\partial t^2} \qquad \text{(A. 3)}$$

Where c_T and c_L are the shear and compression waves' velocities. Scalar potential and vector potential themselves are the function of r, θ, and z (related to cylindrical coordinates).

$$\Phi = f(r)\Theta_\phi(\theta)e^{i(\omega t-\xi)}$$
$$\Psi_r = h_r(r)\Theta_r(\theta)e^{i(\omega t-\xi)} \qquad \text{(A. 4)}$$
$$\Psi_\theta = h_\theta(r)\Theta_\theta(\theta)e^{i(\omega t-\xi)}$$
$$\Psi_z = h_z(r)\Theta_z(\theta)e^{i(\omega t-\xi)}$$

Based on the theory of elasticity, three displacements and six stress components can be written as equations (A.5) and (A.6).

$$u_r = \frac{\partial\Phi_j}{\partial r} + \frac{1}{r}\frac{\partial\Psi_{z_j}}{\partial\theta} - \frac{\partial\Psi_{\theta_j}}{\partial z}$$
$$u_\theta = \frac{1}{r}\frac{\partial\Phi_j}{\partial r} + \frac{\partial\Psi_{r_j}}{\partial\theta} + \frac{\partial\Psi_{z_j}}{\partial z} \qquad \text{(A. 5)}$$
$$u_z = \frac{\partial\Phi_j}{\partial z} + \frac{1}{r}\frac{\partial\left(r\Psi_{\theta_j}\right)}{\partial r} - \frac{1}{r}\frac{\partial\Psi_{r_j}}{\partial\theta}$$
$$\sigma_{rr_j} = \lambda_j\nabla^2\Phi_j + 2\mu_j\frac{\partial u_{r_j}}{\partial r}$$

$$\sigma_{rr_j} = \lambda_j \nabla^2 \Phi_j + 2\mu_j \left(\frac{u_{r_j}}{r} + \frac{1}{r} \frac{\partial u_{\theta_j}}{\partial \theta} \right)$$

$$\sigma_{zz_j} = \lambda_j \nabla^2 \Phi_j + 2\mu_j \frac{\partial u_{z_j}}{\partial z} \qquad \text{(A. 6)}$$

$$\sigma_{r\theta_j} = \mu_j \left(\frac{1}{r} \frac{\partial u_{r_j}}{\partial \theta} + \frac{\partial u_{\theta_j}}{\partial r} - \frac{u_{\theta_j}}{r} \right)$$

$$\sigma_{rz_j} = \mu_j \left(\frac{\partial u_{r_j}}{\partial z} + \frac{\partial u_{z_j}}{\partial r} \right)$$

$$\sigma_{\theta z_j} = \mu_j \left(\frac{\partial u_{\theta_j}}{\partial z} + \frac{1}{r} \frac{\partial u_{z_j}}{\partial \theta} \right)$$

Where j can be replaced by P for displacement and stress components of pile/pole or S for soil. The boundary conditions require that the stresses in the pile equal the stresses in the soil at the soil-pile interface and that the displacements in the pile equal the displacements in the soil at the soil-pile interface [130]. Considering embedded situation, and boundary conditions, there will be six equations with six unknowns for pile/pole in the isotropic case to be solved. The solution of these equations in cylindrical coordinates produces Bessel and Henkel functions. Equation (A.7) illustrates aforementioned governing equations in a matrix form.

$$\begin{bmatrix} x_{11} & x_{12} & x_{13} & x_{14} & x_{15} & x_{16} \\ x_{21} & x_{22} & x_{23} & x_{24} & x_{25} & x_{26} \\ x_{31} & x_{32} & x_{33} & x_{34} & x_{35} & x_{36} \\ x_{41} & x_{42} & x_{43} & x_{44} & x_{45} & x_{46} \\ x_{51} & x_{52} & x_{53} & x_{54} & x_{55} & x_{56} \\ x_{61} & x_{62} & x_{63} & x_{64} & x_{65} & x_{66} \end{bmatrix} \begin{bmatrix} A_{1_P} \\ A_{4_P} \\ A_{6_P} \\ A_{1_s} \\ A_{4_P} \\ A_{4s} \end{bmatrix} = \begin{bmatrix} 0 \\ 0 \\ 0 \\ 0 \\ 0 \\ 0 \end{bmatrix} \qquad \text{(A. 7)}$$

Where x is the coefficient matrix, A is called vector of unknown constants where “p” refers to pile/pole and “s” refers to soil, and zeros on right hand side refers to pile/pole being homogenous. Components of coefficient matrix are as follows:

$$x_{11} = |\alpha_p| J_n'(|\alpha_p| a)$$

$$x_{12} = -\xi J_n'(|\beta_p|a)$$

$$x_{13} = \frac{n}{a} J_n'(|\beta_p|a)$$

$$x_{14} = -|\alpha_p| H_n'^{(2)}(|\alpha_s|a) \qquad \text{(A. 8)}$$

$$x_{15} = \xi H_n'^{(2)}(|\beta_s|a)$$

$$x_{16} = -\frac{n}{a} H_n'^{(2)}(|\beta_s|a)$$

$$x_{21} = -\frac{n}{a} J_n(|\beta_p|a)$$

$$x_{22} = \frac{n\xi}{|\beta_p|a} J_n\left(|\beta_p|a\right)$$

$$x_{23} = -|\beta_p| J_n'^{(2)}(|\beta_p|a) \qquad \text{(A. 9)}$$

$$x_{24} = \frac{n}{a} H_n^{(2)}(|\alpha_s|a)$$

$$x_{25} = \frac{n\xi}{|\beta_s|a} H_n^{(2)}\left(|\beta_s|a\right)$$

$$x_{26} = |\beta_s| H_n'^{(2)}(|\beta_s|a)$$

$$x_{31} = -i\xi J_n\left(|\alpha_p|a\right)$$

$$x_{32} = -i|\beta_p| J_n\left(|\beta_p|a\right)$$

$$x_{33} = 0 \qquad \text{(A. 10)}$$

$$x_{34} = -i\xi H_n^{(2)}\left(|\alpha_s|a\right)$$

$$x_{35} = i|\beta_s| H_n^{(2)}\left(|\beta_s|a\right)$$

$$x_{36} = 0$$

$$x_{41} = \left[-\lambda_c \left(|\alpha_p|^2 + \xi^2 \right) + 2\mu_p \left(\frac{n^2}{a^2} - |\alpha_p|^2 \right) \right] J_n\left(|\alpha_p| a \right) - 2\mu_p \frac{|\alpha_p|}{a} J_n{}'\left(|\alpha_p| a \right)$$

$$x_{42} = 2\mu_c \xi \left[\left(|\beta_p| - \frac{n^2}{|\beta_p| a^2} \right) \right] J_n\left(|\beta_p| a \right) + \frac{1}{r} J_n{}'\left(|\beta_p| a \right)$$

$$x_{43} = 2\mu_c \frac{n}{a} \left[\left(|\beta_p| J_n{}'\left(|\beta_p| a \right) - \frac{1}{r} J_n\left(|\beta_p| a \right) \right) \right] \qquad \text{(A. 11)}$$

$$x_{43} = 2\mu_c \frac{n}{a} \left[\left(|\beta_p| J_n{}'\left(|\beta_p| a \right) - \frac{1}{r} J_n\left(|\beta_p| a \right) \right) \right]$$

$$x_{44} = -\left[-\lambda_s \left(|\alpha_s|^2 + \xi^2 \right) + 2\mu_s \left(\frac{n^2}{a^2} - |\alpha_s|^2 \right) \right] H_n^{(2)}\left(|\alpha_s| a \right) - 2\mu_s \frac{|\alpha_s|}{a} H_n^{\prime(2)}\left(|\alpha_s| a \right)$$

$$x_{45} = 2\mu_s \xi \left[\left(|\beta_s| - \frac{n^2}{|\beta_s| a^2} \right) \right] H_n^{(2)}\left(|\beta_s| a \right) + \frac{1}{r} H_n^{\prime(2)}\left(|\beta_s| a \right)$$

$$x_{46} = 2\mu_s \frac{n}{a} \left[\left(|\beta_s| H_n^{\prime(2)}\left(|\beta_s| a \right) - \frac{1}{r} H_n^{(2)}\left(|\beta_s| a \right) \right) \right]$$

$$x_{51} = \mu_c \frac{2n}{a} \left[\frac{1}{a} J_n\left(|\alpha_p| a \right) - |\alpha_p| J_n{}'\left(|\alpha_p| a \right) \right]$$

$$x_{52} = \mu_c \frac{2n\xi}{a} \left[J_n{}'\left(|\beta_p| a \right) - \frac{1}{|\beta_p| a} J_n\left(|\beta_p| a \right) \right]$$

$$x_{53} = \mu_c \left[\frac{2|\beta_p|}{a} J_n{}'\left(|\beta_p| a \right) - \left(\frac{2n^2}{a^2} - |\beta_p|^2 \right) J_n\left(|\beta_p| a \right) \right] \qquad \text{(A. 12)}$$

$$x_{54} = -\mu_s \frac{2n}{a} \left[\frac{1}{a} H_n^{(2)}\left(|\alpha_s| a \right) - |\alpha_s| H_n^{\prime(2)}\left(|\alpha_s| a \right) \right]$$

$$x_{55} = -\mu_s \frac{2n\xi}{a}\left[H_n^{\prime(2)}\left(|\beta_s|a\right) - \frac{1}{|\beta_s|a} H_n^{(2)}\left(|\beta_s|a\right)\right]$$

$$x_{56} = -\mu_c\left[\frac{2|\beta_s|}{a} H_n^{\prime(2)}\left(|\beta_s|a\right) - \left(\frac{2n^2}{a^2} - |\beta_s|^2\right) H_n^{(2)}\left(|\beta_s|a\right)\right]$$

$$x_{61} = -i\mu_c 2\xi|\alpha_p| J_n'\left(|\alpha_p|a\right)$$

$$x_{62} = i\mu_c\left(\xi^2 - |\beta_p|^2\right) J_n'\left(|\beta_p|a\right)$$

$$x_{63} = -i\mu_c \frac{n\xi}{a} J_n\left(|\beta_p|a\right)$$

$$x_{64} = i\mu_c 2\xi|\alpha_s| H_n^{\prime(2)}\left(|\alpha_s|a\right) \qquad \text{(A. 13)}$$

$$x_{65} = i\mu_s\left(\xi^2 - |\beta_s|^2\right) H_n^{\prime(2)}\left(|\beta_s|a\right)$$

$$x_{66} = -i\mu_c \frac{n\xi}{a} H_n^{(2)}\left(|\beta_s|a\right)$$

Where J and H are the Bessel and Henkel functions, "n" is the order of these functions. i is the square root of -1, a is the pile/pole radius, ξ is the complex-valued wave number, μ_c is the shear modulus of pile/pole, μ_s is the shear modulus of the soil, λ_c and λ_s are Lame's constants of pile/pole and soil, and α and β are the argument of each Bessel or Henkel function, which are the functions of the frequency in time and spatial domain (ω and ξ). Equation (A.14) shows aforementioned arguments.

$$\alpha_j = \sqrt{\frac{\omega^2}{c_{L_k}^2} - \xi^2}$$

$$\beta_j = \sqrt{\frac{\omega^2}{c_{T_k}^2} - \xi^2} \qquad \text{(A. 14)}$$

j can be replaced by *p* for pile/pole and *s* for soil. C_L is the longitudinal wave velocity, C_T is the shear wave velocity, and *k* refers to the pile/pole or soil properties. One can

simply see the dependency of coefficient matrix components to pile geometry and material properties (radius, Lame's constant and shear modulus), and also to soil material properties (Lame's constant and shear modulus). Solving these equations for the angular frequency (ω), the root will be the wavenumber (ξ), which can be a complex number. The relation between the real part of the wavenumber and the frequency is called dispersion relation.

9.2 Appendix-B: Investigations on the repeatability of the captured signals, and effectiveness of the advanced digital signal processing methodologies on the in-field timber utility poles

Pole 1

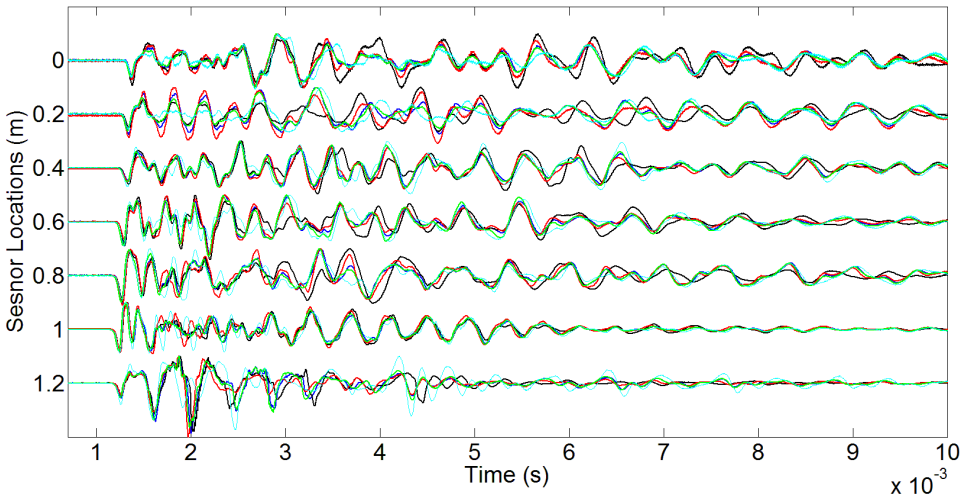

(a)

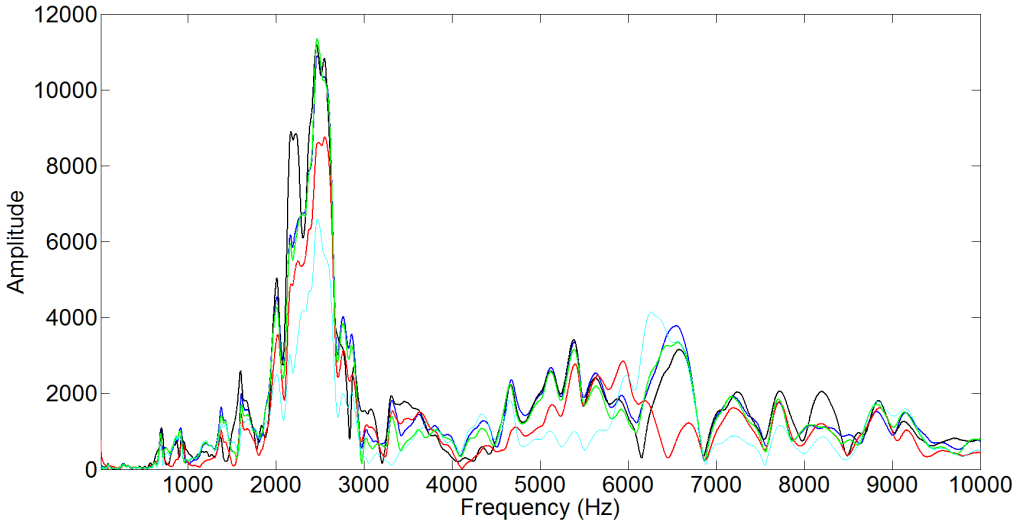

(b)

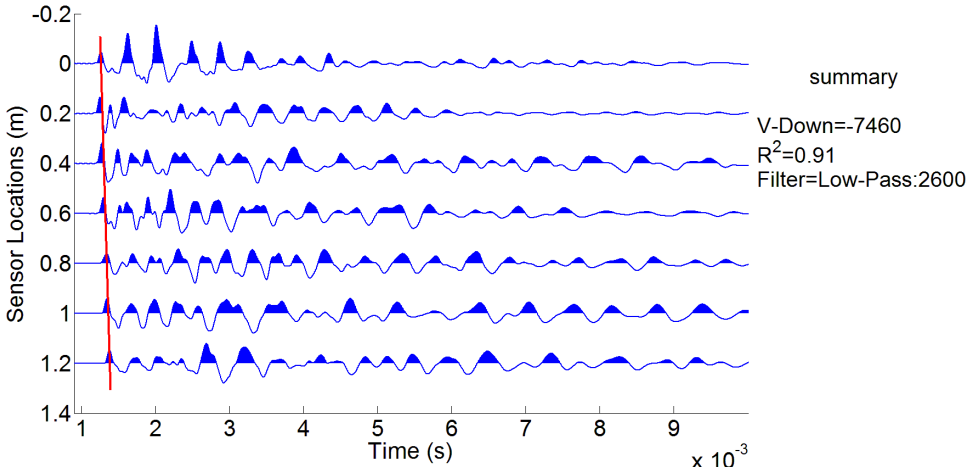

(c)

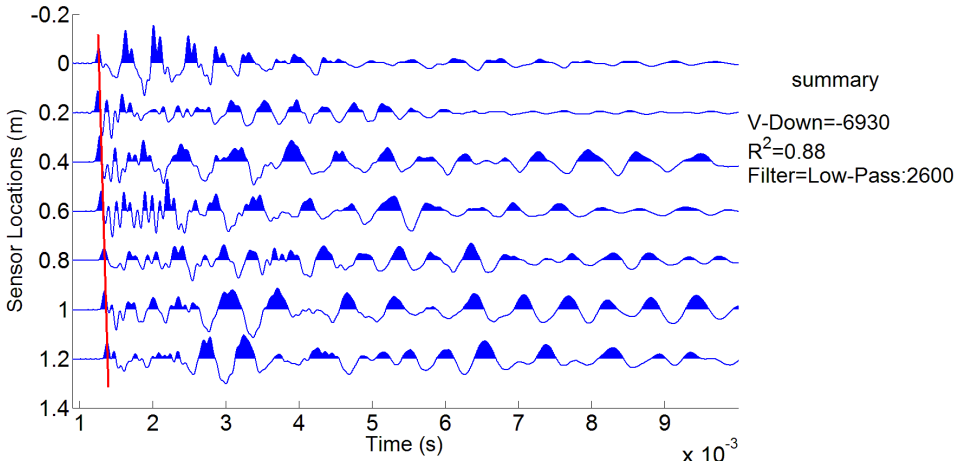

(d)

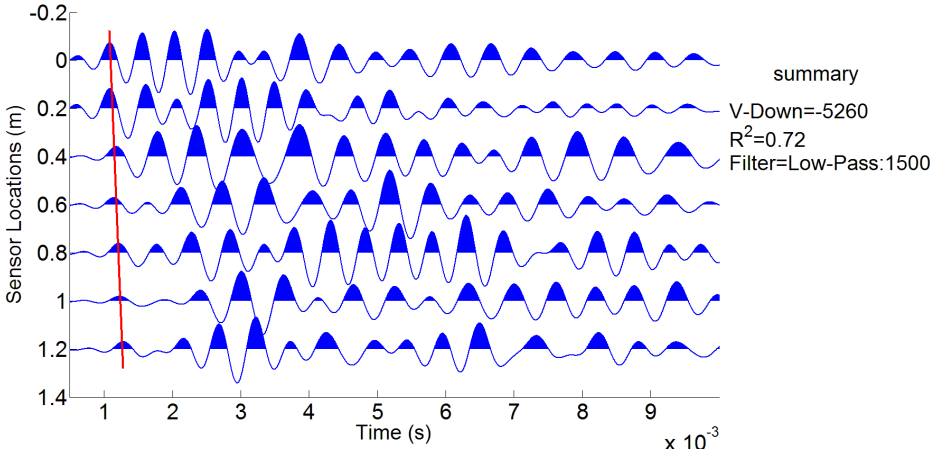

(f)

Figure B. 1: (a) Repeatability of the five tests in all sensors, (b): FFT of all sensors, (c): Captured signals in all sensors after low-pass filtering with 2600 Hz cut-off frequency, (d): Captured signals in all sensors after low-pass filtering with 2600 Hz cut-off frequency followed by predictive deconvolution, and (f): Captured signals in all sensors after low-pass filtering with 1500 Hz cut-off frequency

Pole 2

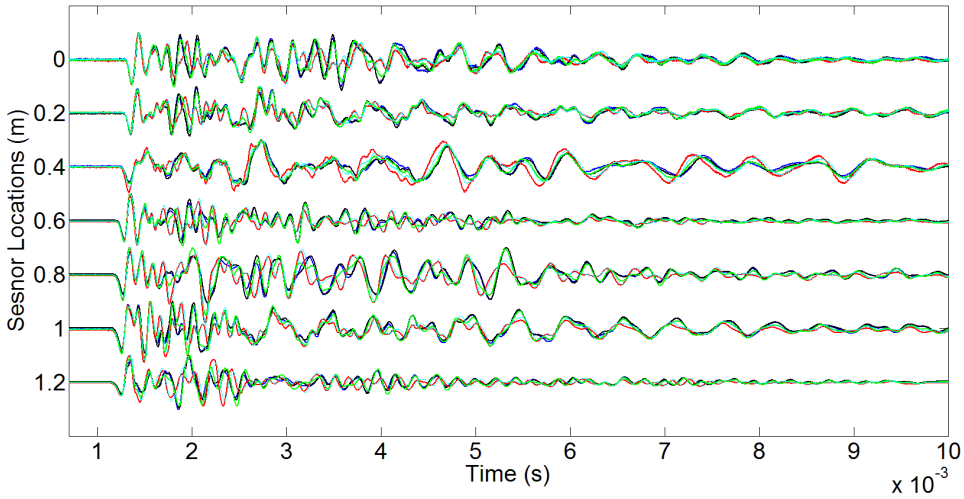
Sesnor Locations (m)
0
0.2
0.4
0.6
0.8
1
1.2
1
2
3
4
5
6
7
8
9
10
Time (s)
x 10^-3

(a)

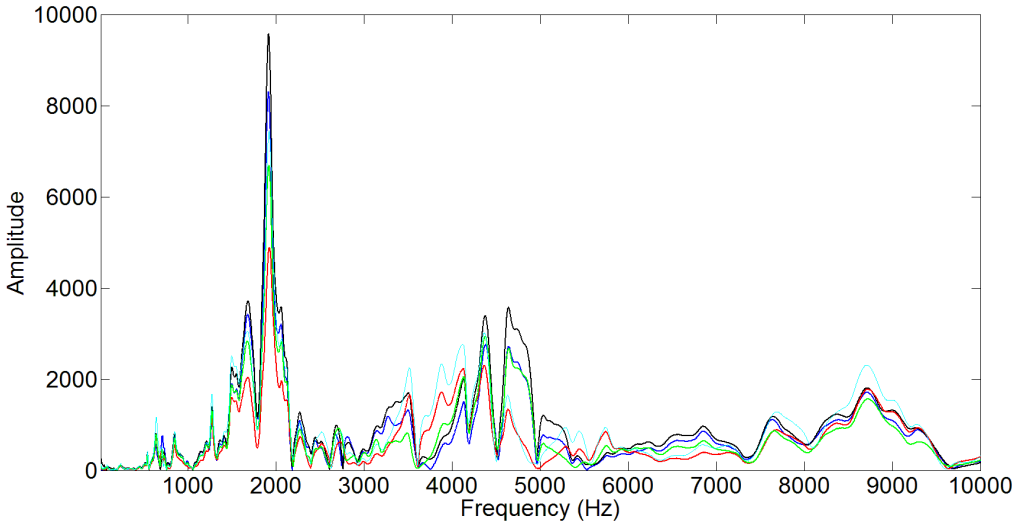
Amplitude
10000
8000
6000
4000
2000
0
1000
2000
3000
4000
5000
6000
7000
8000
9000
10000
Frequency (Hz)

(b)

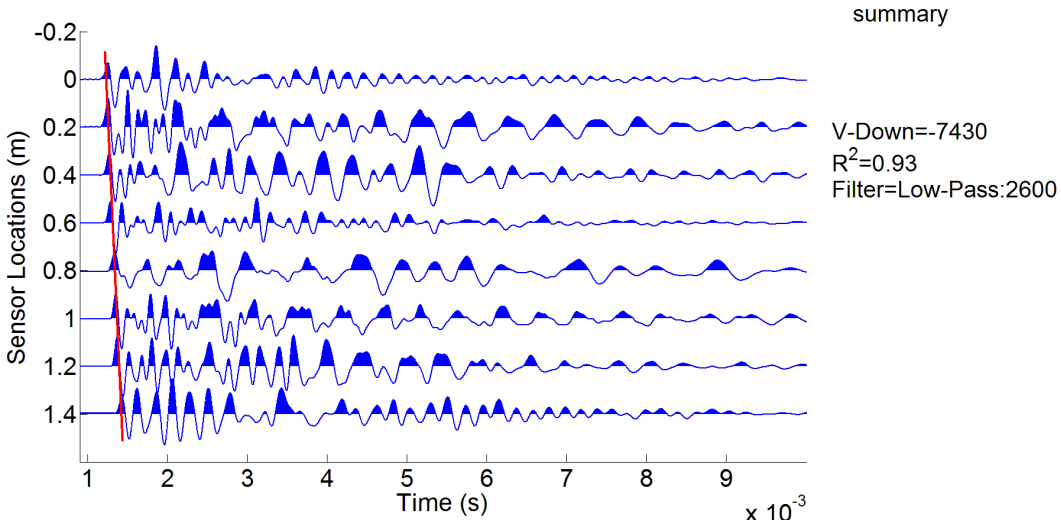
summary
Sensor Locations (m)
-0.2
0
0.2
0.4
0.6
0.8
1
1.2
1.4
1
2
3
4
5
6
7
8
9
Time (s)
x 10^-3
V-Down=-7430
R^2=0.93
Filter=Low-Pass:2600

(c)

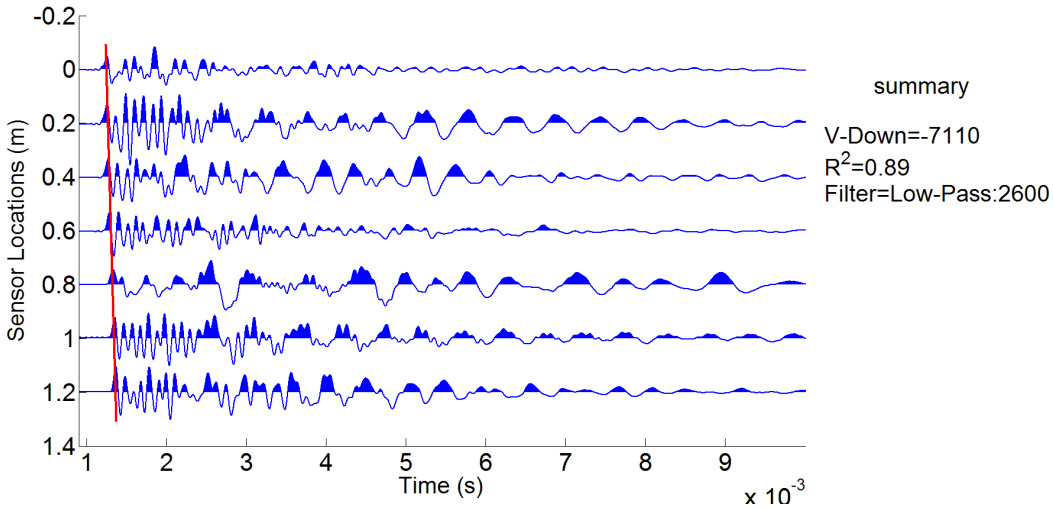

(d)

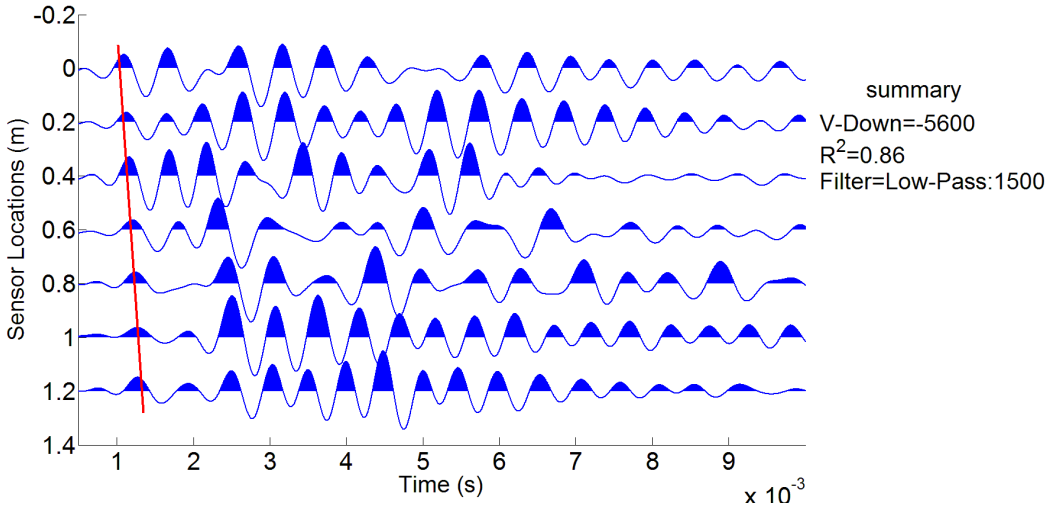

(f)

Figure B. 2: (a) Repeatability of the five tests in all sensors, (b): FFT of all sensors, (c): Captured signals in all sensors after low-pass filtering with 2600 Hz cut-off frequency, (d): Captured signals in all sensors after low-pass filtering with 2600 Hz cut-off frequency followed by predictive deconvolution, and (f): Captured signals in all sensors after low-pass filtering with 1500 Hz cut-off frequency

Pole 3

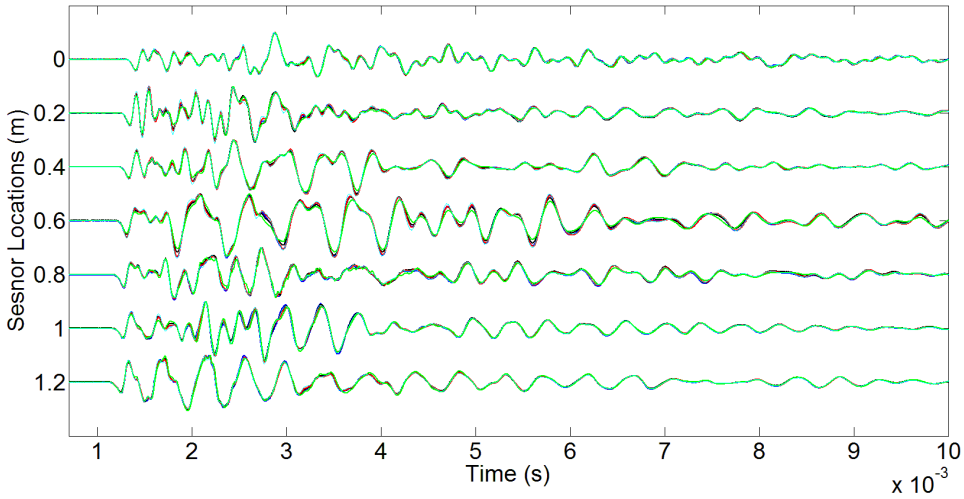
Sesnor Locations (m)
0
0.2
0.4
0.6
0.8
1
1.2
1
2
3
4
5
6
7
8
9
10
Time (s)
x 10^-3

(a)

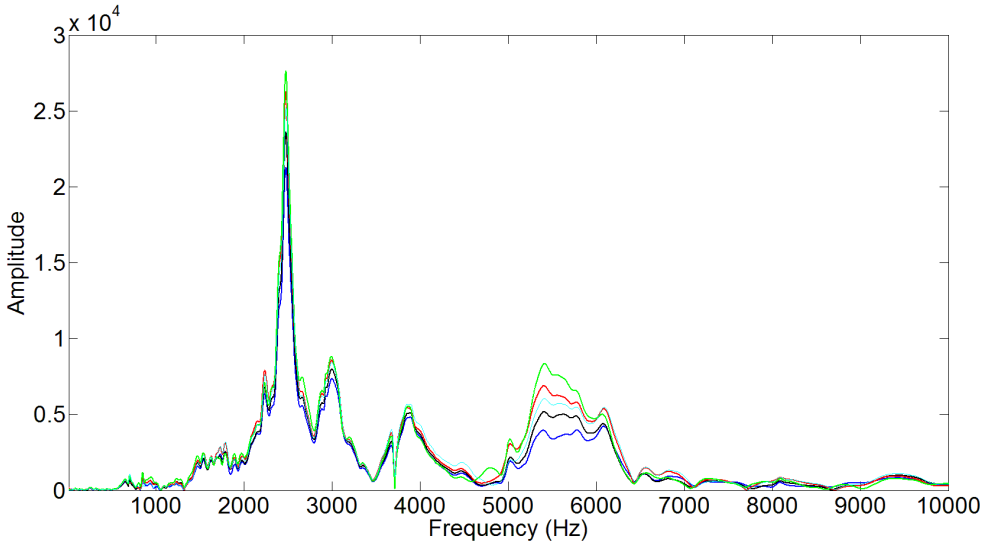
x 10^4
3
2.5
2
1.5
1
0.5
0
Amplitude
1000
2000
3000
4000
5000
6000
7000
8000
9000
10000
Frequency (Hz)

(b)

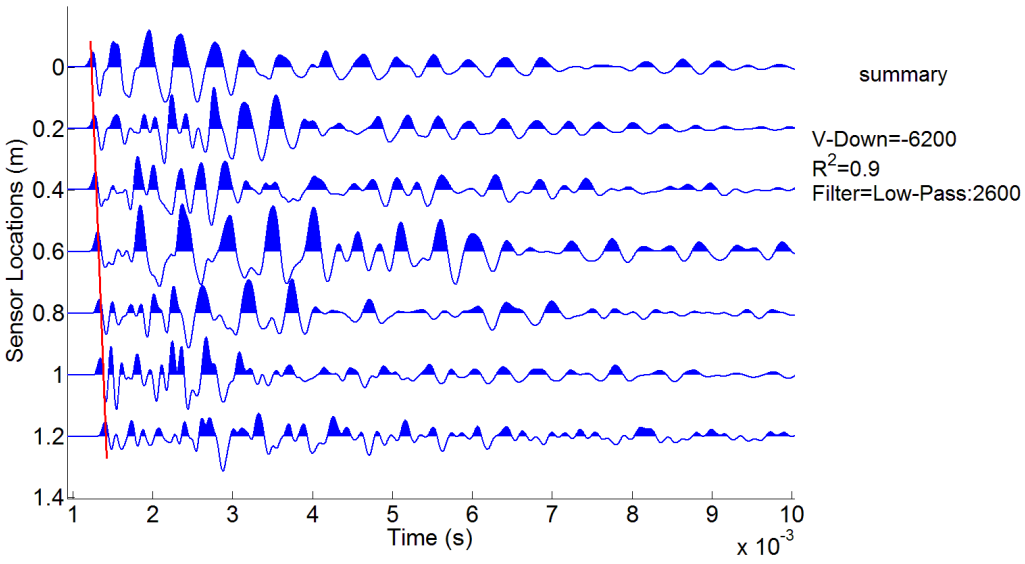
summary
V-Down=-6200
R2=0.9
Filter=Low-Pass:2600
Sensor Locations (m)
Time (s)
x 10-3

(c)

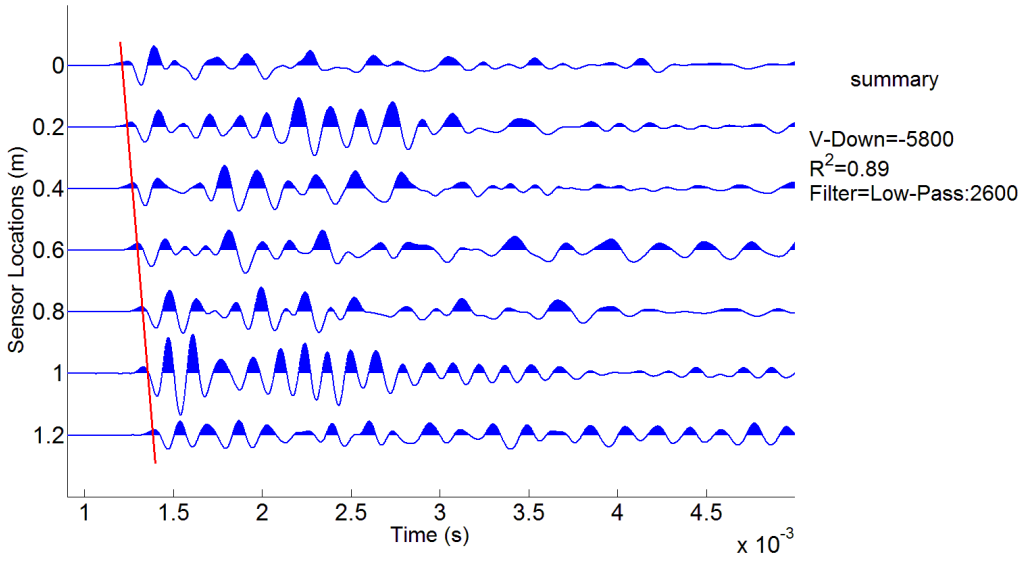
summary
V-Down=-5800
R2=0.89
Filter=Low-Pass:2600
Sensor Locations (m)
Time (s)
x 10-3

(d)

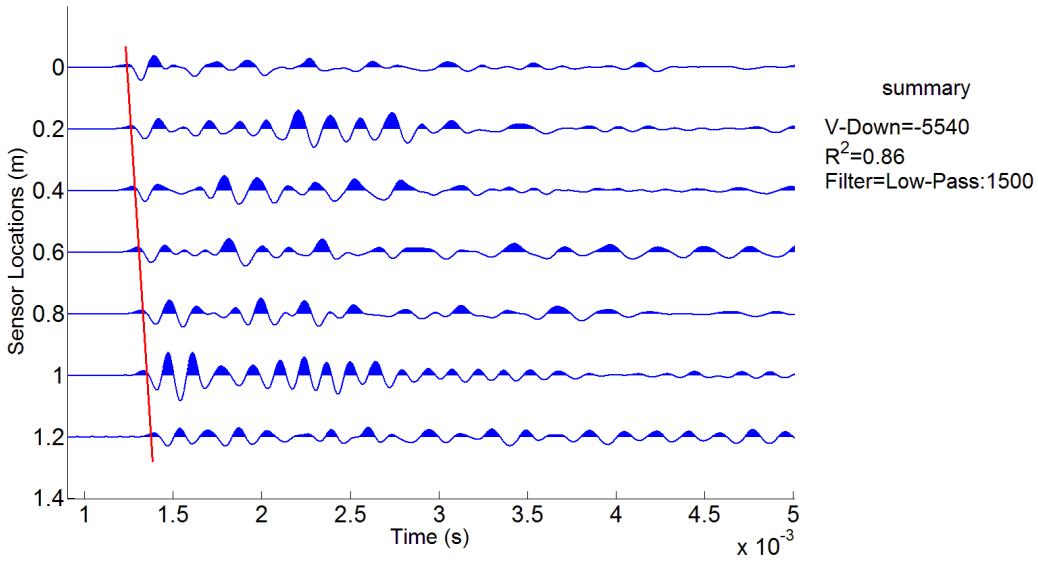

(f)

Figure B. 3: (a) Repeatability of the five tests in all sensors, (b): FFT of all sensors, (c): Captured signals in all sensors after low-pass filtering with 2600 Hz cut-off frequency, (d): Captured signals in all sensors after low-pass filtering with 2600 Hz cut-off frequency followed by predictive deconvolution, and (f): Captured signals in all sensors after low-pass filtering with 1500 Hz cut-off frequency

Pole 4

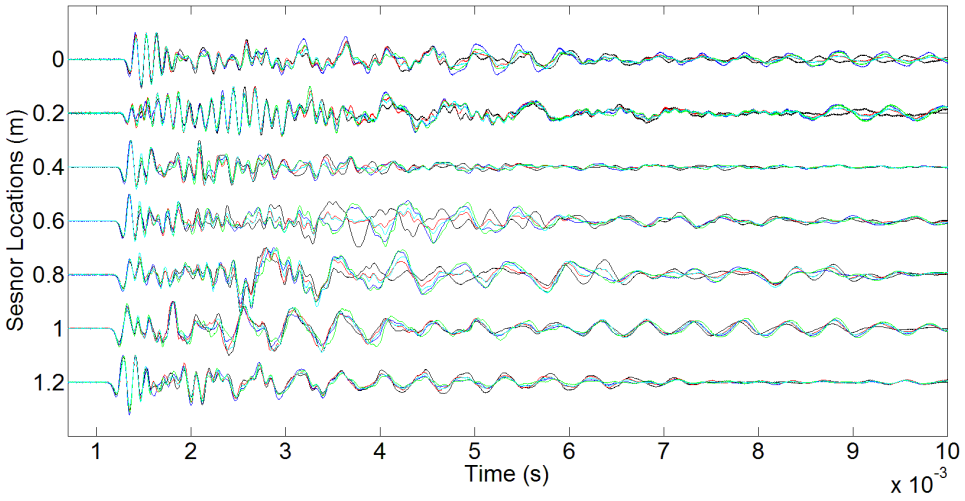

(a)

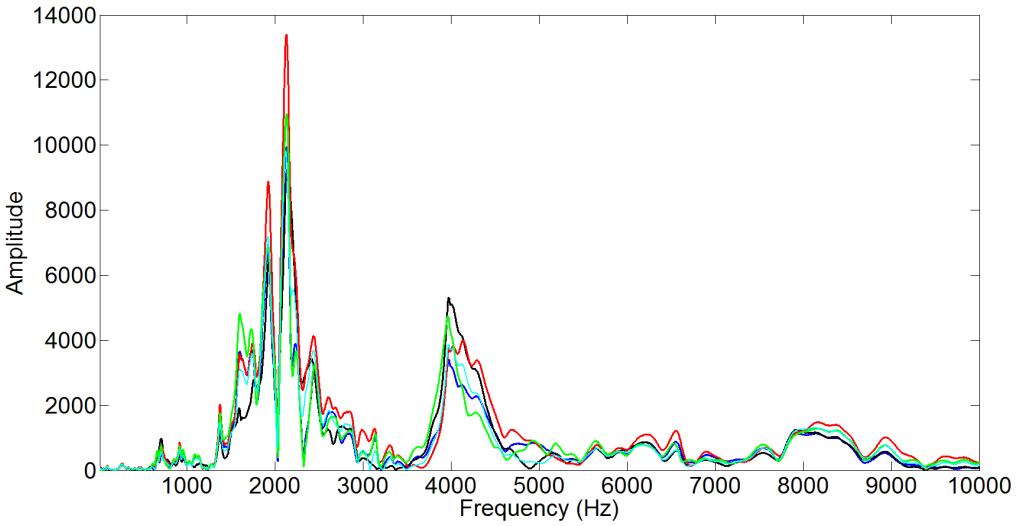
Amplitude
Frequency (Hz)
14000
12000
10000
8000
6000
4000
2000
0
1000
2000
3000
4000
5000
6000
7000
8000
9000
10000

(b)

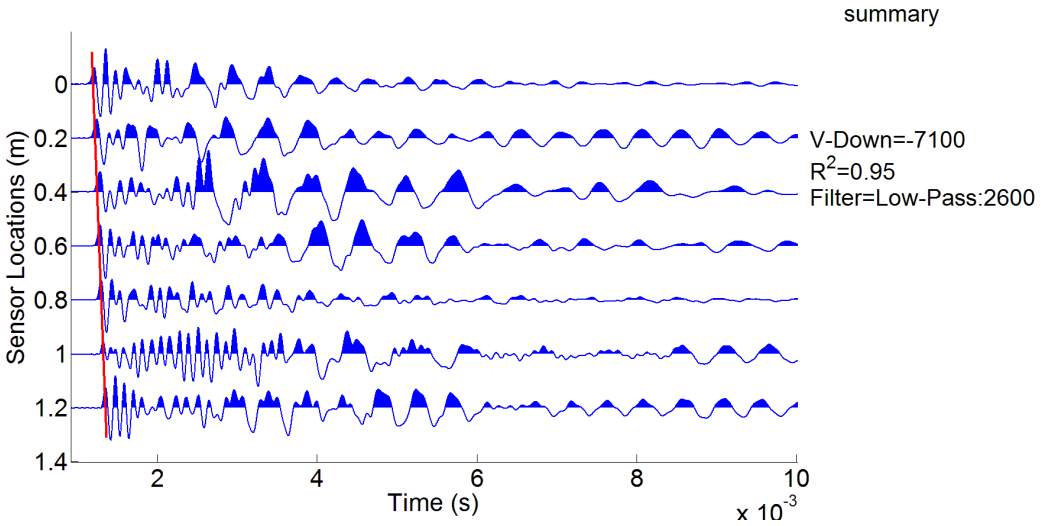
summary
Sensor Locations (m)
Time (s)
x 10^-3
V-Down=-7100
R2=0.95
Filter=Low-Pass:2600

(c)

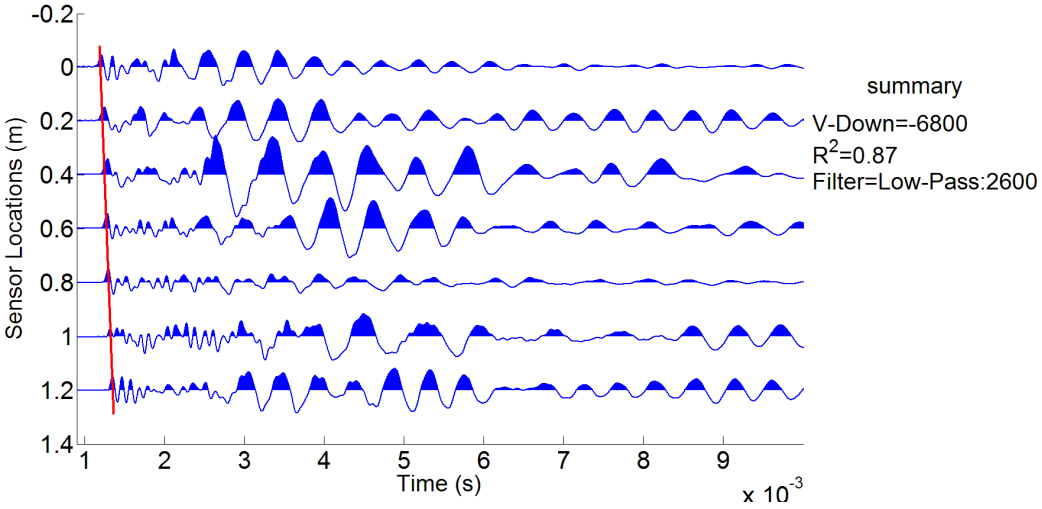
summary
Sensor Locations (m)
Time (s)
x 10^-3
V-Down=-6800
R2=0.87
Filter=Low-Pass:2600

(d)

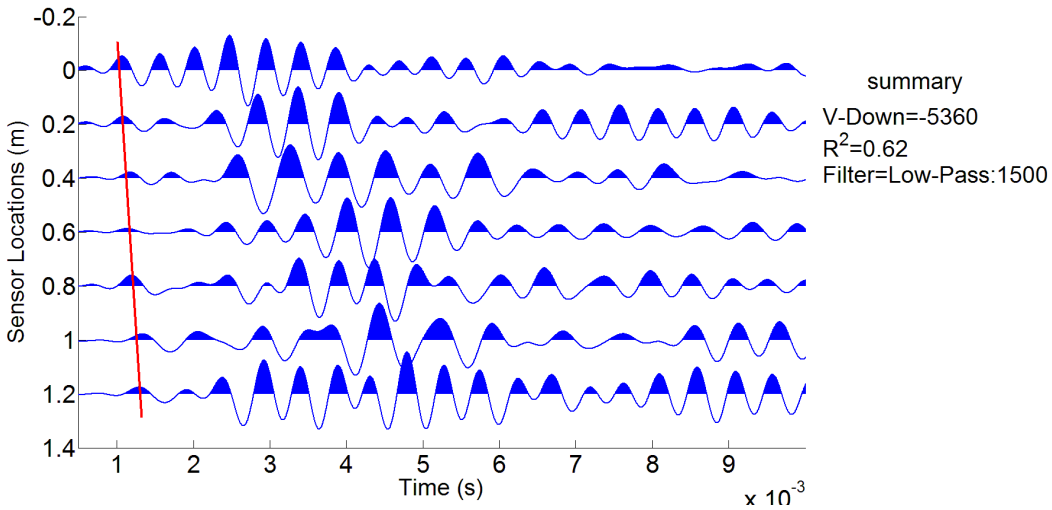

(f)

Figure B. 4: (a) Repeatability of the five tests in all sensors, (b): FFT of all sensors, (c): Captured signals in all sensors after low-pass filtering with 2600 Hz cut-off frequency, (d): Captured signals in all sensors after low-pass filtering with 2600 Hz cut-off frequency followed by predictive deconvolution, and (f): Captured signals in all sensors after low-pass filtering with 1500 Hz cut-off frequency

Pole 5

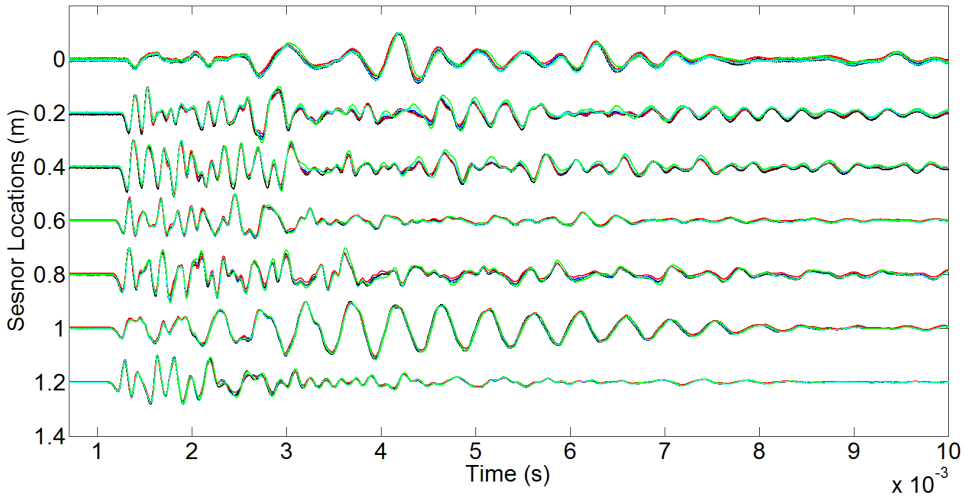

(a)

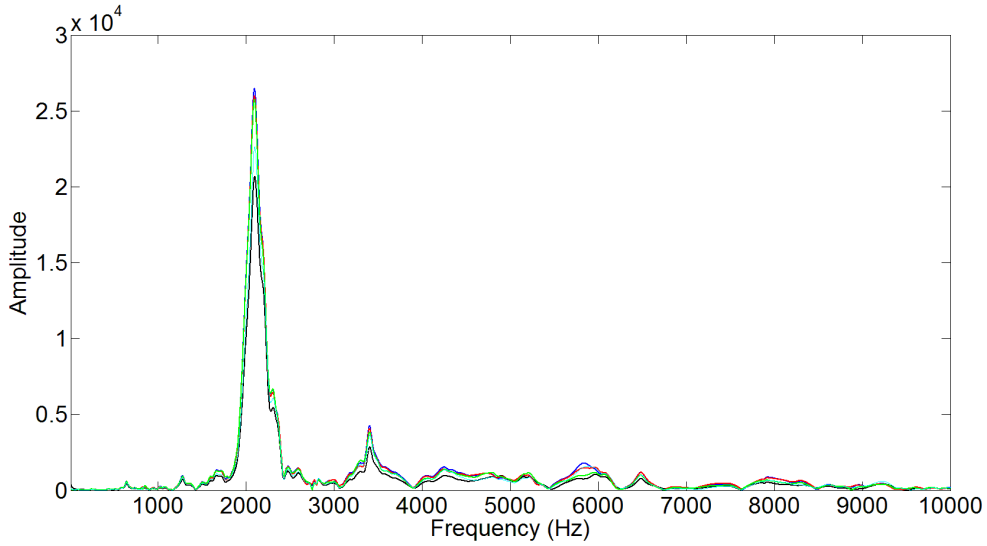
x 10^4
3
2.5
2
1.5
1
0.5
0
Amplitude
1000
2000
3000
4000
5000
6000
7000
8000
9000
10000
Frequency (Hz)

(b)

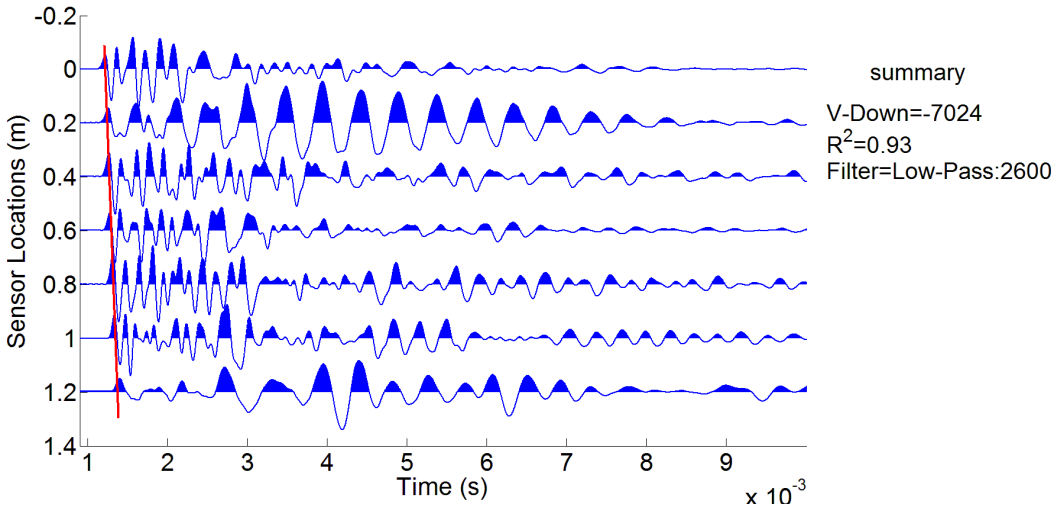
-0.2
0
0.2
0.4
0.6
0.8
1
1.2
1.4
Sensor Locations (m)
1
2
3
4
5
6
7
8
9
Time (s)
x 10^-3
summary
V-Down=-7024
R^2=0.93
Filter=Low-Pass:2600

(c)

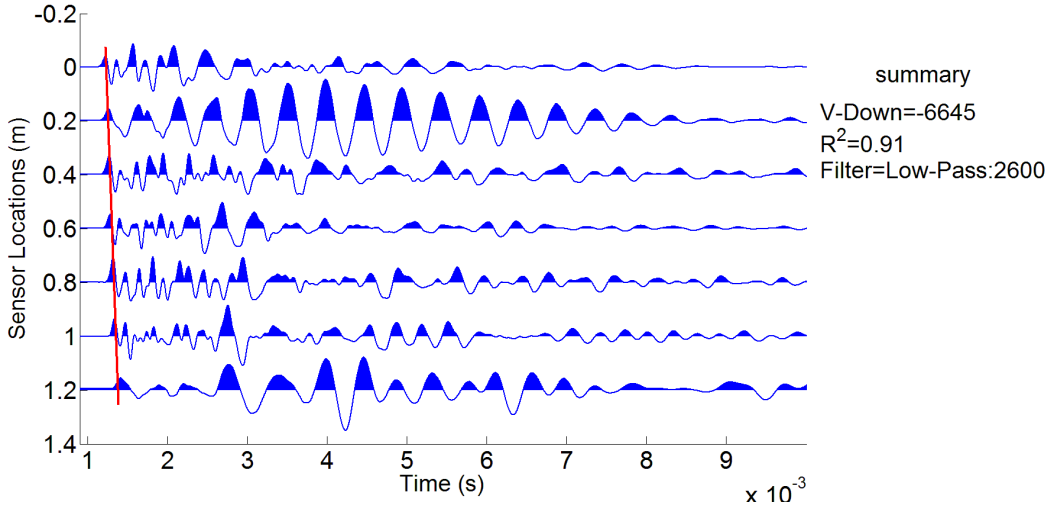
-0.2
0
0.2
0.4
0.6
0.8
1
1.2
1.4
Sensor Locations (m)
1
2
3
4
5
6
7
8
9
Time (s)
x 10^-3
summary
V-Down=-6645
R^2=0.91
Filter=Low-Pass:2600

(d)

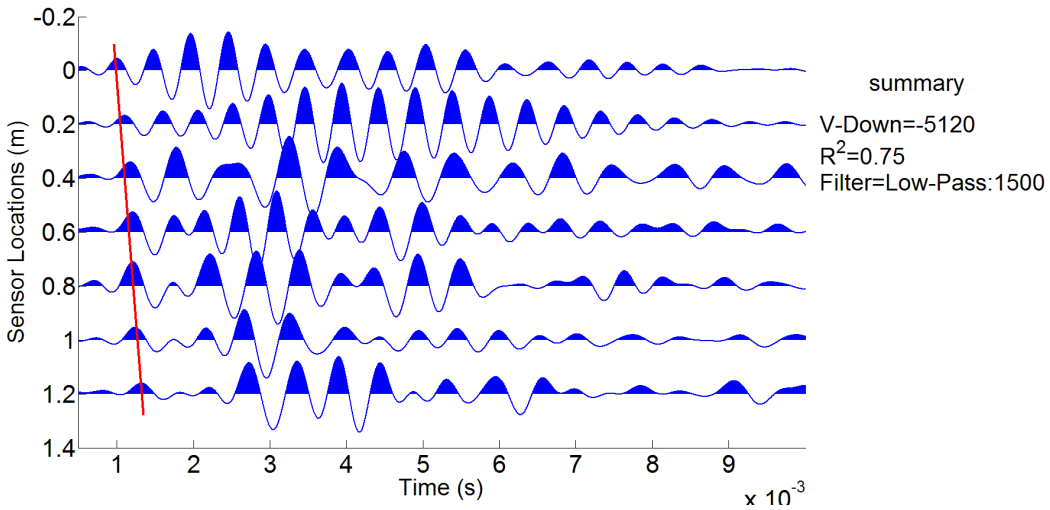

(f)

Figure B. 5: (a) Repeatability of the five tests in all sensors, (b): FFT of all sensors, (c): Captured signals in all sensors after low-pass filtering with 2600 Hz cut-off frequency, (d): Captured signals in all sensors after low-pass filtering with 2600 Hz cut-off frequency followed by predictive deconvolution, and (f): Captured signals in all sensors after low-pass filtering with 1500 Hz cut-off frequency

Pole 6

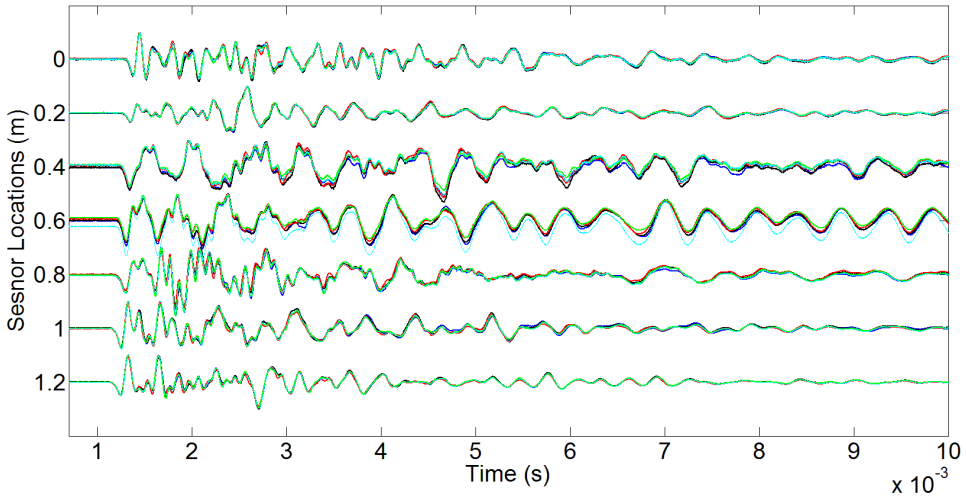

(a)

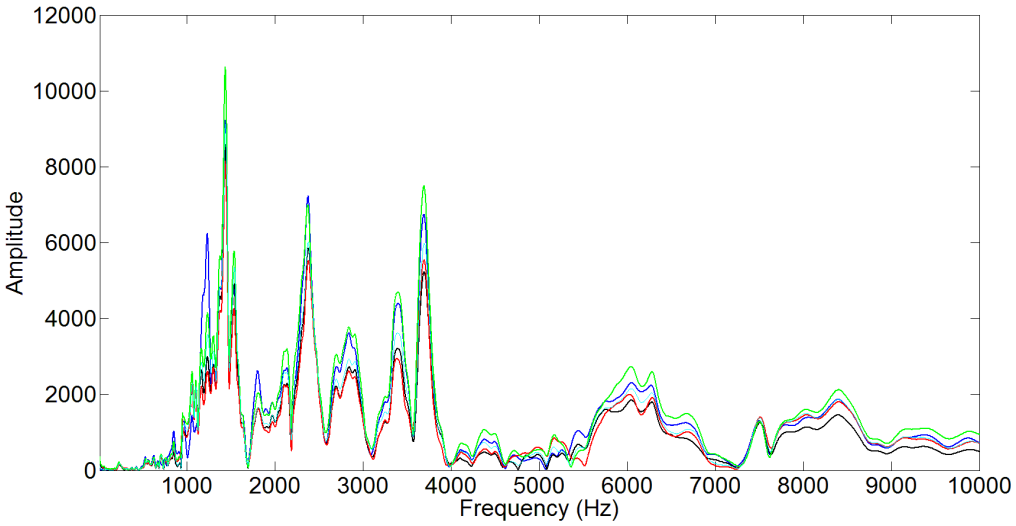
Amplitude
Frequency (Hz)
12000
10000
8000
6000
4000
2000
0
1000
2000
3000
4000
5000
6000
7000
8000
9000
10000

(b)

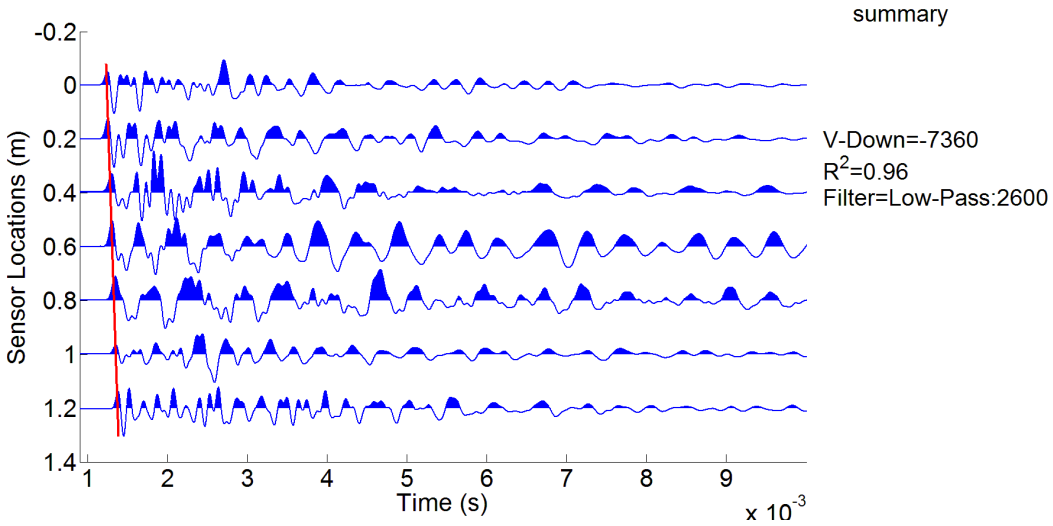
summary
Sensor Locations (m)
Time (s)
x 10^-3
V-Down=-7360
R^2=0.96
Filter=Low-Pass:2600

(c)

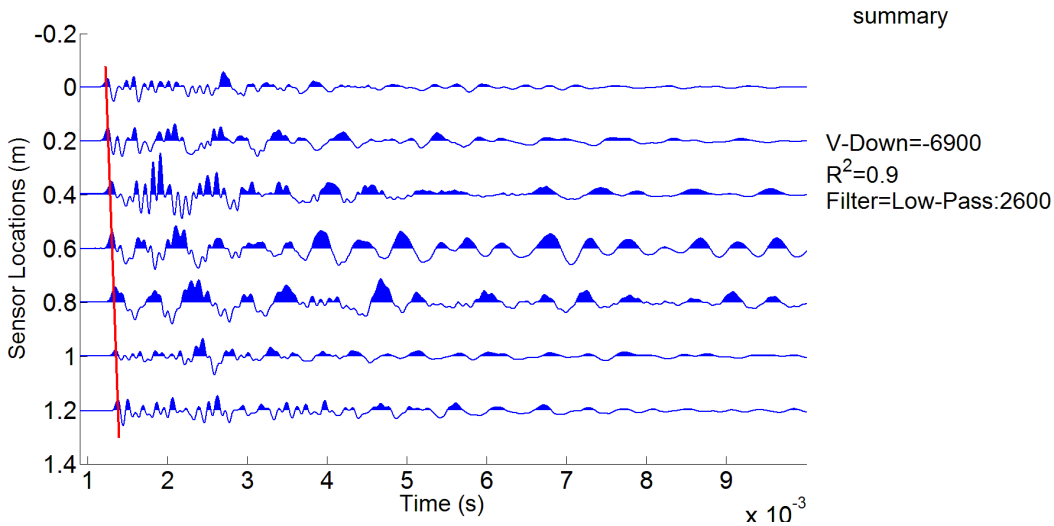
summary
Sensor Locations (m)
Time (s)
x 10^-3
V-Down=-6900
R^2=0.9
Filter=Low-Pass:2600

(d)

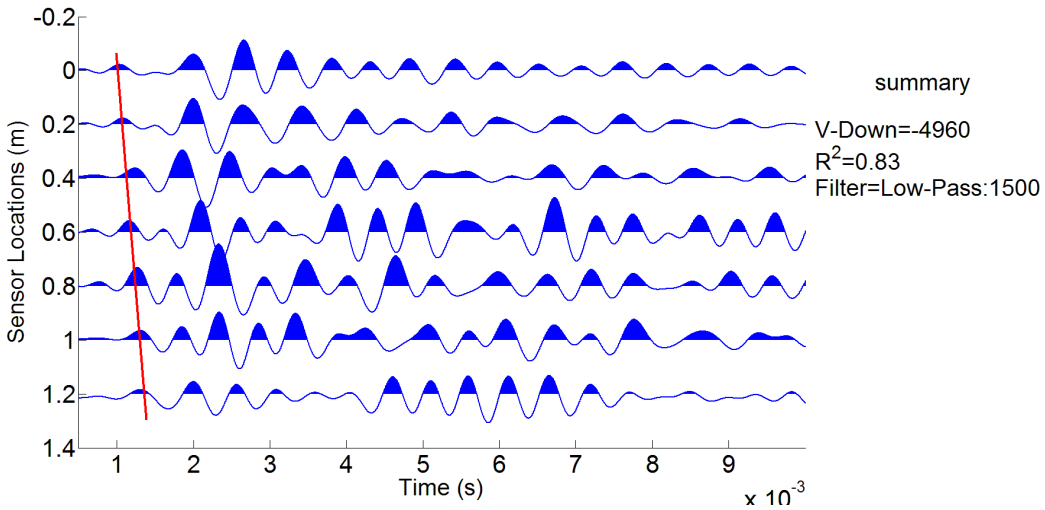

(f)

Figure B. 6: (a) Repeatability of the five tests in all sensors, (b): FFT of all sensors, (c): Captured signals in all sensors after low-pass filtering with 2600 Hz cut-off frequency, (d): Captured signals in all sensors after low-pass filtering with 2600 Hz cut-off frequency followed by predictive deconvolution, and (f): Captured signals in all sensors after low-pass filtering with 1500 Hz cut-off frequency

Pole 7

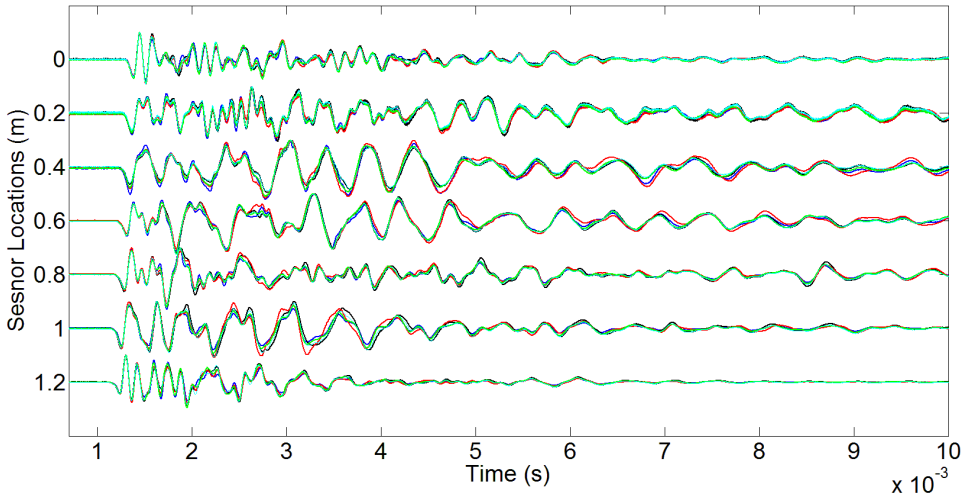

(a)

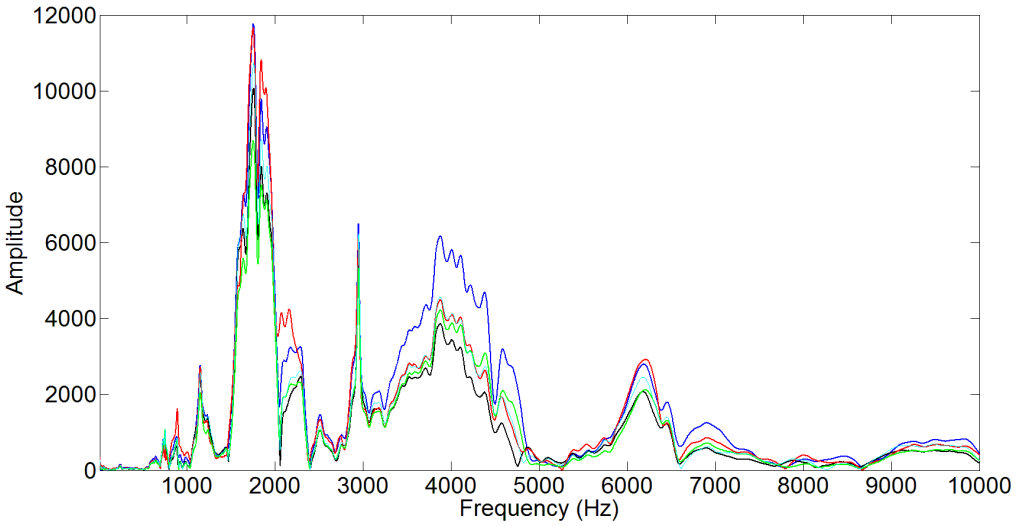
Amplitude
Frequency (Hz)
12000
10000
8000
6000
4000
2000
0
1000
2000
3000
4000
5000
6000
7000
8000
9000
10000

(b)

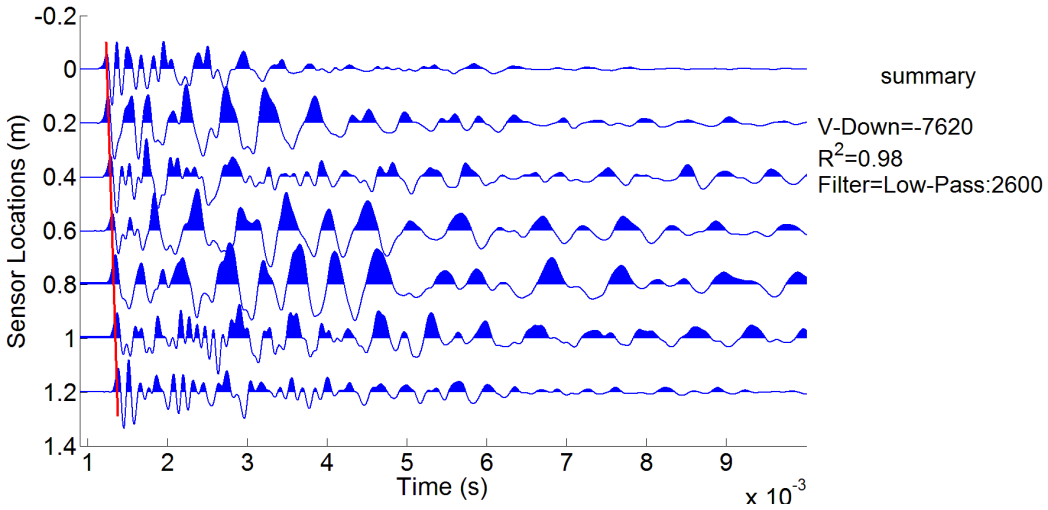
Sensor Locations (m)
Time (s)
x 10^-3
summary
V-Down=-7620
R2=0.98
Filter=Low-Pass:2600

(c)

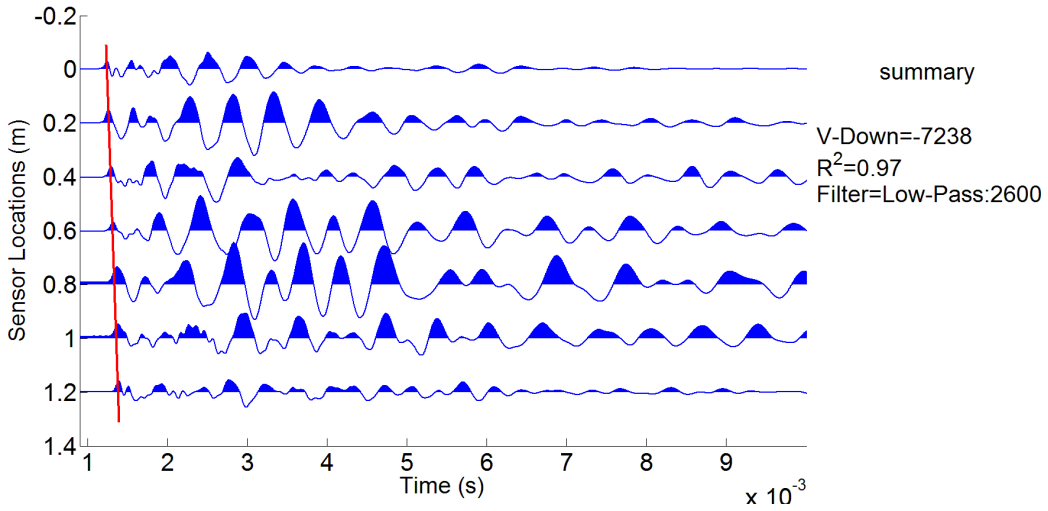
Sensor Locations (m)
Time (s)
x 10^-3
summary
V-Down=-7238
R2=0.97
Filter=Low-Pass:2600

(d)

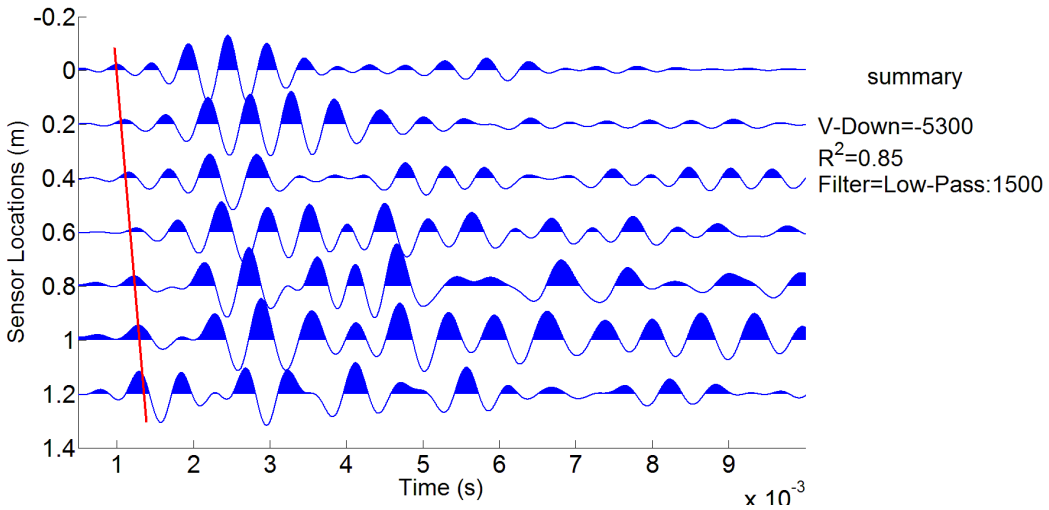

(f)

Figure B. 7: (a) Repeatability of the five tests in all sensors, (b): FFT of all sensors, (c): Captured signals in all sensors after low-pass filtering with 2600 Hz cut-off frequency, (d): Captured signals in all sensors after low-pass filtering with 2600 Hz cut-off frequency followed by predictive deconvolution, and (f): Captured signals in all sensors after low-pass filtering with 1500 Hz cut-off frequency

Pole 8

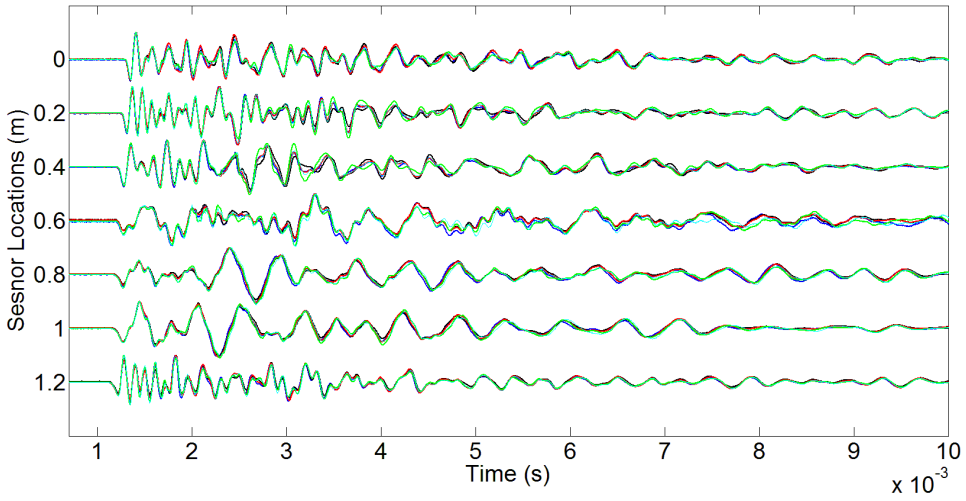

(a)

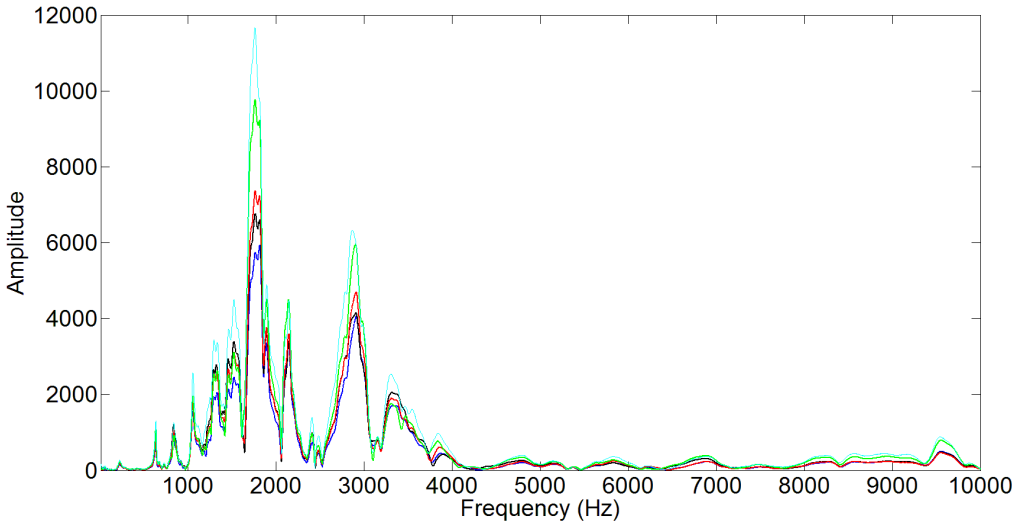
Amplitude
Frequency (Hz)
12000
10000
8000
6000
4000
2000
0
1000
2000
3000
4000
5000
6000
7000
8000
9000
10000

(b)

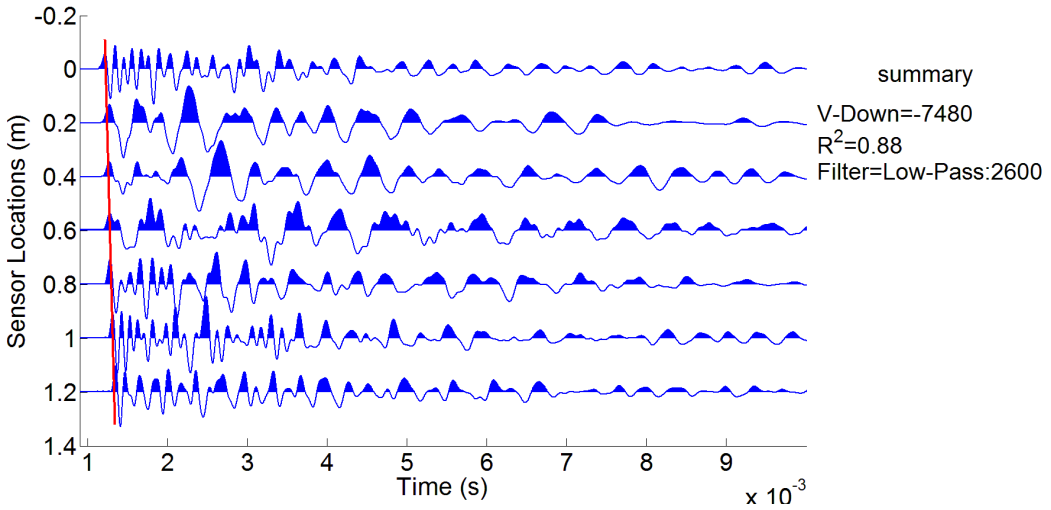
Sensor Locations (m)
Time (s)
x 10^-3
summary
V-Down=-7480
R2=0.88
Filter=Low-Pass:2600

(c)

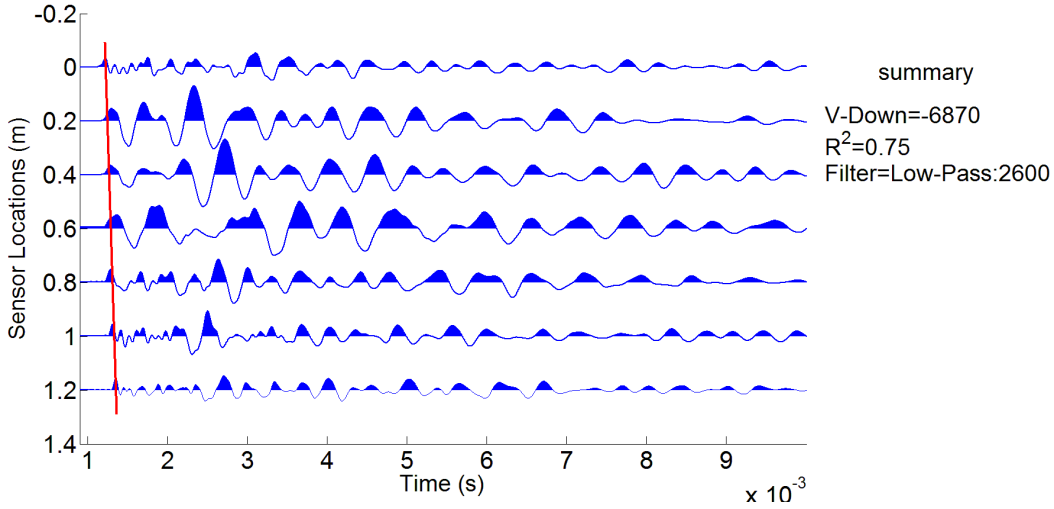
Sensor Locations (m)
Time (s)
x 10^-3
summary
V-Down=-6870
R2=0.75
Filter=Low-Pass:2600

(d)

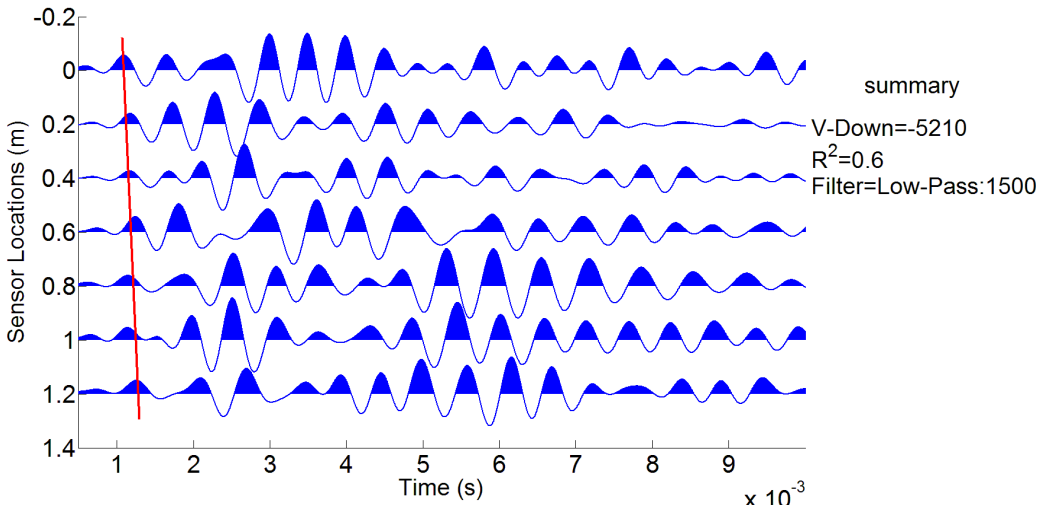

(f)

Figure B. 8: (a) Repeatability of the five tests in all sensors, (b): FFT of all sensors, (c): Captured signals in all sensors after low-pass filtering with 2600 Hz cut-off frequency, (d): Captured signals in all sensors after low-pass filtering with 2600 Hz cut-off frequency followed by predictive deconvolution, and (f): Captured signals in all sensors after low-pass filtering with 1500 Hz cut-off frequency

Pole 9

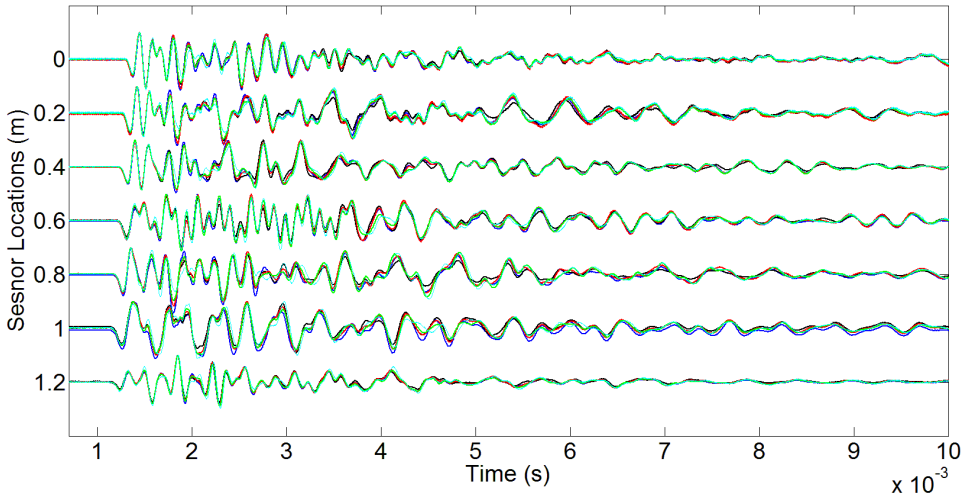

(a)

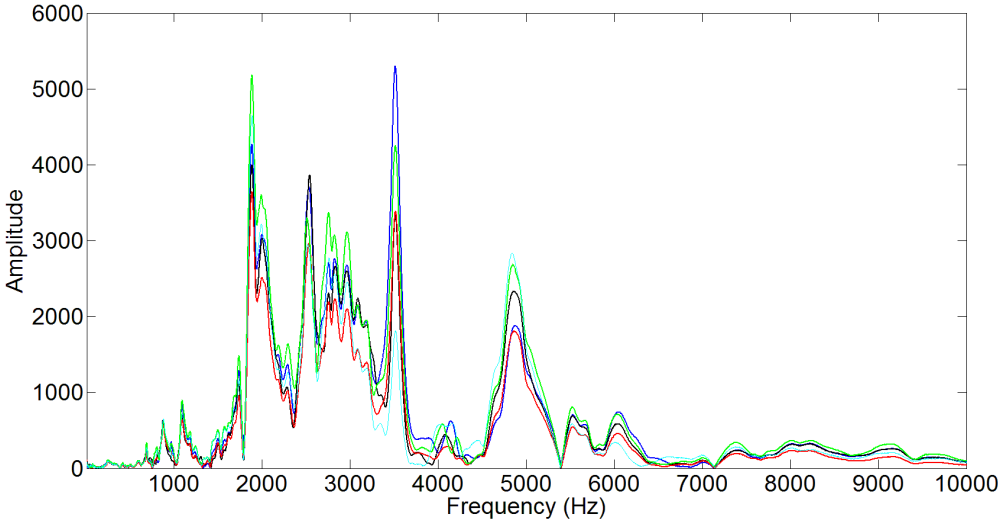
Amplitude
Frequency (Hz)
6000
5000
4000
3000
2000
1000
0
1000
2000
3000
4000
5000
6000
7000
8000
9000
10000

(b)

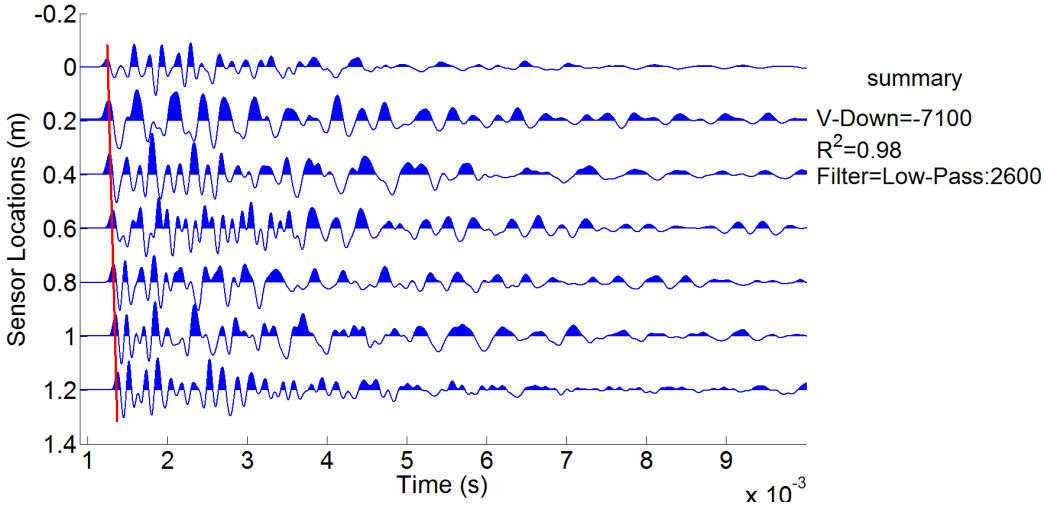
Sensor Locations (m)
Time (s)
x 10^-3
summary
V-Down=-7100
R2=0.98
Filter=Low-Pass:2600

(c)

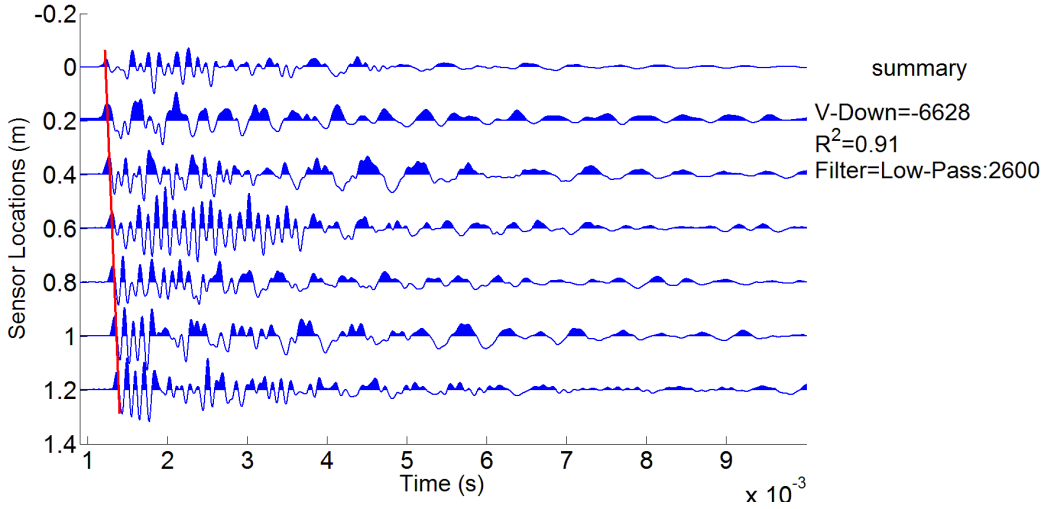
Sensor Locations (m)
Time (s)
x 10^-3
summary
V-Down=-6628
R2=0.91
Filter=Low-Pass:2600

(d)

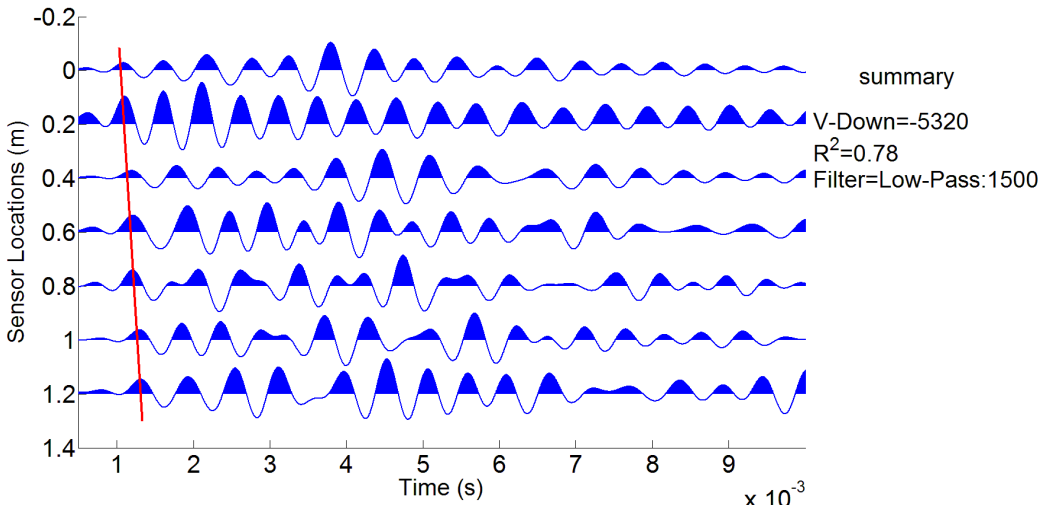

(f)

Figure B. 9: (a) Repeatability of the five tests in all sensors, (b): FFT of all sensors, (c): Captured signals in all sensors after low-pass filtering with 2600 Hz cut-off frequency, (d): Captured signals in all sensors after low-pass filtering with 2600 Hz cut-off frequency followed by predictive deconvolution, and (f): Captured signals in all sensors after low-pass filtering with 1500 Hz cut-off frequency

Pole 10

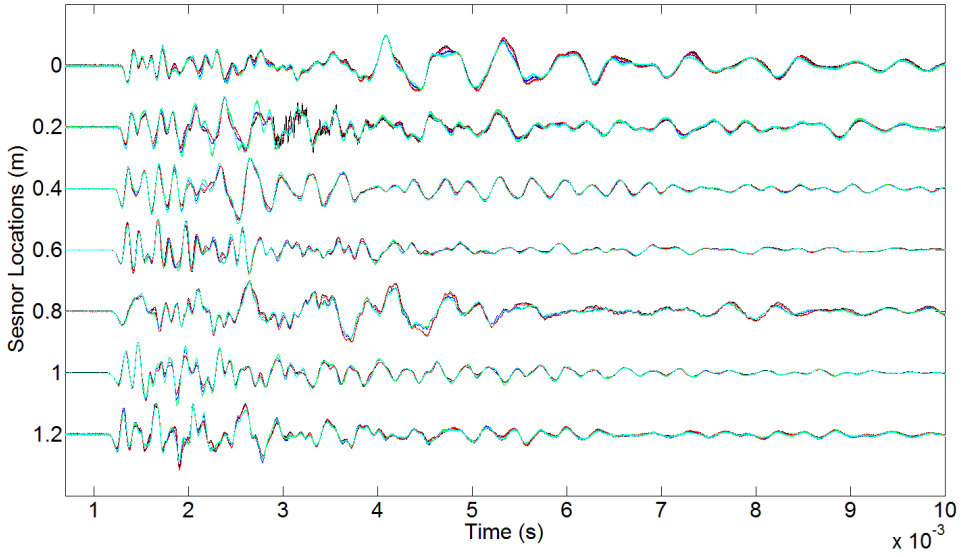

(a)

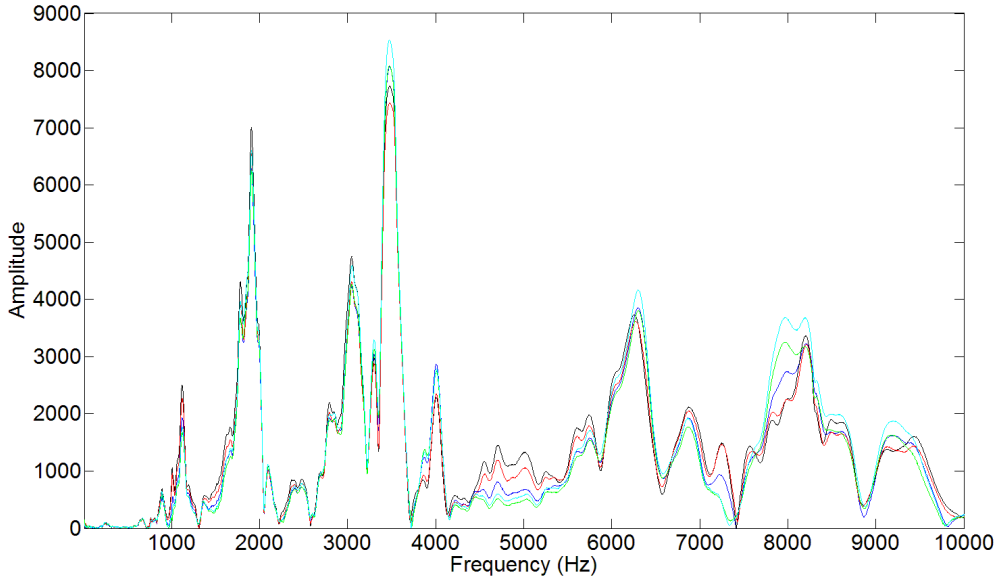
Amplitude
Frequency (Hz)
9000
8000
7000
6000
5000
4000
3000
2000
1000
0
1000
2000
3000
4000
5000
6000
7000
8000
9000
10000

(b)

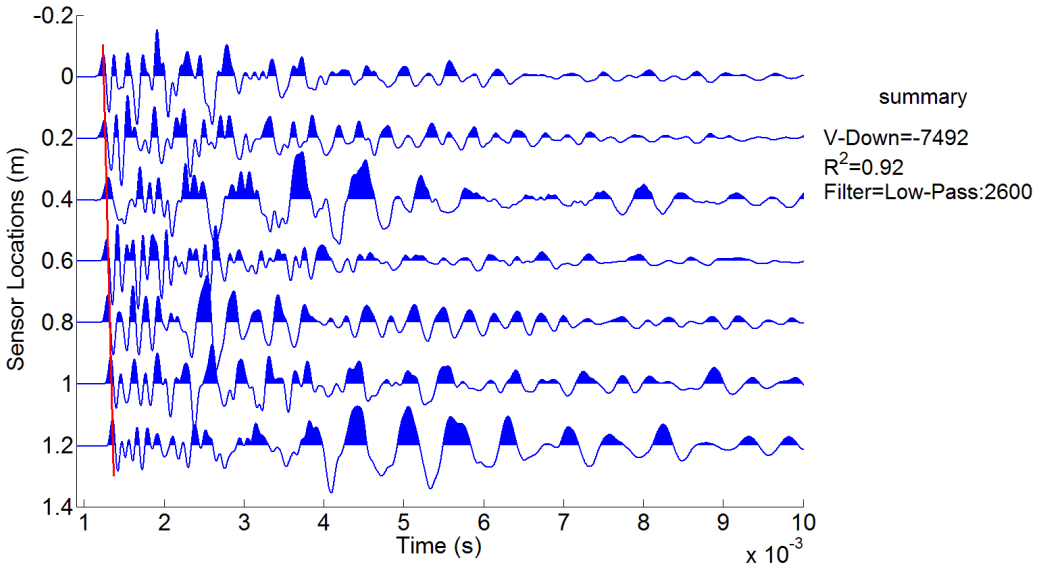
Sensor Locations (m)
Time (s)
x 10-3
-0.2
0
0.2
0.4
0.6
0.8
1
1.2
1.4
1
2
3
4
5
6
7
8
9
10
summary
V-Down=-7492
R2=0.92
Filter=Low-Pass:2600

(c)

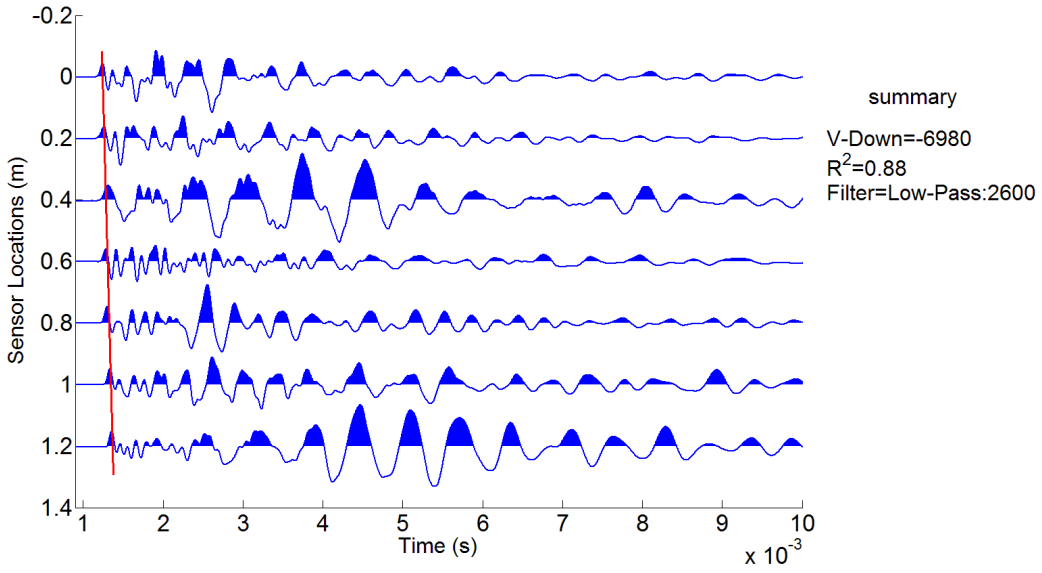

(d)

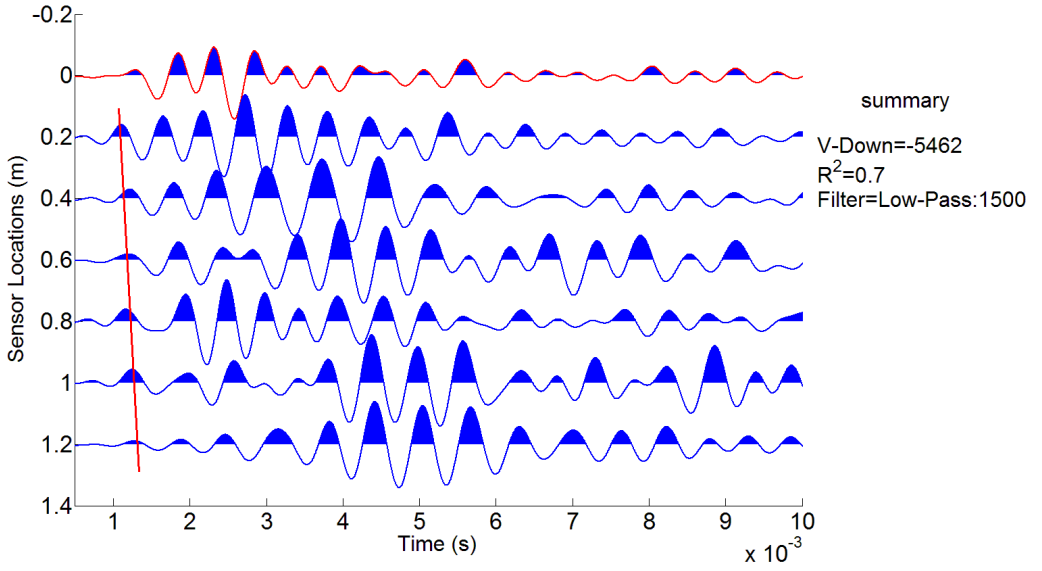

(f)

Figure B. 10: (a) Repeatability of the five tests in all sensors, (b): FFT of all sensors, (c): Captured signals in all sensors after low-pass filtering with 2600 Hz cut-off frequency, (d): Captured signals in all sensors after low-pass filtering with 2600 Hz cut-off frequency followed by predictive deconvolution, and (f): Captured signals in all sensors after low-pass filtering with 1500 Hz cut-off frequency

Pole 11

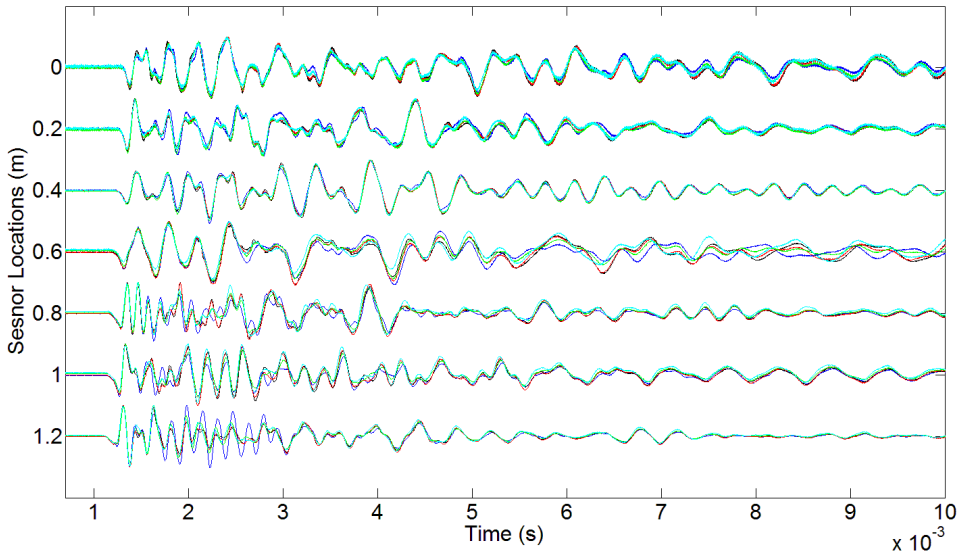
Sesnor Locations (m)
0
0.2
0.4
0.6
0.8
1
1.2
1
2
3
4
5
6
7
8
9
10
Time (s)
x 10^-3

(a)

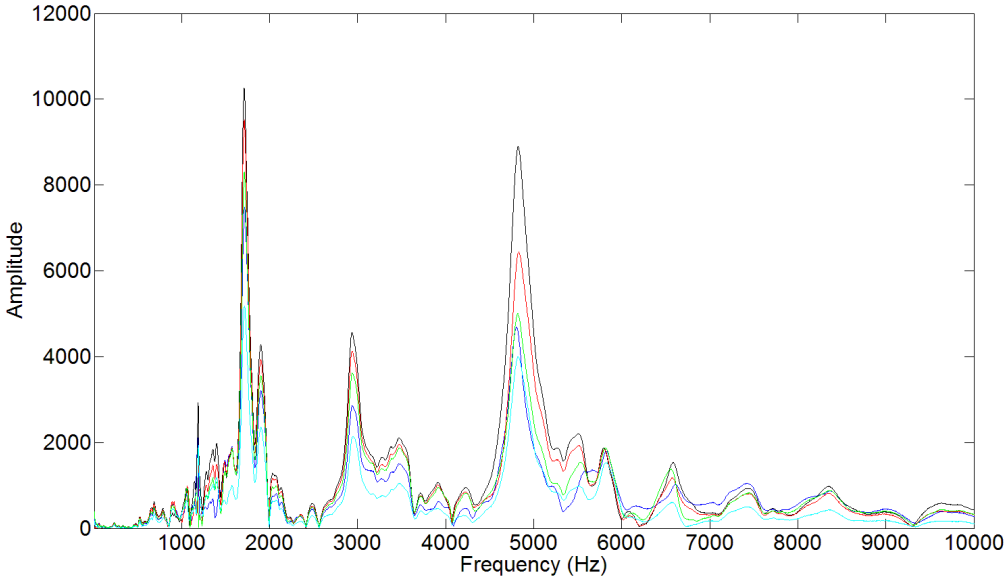
Amplitude
12000
10000
8000
6000
4000
2000
0
1000
2000
3000
4000
5000
6000
7000
8000
9000
10000
Frequency (Hz)

(b)

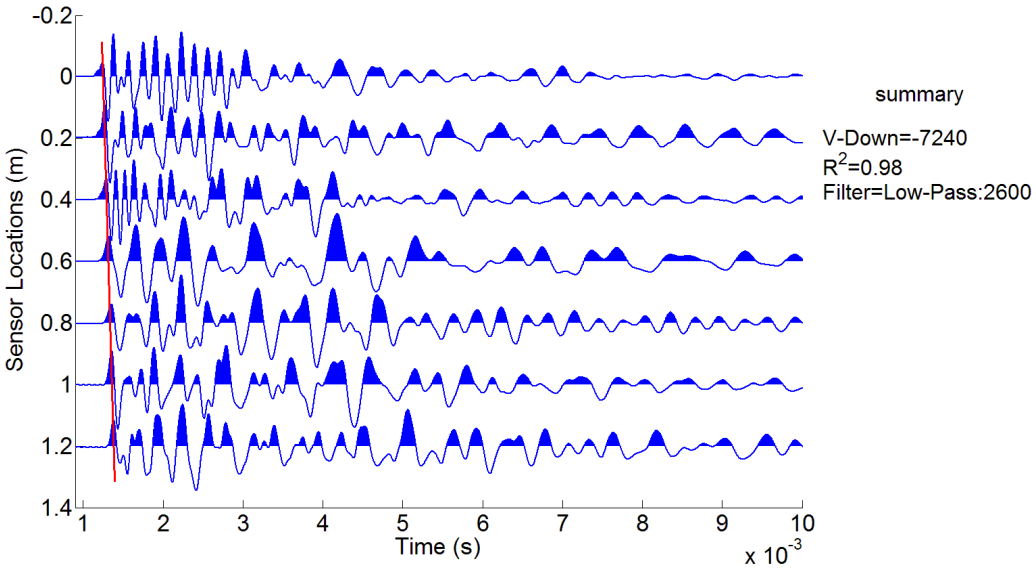
-0.2
0
0.2
0.4
0.6
0.8
1
1.2
1.4
Sensor Locations (m)
1
2
3
4
5
6
7
8
9
10
Time (s)
x 10-3
summary
V-Down=-7240
R2=0.98
Filter=Low-Pass:2600

(c)

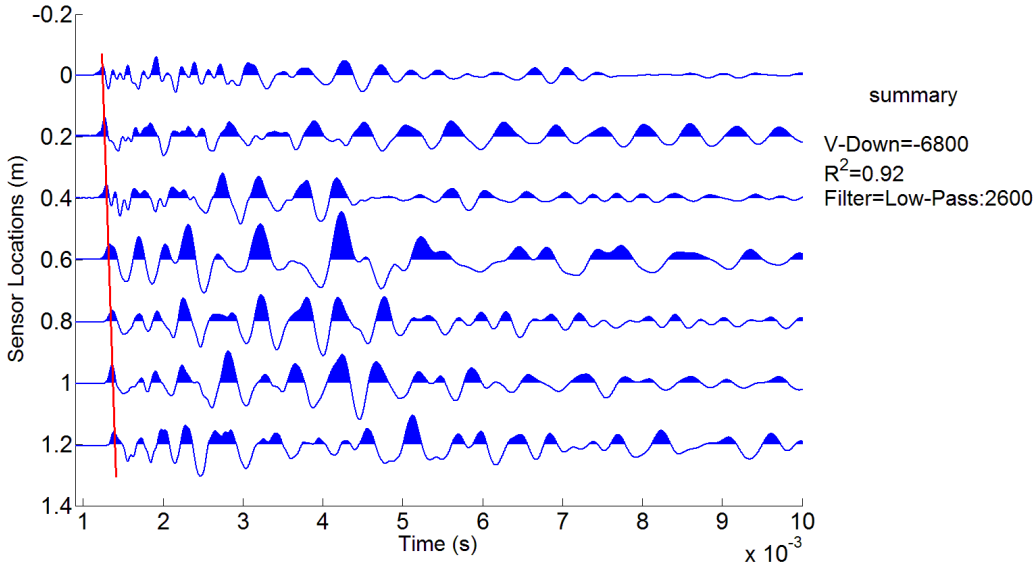
-0.2
0
0.2
0.4
0.6
0.8
1
1.2
1.4
Sensor Locations (m)
1
2
3
4
5
6
7
8
9
10
Time (s)
x 10-3
summary
V-Down=-6800
R2=0.92
Filter=Low-Pass:2600

(d)

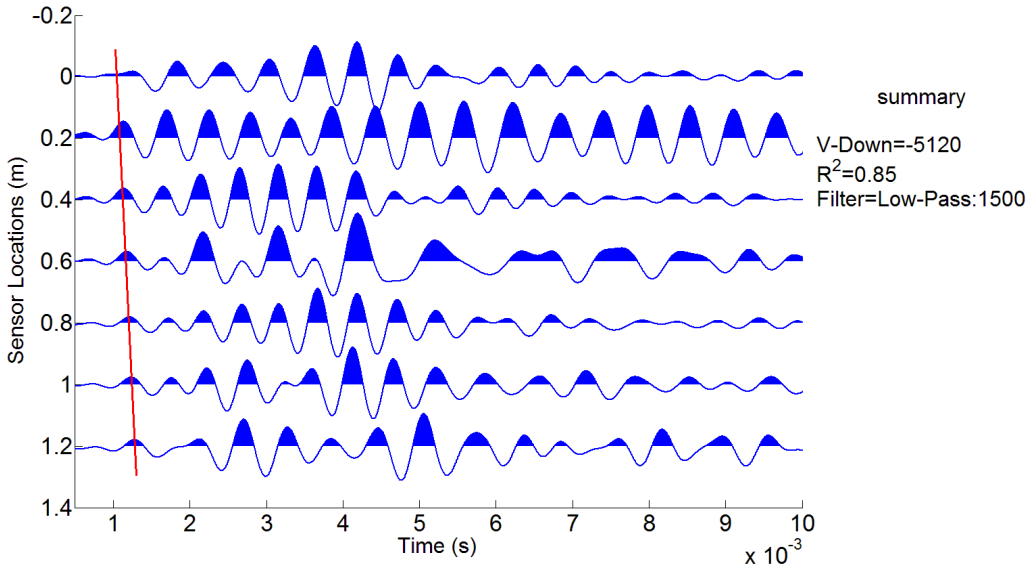

(f)

Figure B. 11: (a) Repeatability of the five tests in all sensors, (b): FFT of all sensors, (c): Captured signals in all sensors after low-pass filtering with 2600 Hz cut-off frequency, (d): Captured signals in all sensors after low-pass filtering with 2600 Hz cut-off frequency followed by predictive deconvolution, and (f): Captured signals in all sensors after low-pass filtering with 1500 Hz cut-off frequency

Pole 12

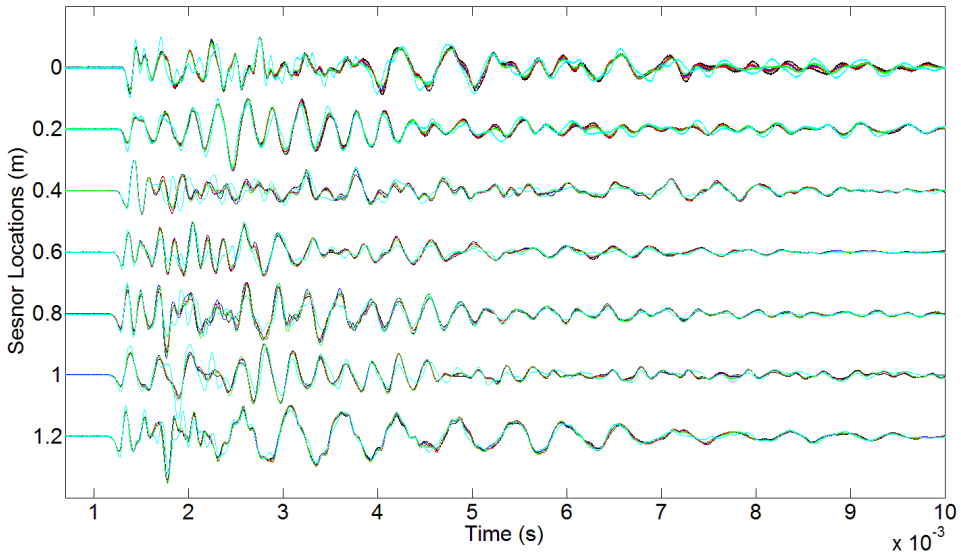

(a)

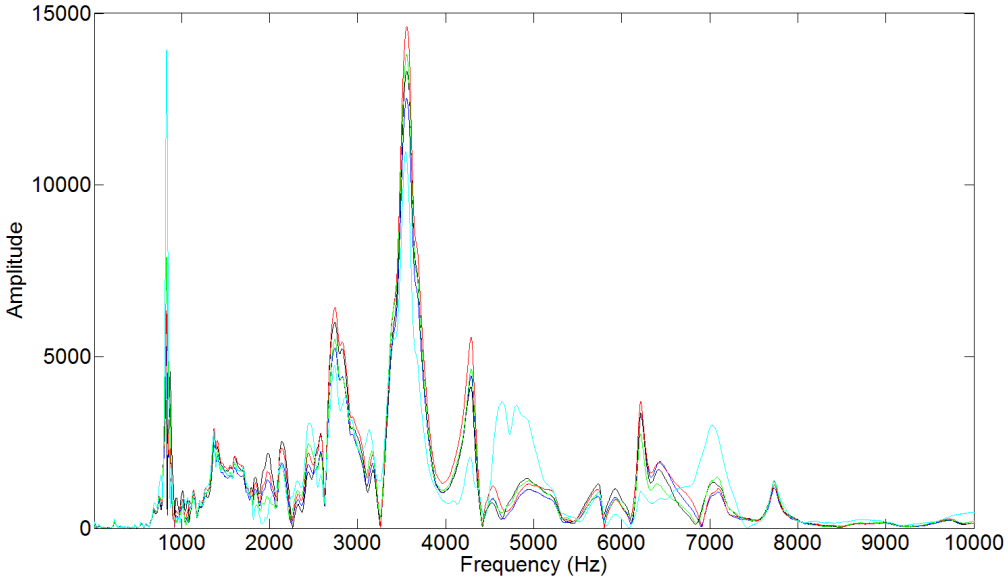
15000
10000
5000
0
Amplitude
1000
2000
3000
4000
5000
6000
7000
8000
9000
10000
Frequency (Hz)

(b)

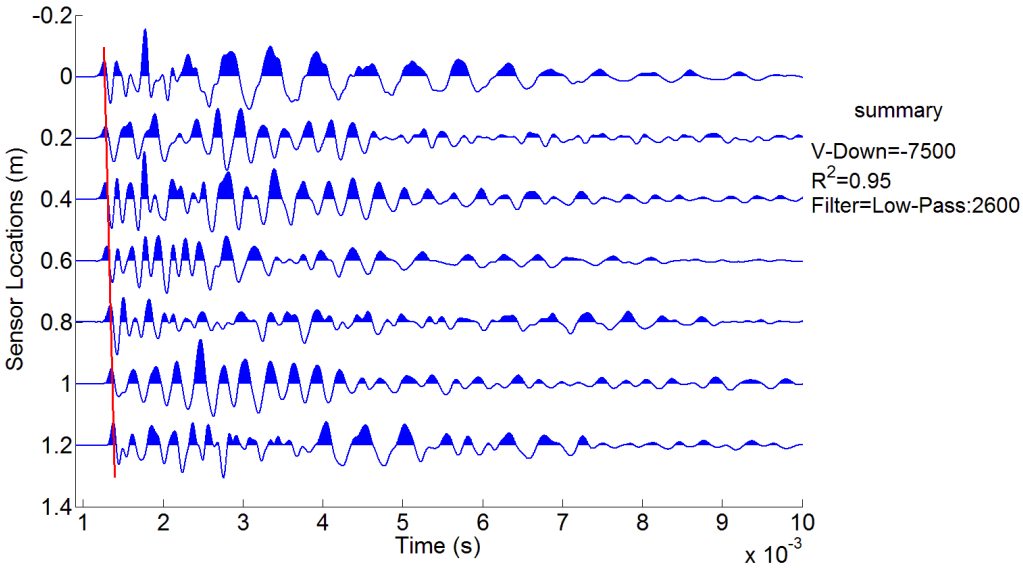
-0.2
0
0.2
0.4
0.6
0.8
1
1.2
1.4
Sensor Locations (m)
1
2
3
4
5
6
7
8
9
10
Time (s)
x 10-3
summary
V-Down=-7500
R2=0.95
Filter=Low-Pass:2600

(c)

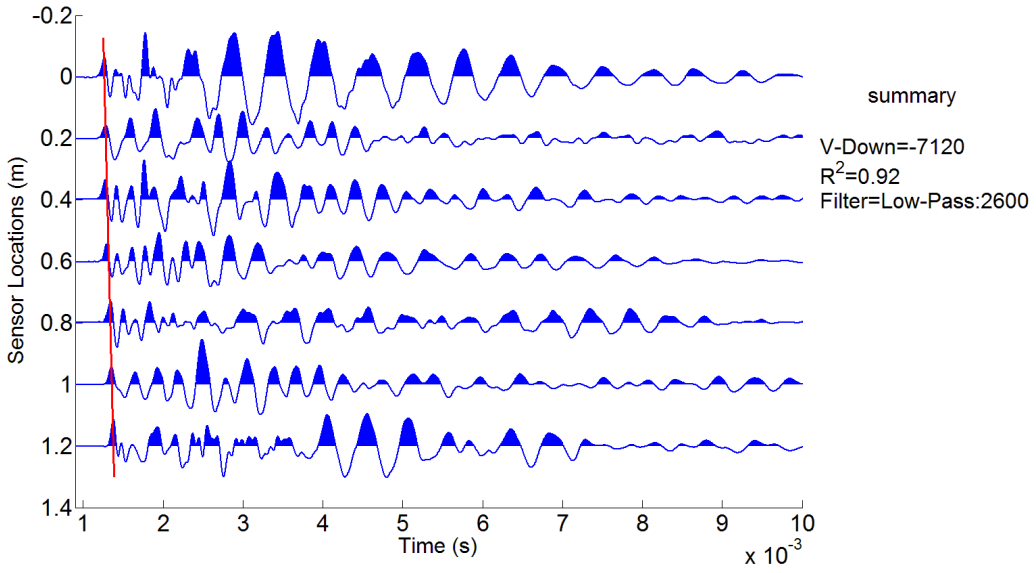

(d)

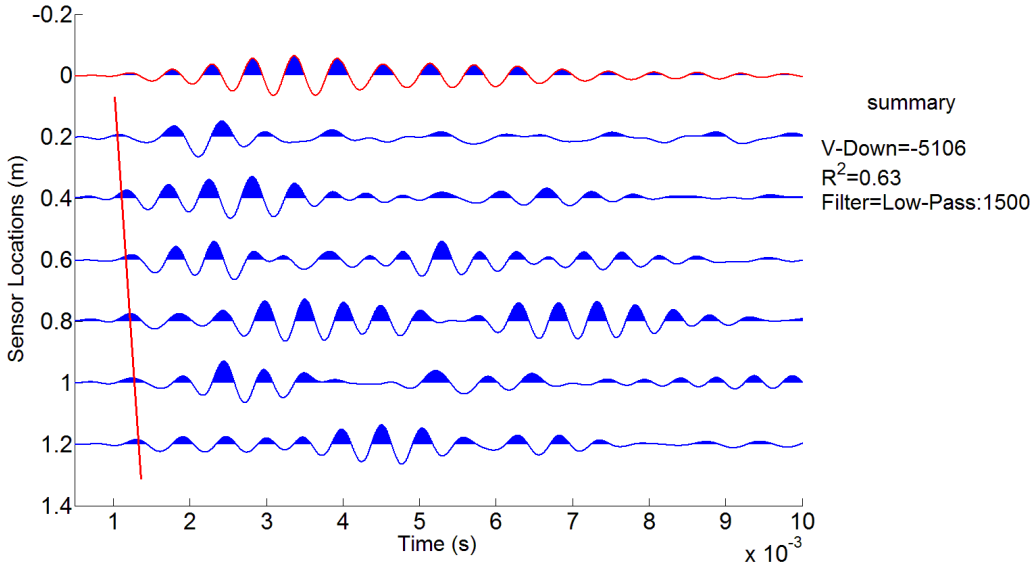

(f)

Figure B. 12: (a) Repeatability of the five tests in all sensors, (b): FFT of all sensors, (c): Captured signals in all sensors after low-pass filtering with 2600 Hz cut-off frequency, (d): Captured signals in all sensors after low-pass filtering with 2600 Hz cut-off frequency followed by predictive deconvolution, and (f): Captured signals in all sensors after low-pass filtering with 1500 Hz cut-off frequency

Pole 13

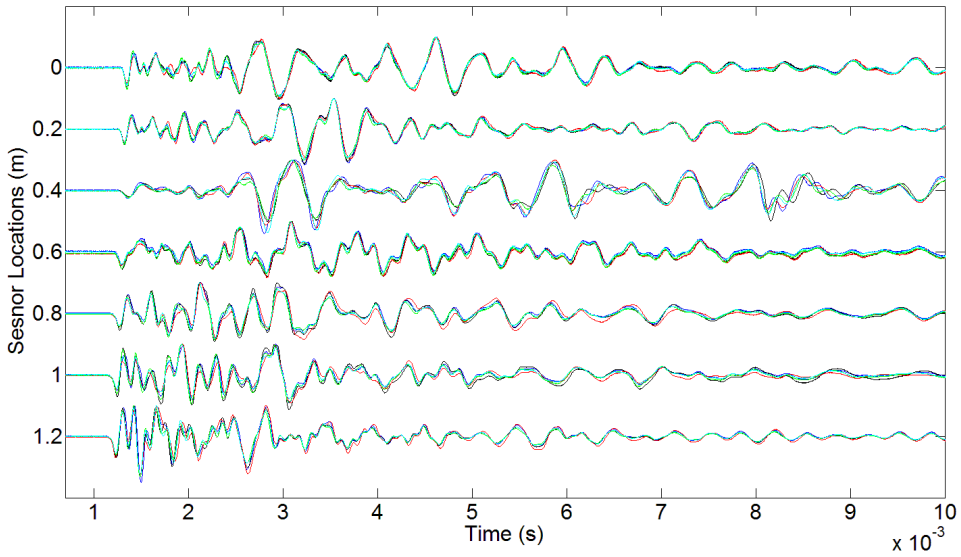
Sesnor Locations (m)
0
0.2
0.4
0.6
0.8
1
1.2
1
2
3
4
5
6
7
8
9
10
Time (s)
x 10^-3

(a)

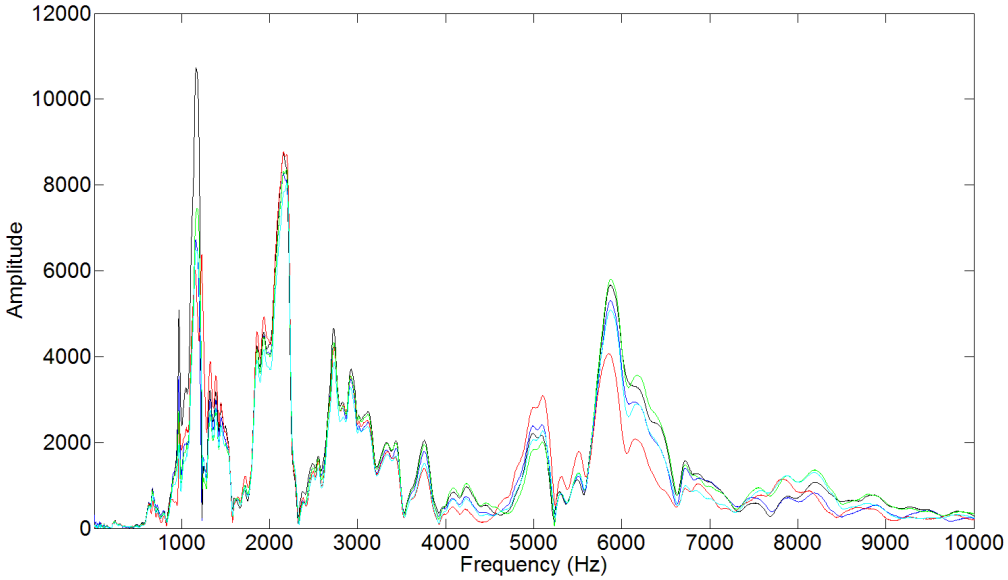
Amplitude
12000
10000
8000
6000
4000
2000
0
1000
2000
3000
4000
5000
6000
7000
8000
9000
10000
Frequency (Hz)

(b)

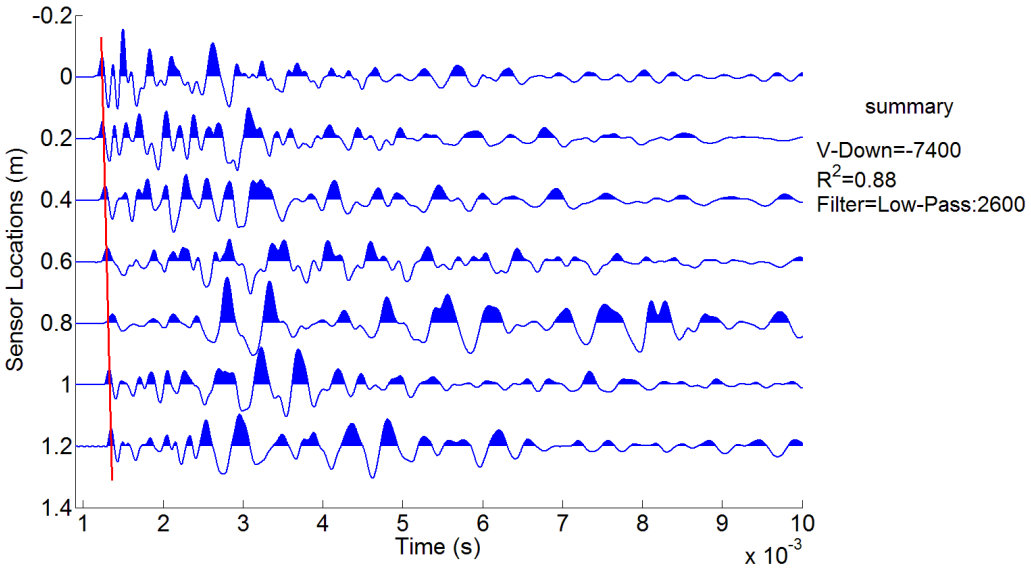
-0.2
0
0.2
0.4
0.6
0.8
1
1.2
1.4
Sensor Locations (m)
1
2
3
4
5
6
7
8
9
10
Time (s)
x 10-3
summary
V-Down=-7400
R2=0.88
Filter=Low-Pass:2600

(c)

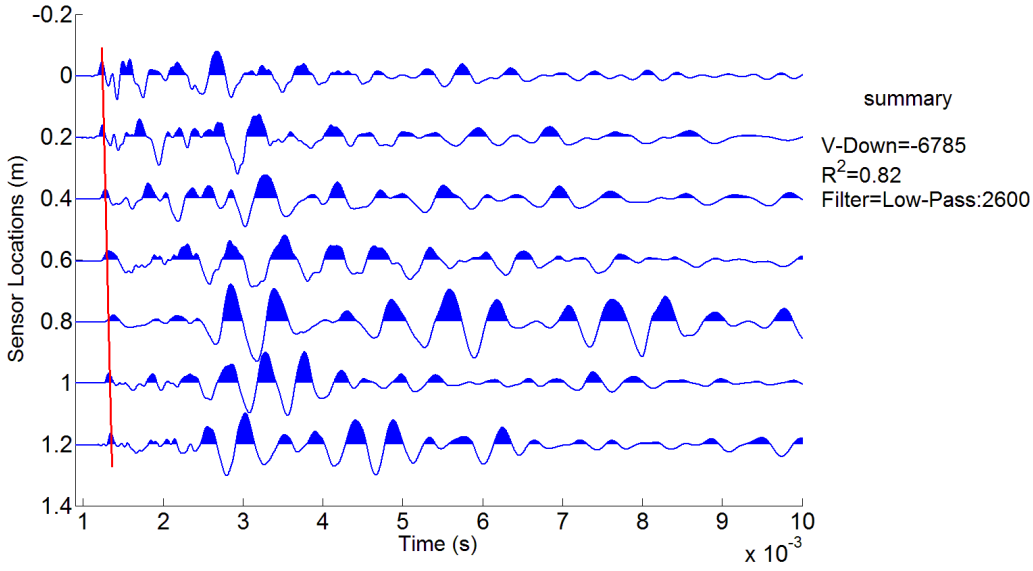
-0.2
0
0.2
0.4
0.6
0.8
1
1.2
1.4
Sensor Locations (m)
1
2
3
4
5
6
7
8
9
10
Time (s)
x 10-3
summary
V-Down=-6785
R2=0.82
Filter=Low-Pass:2600

(d)

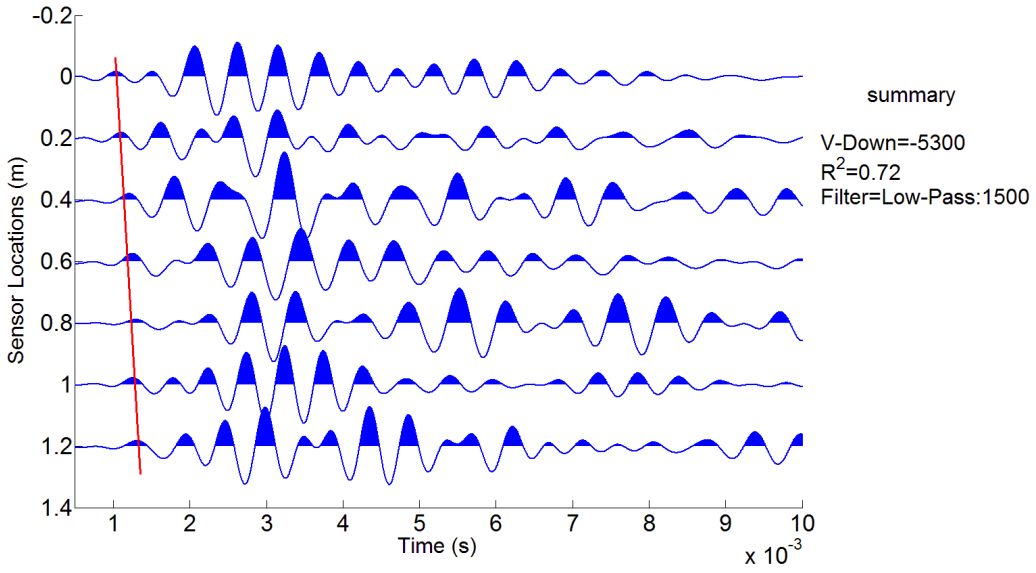

(f)

Figure B. 13: (a) Repeatability of the five tests in all sensors, (b): FFT of all sensors, (c): Captured signals in all sensors after low-pass filtering with 2600 Hz cut-off frequency, (d): Captured signals in all sensors after low-pass filtering with 2600 Hz cut-off frequency followed by predictive deconvolution, and (f): Captured signals in all sensors after low-pass filtering with 1500 Hz cut-off frequency

Pole 14

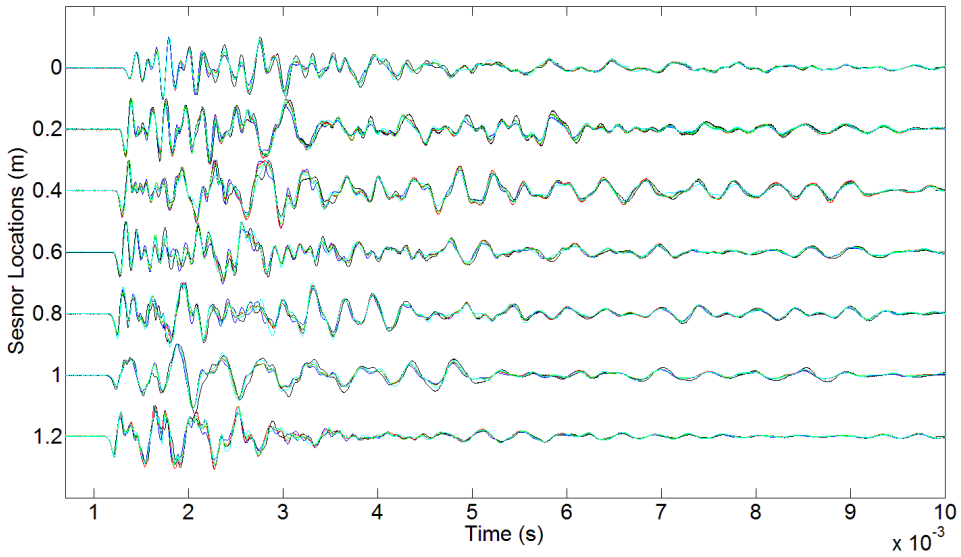

(a)

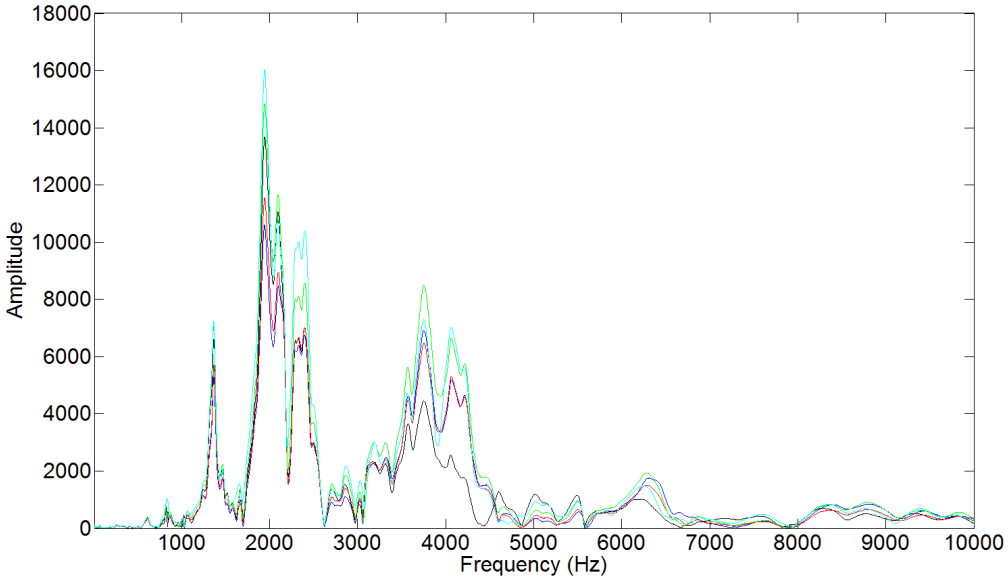
Amplitude
Frequency (Hz)
18000
16000
14000
12000
10000
8000
6000
4000
2000
0
1000
2000
3000
4000
5000
6000
7000
8000
9000
10000

(b)

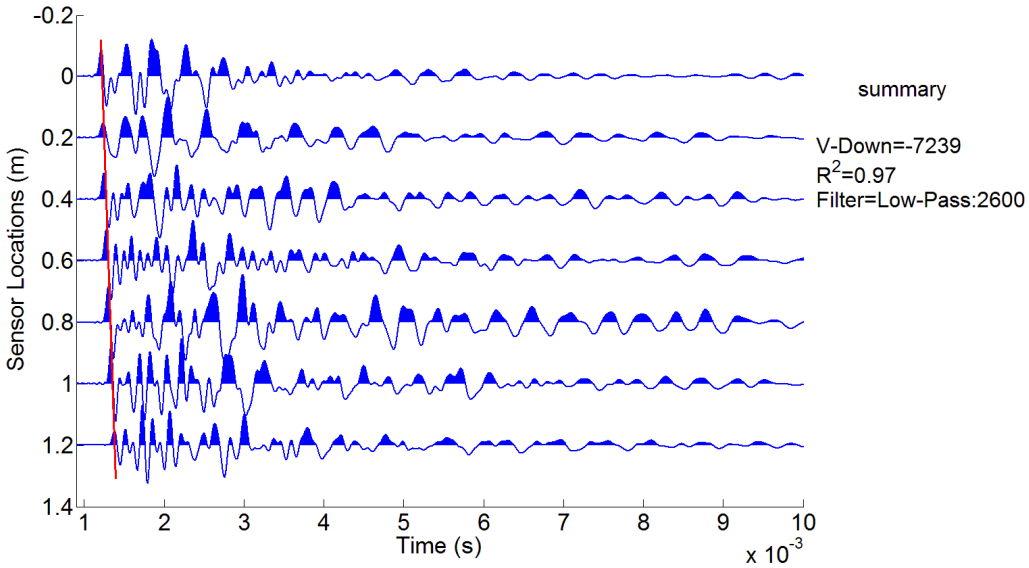
Sensor Locations (m)
Time (s)
x 10^-3
-0.2
0
0.2
0.4
0.6
0.8
1
1.2
1.4
1
2
3
4
5
6
7
8
9
10
summary
V-Down=-7239
R2=0.97
Filter=Low-Pass:2600

(c)

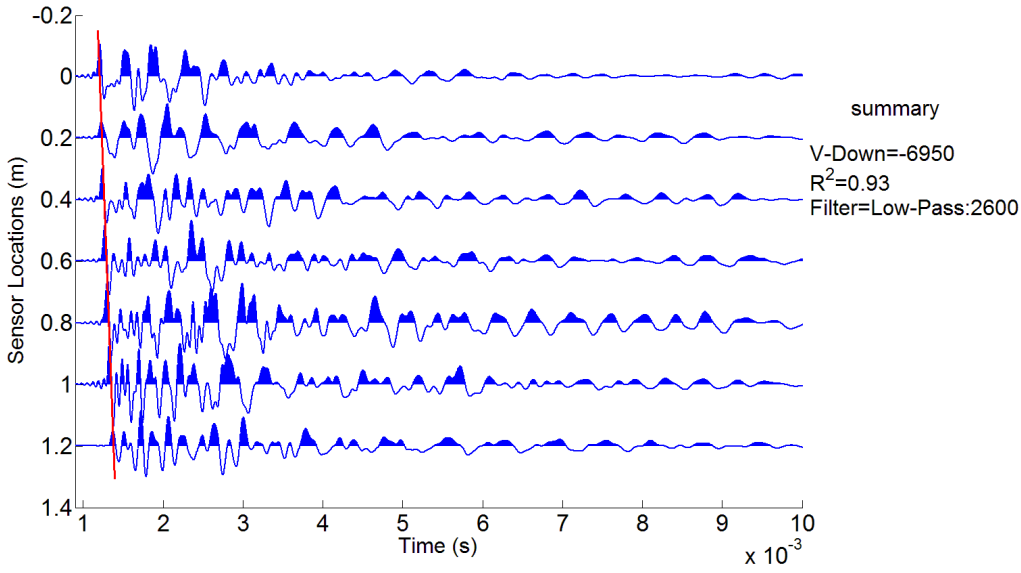

(d)

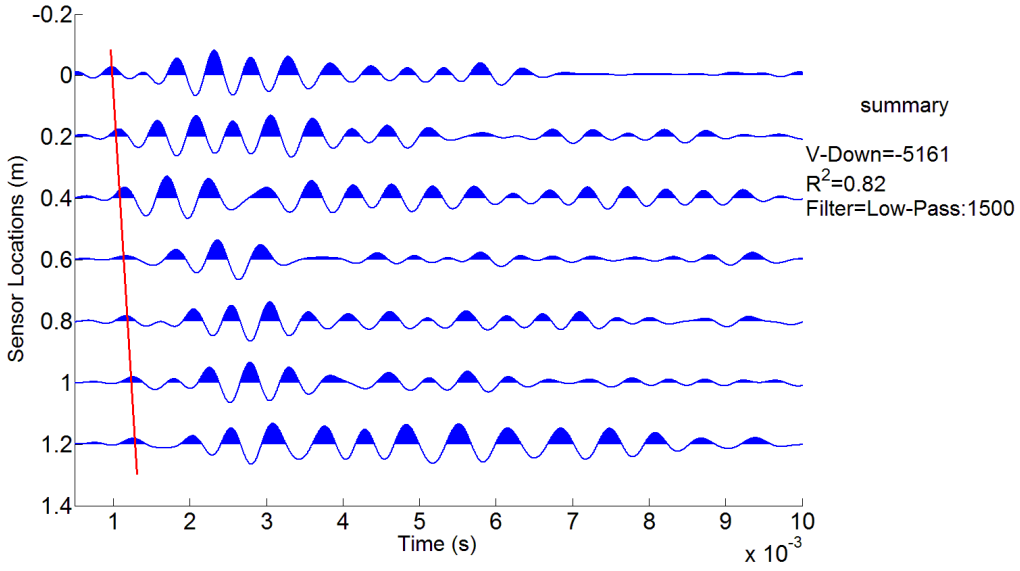

(f)

Figure B. 14: (a) Repeatability of the five tests in all sensors, (b): FFT of all sensors, (c): Captured signals in all sensors after low-pass filtering with 2600 Hz cut-off frequency, (d): Captured signals in all sensors after low-pass filtering with 2600 Hz cut-off frequency followed by predictive deconvolution, and (f): Captured signals in all sensors after low-pass filtering with 1500 Hz cut-off frequency

Pole 15

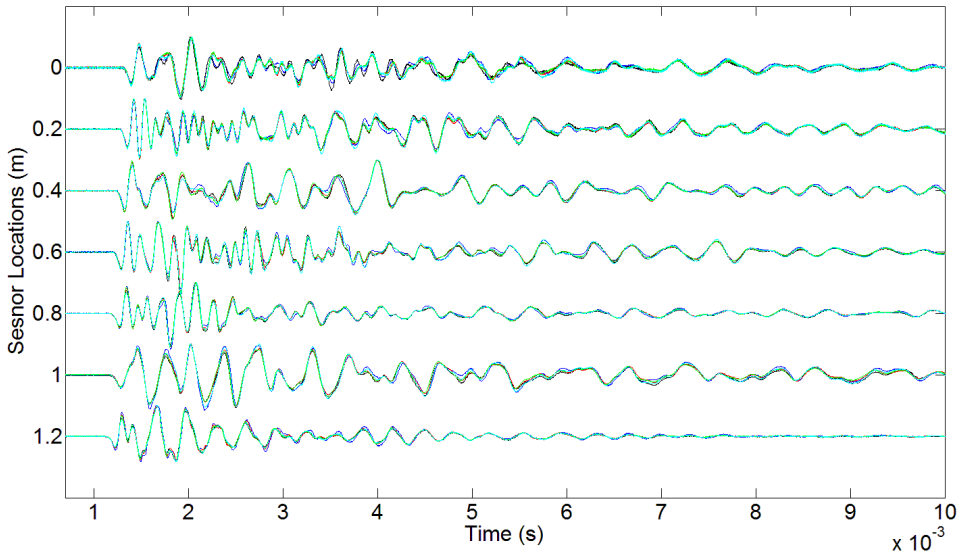
Sesnor Locations (m)
0
0.2
0.4
0.6
0.8
1
1.2
1
2
3
4
5
6
7
8
9
10
Time (s)
x 10^-3

(a)

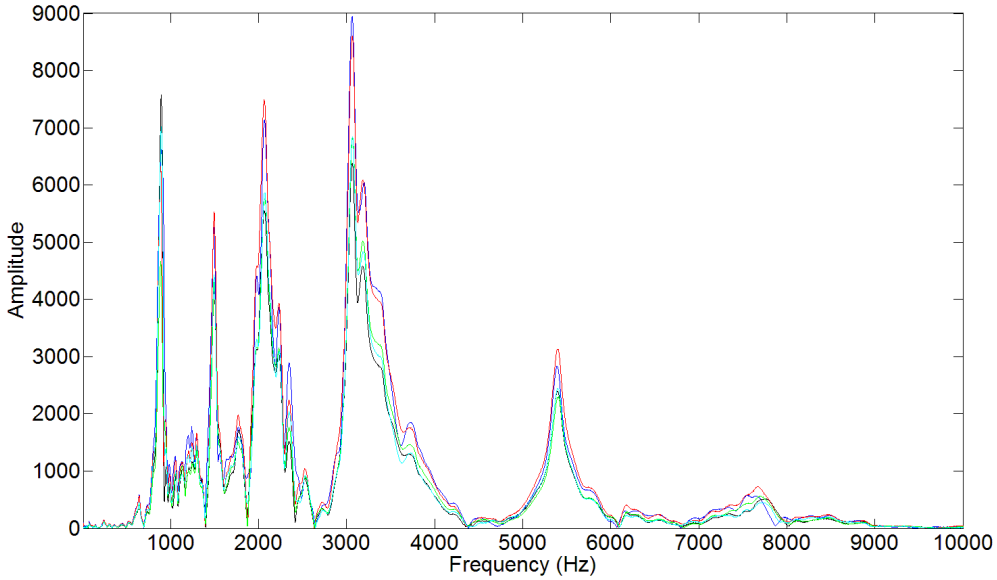
Amplitude
9000
8000
7000
6000
5000
4000
3000
2000
1000
0
1000
2000
3000
4000
5000
6000
7000
8000
9000
10000
Frequency (Hz)

(b)

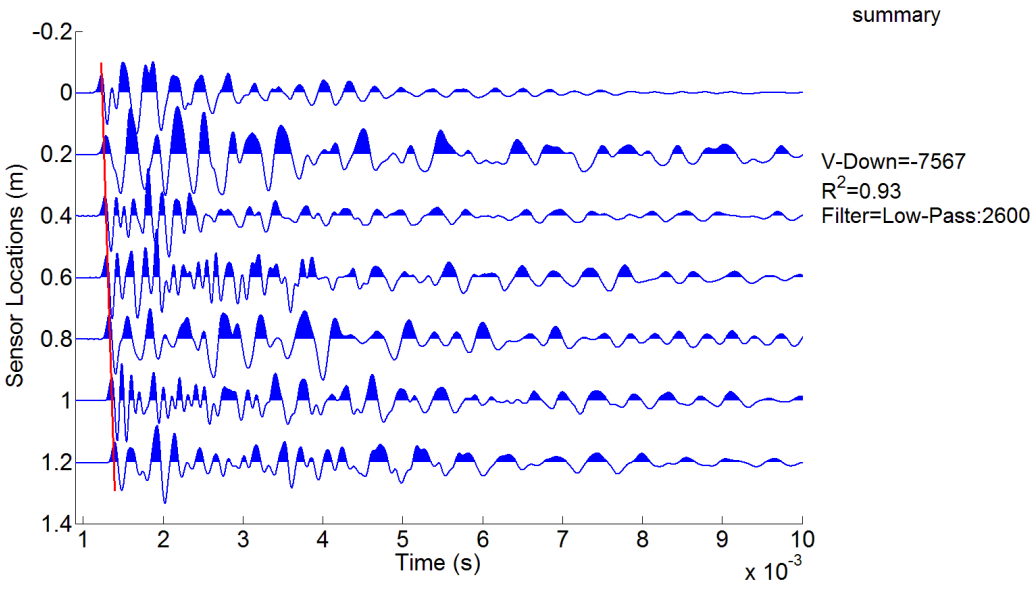
summary
V-Down=-7567
R2=0.93
Filter=Low-Pass:2600
Sensor Locations (m)
Time (s)
x 10-3

(c)

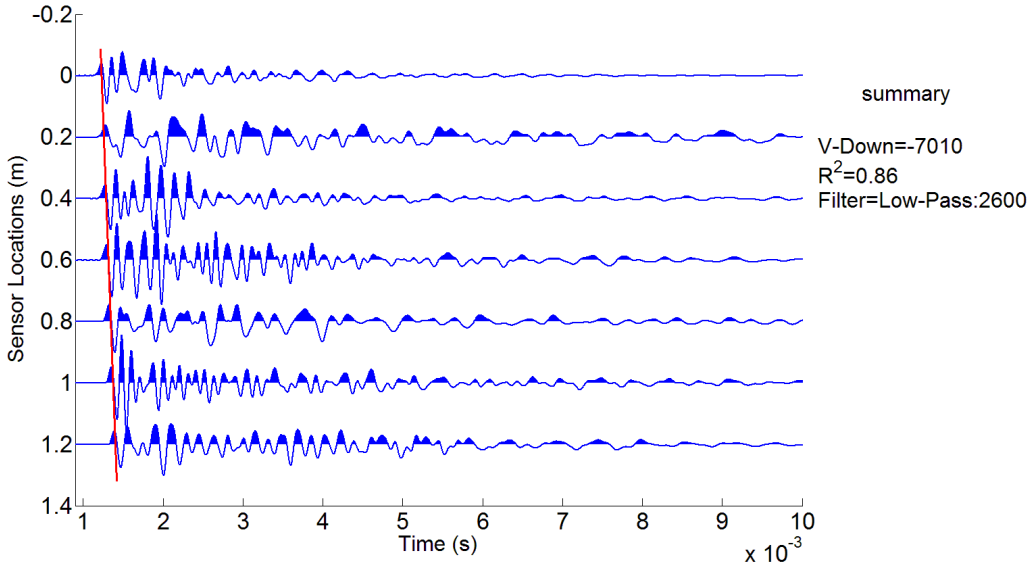
summary
V-Down=-7010
R2=0.86
Filter=Low-Pass:2600
Sensor Locations (m)
Time (s)
x 10-3

(d)

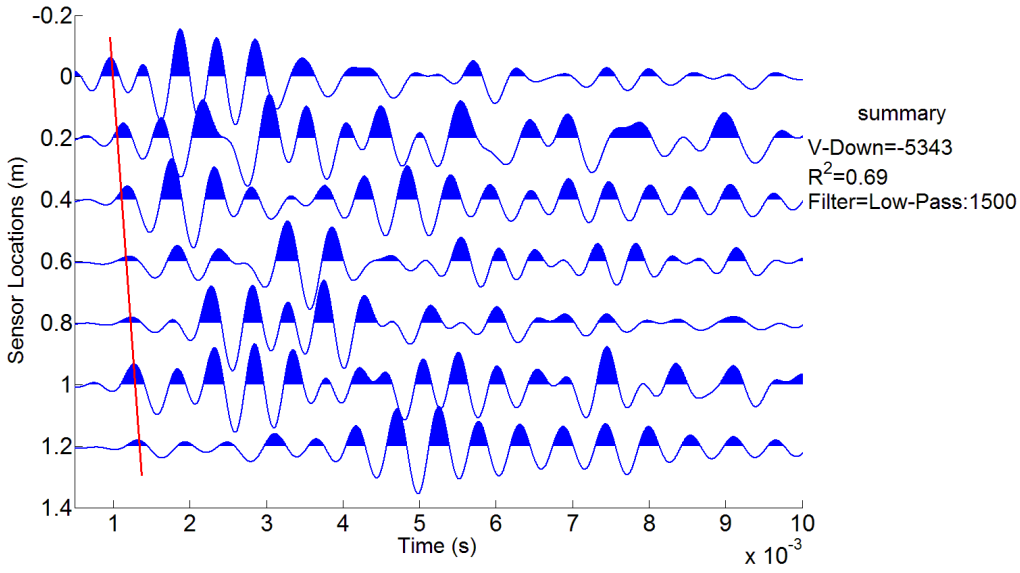

(f)

Figure B. 15: (a) Repeatability of the five tests in all sensors, (b): FFT of all sensors, (c): Captured signals in all sensors after low-pass filtering with 2600 Hz cut-off frequency, (d): Captured signals in all sensors after low-pass filtering with 2600 Hz cut-off frequency followed by predictive deconvolution, and (f): Captured signals in all sensors after low-pass filtering with 1500 Hz cut-off frequency

10 Bibliography

[1] A. G. Davis, "Nondestructive Test Methods for Evaluation of Concrete in Structures," AMERICAN CONCRETE INSTITUTE, Farmington Hills, Michigan ACI 228.2R-98, 1998.

[2] Y. H. Huang and S. H. Ni, "Experimental study for the evaluation of stress wave approaches on a group pile foundation," *NDT and E International,* vol. 47, pp. 134-143, 2012.

[3] R. J. P. Ross, R.F. , "'Nondestructive testing for assessing wood members in structures," in *USDA* vol. FPL-GTR-70, ed, 1994, pp. 1-40.

[4] J. S. Bendat and A. G. Piersol, *Engineering applications of correlation and spectral analysis*. United States: J. Wiley, 1993.

[5] J. M. T. Romano, R. Attux, C. C. Cavalcante, and R. Suyama, *Unsupervised Signal Processing: Channel Equalization and Source Separation*: Taylor & Francis, 2010.

[6] N. Wiener, *Extrapolation Interpolation & Smoothing*: MIT PRESS, 1949.

[7] E. A. Robinson, "Predictive decomposition of time series with application to seismic exploration," *Geophysics,* vol. 32, pp. 418-484, 1967.

[8] I. T. Jolliffe, *Principal Component Analysis*. New york: Springer series in statistics, 2002.

[9] C. C. Aggarwal and C. K. Reddy, *Data Clustering: Algorithms and Applications*: Taylor & Francis, 2013.

[10] H. Yanai, K. Takeuchi, and Y. Takane, *Projection Matrices, Generalized Inverse Matrices, and Singular Value Decomposition*: Springer, 2011.

[11] T. E. Michaels, J. E. Michaels, and M. Ruzzene, "Frequency-wavenumber domain analysis of guided wavefields," *Ultrasonics,* vol. 51, pp. 452-66, May 2011.

[12] K. H. Crews, A. , "'Strength assessment of timber utility poles in Australia," *New Zealand Timber Design Journal,* vol. 9, 2000.

[13] H. Kent, "Options for the continued supply of power poles," Queensland Department of Primary Industries and Fisheries, Presentation for the March 2006 Australian Wood Pole Resources Workshop2006.

[14] L. N. Francis, J., "'A Review–Australian Timber Pole Resources for Energy Networks," Department of Primary Industries & Fisheries2006.

[15] A. Zad, "Determination of Embedded Length and General Condition of Utility Poles Using Non-Destructive Testing Methods " PhD, Univerisyt of Technology Sydney, 2014.

[16] D. W. Green, Winandy, J.E. & Kretschmann, "Mechanical properties of wood," in *Wood handbook: wood as an engineering material*, ed. Madison. WI.: USDA Gen., 1999.

[17] R. Falk, Patton-Mallory, M. & McDonald, K. , "Nondestructive testing of wood products and structures: state-of-the-art and research needs," presented at the Nondestructive Testing and Evaluation for Manufacturing and Construction, New York, 1990.

[18] B. D. Stockton, "Unguyed Distribution Poles – Strength Requirements," Department of Agriculture: Rural Utilities Service2003.

[19] M. Nguyen, Foliente, G. & Wang, X.M. , "State-of-the-Practice & Challenges in Non-Destructive Evaluation of Utility Poles in Service," *Key Engineering Materials,* vol. 270, pp. 1521-8, 2004.

[20] R. J. Ross, Pellerin, R.F., Volny, N., Salsig, W.W. & Falk, R.H. , "Inspection of timber bridges using stress wave timing nondestructive evaluation tools," USA1999.
[21] L. Cartz, *Nondestructive Testing: Radiography, Ultrasonics, Liquid Penetrant, Magnetic Particle, Eddy Current*: Asm International, 1995.
[22] D. Ensminger and L. J. Bond, *Ultrasonics: Fundamentals, Technologies, and Applications, Third Edition*: Taylor & Francis, 2011.
[23] D. O. Thompson, and D. E. Chimenti, eds., "Review of Progress in Quantitative Nondestructive Evaluation," in *Plenum: AIP Conference*, 1980-2009.
[24] C. M. V. Tanasoiu, C. Tanasoiua, "Nondestructive Testing Techniques and Piezoelectric Utrasonics Transducers for wood and Built-in wooden structures," *Journal of Optoelectronics and Advanced Materials Vol. 4,* vol. 4, pp. 949 - 957, 2002.
[25] M. Larry, D. Olson, F. Jalinoos, and M. F. Aquad, "Determination of Unknown Subsurface Bridge Foundation," presented at the International Water Resources Engineering Conference, Memphis, Tennessee, USA, 1998.
[26] P. S. LLC. (2010). Available: http://www.parkseismic.com/Whatisseismicwave.html
[27] J. Paquet, "Etude Vibratoire des Pieux en Beton: Reponse Harmonique et Impulsionelle, Application au Controle," *Annales de L'Institut Technique du Batiment et Des Travaux Publics,*1968.
[28] J. Steinbach and E. Vey, "Caisson Evaluation by Stress Wave Propagation Method," *Journal of the Soil Mechanics and Foundations Division,* vol. 101, pp. 361-378, 1975.
[29] H. M. Van koten, P., "Interpretation of Results from Integrity Tests and Dynamic Load Tests," Rotterdam, Balkema1981.
[30] Y. H. Huang, S. H. Ni, K. F. Lo, and J. J. Charng, "Assessment of identifiable defect size in a drilled shaft using sonic echo method: Numerical simulation," *Computers and Geotechnics,* vol. 37, pp. 757-768, 2010.
[31] J.L.Briaud, "The National Geotechnical Experimentation Sites at Texas A&M University: Clay and Sand - A Summary," Texas A&M University, USA1997.
[32] C. Chree, "The Equations of an Isotropic Elastic Solid in Polar and Cylindrical Co-ordinates their Solution and Application," *Transactions of the Cambridge Philosophical Society,* vol. 14, 1889.
[33] A. E. H. Love, *A treatise on the mathematical theory of elasticity*: Cambridge University Press, 2013.
[34] H. Kolsky, *Stress waves in solids* vol. 1098: Courier Dover Publications, 1963.
[35] R. J. Wasley, *Stress Wave Propagation in Solids: An Introduction* vol. 7: M. Dekker, 1973.
[36] G. E. Hudson, "Dispersion of elastic waves in solid circular cylinders," *Physical Review,* vol. 63, p. 46, 1943.
[37] H. N. Abramson, "The propagation of flexural elastic waves in solid circular cylinders," University of Texas at Austin, 1956.
[38] J. Holt, C. Shunyi, and R. Douglas, "Determining lengths of installed timber piles by dispersive wave," Transportation Research Board1994.
[39] J. Holt, "Finding the lengths of installed steel-H-piles by dispersive bending wave propagation methods," in *Fifth International Conference on the Application of Stress-Wave Theory to Piles*, 1996, p. 13.

[40] M. L. Hughes, G. J. Rix, and L. J. Jacobs, "Nondestructive determination of pile tip elevation using modal analysis," in *Non-Destructive Evaluation Techniques for Aging Infrastructure & Manufacturing*, 1998, pp. 522-530.
[41] R. Finno, H. Chao, and J. Lynch, "Nondestructive Evaluation of In Situ Concrete Piles at the Advanced Waterfront Technology Test Sites, Port Hueneme, California, report for the Naval Facilities Engineering Service Center," *Washington, DC, USA,* 2001.
[42] J. D. Holt, "Comparing the Fourier phase and short kernel methods for finding the overall lengths of installed timber piles," Ph.D. 9974566, North Carolina State University, United States -- North Carolina, 1994.
[43] M. F. Aquad and L. D. Olson, "NCHRP 21-5 research results on determination of unknown bridge foundation depths," 1998, pp. 139-144.
[44] E. Olson, "Parallel seismic software guide," O. Instruments, Ed., ed: Olson Instruments, 2006.
[45] H.Y.Wang., "Comparison and Evaluation of Stress Wave Non-Destructive Testing Techniques on Piles," Master, Chao Yang University of Technology, 2003.
[46] E. Olson, "Parallel seismic software guide," Olson Instruments2006.
[47] M. Subhani, "Study on Behavior of Guided Wave Propagation in Utility Timber Poles," PhD, University of Technology Sydney, 2014.
[48] H. Wang, "Theoretical Evaluation of Embedded Plate-Like and Solid Cylindrical Concrete Structures with Guided Waves," PhD, Northwestern University, EVANSTON, ILLINOIS, USA, 2004.
[49] D. Royer and E. Dieulesaint, *Elastic Waves in Solids I: Free and Guided Propagation*: Springer, 2000.
[50] K. F. Graff, *Wave Motion in Elastic Solids*: Dover Publications, 2012.
[51] J. James J. Lynch, "Experimental Verification of Flexural Guided Waves in Concrete Cylindrical Piles," PhD, NORTHWESTERN UNIVERSITY, EVANSTON ILLINOIS, USA, 2007.
[52] M. Subhani, J. C. Li, H. Gravenkamp, and B. Samali, "Effect of elastic modulus and poisson's ratio on guided wave dispersion using transversely isotropic material modelling," *Advanced Materials Research,* vol. 778, pp. 303-311, 2013.
[53] D. Schlichthärle, *Digital Filters: Basics and Design*: Springer, 2011.
[54] V. K. Madisetti, *The Digital Signal Processing Handbook*, Second ed.: CRC Press, 2010.
[55] R. W. S. Alan V. Oppenheim, *Discrete- Time Signal Processing*, third ed.: Prentice Hall, 2009.
[56] T. R. Fasel, "Chaotic Ultrasonic Excitation and Statistical Pattern Recognition for Structural Damage Classification," Doctor of Philosophy, UNIVERSITY OF CALIFORNIA, SAN DIEGO, SAN DIEGO, 2009.
[57] K. Ohta and T. Watanabe, "Quantitative ultrasonic flaw detection by synthetic waveform generator and Finite Impulse Response (FIR) filter," 1996.
[58] V. Alexandria, "Ultrasonic Detection Measurement System Using a Tunable Digital Filter with 4x Interpolator," Malaysia Patent, 2010.
[59] J. L. Y. Lee, "Improved Rolling Dynamic Deflectometer Testing and Analysis Procedures," Doctor of Philosophy, The University of Texas at Austin, Austin, Texas, 2006.

[60] T. Parks and J. McClellan, "Chebyshev Approximation for Nonrecursive Digital Filters with Linear Phase," *Circuit Theory, IEEE Transactions on,* vol. 19, pp. 189-194, 1972.
[61] L. J. Karam and J. H. McClellan, "Complex Chebyshev approximation for FIR filter design," *Circuits and Systems II: Analog and Digital Signal Processing, IEEE Transactions on,* vol. 42, pp. 207-216, 1995.
[62] L. J. Karam and J. H. McClellan, "Design of optimal digital FIR filters with arbitrary magnitude and phase responses," in *IEEE International Symposium on Circuits and Systems Connecting the World., 1996*, 1996, pp. 385-388 vol.2.
[63] I. W. Selesnick, M. Lang, and C. S. Burrus, "Constrained least square design of FIR filters without specified transition bands," *Signal Processing, IEEE Transactions on,* vol. 44, pp. 1879-1892, 1996.
[64] D. Burnside and T. W. Parks, "Optimal design of FIR filters with the complex Chebyshev error criteria," *Signal Processing, IEEE Transactions on,* vol. 43, pp. 605-616, 1995.
[65] K. Steiglitz, T. W. Parks, and J. F. Kaiser, "METEOR: a constraint-based FIR filter design program," *Signal Processing, IEEE Transactions on,* vol. 40, pp. 1901-1909, 1992.
[66] R. W. Ramírez, *The FFT: Fundamentals and Concepts*: Prentice Hall PTR, 1985.
[67] E. D. Katzke, "Nondestructive Evaluation of Asphalt Pavement Surface Layers Using Stress Wave Testing," North Carolina State University., 1997.
[68] J. S. Bendat and A. G. Piersol, "Engineering applications of correlation and spectral analysis," *New York, Wiley-Interscience, 1980. 315 p.,* vol. 1, 1980.
[69] W. A. M. a. A. A. Al-Shuhail, *Processing of Seismic Reflection Data Using Matlab*: Morgan & Claypool, 2011.
[70] Ö. Yilmaz, "Seismic Data Analysis: Processing, Inversion, and Interpretation of Seismic Data ", ed, 2001.
[71] M. R. G. a. R. Fisher, "Applied Seismology: A Comprehensive Guide to Seismic Theory and Application," Tulsa, Oklahoma: PennWell2005.
[72] I. Morozov, "Lectures: Seismology and Ground Penetrating Radar,", 2011.
[73] I. Morozov, "Lecture 8: Convolution," , 2011.
[74] E. A. Robinson., "Predictive decomposition of time series with applications to seismic exploration," PhD, Department of Geology and Geophysics, MIT, USA, 1954.
[75] S. Treitel, "Predictive deconvolution-theory and practice," *Geophysics,* vol. 34, pp. 155-169, 1969.
[76] V. Krishnan, *Probablity and Random Process*: Wiley, 2006.
[77] A. T. Walden, "Robust deconvolution by modified Wiener filtering," *Geophysics,* vol. 53, pp. 186-191, 1988.
[78] C. Hadziioannou, E. Larose, A. Baig, P. Roux, and M. Campillo, "Improving temporal resolution in ambient noise monitoring of seismic wave speed," *Journal of Geophysical Research. Solid Earth,* vol. 116, 2011.
[79] D. J. Jin and J. R. Rogers, "Homomorphic deconvolution," *Geophysics,* vol. 48, pp. 1014-1016, 1983.
[80] M. S. Egan, K. L. Craft, R. Reed, and Anonymous, "Dip-dependent deconvolution," *SEG Abstracts,* vol. 1988, pp. 731-733, 1988.
[81] X. Wang, A. Chaney, M. Martin, M. Perz, and Anonymous, "Surface consistent deconvolution on seismic data with surface consistent noise," *Program with*

Abstracts - Geological Association of Canada; Mineralogical Association of Canada: Joint Annual Meeting, vol. 25, pp. 0-unpaginated, 2000.

[82] S. A. Levin, "Surface-consistent deconvolution," *Geophysics,* vol. 54, pp. 1123-1133, 1989.

[83] D. R. Hutchinson and M. W. Lee, "Processing and attenuation of noise in deep seismic-reflection data from the Gulf of Maine," *Marine Geophysical Researches,* vol. 11, pp. 51-67, 1989.

[84] P. P. G. Bruno and A. Castiello, "High-resolution onshore seismic imaging of complex volcanic structures: An example from Vulcano Island, Italy," *Journal of Geophysical Research B: Solid Earth,* vol. 114, 2009.

[85] T. J. Ulrych, M. Porsani, J. T. Fokkema, W. S. P. Leaney, E. P. Schlumberger, and Anonymous, "Predictive deconvolution in the frequency domain," *SEG Abstracts,* vol. 1988, pp. 727-730, 1988.

[86] B. Jozi, Dackermann, U., Braun, R., Li, J., Samali, B., "Separation of Bi-directional Stress waves for the non-Destructive Condition Assessment of In-service Timber Utility Poles," presented at the The 6th International Conference on Structural Health Monitoring of Intelligent Infrastructure, Hong Kong, 2013.

[87] A. K. Takahata, E. Z. Nadalin, R. Ferrari, L. T. Duarte, R. Suyama, R. R. Lopes, *et al.*, "Unsupervised Processing of Geophysical Signals: A Review of Some Key Aspects of Blind Deconvolution and Blind Source Separation," *Signal Processing Magazine, IEEE,* vol. 29, pp. 27-35, 2012.

[88] M. Bekara and M. van der Baan, "Local singular value decomposition for signal enhancement of seismic data," *Geophysics,* vol. 72, pp. V59-V65, 2007.

[89] S. L. M. Freire and T. J. Ulrych, "Application of singular value decomposition to vertical seismic profiling," *Geophysics,* vol. 53, pp. 778-785, 1988.

[90] V. D. Vrabie, J. I. Mars, and J. L. Lacoume, "Modified singular value decomposition by means of independent component analysis," *Signal Processing,* vol. 84, pp. 645-652, 2004.

[91] V. D. Vrabie, N. Le Bihan, and J. I. Mars, "Multicomponent wave separation using HOSVD/unimodal-ICA subspace method," *Geophysics,* vol. 71, pp. V133-V143, 2006.

[92] Y. Yuan, Y. Liu, J. Zhang, X. Wei, and T. Chen, "Reservoir prediction using multi-wave seismic attributes," *Earthquake Science,* vol. 24, pp. 373-389, 2011.

[93] X.-f. Liu, X.-d. Zheng, G.-c. Xu, L. Wang, and H. Yang, "Locally linear embedding-based seismic attribute extraction and applications," *Applied Geophysics,* vol. 7, pp. 365-375, 2010.

[94] R. B. Bapat, *Linear Algebra and Linear Models*: Springer Verlag, 2000.

[95] M. J.B., "Some Methods for Classification and Analysis of Multivariate Observations," presented at the Proceedings the fifth Berkeley Symposium on Mathematical Statistics and Probability, USA, 1967.

[96] E. W. Forgy, "Cluster analysis of multivariate data: efficiency versus interpretability of classifications," *Biometrics,* vol. 21, pp. 768-769, 1965.

[97] J. Hartigan, *Clustering Algorithms*: Books on Demand, 1975.

[98] J. A. W. Hartigan, M. A., "Algorithm AS 136: A K-Means Clustering Algorithm," *Journal of the Royal Statistical Society,* vol. 28, pp. 100-108, 1979.

[99] J. Yousefi, M. Ahmadi, M. N. Shahri, A. R. Oskouei, and F. J. Moghadas, "Damage Categorization of Glass/Epoxy Composite Material Under Mode II Delamination Using Acoustic Emission Data: A Clustering Approach to Elucidate Wavelet Transformation Analysis," *Arabian Journal for Science and Engineering,* vol. 39, pp. 1325-1335, 2014.

[100] D. Crivelli, M. Guagliano, and A. Monici, "Development of an artificial neural network processing technique for the analysis of damage evolution in pultruded composites with acoustic emission," *Composites Part B: Engineering,* vol. 56, pp. 948-959, 2014.
[101] O. K. Ihesiulor, K. Shankar, Z. Zhang, and T. Ray, "Delamination detection with error and noise polluted natural frequencies using computational intelligence concepts," *Composites Part B: Engineering,* vol. 56, pp. 906-925, 2014.
[102] S. F. Jiang and J. Yao, "Structural damage identification method based on rough set and data fusion," *Gongcheng Lixue/Engineering Mechanics,* vol. 26, pp. 207-213, 2009.
[103] L. Gelman, B. Murray, T. H. Patel, and A. Thomson, "Novel decision-making technique for damage diagnosis," *Insight: Non-Destructive Testing and Condition Monitoring,* vol. 55, pp. 428-432, 2013.
[104] J. Moll, P. Kraemer, and C. P. Fritzen, "Compensation of environmental influences for damage detection using classification techniques," in *Proc. 4th EWSHM*, 2008, pp. 1080-1087.
[105] S. Kabir and P. Rivard, "Damage classification of concrete structures based on grey level co-occurrence matrix using Haar's discrete wavelet transform," *Computers and Concrete,* vol. 4, pp. 243-257, 2007.
[106] F. Mejia, N. Nemati, and A. Nanni, "Data mining scheme for the characterization of AE signals in steel elements subject to fatigue cracking," in *Nondestructive Characterization for Composite Materials, Aerospace Engineering, Civil Infrastructure, and Homeland Security*, 2012.
[107] M. T. Hanna, "Velocity filters for multiple interference attenuation in geophysical array data," *Geoscience and Remote Sensing, IEEE Transactions on,* vol. 26, pp. 741-748, 1988.
[108] PCB Piezotronics, "Impact hammer model 086C03 Installation and Operating Manual," PCB group Co.
[109] G. Fu, *Inspection and monitoring techniques for bridges and civil structures*: Woodhead Publishing Limited, 2005.
[110] L. J. Bond, "Review of existing NDT technologies and their capabilities AGARD/SMP Review of Damage Tolerance for Engine Structures," Non-Destructive Evaluation. AGARD, Luxembourg: AGARD1988.
[111] C. Fritsch and A. Veca, "Detecting small flaws near the interface in pulse-echo," *Ultrasonics,* vol. 42, pp. 797-801, Apr 2004.
[112] G. Trtnik and M. Gams, "Recent advances of ultrasonic testing of cement based materials at early ages," *Ultrasonics,* vol. 54, pp. 66-75, 1// 2014.
[113] A. Praveen, K. Vijayarekha, S. T. Abraham, and B. Venkatraman, "Signal quality enhancement using higher order wavelets for ultrasonic TOFD signals from austenitic stainless steel welds," *Ultrasonics,* vol. 53, pp. 1288-92, Sep 2013.
[114] J. A. Bogas, M. G. Gomes, and A. Gomes, "Compressive strength evaluation of structural lightweight concrete by non-destructive ultrasonic pulse velocity method," *Ultrasonics,* vol. 53, pp. 962-972, 7// 2013.
[115] H.-Y. Yeh and J.-H. Cheng, "NDE of metal damage: ultrasonics with a damage mechanics model," *International Journal of Solids and Structures,* vol. 40, pp. 7285-7298, 12/ 2003.
[116] Y. H. Kim, S.-J. Song, and J. Y. Kim, "A new technique for the identification of ultrasonic flaw signals using deconvolution," *Ultrasonics,* vol. 41, pp. 799-804, 5/ 2004.

[117] R. K. y. R. Raisutis, E. Žukauskas, L. Mažeika, A. Jankauskas, "Application of ultrasonic guided waves for investigation of structural components of tidal power plants," presented at the NDT&E of Composite Materials, 2011.
[118] L. Capineri, H. G. Tattersall, M. G. Silk, and J. A. G. Temple, "Time-of-flight diffraction tomography for NDT applications," *Ultrasonics,* vol. 30, pp. 275-288, 1992.
[119] A. Ruiz, N. Ortiz, A. Medina, J. Y. Kim, and L. J. Jacobs, "Application of ultrasonic methods for early detection of thermal damage in 2205 duplex stainless steel," *NDT & E International,* vol. 54, pp. 19-26, 3/ 2013.
[120] B. Chassignole, R. El Guerjouma, M. A. Ploix, and T. Fouquet, "Ultrasonic and structural characterization of anisotropic austenitic stainless steel welds: Towards a higher reliability in ultrasonic non-destructive testing," *NDT & E International,* vol. 43, pp. 273-282, 6/ 2010.
[121] R. Szymani, McDonald, K.A., "Defect detection in lumber: state of the art," *Forest Products,* vol. 31(11), pp. 34-44, 1981.
[122] W. W. Wilcox, "Detection of early stages of wood decay with ultrasonic pulse velocity," *Forest Products,* vol. 38(5), pp. 68-73, 1988.
[123] J. Cowe, J. Gittins, and D. H. Evans, "Improving performance of pulse compression in a Doppler ultrasound system using amplitude modulated chirps and Wiener filtering," *Ultrasound Med Biol,* vol. 34, pp. 326-33, 2008.
[124] V. Giurgiutiu, "Tuned Lamb Wave Excitation and Detection with Piezoelectric Wafer Active Sensors for Structural Health Monitoring," *Journal of Intelligent Material Systems and Structures,* vol. 16, pp. 291-305, April 1, 2005 2005.
[125] M. Pollakowski, *The Application of the Pulse-compression Technique to Ultrasonic Non-destructive Testing*: Ruhr-University Bochum, 1994.
[126] R. O. M. Toshino, A. Nagemune and K. Nishifuji, "Next generation on-line ultrasonic testing system, using real-time chirp pulse compression processing," in *Materials Science Forum*, 1996, pp. 791-798.
[127] J. E. Michaels, S. J. Lee, J. S. Hall, and T. E. Michaels, "Multi-mode and multi-frequency guided wave imaging via chirp excitations," in *Health Monitoring of Structural and Biological Systems*, 2011, pp. 79840I-79840I-11.
[128] S. J. L. Jennifer E. Michaels, Anthony J. Croxford, Paul D. Wilcox, "Chirp excitation of ultrasonic guided waves," *Ultrasonics,* vol. 53, pp. 265–270, 2013.
[129] K. F. Graff, *Wave Motion in Elastic Solids*: Dover Publications, 1975.
[130] A. Hanifah, "Theoretical evaluation of deep foundation using guided wave approcah " PhD, Northwestern Univ., USA, 1999.